UNIVERSITÉ LIBRE DE BRUXELLES

Gamma-ray and Neutrino Lines from Dark Matter:

Multi-messenger and Dedicated Smoking Gun Searches

Chaïmae El Aisati

Doctoral Thesis in Physics
Service de Physique Théorique – Faculté des Sciences

Thesis Supervisor:
Prof. Dr. Thomas Hambye (ULB)

Doctoral Examination Committee:
Prof. Dr. Juan Antonio Aguilar Sánchez (ULB)
Prof. Dr. Alejandro Ibarra (Technische Universität München, Germany)
Prof. Dr. Carlos Pérez de los Heros (Uppsala University, Sweden)
Prof. Dr. Maxim Pospelov (Perimeter Institute and Victoria University, Canada)
Prof. Dr. Peter Tinyakov (ULB)

Private Defense 18th of January 2018.
Public Defense 2nd of February 2018.

Abstract

Identifying what makes up the Dark Matter is a long-standing problem to which the abundance of gravitational and cosmological evidence fails to answer. Indirect detection techniques have the aim to unveil the nature of Dark Matter by catching and identifying the products of potential decays and/or annihilations. The work exposed in this thesis is in line with this strategy and has for common thread the quest for line(-like) features in the extraterrestrial fluxes of gamma-rays and neutrinos. The motivation behind this specific interest is that, due to the absence of astrophysical counterparts beyond the GeV scale, these features constitute the ultimate probes (also called "smoking guns") of the existence of Dark Matter.

The thesis is organized in three Parts, the first of which is an introduction to the different facets of the Dark Matter conundrum and why it is *not* a trivial issue. The works involving gamma-ray line considerations are gathered in Part II, and those exclusively focusing on neutrino lines in Part III.

Part II focuses on the effective field theory of Dark Matter decay, first in the context of millicharged particles decaying to gamma-ray lines, and then in the context of (neutral and millicharged) Dark Matter decays involving the simultaneous emission of gamma-ray and neutrino lines. In both cases, the simultaneous emission of cosmic rays is unavoidable and the decays are constrained in a multi-messenger fashion. The complementarity of the results obtained is used to derive model-independent constraints on the Dark Matter lifetime, and shows the possibility to exclude or distinguish some specific scenarios on the basis of an explicit experimental conjecture.

After an introduction to the neutrino detection principles and to the operation of the IceCube detector, Part III focuses on two careful searches for spectral features in the neutrino spectrum. The main goal behind these analyses, conducted in two different regions of the energy spectrum but using the same likelihood ratio procedure, is to popularize dedicated energy distribution studies by showing their ability to reach sensitivity levels comparable to—sometimes even going beyond—those obtained with angular distribution studies or even in the context of gamma-ray line searches.

Keywords: Dark Matter, Indirect Detection, Smoking Guns, Cosmic Rays, Gamma-ray Lines, Neutrino Lines, IceCube.

Résumé

L'identification de ce qui compose la Matière Noire est un problème de longue date auquel l'abondance d'évidences gravitationnelles et cosmologiques ne peuvent répondre. Les techniques de détection indirecte ont pour but de découvrir la nature de la Matière Noire en capturant et identifiant les produits de potentielles désintégrations et/ou annihilations. Le travail exposé dans cette thèse s'inscrit dans cette stratégie et a pour fil conducteur la recherche de raies dans les flux extra-terrestres de rayons gammas et de neutrinos. La motivation derrière cet intérêt particulier est que, dû à l'absence d'équivalents d'origine astrophysique au delà de l'échelle du GeV, ces raies constituent les preuves absolues (également appelées "pistolets fumants") de l'existence de la Matière Noire.

Cette thèse est organisée en trois parties, dont la première est une introduction aux différentes facettes de la problématique de la Matière Noire et aux raisons pour lesquelles il ne s'agit pas là d'un banal problème. Les travaux faisant référence aux raies de photons sont rassemblés dans la Partie II, et ceux se concentrant exclusivement sur les lignes de neutrinos dans la Partie III.

La Partie II se concentre sur la théorie effective de la désintégration de la Matière Noire, d'abord dans le contexte de particules millichargées se désintégrant en raies gamma, et ensuite dans le contexte des désintégrations de Matière Noire (neutre et millichargée) impliquant l'émission simultanée de raies de neutrinos et de photons. Dans les ceux cas, l'émission simultanée de rayons cosmiques est inévitable, et les désintégrations sont contraintes par une approche "multi-messagers". La complémentarité des résultats obtenus est utilisée pour dériver des contraintes sur le temps de vie de la Matière Noire qui sont indépendantes des modèles, et montre qu'il est possible d'exclure ou de distinguer des scénarios spécifiques sur base d'une conjecture expérimentale explicite.

Après une introduction aux principes de détection des neutrinos et au fonctionnement du détecteur IceCube, la Partie III se concentre sur deux recherches détaillées de raies dans le spectre de neutrinos. Le but principal derrière ces analyses, conduites dans deux régions différentes de spectre d'énergie mais utilisant la même procédure du rapport de vraisemblance, est de populariser les études consacrées aux distributions d'énergie en montrant leur capacité à atteindre des niveaux de sensibilité comparables à—voire meilleurs que—ceux obtenus sur base d'études de distributions angulaires ou même dans le contexte des recherches de raies de photons gammas.

Mots-Clés: Matière Noire, Détection Indirecte, Pistolet Fumant, Rayons Cosmiques, Raies de Rayons Gammas, Raies de Neutrinos, IceCube.

Acknowledgements

"Yesterday I was clever, so I wanted to change the world.
Today I am wise, so I am changing myself."

— Jalaluddin Rumi

All good things must come to an end, they say. And the last five years that I spent at the Service de Physique Théorique are no exception. In what rather seemed the blink of an eye, I have found myself writing this thesis, eager to share the work done over the past years in a proper and concise doctoral dissertation. In the beginning, as any student who is just starting in this field of research, I thought I could solve the biggest problems of Physics, become famous, get a Nobel prize for my discoveries and live happily ever after. This, obviously, never happened and the little budding researcher in me was soon confronted to the bitter reality of the never-ending chains of problems. With them, my expectations—in terms of scientific achievements—had no other choice than to lower over the course of time, and so I learned to be more humble in both my ignorance and my knowledge of things.

The doctoral training *per se* has been a globally positive experience, but I do not hide the fact that it came with its load of frustrations and stress. Constantly being in a position of problem solving has taught me to think and work systematically, and has made me acquire some level of independence in my quests. In addition, I was delighted not to have to wake up anymore at 6 am on a daily basis, even though this newly acquired flexibility sometimes meant to work on week-ends or late at night, or both. Besides the research, I have had the opportunity to tutor few hours a week master and undergraduate students. On days where the research was not great, they made me feel useful to something.

As you already know, the dissertation that you *may* be about to read—some of you could just be here for the acknowledgements—is the result of several years of labour. Yet, at the end of the day, the "thesis experience" involved not only myself, but also a bunch of people to whom I would like to pay tribute for making it possible.

First things first, I would like to express my deepest gratitude to my supervisor, Thomas Hambye. I started my first year in the group as a master student under his supervision. Even if we barely knew each other back then, when I later that first year explained that I would be interested in pursuing a PhD after the master thesis, he gave me that opportunity and intensively helped me with the different grant applications that were available at the time. Thank you Thomas for making it possible and believing that I would make a good PhD candidate, for your patience during all these

years and your time. I will certainly not forget your kindness and understanding. When the sky once fell down on my head as I could not see the end of the tunnel, they helped me get back on track. Speaking of grants, I gratefully acknowledge the financial support of the FRIA and the Service de Physique Théorique (ULB).

My gratitude also goes to the members of the jury who showed their interest in this work and took the time to carefully read it and comment it. I warmly thank Jean-Marie Frère, Peter Tinyakov, Michel Tytgat, and Laura Lopez Honorez, the other permanent members of the group. Most of you have been involved in earlier stages of my academic education, of which I keep great memories. Your peculiar senses of humour—each of you on a different level—have brightened lectures, journal clubs and seminars. Laura, thank you for bringing so much positive energy and punch. I still wonder how you do it.

Tiziana Scarnà, know that your presence has so many times comforted the shy and insecure student that I was when I joined the group. It felt genuinely great to have someone like you to talk to, work with and get to know on the personal level. Michael Gustafsson, working with you has been a very enriching experience. To this day, your curiosity of things—whether they are related to science or not—amazes me just as your meticulousness and the ability that you have to put your finger on what is wrong. This is undoubtedly where part of the criticism that I have acquired over the past four years finds its roots. Thank you for being the person you are. Camilo García Cely, muchas gracias por ser este súper colega con quien pude hablar de cualquier cosa, sea en Inglés, Francés o en Español. Te deseo todo lo mejor en tu carrera y en tu futuro, te lo mereces. Federica Giacchino, I hope that you enjoyed discussing French grammar—and French in general—with me. I myself learned a number of things while trying to explain them to you. Most importantly, thank you for regularly flooding the office with the divine smell of a fresh italian coffee! I will definitely miss the crackle of your mini-*machinetta* even though I ended up buying my own for home, and I miss even more the genuine friend that you have become.

I would also like to warmly thank Lisa Unger from the Department of Physics and Astronomy in Uppsala, Sweden. PhD student herself, her help has been precious in the framework of the fourth project presented in this thesis. In this context, I also thank the IceCube Collaboration for giving me the opportunity to work on neutrino data. With this project, I was able to illuminate some of the grey zones that I had, and gain a wider knowledge of what experimental science was about. I also thank the kind members of the experimental group at the Iihe for their hospitality, and in particular Catherine, Juan, Jan, and Isabelle, the dark matter team there.

I, of course, do not forget all the other amazing people met at or through the Service de Physique Théorique: the young Luca, Nicolas, Xiaoyong, Fabio, Federico, Lorenzo, Mikaël & Natalie, Simon & Elodie, Sabir, Bryan & Chabe, Lucien, Julian & Rachel, Daniele, Yongchao, Armando, Maxim, Stefano, Sacha, Laurent, Jérémy, Pol, Anne, Samy, Guillaume, Etienne. Thank you everybody for the nice and enriching conversations we had throughout the years, for the dinners, the shared crazy laughs, and the unforgettable wedding parties (congrats again to the newlyweds!). Welcome again to Yoann and Raghuveer, the two post-docs who have joined the group this

year. I wish you successful collaborations in the department. I am also indebted to the secretaries, Isabelle and Sarah, for their kindness, their efficiency and the amazing job that they do in helping us with the paperwork.

Special greetings go to Céline, Gwen, Laure-Anne, Virginie, Sylvie, Rachel, Cédric, Thomas, Amaury and Gaëtan. Céline and Gwen, my college and PhD years would certainly not have been the same without you. Cédric, thanks a bunch for saving me on many occasions of the troubles encountered on my computer, notably back in the days when I could not have a minimal conversation with a computer terminal.

Last but not least, I want to thank friends and relatives for their everlasting support, love and care, for always cheering me up and for their everly-high esteem of me. The list would be very long if I had to name every single one of my supporters, but a few names stand out of from the crowd. Firdaws and Hussein, thank you for making home this place full of love, yet nothing like a long quiet river. From the very bottom of my heart, I now wish to thank my mother, Ouafila. You have supported me since day one, shared my struggles, my happinesses, and done so much more than words can say. Without your presence, your care and your concern, I wonder whom I would have become, and I wonder how I could have survived in this cold and dark Universe. I owe you everything.

Table of Contents

Part II

Part III

Appendices

List of Abbreviations and Acronyms

AMS	Alpha Magnetic Spectrometer
ARA	Askaryan Radio Array
ARIANNA	Antarctic Ross Ice-Shelf ANtenna Neutrino Array
ATWD	Analog Transient Waveform Digitizer
BSM	Beyond the Standard Model
BDT	Boosted Decision Tree
CC	Charged Current
CDM	Cold Dark Matter
CHAMP	CHArged Massive Particle
CL	Confidence Level
CMB(R)	Cosmic Microwave Background (Radiation)
COG	Center Of Gravity
CORSIKA	COsmic Ray SImulation for KAscades
CR	Cosmic Ray
DAQ	Data Acquisition System
DM	Dark Matter
DOM	Digital Optical Module
DOM MB	DOM Main Board
EFT	Effective Field Theory
Eq.	Equation
fADC	fast Analog-to-Digital Converter
FERMI-LAT	FERMI Large Area space Telescope
Fig.	Figure
FRW	Friedmann-Robertson-Walker
GC	Galactic Center
HDM	Hot Dark Matter
HE	High Energy
HESS	High Energy Stereoscopic System
HLC	Hard Local Coincidence
IB	Internal Bremsstrahlung
ICL	IceCube Laboratory
LC	Local Coincidence
ΛCDM	Λ Cold Dark Matter
LE	Low Energy
MC	Monte Carlo
MDM	Mixed Dark Matter
NC	Neutral Current

NFW	Navarro Frenk White
PAMELA	Payload for AntiMatter Exploration and Light-nuclei Astrophysics
PDF	Probability Density Function
PINGU	Precision IceCube Next Generation Upgrade
PMNS	Pontecorvo-Maki-Nakagawa-Sakata
PMT	PhotoMultiplier Tube
QFT	Quantum Field Theory
SD	Spin-Dependent
Sec.	Section
SI	Spin-Independent
SLC	Soft Local Coincidence
SMT	Simple Multiple Trigger
SM	Standard Model
SPATS	South Pole Acoustic Test Setup
(Super) CDMS	(Super) Cryogenic Dark Matter Search
TS	Test Statistic
Tab.	Table
vev	Vacuum Expectation Value
WIMP	Weakly Interacting Massive Particle

List of Figures

List of Tables

Introduction

"A little garden in which to walk, and immensity in which to dream.
At one's feet that which can be cultivated and plucked;
over head that which one can study and meditate upon:
some flowers on earth, and all the stars in the sky."

— Victor Hugo, *Les misérables*

For millenia, the sky has been a tremendous source of questioning, reflexion and concern for human beings. He who gazes into the night sky finds himself hypnotized, with no other choice than to surrender to the call of the infinite. Before the immensity, we are invited to experience fear, excitement, amazement, and above all humility. It bewilders us, and, animated by the curiosity, we have always felt the need to demystify it.

Over the past centuries, great minds, sometimes armed with but a few simple tools, have pushed away the boundaries of our Universe to an unprecedented level. In particular, the XX$^{\text{th}}$ century has marked a new era in research. With high-tech accelerators, satellites and particle detectors of all kinds making their way into the scientists' toolbox, as well as worldwide collaborations seeing the light of the day, fundamental research has never been the same. The frenzied production of new experimental results coupled to the hard work of an army of imaginative theoreticians have led to the development of the Standard Model of Particle Physics in the 1970s, followed by its incorporation into the Standard Model of Cosmology (ΛCDM) in the late 1990s. The latter, a descriptive model of the evolution of the Universe, has shown to be very successful at explaining the experimental data collected to this day.

So, are we done? Have we scientists finally come up with a detailed, comprehensive and global picture, a Theory Of Everything? Of course not. And this may never happen. The journey to ΛCDM has undoubtedly made us acquire priceless knowledge, but only so that we could be aware of the many more gray areas to be addressed. In particular, among the ingredients needed for ΛCDM to be successful, there is *a lot* of matter. How much? A simple and short answer would be "a lot more than can actually be seen", and by "be seen" we refer to the matter that we are familiar with, that which we are made of and whose building blocks are successfully encoded within the Standard Model (SM) of Particle Physics. According to the latest Planck data [1], about 6 times more matter is needed, and this conclusion backs up a little

more than one century of gravitational evidence: from the cosmological to the galactic scales, a non-shining and yet dominant component of matter, commonly referred to as *dark* matter (DM), helps in solving the discrepancies between observations and predictions based on luminosity estimates. Moreover, the fact that DM can address the problem at all scales challenges alternative approaches such as modified gravity. Throughout the thesis, we will take the side of the particle physicist and assume that DM comes in the form of (almost) non-visible, likely cold particles.

Identifying clean detection channels for dark matter is key for a discovery: not only would you open a bottle of champagne, but you would also get to know the DM particle on a personal level. Of the three main detection strategies elaborated over the years (direct, indirect and collider), we will *exclusively* focus on the *indirect* detection of particle DM for as far as this strategy is concerned, clean detection channels are easy to identify. The *smoking guns*, as they call it, sum up to a couple of signatures: mono-energetic fluxes of gamma-rays and neutrinos beyond the GeV scale. Contrarily to sub-GeV energies, where transition processes can create line(-like) features in the photon spectrum and where you also find many sources of neutrinos displaying a cut-off, astrophysical processes are *not* expected to produce any of these features above ~ 1 GeV, justifying why the lines and—to a broader extent—sharp features are interesting probes of the DM particle both in the photon and neutrino realms.

The thesis presented here situates itself in this context of smoking-gun searches for DM. Models involving these features do exist on the dark market, but rather than studying one of them in particular, or a selection of models, our aim is to draw interesting conclusions as model-independently as possible. The effective approach is in a good position to help us achieve that goal, and this is why we will extensively use it in a couple of projects. The reader will also notice that the nature of the projects exposed in this thesis range from theoretical to phenomenological and experimental, reflecting the interests of the author.

The IceCube experiment has generated a *lot* of attention back in 2013, after the Collaboration shed light on the existence of a flux of extra-terrestrial neutrinos [2]. Neutrinos are a natural by-product of astrophysical processes, but a contribution from more exotic scenarios is not excluded. In particular, the very high energies involved for some of the events (>PeV) coupled to the presence of a gap of events just below 1 PeV and a bump around 50 TeV are puzzling (see *e.g.* Ref. [3]). Many people including myself have seen in these features a potential manifestation of particle DM, but unfortunately—in my humble opinion—no study has been conclusive in these terms.

With this in mind, let us now move on to the structure of this dissertation, divided into eight chapters. In **Chapter 1**, the state of the art of the DM conundrum is presented, including many of the experimental aspects related to the DM quest. In **Chapter 2**, we discuss in a model-independent approach the search for gamma-ray lines induced by millicharged DM decay. This includes the development of the effective theory associated to this production and the study of the corresponding phenomenology. In **Chapter 3**, the possibility to produce mono-energetic gamma-rays and neutrinos in a same decay is studied. The effective approach is again used to systematize the analysis of the phenomenology. **Chapters 4** and **5** are respectively

dedicated to introducing the properties of the neutrino and the IceCube detector's architecture and Data Acquisition. With this done, we start by exposing in **Chapter 6** our first search for monochromatic neutrinos and sharp features in a 2-year neutrino sample that IceCube had made publicly available together with the relevant informations needed for such an analysis. In **Chapter 7**, we dive on a serious level into the experimental world through a dedicated analysis which I performed *within* the IceCube Collaboration as an associate member. This work consisted in the extension of an already existing one-year cascade sample to 5 years of data taking. Even if this sounds like a minor task, it was actually far from trivial since the IceCube Collaboration had changed some of its filters between 2011 and 2012, making the adaptation of some scripts used to derive the cascade sample mentioned above a real challenge! We finally close this dissertation with our **General Conclusions**.

Before we begin, you can already find below the list of published articles:

- *Chapter 2:* C. El Aisati, T. Hambye and T. Scarnà, "Can a millicharged dark matter particle emit an observable gamma-ray line?," 23 pp, JHEP **1408** (2014) 133 Doi:10.1007/JHEP08(2014)133 [arXiv:1403.1280 [hep-ph]].
- *Chapter 6:* C. El Aisati, M. Gustafsson and T. Hambye, "New Search for Monochromatic Neutrinos from Dark Matter Decay," 12 pp, Phys. Rev. D **92** (2015) no.12, 123515 Doi:10.1103/PhysRevD.92.123515 [arXiv:1506.02657 [hep-ph]].
- *Chapter 3:* C. El Aisati, M. Gustafsson, T. Hambye and T. Scarnà, "Dark Matter Decay to a Photon and a Neutrino: the Double Monochromatic Smoking Gun Scenario," 19 pp, Phys. Rev. D **93** (2016) no.4, 043535 Doi:10.1103/PhysRevD.93.043535 [arXiv:1510.05008 [hep-ph]].

The analysis presented in Chapter 7 will be submitted for publication in the coming months. There is another article that has been published this last year, but we make the choice not to discuss it in this—we believe—"already well-stocked" thesis. In a nutshell, the article consisted in a logical follow-up of the analyses of Chapters 6 and 7, as it was dedicated to the search and study of models that can, thanks to the Sommerfeld enhancement, lead to visible fluxes of monochromatic neutrinos induced by annihilating DM. If the reader happens to have an interest in this topic, he can find the article under the following reference:

- C. El Aisati, C. Garcia-Cely, T. Hambye and L. Vanderheyden, "Prospects for discovering a neutrino line induced by dark matter annihilation," JCAP **1710** (2017) no.10, 021 Doi:10.1088/1475-7516/2017/10/021 [arXiv:1706.06600 [hep-ph]].

Part I
Dark Matter

CHAPTER 1

The Dark Matter Conundrum

"Dark Matter is needed to hold galaxies together. Your mind is a Galaxy. More dark than light. But the light makes it worthwhile."

— Matt Haig, *The Humans*

The twentieth century has witnessed the birth of the DM problem after a long and difficult labor, as it took more than 40 years for the scientific community to eventually recognize the newborn problem and tackle it on a serious level. The first hints of the issue, which can be epitomized as the observation of a discrepancy between the amount of visible matter and that needed to hold visible astrophysical systems together, date back to the works of E. Öpik (1915) [4], J. Jeans (1922) [5] and J. H. Oort (1932) [6] who all studied the motions of stars near our galactic plane. They found that stars with velocities large enough to overcome the gravitational attraction of the *luminous* content of the Galaxy were not escaping it, hence the mismatch. Soon after, F. Zwicky arrived at the same conclusion with a larger system (1933) [7], but even so, not much attention was drawn on these observations until the late 1970s. Around that time, optical and radio measurements of the rotation curves of many galaxies had become available and their flat behaviour at large distances was established on a strong footing [8].

The increasing amount of astronomical data suggesting the presence of large quantities of DM on many scales naturally lead the scientific community to wonder about the very nature of this new form of matter and if it could have taken an important *rôle* throughout the history of the Universe. The following couple of sections that the reader is about to peruse explain why DM (cold DM in particular) is a blessing to cosmologists. Moreover, and in contrast to alternatives like modified gravity, the appeal of the DM hypothesis resides in its unique ability to intervene and unravel discrepancies over a wide range of scales and times. The thesis falling in this line of thought, we start by reviewing some of the key evidence for the existence of DM. Since we also assume that the DM is made of particles, we then adopt the point of view of the particle physicist by discussing the constraints that a particle must satisfy in order to be a *good* DM candidate. We also devote a section to some of the theoretical aspects of model-building and effective field theory, which we will come across later on. Lastly, we give an overview of the experimental efforts aiming at detecting DM other than gravitationally and discuss smoking-gun signatures. The latter have inspired all of my PhD projects, which are exposed in Parts II and III.

1.1 Cosmological Evidence

The main success of modern cosmology is undeniably the elaboration of a standard cosmological model that shows incredible agreement with data. This model, called Lambda Cold Dark Matter (ΛCDM), is the fruit of a successful marriage of the Standard Model of Particle Physics with statistical physics and General Relativity. The result is a description of the Universe in terms of the Friedmann-Robertson-Walker (FRW) metric—at first order—and whose evolution is dictated by that of the energy content: matter (baryons, leptons, possibly DM), radiation and dark energy—to which the Λ in ΛCDM refers. Today, DM and dark energy are responsible for most of the energy budget of our Universe. The quantitative appreciation of this statement is realised through the density parameters Ω_X defined as the ratio of the energy density of component X to the critical energy density ρ_c:

$$\Omega_X \equiv \frac{\rho_X}{\rho_c}, \quad \text{with} \quad \rho_c \equiv \frac{3H_0^2}{8\pi G}, \tag{1.1}$$

where G is the gravitational constant and $H_0 = (67.74 \pm 0.46)\text{km}/(\text{s Mpc})$ gives the measured Hubble rate today at 1σ CL [1]. Different experiments may be sensitive to one or several of the ΛCDM parameters. The PLANCK Collaboration, which is the current leader in the field, provides the finest measurements of these parameters. We report here their latest results (central values, the "0" subscript refers to the quantity *today*), obtained from a fit to the Cosmic Microwave Background Radiation (CMBR), lensing and Baryon Acoustic Oscillation data [1]:

$$\Omega_{\text{m},0} = 0.3089, \quad \Omega_{\text{DM},0} = 0.2602, \quad \text{and} \quad \Omega_{\Lambda,0} = 0.6911. \tag{1.2}$$

Besides these results, structure formation data also provide strong evidence for DM and are discussed in the second part of this section, after we overview the physics of the CMB. To give the reader some markers, and even if we will not discuss them all, a timeline of the important events taking place in the early Universe is presented in Fig. 1.1.[1] Astrophysical hints are discussed in the next section.

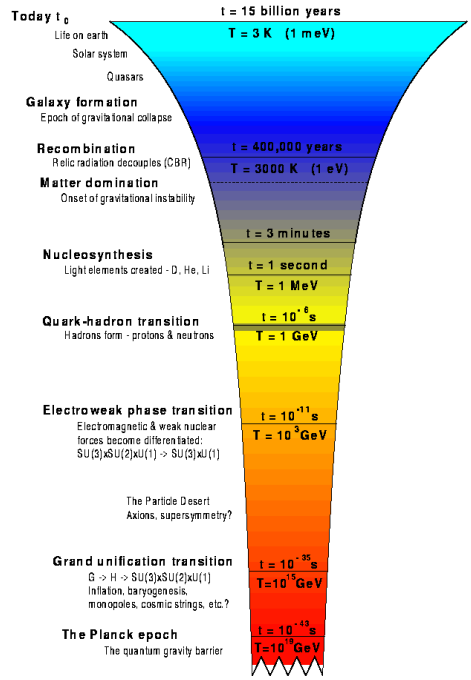

Figure 1.1: A "brief" outline of the chronology of the Universe. Picture taken from [9].

[1] To quench his thirst, the reader is referred to the usual textbooks in the field, such as Refs. [10, 11, 12].

1.1.1 The Cosmic Microwave Background

The accidental discovery of the CMBR by A. Penzias and R. Wilson in 1964 [13] is akin to a little revolution in the field of cosmology. The observation of this radiation with the properties predicted little before and independently by strong advocates of the Big Bang [14] ruled out once and for all the Steady State model—the Universe is, has been, and will always be the same—in favour of the Big Bang model—the Universe started in a hot and dense state before expanding. The reach of the discovery goes even beyond this "mere" result, for it was soon realised that the CMB fluctuation pattern was far from innocuous, triggering the development of very precise instruments—examples include Cobe, Wmap and Planck—to map the CMB sky. Nowadays, analysing CMB data has become the most sensitive way to extract the value of cosmological parameters. So, how is the information extracted from the CMB map? In particular, how is it linked to the DM density parameter Ω_{DM}?

For the observers that we are, the CMB temperatures lay on a two-dimensional sphere. Let us then denote by $\Delta T(\theta, \phi)$ the temperature difference measured in the direction ($\sin\theta\cos\phi$, $\sin\theta\sin\phi$,$\cos\theta$) with respect to $T_0 = 2.725$ K, the average temperature (θ and ϕ denote usual angles in a spherical coordinates system). It should be noted that the CMB is very uniform and deviations from T_0 only start to be observed below the 10^{-5} level. As any other function on the sphere, $\Delta T(\theta, \phi) \equiv T(\theta, \phi) - T_0$ can be decomposed over the basis of spherical harmonics, the so-called Y_{lm}s:

$$\Delta T(\theta, \phi) = \sum_{l \in N} \sum_{m=-l}^{m=+l} a_{lm}\, Y_{lm}(\theta, \phi) \tag{1.3}$$

This decomposition is comparable to a Fourier transform in a curved space (here, a sphere) with some of the borders identified (hence a series in place of an integral). The a_{lm}s are naturally referred to as the *harmonic* coefficients of the expansion and their knowledge $\forall\ l, m$ is equally valuable to the knowledge of T everywhere on the sphere.[2] There is thus no loss of information by storing the a_{lm}s instead of $T(\theta, \phi)$, and the inversion is easy:

$$a_{lm} = \int_0^{2\pi} d\phi \int_0^{\pi} \sin\theta\, d\theta\, \Delta T(\theta, \phi)\, Y^{\star}_{lm}(\theta, \phi). \tag{1.4}$$

As l increases, the behaviour displayed by the spherical harmonics is more and more oscillatory and, together with the corresponding a_{lm}, they reproduce more and more of the details of the CMB map. For instance, the spherical harmonic with $l = 0$ is a constant function over the entire sphere, actually corresponding to the average CMB temperature T_0. The fluctuations around this value are stored in the higher momenta ($l > 0$). Even if this approach in terms of harmonic coefficients does not look natural at first, it ends up being a very useful one, for it gives the ability to isolate what happens at a given angular scale $\theta \sim \pi/l$. It is also widely used for image processing under

[2] In practice, "real" detectors have a finite resolution. Therefore, the knowledge of the harmonic coefficients up to some l_{max} is enough to reconstruct the map (the better the resolution, the higher the l_{max}). All coefficients with a higher l than l_{max} would provide sub-resolution information not accessible by the detector whatsoever.

what is generically called "inverse problems". We are just dealing with one of their many applications.

Pragmatically, we only have one Universe to sample the a_{lm}s from. This limitation is fortunately overcome because the a_{lm}s follow the same distribution at a given l (no matter the m), meaning that we can extract their distribution using different patches of our sky. A relevant observable should give us an idea of the typical fluctuation on a given scale. It is therefore defined through the variance of the harmonic coefficients:

$$\langle a_{lm}\, a^{\star}_{l'm'} \rangle = \mathcal{C}_l\, \delta_{ll'}\, \delta_{mm'}, \tag{1.5}$$

giving

$$\mathcal{C}_l = \frac{1}{2l+1} \sum_{m=-l}^{m=+l} \big\langle |a_{lm}|^2 \big\rangle . \tag{1.6}$$

On top of considerations such as the instrumental resolution and noise—which we do not discuss—, there exists an intrinsic error associated to the measurement of $\mathcal{C}_l$, given by $\Delta\mathcal{C}_l = \sqrt{2/(2l+1)}$. This quantity is referred to as the *cosmic variance* and simply reflects the fact that at lower l, less independent patches are available in the sky to sample the a_{lm}s, resulting in a less precise estimation of the variance of their distribution. This effect is clearly visible in the power spectrum measured by PLANCK, and shown in Fig. 1.2 (growing relative error as we go to lower l).[3] Note the slightly different quantity on the left axis,

$$\mathcal{D}_l \equiv \frac{l(l+1)}{2\pi} \mathcal{C}_l \ , \tag{1.7}$$

which highlights the *Sachs-Wolfe* plateau at low values of the multipole moment l [10]. We decide not to elaborate on this particular feature, and will simply add that because large-scale fluctuations ($l \lesssim 100$) have evolved the least, the plateau reflects the initial conditions set by inflation.

After the plateau, the CMB power spectrum displays a series of peaks and troughs at specific values of the multipole moment l. We are about to see that they are directly linked to the energy content—in particular that of DM—at the time of *recombination*.

The phenomenon behind these features goes under the name of *Baryon Acoustic Oscillations*. Before recombination, photons and baryons[4] were tightly coupled together and behaved as one entity, the baryon-photon fluid. In the presence of the (primordial) quantum fluctuations predicted by inflation, density perturbations are generated here and there, pulling the fluid—via the baryons it contains—towards the corresponding gravitational potential wells. In parallel, the radiation pressure of the photons has a repelling action when they reach a given density, resulting in a bouncing of the photon-baryon fluid between the wells and hills of the total potential. Regions

[3] Even if we will not discuss them, let us add that besides the temperature maps of the CMB, polarization maps also exist and target the study of inflationary models.

[4] Charged leptons are usually left out of the conversation because of their small mass but this does not mean that they were not tightly coupled to the photons as well. As for DM, it does *not* participate in the oscillations of the fluid since it is insensitive to radiation pressure.

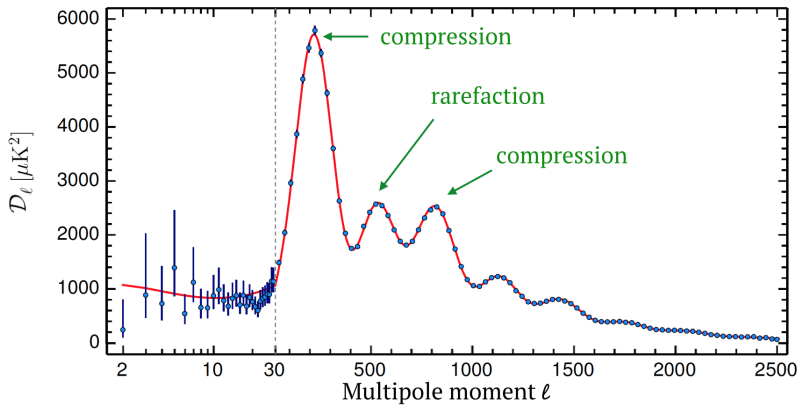

Figure 1.2: The PLANCK 2015 temperature power spectrum (blue) after subtracting foregrounds (such as stars, galaxies, and dust). In red, the output of a standard cosmology (*i.e.* ΛCDM) after a fit to the data. The correspondence of the first few peaks with compression and rarefaction modes of the baryon-photon fluid in the potential wells at recombination is also indicated in green. Note the two different scales on the x-axis (logarithmic below $l = 30$, linear above $l = 100$). Adapted from [1].

of *compression* have a higher temperature T than average, while those of *rarefaction* are colder than average. Obviously, the location of these regions varies with time, but it is only when recombination happens that photons and baryons decouple and that an actual "picture" of the fluid is taken and sent to us via the now free-streaming photons. The story goes a little different for baryons as they continue aggregating in the potential wells, eventually giving birth to the highly non-linear structures (planets, stars, galaxies, . . .) that we observe today.

The dynamics of the bouncing baryon-photon fluid, similar to that of a mass in a gravitational potential and attached to a spring (with the top end of the spring fixed), can be decomposed into a series of independent modes of oscillation $k \in \mathbb{R}$.[5] Those modes k which were at the maximum of their oscillation at recombination contribute to the largest temperature fluctuations ΔT observed in the CMB. Moreover, each of these modes is responsible for a peak, while those modes caught at zero everywhere do not contribute at all; and those in between are in great part responsible for filling in the gaps between the peaks. The location of the first *acoustic peak* is given by the first mode k_1 that entered the horizon and got caught at a maximum of its oscillation by the time of recombination, more precisely at its first compression. This first mode k_1 can be expressed in terms of the sound speed in the baryon-photon plasma as:

$$k_1 = \frac{\pi}{c_s\ t_{\text{decoupling}}}, \tag{1.8}$$

where c_s is the speed of sound and $t_{decoupling}$ the time of decoupling.[6] Quite obvi-

[5] By independent, we mean that the oscillations can be studied mode by mode because the relevant equations of motion are decoupled.

[6] This relation is valid under the assumption of adiabatic perturbations.

ously, multiple integers of k_1 are also caught at their full extension, giving the next acoustic peaks. We denote these modes by $k_n = n\, k_1$, with $n \in \mathbb{N}$. Beware that odd peaks correspond to modes ending up in a compression at the wells (odd n), whilst even peaks are caused by modes ending up in a rarefaction at the wells (even n).[7] The passage from spatial inhomogeneities—characterized by the comoving wavelength $\lambda_n \sim \pi/k_n$—to the angular inhomogeneities of our CMB sky in terms of an angle θ_n is just a matter of geometry. At a comoving distance $d_{\rm A}$, far enough from the last scattering surface, we can write that:

$$\theta_n \approx \lambda_n / d_{\rm A}(t_{\rm decoupling}), \;\; \text{and} \;\; l_n \approx \pi/\theta_n, \tag{1.9}$$

giving $l \sim 200$ as the location of the first acoustic peak. The peaks are shifted towards higher or lower l if we respectively decrease or increase the value of the curvature. This is because curvature has a direct effect on the geodesics, making a given object or length look smaller (larger) than it really is when the space-time is open (closed). The measurement of the location of the peaks (the first one in particular) gives thus a clean access to the curvature parameter. Experimentally, the data is in very good agreement with a flat geometry (at the percent level, see Tab. 4 in Ref. [1]). To make inferences about the baryon content, it is necessary to include the second peak and compare its height to the first one. Indeed, the more the baryons, the higher the odd peaks. This is easily understood with our analogy of the mass attached to a spring and bouncing back and forth in the gravitation potential field. As nicely depicted in Fig. 1.3, more baryons (the larger mass) go deeper in the potential wells, increasing there the level of compression—correspondingly, the level of rarefaction at the potential hill. As they bounce up, both masses (see figure) reach the same level of compression at the hill, that is to say the same level of rarefaction at the well. The odd peaks of the CMB spectrum are therefore increased with respect to the even ones, and it is possible to extract Ω_b from the ratio of the first to the second acoustic peak. Adding baryons also slows down the oscillations, slightly shifting the position of the peaks to higher l. Another effect, clearly visible starting from the third peak, is the exponential *damping* of the spectrum ($l \gtrsim 1000$). This is partly caused by the non-zero mean-free path of the photons during recombination (which is not strictly speaking an instantaneous process), and so they are more efficient at erasing the small-scale structures in the CMB by equilibrating their temperatures. Last, but certainly not the least, it is possible to extract some information on $\Omega_{\rm matter}$—and so, on $\Omega_{\rm DM}$—by taking the third peak into account. Because of the damping, a third peak with a similar or higher intensity than the second one—as is the case experimentally—indicates the presence of extra-matter that provides the gravitational potential necessary to enhance the compression phases in the wells, and by that the third peak.

It is possible to perform a consistency check by looking at the damping scale. We have already highlighted the influence of Ω_b on this scale. Adding more matter influences the age of the Universe at recombination, and therefore the distance that photons can travel. Lastly, curvature has a direct effect on their mean-free path. The starting point of the damping being sensitive to $\Omega_{\rm curvature}$, Ω_b and $\Omega_{\rm matter}$, it is a great

[7] We specify where it happens because a compression in a well is automatically associated to a rarefaction in the corresponding hill—which then contributes to the same peak—, and *vice-versa*.

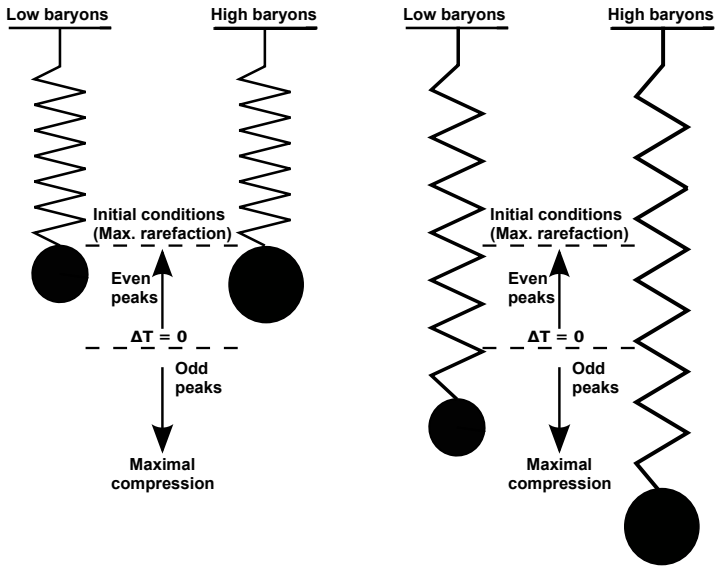

Figure 1.3: The effect of baryon loading on the acoustic peaks. The subfigures give a snapshot of the oscillation at a time when maximum compression is achieved in (left) the potential hill and (right) the potential well. In each panel, the cases of low and high baryon densities, respectively represented by the small and large mass, are confronted. *Left:* Both masses start at the top of the hill of the potential and they come back to the exact same point after any integer number of periods, meaning that baryon loading has no effect on the intensity of the rarefaction phases in the wells. *Right:* The mass loaded with more baryons dives deeper into the potential well, allowing for more compression there. Heavily inspired from Ref. [15].

way to test the consistency of the values inferred with the first three peaks.

The values obtained by the Planck Collaboration have been quoted earlier in this section, clearly showing that DM, even if unidentified, is the dominant form of matter.

1.1.2 Structure formation

Now that we have seen how the BAOs were made responsible for the features displayed by the CMB power spectrum, it is natural to wonder about the existence or not of a counterpart to these features in the distribution of *matter*. To do so, and in the same way that $\mathcal{C}_l$ was introduced—to the difference that we are now working with a 3-dimensional field—let us define the matter power spectrum $P(k)$ via the variance of the Fourier transform of the matter density contrast $\delta(\vec{x})$. That is,

$$\langle\, \delta(\vec{k})\delta(\vec{k}')\,\rangle = (2\pi)^3\, P(k)\, \widetilde{\delta}^3(\vec{k}-\vec{k}') \tag{1.10}$$

with

$$\delta(\vec{x}) \equiv \frac{\rho(\vec{x})-\rho_0}{\rho_0} \;\text{ and }\; \vec{x},\vec{k},\vec{k}' \in \mathbb{R}^3, \tag{1.11}$$

ρ_0 being the average matter density. The $\widetilde{\delta}$ and the $\langle\ \rangle$ symbols respectively denote the Dirac delta function and a volume average. The choice of the absence of vector notation in some places simply comes from isotropy arguments.

The power spectrum $P(k)$ can be defined for a particular component of matter (*e.g.* baryons) or a particular type of structure (*e.g.* galaxies), in which case the corresponding subscript may be appended. Experimentally, we only have access to light—as nicely pointed out by the epigraph of this chapter—, so making inferences on the matter power spectrum is *not* a trivial task. A naive or simple assumption would be that light traces matter—up to some constant factor—, but we know that this cannot be true at all scales.[8] To correctly reconstruct the power spectrum of *all* the matter from galaxy data, computer simulations may be used to estimate the bias [16]. A discussion of the bias issue and a couple other effects that also need to be taken into account in reconstructing the matter power spectrum can be found in Ref. [17]. A more simple way to estimate $P(k)$ is to measure the distance between pairs of galaxies (and repeat that process for as many pairs of galaxies as observed) and plot the corresponding distribution. We measure the degree of clustering by defining the two-point correlation function $\xi(r)$ as the excess probability, with respect to a random distribution, to find a galaxy at distance r from another one [18]. It can be shown that $\xi(r)$ is related to $P(k)$ through the following expression [11]:

$$\xi(r) \;=\; \frac{1}{2\pi^2}\int dk\; k^2 P(k)\frac{\sin(kr)}{kr}, \tag{1.12}$$

where k is the wave number (the same as that involved earlier in Eq. (1.10)). Given a model of inflation, it is possible to compute the power spectrum $P(k)$ and perform the above integral to compare it with the observed correlation function (an example of which is shown in Fig. 1.4). It is also possible to compare $P(k)$ to the observed spectrum, in which case the inversion of Eq. (1.12) requires the knowledge of $\xi(r)$ at all scales. In practice, $\xi(r)$ can be approximated by a power-law [16],

$$\xi(r) = \left(\frac{r}{r_0}\right)^{-\gamma},\ \text{with}\ r_0 \sim 6\text{h}^{-1}\,\text{Mpc}\ \text{and}\ \gamma \sim 1.8 \tag{1.13}$$

which could then be used as the integrand in the inversion of Eq. (1.12). Given a galaxy, the correlation length denoted by r_0 gives the typical distance at which another galaxy is expected with probability one. We present in Fig. 1.4 the power spectrum $P(k)$ and correlation function $\xi(r)$ recently measured by SDSS-IV with quasars. Beware of the slightly different quantities on the y-axis ($\times r^2$ and $\times k$, respectively), used for enhancing the spectra as the variable on the x-axis increases.

[8] An example of observational evidence against that assumption comes from the fact that galaxy-galaxy and cluster-cluster correlation functions do not look the same.

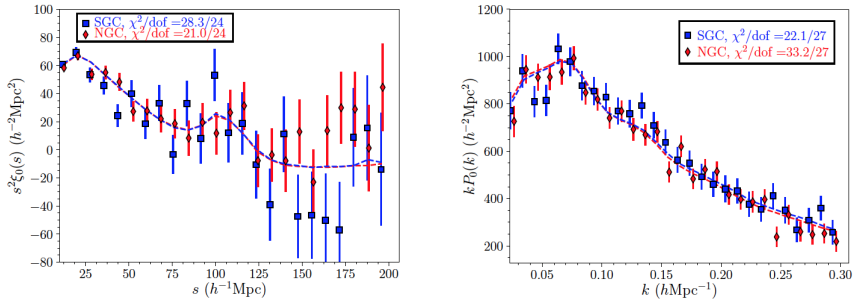

Figure 1.4: Correlation function (left) and matter power spectrum (right) measured by SDSS-IV (2017). The data in red diamond comes from the Northern Galactic Cap (NGC), and that in blue squares from the Southern Galactic Cap (SGC). The dashed curves correspond to the mock samples' mean distribution, with which the level of agreement is given in the top left corners. Both figures are taken from [19].

To understand what is looked for in $\xi(r)$ or $P(k)$, let us discuss a few more things. Take a perturbation mode k outside of the horizon some time when the Universe was still radiation dominated. As long as this mode is outside of the horizon, perturbation growth through gravity is possible, but if it re-enters the horizon when the Universe is still radiation dominated, the growth freezes (existence of a radiation pressure). This picture changes at matter-radiation equality, after which there are no more restrictions on which perturbation mode may or may not grow. Still, recall that photons and baryons are still tightly coupled and all they can do then is oscillate until recombination. The former are then released away and only then may the baryon perturbations finally grow.

In the absence of a large amount of non-baryonic matter, the structures observed today would display fluctuations smaller than the 0.01 % level at recombination—like those of the CMB—, far below the observed 0.1 %. Assuming the presence of non-baryonic matter solves this issue, for this type of matter is insensitive to the photon radiation pressure after equality, providing the deep enough wells for structure formation. Moreover, if there was no DM, the power spectrum should display a harmonic series of bumps—the counterpart of the CMB acoustic peaks—and their absence (see Fig. 1.4) is used to constrain the $\Omega_{\mathrm{baryon}}/\Omega_{\mathrm{matter}}$ ratio.

The horizon size at matter-radiation equality, $\lambda_{\mathrm{horizon}}(\mathrm{t_{eq}})$, can also be extracted because it separates modes which were allowed to grow until then from those which had frozen, and is therefore associated with a change of behaviour in the power spectrum around $k \sim (2\pi)/\lambda_{\mathrm{horizon}}$. The "turnover" point, as they call it, is clearly visible in Fig. 1.4. Note that the peak is located a little further than expected because the spectrum is multiplied by k. The damping at small scales (large k) is analogous to that observed in the CMB spectrum. Note also the presence of a bump in the left figure. The position of this bump gives us an idea of the typical extension of the baryon perturbation shell at decoupling and is therefore used as an estimator of the size of the sound horizon at that time (standard ruler), a quantity sensitive to some of the cosmological parameters [20].

All in all, ΛCDM remarkably fits the large-scale structures (see also Fig. 1.5). More details on what is hiding behind the **Cold** DM statement are presented in Sec. 1.3.4. We also discuss the collisionlessness assumption in Sec. 1.3.5.

1.2 Astrophysical Evidence

1.2.1 Galaxy clusters

The first hint for the existence of DM on galaxy cluster scales is attributed to Swiss astronomer F. Zwicky [7]. Assuming that the cluster is a N-body system that has reached equilibrium—each body corresponds here to a galaxy—, the virial theorem gives:

$$\langle E_{\text{kin}} \rangle = -\frac{1}{2} \langle E_{\text{pot}} \rangle , \tag{1.14}$$

where E_{kin} is the kinetic energy of the system, E_{pot} its potential energy, and the bracket notation denotes the time average of the corresponding quantities. For a system ruled by gravity, Eq. (1.14) can be brought to the following form:

$$\frac{v^2(r)}{2} = \frac{GM(r)}{2r}, \tag{1.15}$$

where $v(r)$ corresponds to the velocity of a body—here, a galaxy—at distance r from the baryo-center of the system, and $M(r)$ denotes the mass contained in a sphere of radius r centered at the baryo-center. Since the behaviour of v as a function of r is in one-to-one correspondence with that of M, Zwicky estimated the velocities of the galaxies in the Coma cluster by simply adding up the masses of its luminous content. With about 800 galaxies ($\sim 800 \times 10^9$ stars) contained in the cluster, a velocity of about 80km/s was expected for the outermost galaxies. The observed value being of ~ 1000km/s, Zwicky invoked the presence of DM to remove the discrepancy. In other words, huge quantities of invisible matter were needed to hold back the cluster. Posterior works have since then confirmed this observation (to a slightly lesser extent, though, since the presence of gas, accountable for ~ 10 times more mass than the galaxies, was not known by Zwicky at the time).

1.2.2 Galactic rotation curves

We have seen in Sec. 1.2.1 how DM was blamed for the large galaxy velocities observed by Zwicky. Well, guess what? Not long after, in 1939, the same kind of observation was made at galaxy scales [21]. Just as galaxies were found with large velocities in the Coma cluster, the observed galactic rotation curve of the Andromeda galaxy M31 did not fall off like expected at large radii ($v(r) \propto r^{-0.5}$), as larger circular velocities were observed. The development of the 21-cm astronomy in the 1950s with leftover dishes from World War II allowed to extend measurements further away from the center, confirming the flat nature of Andromeda's rotation curve and that of many other galaxies (see *e.g.* [22]).

1.2.3 The Local Group timing argument

The Local Group contains around 50 galaxies among which we find the Milky Way and Andromeda M31, 700 kpc away from each other. They are the most massive and most luminous galaxies in the group,[9] and instead of receding away from each other—as we would expect from the Hubble flow—they approach each other at a velocity of about 120 km/s, meaning that the gravitational attraction is large enough to overcome expansion. In 1959, F. Kahn and L. Woltjer estimated that a reduced mass of at least $1.8 \times 10^{12} M_\odot$ was needed to explain the current configuration of the system, a value about 6 times larger than the observed reduced mass of M31 and the Milky Way (gas+stars) [23].

1.2.4 Lensing

Lensing is one of the recently developed techniques aiming at measuring gravitational potentials. The idea behind is that mass bends light trajectories, making background events look distorted. Depending on the level of distortion, gravitational lensing can be classified as:

- **strong** lensing: in that case, distortions are clearly visible (Einstein rings, multiple images and arcs);
- **weak** lensing: the distortions—which are small—of the background objects are looked at statistically;
- or **micro**lensing: distortions are not visible but the intensity of the light received from an object in the background varies with time.

In the context of DM, the most popular system observed with the lensing technique is certainly that of the **Bullet cluster**. The name actually refers to *two* merging clusters observed in the late 1990s by Tucker *et al.* [24]. This event, which took place ~ 100 Myrs ago, provides a unique probe of the existence of DM. During the merger, the galaxies of the two clusters behave like collisionless particles and pass through each other, unaffected, while the two gas components interact, collide and slow down. If there was no DM, a measure of the gravitational potential should be directly correlated with the distribution of the gas, which accounts for ~ 10 times more mass than the galaxies. The results of the weak-lensing analysis performed in 2006 by Clowe *et al.* [25] show that most of the gravitating mass is centered around the galaxies, meaning that two massive dark halos must have passed through each other as well. That they happen to be superimposed with the concentration of galaxies reflects the collisionlessness of their interactions. A precise measurements of the offset between the potential wells and galaxies may be used to constrain self-interacting DM (see Sec. 1.3).

1.2.5 The small-scale crisis

In Sec. 1.1.2, we have introduced the matter power spectrum $P(k)$ as the relevant observable to study the clumping of matter at different scales $\lambda \sim 2\pi/k$. As can be seen from Fig. 1.5, the standard cosmological paradigm is in excellent agreement with

[9] For this reason, the effect of the other galaxies on the dynamics of M31 and the Milky Way can be ignored in a first approximation.

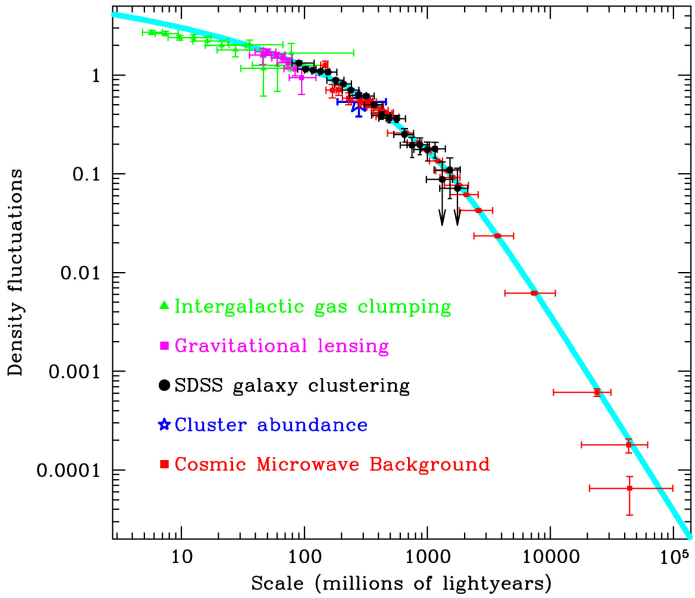

Figure 1.5: Density fluctuations as a function of scale. Compared to Fig. 1.4, this one has the merit to extend to lower scales, where we clearly see that the ΛCDM model (continuous blue line) tends to over-estimate the clumping. The different categories of data used are indicated on the figure. By M. Tegmark (2004) [27].

the observed density fluctuations at large scales, but fails at galaxy and groups of galaxy scales ($\lesssim$ Mpc) where more structures are predicted.

Because the realm of structure formation involves non-linear physics, computer simulations are an important tool for its exploration, if not *the* most important one. Over the years, the *small-scale crisis* of ΛCDM has manifested itself in different astrophysical systems as what seem to be anomalies. We discuss some of the main ones herebelow.

- The **"missing satellite"** problem: N-body simulations of CDM halos and groups of halos predict the existence of subhalos in abundance. Typically, $\mathcal{O}(100-1000)$ subhalos are expected for a halo like the Milky Way, but only $\mathcal{O}(10)$ are observed. For low-mass subhalos, invisibility could be explained by a low star formation rate due to *e.g.* supernovae winds ejecting gas out of the subhalo and inhibiting the collapses there. The faintness and the limited sky coverage of these structures can also be invoked to explain the small observed statistics. Even though the increase of experimental sensitivity could potentially lead to an order of magnitude more detections in the future (see *e.g.* [26]), there is however no apparent reason why high-mass subhalos do not shine. This constitutes part of the "too big to fail" problem, which we discuss at the next bullet.

- The **"too big to fail"** problem: dwarf spheroidal galaxies are known to be objects with one of the highest mass-to-light ratios—black holes aside. As such, they are

expected to host the densest DM halos. Unfortunately, the velocities observed from the Milky Way's brightest dwarf spheroidal ($2 - 25$km/s) are inconsistent with those predicted from CDM-only simulations, which are typically higher than 30km/s. These predicted high-mass DM halos are thus not superimposed with the densest possible objects that we know about. What has happened to them is puzzling, even more puzzling since, in principle, they could not have failed star formation and should be visible: their high densities would have acted against feedback processes which tend to inhibit a collapse.[10] In particular, these high-mass subhalos have a high concentration of DM predicted at their center. This generic feature of halos (and subhalos in general) constitutes the "core-cusp" problem discussed next.

- The **cusp *vs* core** problem: knowing how DM is distributed is essential to any DM-related analysis. The amount of DM inferred from cosmological probes, $\Omega_{\rm DM} = 0.2647$, is a *global* measure of its density. With the formation of structures, *local* over- and under-densities have developed, and these are probed experimentally by observing the kinematics of light-emitting objects such as stars and galaxy satellites. The kinematics of the stars observed in dwarfs and low surface brightness galaxies—these are objects with low backgrounds, even in their innermost part—indicate that the concentration of matter is compatible with cored density profiles. Simulation-wise, the DM density profile increases towards the center, it is said to be *cuspy* (see Sec.1.2.6).

A comprehensive discussion of the small-scale crisis can be found in Ref. [28]. Before jumping to conclusions too quickly and blame ΛCDM for being wrong—which would be sad given its success in many other respects—, we want to stress that our lack of understanding regarding structure formation dynamics is likely the first to blame, and simulations are merely a reflection of this. Recent efforts at incorporating baryon and gas dynamics have led to progress in the field. Until recently, and if implemented, the effect of the baryon dynamics on DM was—undoubtedly for the sake of simplicity—reduced to an "adiabatic" correction, meaning that the gravitational potential is assumed to slowly change with respect to the relevant dynamical time scales. Yet, a galaxy is in general far from quiet, and the adiabatic assumption may hence naturally break down because of the presence of **dynamical frictions** and **outflows**. Part of the energy released by these feedback processes can be passed on to DM.[11] With more energy, the DM distribution migrates to larger radii, solving the core-cusp problem. A short accessible discussion on this topic can be found in [29].

No matter what, a deep understanding of baryon dynamics and their interplay with the DM potential is required on the long term. The consensus is that baryons could partly or completely solve some of the small-scale problems (but not all of them simultaneously). However, the mere fact that simulations need a deep revision does not mean that the assumptions behind the ΛCDM paradigm are not challengeable, and questioning them *as well* is part of the scientific method. In particular, DM properties such as its velocity at decoupling (see Sec. 1.3.4) or the existence of self-interactions

[10] By "feedback processes", we refer to any process that provides energy against collapse. Supernova winds and black hole radiation are two examples of feedback.

[11] Under the assumption of collisionless DM, the transfer is exclusively done through gravitational interactions.

(see Sec. 1.3.5) may impact (positively or negatively) structure formation, and may solve one or more of the problems linked to the smale-scale crisis.

1.2.6 Popular halo density profiles

In this section, we review some of the most popular DM density profiles. Observations show clear evidence for a flattening of the rotation curves at large radii, corresponding to a density distribution $\rho(r)$ falling off as $\sim r^{-2}$. At small radii, there is no generic behaviour observed as mentioned earlier but the tendency remains that of a cored profile. On the other hand, simulations predict a cusp, like the first two profiles exposed below (Eqs. (1.16) and (1.17)). To ease the comparison, they are all plotted as a function of r in Fig. 1.6 (the choice of the different parameters is given in the caption). Note that these profiles share the spherical symmetry, and that we will not consider possible deviations from that assumption (such as elliptical halos).

- **Navarro-Frenk-White** (NFW):

$$\rho_{\rm NFW}(r) = \rho_s \frac{r_s}{r} \left(1 + \frac{r}{r_s}\right)^{-2} \tag{1.16}$$

- **Einasto**:

$$\rho_{\rm Einasto}(r) = \rho_s \exp\left(-\frac{2}{\alpha}\left[(r/r_s)^\alpha - 1\right]\right) \tag{1.17}$$

- **Isothermal**: According to Eq. (1.15) and $\rho(r) = dM(r)/(4\pi r^2 dr)$, this density distribution is suggested by flat rotation curves at large radii ($\rho(r) \propto r^{-2}$).

$$\rho_{\rm iso}(r) = \frac{\rho_s}{1 + (r/r_s)^2} \tag{1.18}$$

  This profile, like the next one, enters in the category of cored profiles (see Fig. 1.6).

- **Burkert**:

$$\rho_{\rm Burkert}(r) = \frac{\rho_s}{(1 + r/r_s)(1 + (r/r_s)^2)} \tag{1.19}$$

The above profiles are normalised so as to recover the local density $\rho_\odot$ of DM at the Sun position $r_\odot$. The value of this density is inferred from galactic dynamics, and the value that we will use in the different analyses is $\rho_\odot = 0.39\text{Gev cm}^{-3}$ (typically in combination with the NFW profile).

1.3 The particle physicist's approach I: constraints on particle dark matter

While it is true that objects like undetected planets, red and brown dwarfs may make up some part of the local DM, they cannot be made responsible for all of the evidence discussed in the previous section. In particular, cosmological data suggests that DM is *non*-baryonic and that it was around at the time of decoupling, long before the formation of any structure. In that respect, we believe it legitimate to think of DM

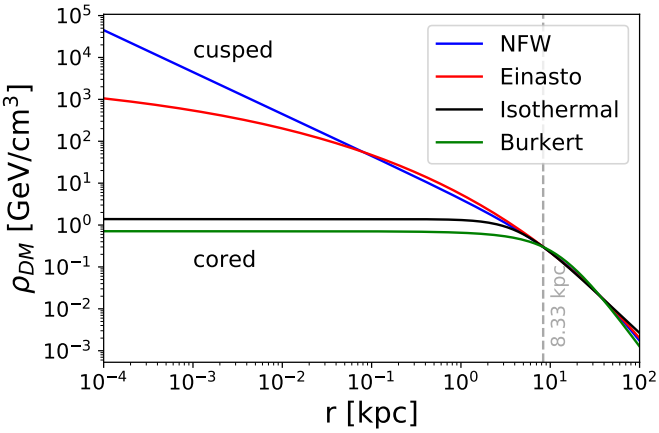

Figure 1.6: A few popular density profiles $\rho(r)$ for the galactic DM halo as a function of r, the distance to the galactic center (GC). Our location, 8.33 kpc away from the GC, is indicated by the vertical gray dashed line. The blue, red, black and green lines respectively correspond to the NFW ($\rho_s = 0.184\text{GeV cm}^{-3}, r_s = 24.42\text{kpc}$), Einasto ($\rho_s = 0.033\text{GeV cm}^{-3}, r_s = 28.44\text{kpc}, \alpha = 0.17$), isothermal ($\rho_s = 1.387\text{GeV cm}^{-3}, r_s = 4.38\text{kpc}$) and Burkert ($\rho_s = 0.712\text{GeV cm}^{-3}, r_s = 12.67\text{kpc}$) profiles.

as made of particles.[12] Again, this is one of the assumptions cherished by this thesis. It is premature to tell whether these particles that make up the DM are elementary or composite, but for sure they have mass. Particle DM, as we will call it now, is a mystery in itself but it does not mean that we know absolutely nothing about it. Not seeing particle DM *also* means that some of its properties are tightly constrained. Yes, whether you are elaborating the most elegant or the most intricate theory, you will have to bear in mind all of these constraints, like a checklist. We propose to review in this section the requirements that lay on the shoulder of particle DM. Fairly quickly, it will become evident why physics beyond the SM is mandatory.

1.3.1 Mass

All of the evidence exposed in the previous section leads to the qualitative statement that particle DM is massive. But is *any* choice of mass fine? In other words, if you are a theoretician, how much room do you have to play with this parameter?

Recall that the smallest observed structures of DM are halos. To avoid their destruction—and *a fortiori* that of larger structures—because of the uncertainty principle of Heisenberg, we want particle DM to behave classically on any scale larger than the typical size of a halo. This requirement of "classicality" is implemented differently depending on the spin considered. Given a mass m_{DM} and typical velocity

[12] The possibility that extended objects account for (part of) the DM is not completely ruled out though. In particular, there is still a mass range where primordial black holes could account for a substantial fraction of the DM [30].

$v = 200$km/s, we ask in the bosonic case for the de Broglie length,

$$\lambda_{\text{de Broglie}} = \frac{h}{m_{\text{DM}} v}, \tag{1.20}$$

where $h = 2\pi$ is the Planck constant in natural units, to be smaller than 1 kpc (a typical dwarf galaxy size):

$$\lambda_{\text{de Broglie}} \lesssim 1\text{kpc}. \tag{1.21}$$

This implies that

$$m_{\text{DM}} \gtrsim 10^{-22}\text{eV}. \tag{1.22}$$

In the case of fermionic DM, the Pauli blocking must be considered as well, and it actually leads to a tighter constraint on m_{DM} than that found at Eq. (1.22), called the Tremaine-Gunn bound [31]:

$$m_{\text{DM}} \gtrsim \mathcal{O}(10)\text{eV}. \tag{1.23}$$

We now turn to the upper limit. The idea behind is that, as DM moves around and passes through galaxies or clusters of stars, a reheating of these structures can take place. Over a long period of time, this reheating is expected to lead to their disruption. The fact that we still find these structures to this day puts the following upper bound on the DM mass [32]:

$$m_{\text{DM}} \lesssim 10^3 M_\odot \sim 10^{70}\text{eV}. \tag{1.24}$$

The reader will agree that our ballpark of viable DM masses is humongous, challenging the imagination of both theoreticians and experimentalists to acquire sensitivity in the largest range of masses possible. A (non-exhaustive) compilation of candidates that have seen the light of day (and the corresponding ranges of masses) is presented in Fig. 1.7.

It should be noted that under the assumption of a thermal relic (see below) and given the Ω_{DM} parameter measured by Planck, the unitarity of the S-matrix sets the following bound on the DM particle mass [33]:

$$m_{\text{DM}} \lesssim \mathcal{O}(100)\text{ TeV}. \tag{1.25}$$

1.3.2 Lifetime

Cosmological data tell us that particle DM was around in the early Universe, at least around redshift $z \sim 1000$. We also know that it is present today by observing the rotation curves of low-redshift galaxies, including ours. If the DM particle is not perfectly stable (because of, *e.g.*, the absence of an exact symmetry forbidding the decay), a set of constraints apply. A first natural and conservative estimate of the room left for decay consists in requiring a lifetime τ_{DM} greater than the age of the Universe τ_U:

$$\tau_{\text{DM}} \gtrsim \tau_U \simeq 4 \times 10^{17}\text{seconds}. \tag{1.26}$$

At first, this may seem like a tight bound, but experimental constraints from indirect detection experiments can actually do better than Eq. (1.26). The limit may also significantly vary depending on the decay channels available (but still above τ_U).

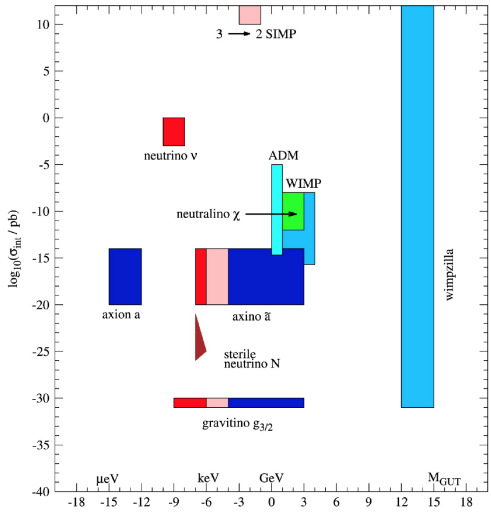

Figure 1.7: Compilation of DM particle candidates together with the mass ranges where they can be found, and their typical scattering cross sections with usual matter. From [34] via [35].

In the projects presented in this thesis, when assuming the decay of DM, we will specifically be interested in final states with monochromatic photons and neutrinos.[13] As we explain in Sec. 1.5.3, these decay channels give the tightest bounds on $\tau_{\rm DM}$ because the corresponding fluxes $d\Phi/dE$ are very peaked around $E = m_{\rm DM}/2$,[14] allowing for more sensitivity to the signal. Almost all of the projects presented in this thesis will involve the derivation of DM lifetime constraints (though in different contexts). We prefer to introduce the relevant limits when necessary, but the value of 10^{27}s can be kept in mind. On theoretical grounds, such a large lifetime presupposes the existence of an exact symmetry (such as $\mathbb{Z}_2$) or *very* weak interactions. The latter can be motivated by new high-energy Physics, in analogy to the modelling of proton decay in the context of grand unified theories (see Sec. 1.4.2).

Before moving on, let us emphasize that the discussion hereabove does not apply—and may consequently be skipped—if you have a perfectly stable DM particle candidate. Also, if your candidate is completely segregated from the SM sector, it will not produce any SM particle in the final state, and in this case only Eq. (1.26) applies.

1.3.3 Charge

In its broad acceptation, the "charge" of a particle refers to the strength of its interactions with a gauge boson. Restricting ourselves to the SM gauge group, particle DM could in principle interact via the electromagnetic, strong and electroweak forces. The first two of these interactions are well constrained, leaving little room for sizable charges.

[13] The "monochromatic" requirement will sometimes be loosened to that of "sharp features".
[14] Modulo *e.g.* reconstruction and electroweak correction effects.

Massive **electrically** charged—and stable—particles, also referred to as CHArged Massive Particles (CHAMPs), are predicted in some extensions of the SM. With a charge of one—and depending on the sign of the charge—, they are able to bind with electrons e^- or α particles to form states that look like heavy hydrogen or even with protons p to form what are called neutralCHAMPs. They have been proposed as DM candidates but dedicated studies have basically ruled them out [36].

Besides the CHAMPs, scenarios where particle DM "naturally" gets a tiny charge also exist, and we review a couple of them in Chap. 2. The DM predicted in this type of scenarios is typically referred to as *mini-* or ***milli*charged** DM. A compilation of the constraints in the (ϵ, m) parameter space, where $\epsilon \equiv |q|/e$ is the millicharge,[15] is given in Fig. 1.8. They come from studies related to the effects of millicharged DM on the CMB, on the neutrino magnetic moment, the Sun, sub-eV cosmology, etc. More details can be found in the references cited in the figure. For the left subfigure, the existence of a dark photon is assumed, but not for the right subfigure. For the sake of clarity and simplicity, we will actually use in Chap. 2 a model-independent bound coming from CMB considerations [37]:

$$|q|/e < 1.8 \times 10^{-6} \left(\frac{m_{\rm DM}}{\rm GeV}\right)^{1/2} \tag{1.27}$$

More recently, a competitive bound has been obtained by K. Kadota *et al.* from the consideration of the magnetic fields of galaxy clusters [38]. It is displayed in Fig. 1.9 but we have decided not to use it due to the lack of publication in a Journal.

In principle, **colored** particles of DM could exist in nature but they are expected to confine inside hadrons below a temperature of ~ 180 MeV. Constraints on the power of their interactions with nuclei come from searches underground, in cosmic rays (CRs) and from studies of the ability of colored DM to heat the Earth core. The typical cross section of a strong interaction lies in the $10^{-25} - 10^{-24}$cm^2 range, but these values are already tightly constrained, leaving little hope for ever finding colored DM [36].

In the visible sector,[16] we conclude that the weak interactions are the only possible sizable interaction left for particle DM. From there, a famous DM candidate takes its name, the Weakly Interacting Massive Particle, or WIMP. As we will see (Sec. 1.5.1), the cross sections of the weak interaction (typically $\sim 10^{-44}$cm^2) are currently being probed by many experiments. Note that a departure from the assumption that DM is exactly neutral will be taken in Chap. 2, where we study a class of interesting imprints of millicharged DM in the γ-ray flux.

1.3.4 Cold versus warm dark matter

In Sec. 1.1.2, we have introduced the matter power spectrum $P(k)$ as the relevant observable to study the clumping of matter at different scales $\lambda \sim 2\pi/k$. The standard

[15] Beware that the ϵ in Figs. 1.8 and 1.9 is different from the kinetic mixing parameter used in Chap. 2. Besides, these limits are obtained assuming that the millicharged particle is non-relativistic. If not, searches for fast ionising millicharged particles would become relevant.

[16] By this, we mean the SM sector.

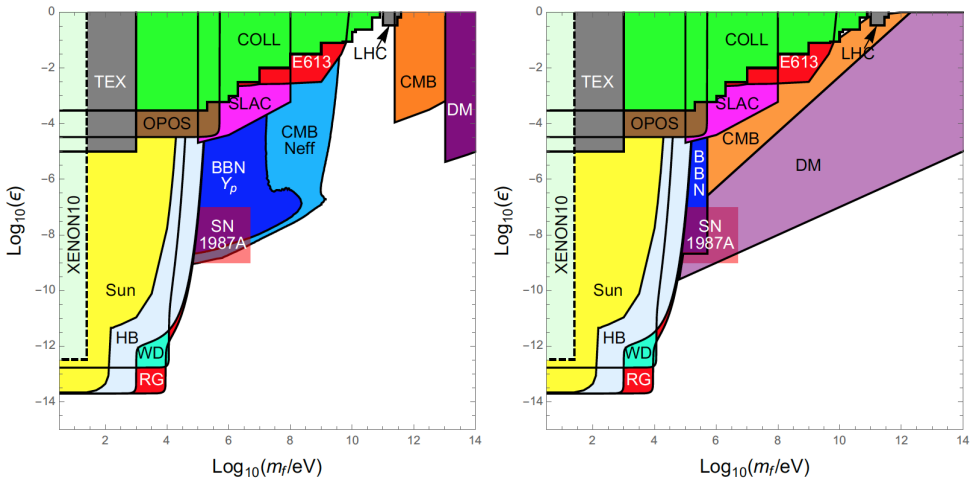

Figure 1.8: Compilation of constraints on millicharged particles in the millicharge *vs* mass plane, assuming (left) a model with a massless hidden photon (right) a model with no hidden photon. Figure taken from [39], where references to the individual constraints may be found.

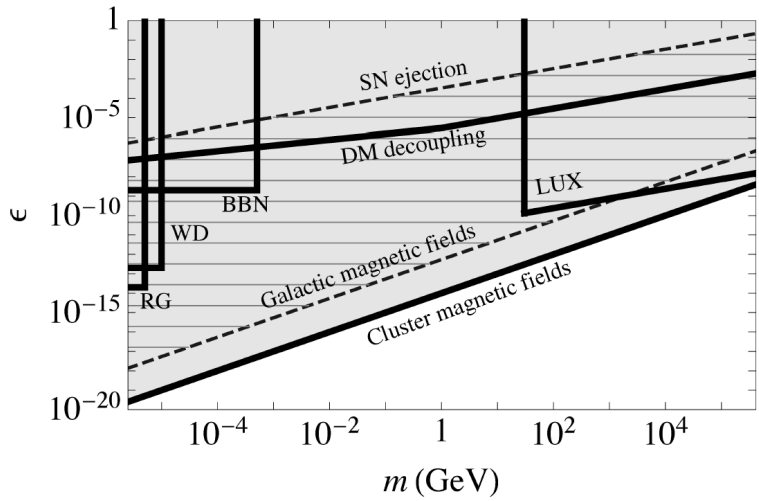

Figure 1.9: Recent constraint on millicharged particles in the millicharge *vs* mass plane, obtained from galaxy cluster magnetic field considerations. From [38].

cosmological paradigm nicely reproduces the observed spectrum at large scales, but fails to do so at galactic scale ($\lesssim 1$ Mpc)—more structures predicted (see Fig. 1.5). To "erase" some of the small-scale predicted imprints, stepping out of the ΛCDM may be necessary.

The DM particle velocity is one of the most obvious parameter that we can play with. Cold DM—as in ΛCDM—refers to DM particles that are non-relativistic when

structures began to form, and that are therefore not able to smooth out small-scale density perturbations. The relevant quantity to discuss this is the free-streaming length $\lambda_{\rm FS}$ of a particle, defined as:

$$\lambda_{\rm FS} = \int_{t_{\rm dec}}^{t_{\rm eq}} \frac{v(t)}{a(t)}\, dt, \tag{1.28}$$

where $v(t)$ is the velocity of the particle, $a(t)$ is the scale factor, and $t_{\rm eq}$ corresponds to the time when structures begin to grow, that is to say the time of matter-radiation equality. In other words, $\lambda_{\rm FS}$ is the distance that a particle can travel once it decouples from the plasma, and until structure formation begins. If $\lambda_{\rm FS} < \mathcal{O}(1\ \text{Mpc})$, particle DM is referred to as **Cold**. In this scenario, structure formation proceeds in a *bottom-up* fashion, with galaxies forming first, then clusters, and so on. If $\lambda_{\rm FS} > \mathcal{O}(1\ \text{Mpc})$, we speak of **Hot** DM. In that case, free-streaming has the consequence that structures take more time to grow. Moreover, they do so in what is called the *top-down* fashion, with large scale structures forming first, and then smaller sized objects forming from the fragmentation of the larger objects. In particular, the voids and the filamentary structure of the cosmic web are more pronounced in comparison to the predictions from CDM [40]. At the observational level though, HDM cannot satisfactorily reproduce structure formation data,[17] by contrast with CDM [41]. To address the small-scale crisis (or at least some facets of it like the missing satellite problem), DM particles can be taken mildly relativistic ($\lambda_{\rm FS} \sim \mathcal{O}(1\ \text{Mpc})$) in which case they are labelled as **Warm** [42].

That hot particles cannot make up all of the DM does not prevent for Mixed DM scenarios (MDM), where *only* a sub-component of the DM particles is made hot. Within the SM, the best candidates for HDM are neutrinos. They decouple from the thermal bath at a temperature of about 1 MeV, well before recombination, and while relativistic since $m_\nu \ll 1$MeV. Their relic density Ω_ν can be evaluated through the following expression [11]

$$\Omega_\nu h^2 = \frac{\sum_i m_{\nu_i}}{90\text{eV}}\ , \tag{1.29}$$

where the sum runs over the different neutrino mass eigenstates. This sum can be constrained by cosmological probes to $\sum_i m_{\nu_i} < 0.17$eV (95 % CL) [43],[18] meaning that neutrinos could indeed make up some of the DM, but would at most contribute at the percent level.

1.3.5 Collisionless dark matter

Besides including baryons or make DM warm, questioning the collisionless nature of particle DM constitutes another source of investigation to (possibly) reconcile simulations with observational data. With the famous example of the Bullet Cluster exposed

[17] For instance, galaxies only appear starting from redshift $z \sim 1-2$ in the HDM scenario, while they are observed as early as redshift $z \sim 3$.

[18] As we will see in Chapter 4, neutrino oscillation experiments are only sensitive to the difference of mass squared $\Delta_{ij} \equiv m_i^2 - m_j^2$ with $j = 1, 2, 3$ and not the absolute scale of their mass, to which cosmology *is* sensitive.

previously, the reader has already gotten the feeling that DM self-interactions, if any, were constrained. Indeed, the fact that the gravitational potential wells inferred through weak lensing coincide with the location of the galaxies—which are collisionless since they have clearly passed through each other—not only suggests the presence of DM, but its collisionless nature as well. If DM was self-interacting, the locations of these wells would have an offset with respect to those of the galaxies. In other words, the DM halos—and hence the wells—would not make it as far. This can be translated into a limit on $\sigma/m_{\rm DM}$, the self-interaction cross section normalized to the DM particle mass, of which we quote the latest result that we know about [44]:

$$\sigma/m_{\rm DM} \lesssim 1{\rm cm}^2. \tag{1.30}$$

However, within a radius of about the mean free path of the DM particle, N-body simulations show that the effect of self-interactions on halos and clusters is to make them more spherical and less dense at the center (keeping the behaviour of CDM beyond that radius). More quantitatively, self-interactions with $\sigma/m_{\rm DM} \gtrsim 0.5{\rm cm}^2{\rm g}^{-1}$ could solve the core-cusp and too-big-to-fail problems. In parallel, measurements of the ellipticity and central density of some clusters give the following bound: $\sigma/m_{\rm DM} \lesssim 1{\rm cm}^2{\rm g}^{-1}$, leaving $0.5{\rm cm}^2{\rm g}^{-1} - 1{\rm cm}^2{\rm g}^{-1}$ as the range of $\sigma/m_{\rm DM}$ in concordance with astrophysical constraints while solving the core-cusp and too-big-to-fail problems. It should also be noted that σ could be velocity-dependent, in which case some of the above constraints could be relaxed or reconciled since the typical DM particle velocity changes across different astrophysical systems (see *e.g.* [45]). A summary of the constraints existing on $\sigma/m_{\rm DM}$ can be found in Tab.1 of Ref. [28].

Another attempt at resolving the small-scale crisis has to do with the usually assumed adiabatic nature of DM gravitational interactions with baryons, as already discussed in Sec. 1.2.5.

1.3.6 Dark matter abundance

In Sec. 1.1, we have introduced the density parameter $\Omega_{\rm DM}$—also called *relic density* or *relic abundance*—as the relevant observable to track the global amount of DM in our Universe. To reproduce this number, several DM production mechanisms exist on the market, but the most popular of them is certainly the production of WIMPs as thermal relics from the Big Bang.

The history of a thermal relic is simple to grasp. The particles present in the early Universe start in thermodynamic equilibrium with the rest of the plasma because of high interaction rates back then. By "high", we mean in comparison with the expansion rate H, since the expansion tends to send particles away from each other, thereby diminishing the probability of encounters and the realisation of equilibrium. In other words, as long as a given species satisfies the criterion that $\Gamma \gg H$, it is able to keep up with the thermal bath and is said to be in equilibrium. During that time, the number density is given by the equilibrium distribution which, under the assumption that the DM is non-relativistic, takes the following form:

$$n_{\rm eq}(T) \equiv g \left(\frac{m_{\rm DM} T}{2\pi}\right)^{3/2} e^{-m_{\rm DM}/T}, \tag{1.31}$$

where T is the temperature of the photons and g gives the degeneracy factor of particle DM. As time goes by, m/T increases and the abundance of DM is therefore "Boltzmann suppressed". This behaviour is clearly observed in Fig. 1.10. When $\Gamma \sim H$, the species decouples and its density as a function of time evolves independently of what happens in the thermal bath. If the particles are non-relativistic at the time of decoupling, their (comoving) number density *freezes out* instead of dropping to zero (as would have been the case if they were still in thermal equilibrium). Technically, it is possible to precisely follow the abundance of each species by solving a set of generally coupled Boltzmann equations (one for each species). This task is generally non-trivial, as it may require the use of numerical tools (especially around the time of freeze out). Under some mild assumptions, it is possible to show that the abundance of a generic WIMP, non relativistic at the time of decoupling, is directly correlated to its inverse velocity-averaged annihilation cross section $\langle \sigma_{\text{ann}} v \rangle$ [11]:

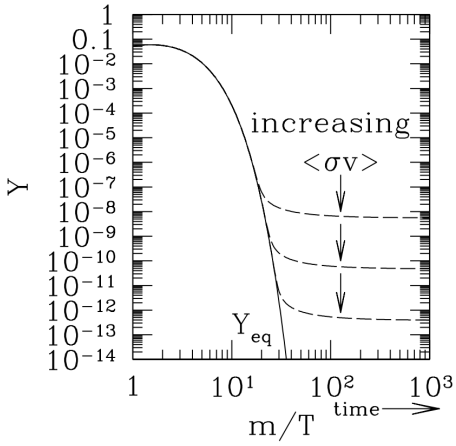

Figure 1.10: Illustration of the evolution of the DM abundance ($\propto Y$) as a function of time ($\propto m/T$) in the freeze-out scenario. The mass of the DM particle is denoted by m, and T is the temperature of the photons. From [46].

$$\Omega_{\text{DM}} h^2 \approx \frac{3 \times 10^{-27} \text{cm}^3 \text{s}^{-1}}{\langle \sigma_{\text{ann}} v \rangle}. \tag{1.32}$$

The success of the WIMP paradigm relies on the easiness to reproduce the correct relic abundance with an electroweak mass scale and typical weak couplings. With a little bit of dimensional and/or basic tree-level Feynman diagram analysis, it is possible to guesstimate an electroweak $\langle \sigma_{\text{ann}} v \rangle$:

$$\langle \sigma_{\text{ann}} v \rangle \approx 3 \times 10^{-26} \text{cm}^3 \text{s}^{-1} \times \left(\frac{100 \text{GeV}}{m_{\text{DM}}} \right) \times \left(\frac{g}{7 \cdot 10^{-2}} \right), \tag{1.33}$$

which has led to using the terminology "WIMP miracle" in the literature. Besides the WIMP miracle, what is also natural about the thermal relic scenario is that it does *not* require large couplings between the DM and SM particles to induce the initial thermalisation of the two sectors.

Other scenarios besides the popular freeze out are proposed in the literature, of which we quote the *freeze-in* scenario which consists in the production of DM in the early Universe through decays or annihilations of *other* species [47]. In contrast to the freeze-out mechanism, the production of DM is here an out-of-equilibrium process, and the number density of DM increases with time until it reaches the desired relic abundance.

1.3.7 Big Bang Nucleosynthesis

Big Bang Nucleosynthesis refers to the production of light elements when the Universe was but a few seconds to a few minutes old. In contrast to stars, where the light elements can fuse into carbon C and up to iron Fe, the early Universe could only provide the conditions for the synthesis of *light* elements, such as helium ^{4}He, deuterium D, tritium ^{3}H, and—to a lesser extent—lithium ^{7}Li. The measurement of the primordial abundances of these elements[19] is made possible by observing regions in the sky depleted from "recent activity", that is to say low-metallicity environments, or by studying the behaviour of their abundance at different metallicities and then extrapolate to zero metallicity [48].

The primordial abundances are very sensitive to the baryon-to-photon ratio η before BBN starts.[20] This ratio is itself fixed by the freeze-out of neutron-to-proton conversion processes, which happened—the freeze out—when the temperature was about $\sim$ 1 MeV. Assuming that DM particles have a thermal history as well, and that they freeze out long before η does, BBN shall not be affected. On the other hand, if DM particles are around during the freeze-out of η, they may inject extra particles in the thermal bath (*e.g.* via annihilation processes). By decaying, these extra particles would produce stable particles (electrons, photons, ...), possibly changing the outcome of η when all this chain of processes is taken into account in the Boltzmann equations. Since η is experimentally bounded, as already said, DM properties such as the annihilation or scattering cross-sections—which are model-dependent—may be constrained as well.

1.4 The particle physicist's approach II: Physics Beyond the Standard Model

The previous section has been dedicated to properties of particle DM and how (well) they could be constrained. As a quick epitome, let us recall that particle DM cannot be baryonic, that it is massive—but the possible range of masses is huge—, that it is stable *or* quasi-stable, that it likely does not carry color, is at most millicharged, cold, likely collisionless, and that it cannot mess up with BBN. Under the SM gauge group, it has weak interactions at the most. To the question of whether any SM particle could play the *rôle* of DM, we have answered that only neutrinos could, but only to the % level since they are hot. Consequently, we are in front of beyond-SM physics. We quickly review in this section the key concepts around the SM and how it may be extended in some circumstances using the effective field theory approach.

1.4.1 Standard Model and Beyond 101

The Standard Model of Particle Physics provides a unified description of the strong, weak and electromagnetic interactions through the concept of gauge symmetry. As

[19] "Primordial" is here used by opposition to a later production, *e.g.* during star burning.

[20] They used to give the most precise measurements of Ω_b when cosmological data was not available yet.

any field theory, it revolves around the study of a Lagrangian density with a specific set of symmetries.[21] In this instance, these symmetries consist in the (non-local) Lorentz symmetry and the $SU(3)_c \times SU(2)_L \times U(1)_Y$ gauge (=local) group.[22] Particles are then classified according to the group *representations* under which they transform.

- Fermions live in the spinorial representation of the Lorentz group, "represented" by the following matrices:

$$M = \exp^{\frac{-i}{2}\omega_{\mu\nu}\sigma^{\mu\nu}}, \tag{1.34}$$

  where $\sigma^{\mu\nu}$ are the generators of the group and the $\omega_{\mu\nu}$ are real parameters which select a specific element in that group. The fundamental representation of these generators is reducible (= block-diagonalizable), giving in the chiral basis:

$$\sigma^{\mu\nu} = \frac{i}{4}\begin{pmatrix} \sigma^\mu\overline{\sigma}^\nu - \sigma^\nu\overline{\sigma}^\mu & 0 \\ 0 & \overline{\sigma}^\mu\sigma^\nu - \overline{\sigma}^\nu\sigma^\mu \end{pmatrix}, \tag{1.35}$$

  where $\sigma^\mu \equiv (\mathbb{1}, \sigma^1, \sigma^2, \sigma^3)$, $\overline{\sigma}^\mu \equiv (\mathbb{1}, -\sigma^1, -\sigma^2, -\sigma^3)$ and where $\{\sigma^i\}$ denote the Pauli matrices. Because of the structure of Eq. (1.35), the two handednesses (**L**eft *vs* **R**ight) of a fermion can be treated separately—they correspond to different physical states. Moreover, the SM is chiral since only left-handed particles transform under $SU(2)_L$. A summary of the fermionic content of the SM is found in Tab. 1.1. The I, II, and III columns correspond to the three generations of leptons experimentally identified.

- Vector bosons transform under the vector representation of the Lorentz group and carry an index μ. In the SM, you only find *gauged* vector bosons, meaning that they *also* live in the *adjoint* representation of $SU(3)_c \times SU(2)_L \times U(1)_Y$.

- Last, the SM incorporates a scalar H, also known as the Brout-Englert-Higgs boson. By "scalar", we mean that it does not transform under the Lorentz group whatsoever. It nonetheless carries non-trivial quantum number under $SU(2)_L \times U(1)_Y$, and is responsible for giving their mass to the particles (including itself) through the electroweak symmetry breaking:

$$SU(3)_c \times SU(2)_L \times U(1)_Y \to SU(3)_c \times U(1)_Q, \tag{1.36}$$

  where Q denotes electric charge. A summary of the bosonic content of the SM is presented in Tab. 1.2.

All of the "regular" SM physics of the particle content just exposed is encoded in the following Lagrangian density:

$$\begin{aligned} \mathcal{L}_{SM} = &-\frac{1}{4}G_{\mu\nu,a}G^{\mu\nu,a} - \frac{1}{4}W_{\mu\nu,i}W^{\mu\nu,i} - \frac{1}{4}B_{\mu\nu}B^{\mu\nu} \\ &+ (D_\mu H)^\dagger (D^\mu H) + m_H^2 H^\dagger H - \frac{1}{2}\lambda (H^\dagger H)^2 \\ &+ i\bar{l}\not{D}l + i\bar{e}\not{D}e + i\bar{q}\not{D}q + i\bar{u}\not{D}u + i\bar{d}\not{D}d \\ &+ (\alpha_e \bar{l}eH + \alpha_u \bar{q}u\widetilde{H} + \alpha_d \bar{q}dH + \text{h.c.}), \end{aligned} \tag{1.37}$$

[21] This is where Group Theory comes in handy.

[22] c is for "color", L is for "left-handed" and Y is for "hypercharge".

$SU(3)_c$	$SU(2)_L$	$U(1)_Y$	I	II	III
1	1	-2	e_R	μ_R	τ_R
3	1	1/3	$u_{R,i}$	$c_{R,i}$	$t_{R,i}$
3	1	-2/3	$d_{R,i}$	$s_{R,i}$	$b_{R,i}$
1	2	-1	$\begin{pmatrix} \nu_e \\ e \end{pmatrix}_L$	$\begin{pmatrix} \nu_\mu \\ \mu \end{pmatrix}_L$	$\begin{pmatrix} \nu_\tau \\ \tau \end{pmatrix}_L$
3	2	1/3	$\begin{pmatrix} u \\ d \end{pmatrix}_{L,i}$	$\begin{pmatrix} c \\ s \end{pmatrix}_{L,i}$	$\begin{pmatrix} t \\ b \end{pmatrix}_{L,i}$

Table 1.1: Fermion content of the SM and charges. The i index carried by doublets and singlets of quarks refers to the triplet representation of $SU(3)_c$.

$SU(3)_c$	$SU(2)_L$	$U(1)_Y$	Boson
1	1	0	B_μ
1	3	0	$W_{\mu,i}$
8	1	0	$G_{\mu,a}$
1	2	-1	H

Table 1.2: Boson content of the SM and charges. The $i = 1, 2, 3$ and $a = 1, 2, ..., 8$ indices respectively refer to the triplet and octuplet (adjoint) representations of $SU(2)_L$ and $SU(3)_c$.

where $\widetilde{H} \equiv i\sigma_2(H^\dagger)^T$, D_μ denotes the covariant derivative—it ensures the local aspect of the symmetry—, and where m_H^2, λ, α_e, α_u, and α_e parametrize the strength of the corresponding terms.

The success of the SM has been established thanks to about four decades of experimental data. It nevertheless features a number of conceptual dissatisfactions of which we take a quick tour. The SM:

- does not explain its particle content (for instance, why there are bosons and why there are fermions);
- displays 19 independent parameters, all obtained from experimental data. If it truly were a fundamental theory, we could likely expect less of them;
- does not incorporate the laws of gravitation;
- does not incorporate neutrino masses (see Sec. 4.4.1), nor explain the matter-antimatter asymmetry, dark energy, and inflation;
- and does not propose any viable DM particle candidate (see Sec. 1.3).

We will not attempt at building any new theory fixing one or several of these issues—let alone a Theory Of Everything—and to avoid the discussion of a series of technicalities linked to the study of a DM model in particular, we will mostly rely on the effective approach.

1.4.2 Effective Field Theory

Generalities The usefulness of the effective approach is tight to its model-independent and systematic qualities. The idea and main concern behind Effective Field Theories (EFTs) is that you do not need to know a theory to its full extent to be able to make inferences in some regions of the parameter space, typically when some parameter is taken "much less than". Popular examples of EFTs include Classical Mechanics, which is nothing more than the $v \ll c$ limit of Special Relativity, which is itself the $g_{\mu\nu} \to \eta_{\mu\nu}$ limit of General Relativity. Another famous example in Particle Physics is given by the Fermi theory, which describes the electroweak interactions at energies E well below m_W, the W-boson mass [49].

The effective approach is useful when a theory displays lots of parameters of which few end up being relevant since, in this way, a great deal of calculations can be skipped. In our case, we will always consider that we work in the low-energy limit of some UV theory, of which the relevant scale is denoted by Λ. The scale of this theory could be somewhere around the GUT scale, $\Lambda_{\text{GUT}} \sim 10^{16}$ GeV, as suggested by the running of the SM coupling constants. There are two main conditions that need to be satisfied in order to use the effective lagrangian:

- At a given dimension, a finite number of parameters ($\Leftrightarrow$ operators) describe the interactions. This condition is trivially satisfied if there exists a finite number of fields at low energy;
- The coefficient in front of each effective interaction term of dimension $k+4$ is suppressed by Λ^k. This second condition offers the opportunity to work within the framework of perturbation theory. This is for instance possible when there is a clear separation of scales between the UV and low-energy physics.

That you can avoid to study an infinite series of effective operators comes down to the precision you want to achieve. By including terms up to k_ϵ, with $k_\epsilon \in \mathbb{N}$, the level of precision that you reach on an amplitude is approximately given by

$$\left(\frac{E}{\Lambda}\right)^{k_\epsilon}. \tag{1.38}$$

In other words, to reach a given level of precision ϵ, you need to include effective operators up to dimension

$$k_\epsilon \simeq \frac{\ln(1/\epsilon)}{\ln(\Lambda/E)} \tag{1.39}$$

The higher the Λ, the sooner you may stop in the effective expansion, but as $E \to \Lambda$, more and more terms must remain in order to keep the same level of accuracy, and at the limit $E = \Lambda$, it is the whole expansion which must be taken into account. At that point, the UV description is clearly the simplest one to use (renormalizable and experimentally accessible). With the range of DM masses probed in Part II, we never fall into this situation though.

On the formal level, an effective interaction is the result of the "integration out" of the massive particles with a mass m much greater than the energy E at which the relevant processes happen. Indeed, if $m \gg E$, those particles cannot be the external

legs of any Feynman diagram and you only find them in propagators (internal legs). At the level of the Green functions, that are the central quantities in QFT, this comes down to literally performing the integration of these fields in the path integral representation of the generating functional $Z[J]$:

$$Z[J] = \int \mathcal{D}\phi \;\; exp^{i\left(S+\int d^4x J\phi + i\epsilon(\ldots)\right)}, \tag{1.40}$$

where the $i\epsilon$ term is not made explicit but is there to guarantee the appropriate boundary conditions for the Feynman propagator, and where $\int \mathcal{D}\phi$ denotes the integral over the field space. The action is denoted by S and the sources J allow to conveniently derive the Green functions. On a "Feynman diagram" basis, you can also understand why a dimension 6 interaction is suppressed by two powers of Λ. For instance, the scalar propagator (= 2-point Green function)

$$\Delta(x_1, x_2) = \frac{1}{(2\pi)^4} \int d^4p \; exp^{ip\cdot(x_1-x_2)} \frac{1}{p^2 + m^2 - i\epsilon\omega(\vec{p})}, \tag{1.41}$$

becomes, in the limit $m^2 \gg p^2$,

$$\Delta(x_1, x_2) = \frac{\delta(x_1, x_2)}{m^2}, \tag{1.42}$$

that is to say a contact interaction suppressed by m^2, where m is the "large" scale.

The explicit construction of the effective lagrangian at the electroweak scale has already been performed by Buchmüller and Wyler in Ref. [50], but they have only taken the SM content into account. Since we are interested in DM particles too, we will rely on our own effective lagrangian $\mathcal{L}_{\text{eff}}$ when we need one, with

$$\mathcal{L}_{\text{eff}} = \mathcal{O}_4 + \frac{\mathcal{O}_5}{\Lambda} + \frac{\mathcal{O}_6}{\Lambda^2} + \frac{\mathcal{O}_7}{\Lambda^3} + \cdots = \sum_{i\in\mathbb{N}} \frac{\mathcal{O}_{i+4}}{\Lambda^i}, \tag{1.43}$$

and where $\mathcal{O}_{i+4}$ contains all our relevant effective operators of dimension $i+4$. Note the possible presence of new $\mathcal{O}_4$ terms, which could lead to observable new physics. They can be removed by invoking tiny coupling constants (this would lack of natural, though) or extra symmetries. Note that $\mathcal{L}_{\text{eff}}$ *must* be Lorentz and gauge invariant. An extensive review of EFT is found in Ref. [51].

In practice... We have already invoked that the works to be exposed in Chapters 2 and 3 involve the study of the DM phenomenology based on a given EFT. More specifically, in those two chapters, we will be interested in the production of gamma-ray (and neutrino) lines from the decay of DM particles. We take a little time here to specify that the two respective lists of effective operators considered there are the mere result of the following set of requirements:

- Each effective operator must involve the DM field;
- Since we are interested in the emission of mono-energetic photons—and neutrinos—(see Sec. 1.5.3 for a motivation), each operator must at least involve two-body decays involving a photon—and a neutrino—in the final state;

- Because gauge invariance must be preserved by the EFT, the emission of a photon must necessarily come through the $U(1)_{\rm em}$ tensor field or through a covariant derivative;
- Lorentz invariance must be preserved.

Besides,

- to avoid redundant phenomenologies, we do not consider those operators that are related by a total derivative term to other operators in the lists;
- we make use of the equations of motion to get rid of some operators. It may indeed happen that these equations show from the start that the emission of *mono-energetic* particles is not possible.

We will see in Chapters 2 and 3 that these requirements make the EFT of DM decay much easier to handle.

1.5 Finding dark matter: from evidence to practice

So far, we have discussed the gravitational pieces of evidence for the existence of a large amount of invisible matter in our Universe (Secs. 1.1 and 1.2). In Sec. 1.3, we have taken the time to expose most of the properties that a particle may or may not have in order to be a good DM candidate. The particulate nature of this new form of matter is still unknown but the hunt is fiercer than ever, as demonstrated by the plethora of experiments and analyses in the literature dedicated to DM. Three main detection strategies have been elaborated. They have their own specificities, but should be used in complementarity with each other.[23] Before we start discussing them, we stress the fact that **indirect detection** is at the heart of all the works presented in the thesis. This is why, in comparison with Secs. 1.5.1 and 1.5.2, more effort and time are devoted to Sec. 1.5.3.

1.5.1 Direct Detection

Generalities The aim of direct-detection experiments is to look for the recoils produced by the scattering of DM particles off a detector's target nuclei. These experiments are conducted on Earth, preferably deep underground to be shielded from cosmic radiation,[24] and are sensitive to the deposition of energy following a recoil. This energy may arise because of heat production (phonons), ionisation (electrons), and scintillation (photons) within the material. To reduce background events, experiments often exploit two of these signals. In principle, the three of them could also be recorded, but to this day no experimental setup has ever done this. Depending on the signal(s) of interest, different classes of target materials are used. For instance, germanium or low-pressure gases are suited for ionisation, crystals and noble-gas

[23] For instance, out of the three techniques, indirect detection is the one that depends the most on astrophysical processes, which are sometime not thoroughly understood.

[24] The radioactivity of the rock and of the detector material itself also naturally contaminate the data. These backgrounds can partly be reduced with the definition of a fiducial volume inside of the detector.

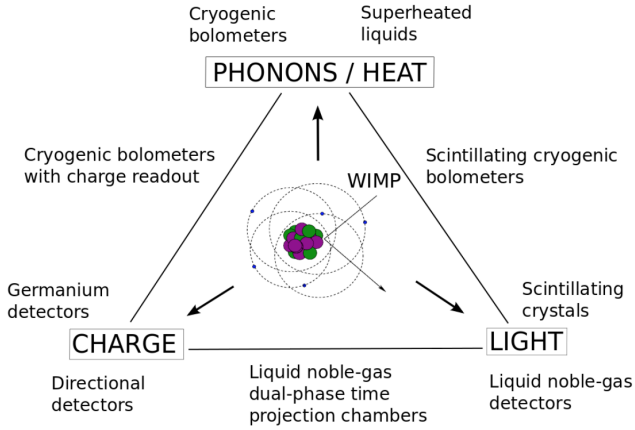

Figure 1.11: Diagram of the different signals probed in direction detection experiments, as well as the corresponding technology used. Those technologies placed in a corner of the triangle detect one of the three signals induced by the recoil (written in the corresponding dotted rectangle), while those in between exploit two of those signals. From [52].

liquids for scintillation, and super-cooled crystals for phonons. This is presented in a triangular fashion in Fig. 1.11. At the center of the triangle would lay a hypothetical future detector exploiting all three signals (phonons, photons *and* electrons). Experiments looking at one type of signal only are located at the corresponding corner, while those looking for two of them lay in between the corresponding two corners.

Besides instrumental effects and the detector's response, the rate of DM-induced events in the detector depends on three main ingredients:

- $\rho_\odot$, the local density of DM (see Sec. 1.2);
- $f_\oplus(\vec{v})$, the local velocity distribution of DM;[25]
- and a differential cross section which encodes the particle and nuclear physics of the scattering process.

In its differential form with respect to the recoil energy E_R, the rate of events as a function of time is given by the following expression,

$$\frac{dR(E_R,t)}{dE_R} = \sum_N N_N \frac{\rho_\odot}{m_{\rm DM}} \int_{v_{\rm min}}^{\infty} \frac{d\sigma_N(E_R,v)}{dE_R}\, v\, f_\oplus(\vec{v},t)\, d^3v, \tag{1.44}$$

where N_N, $d\sigma_N/dE_R$, and $v_{\rm min}$ respectively denote the number of nuclei N per unit mass of the detector, the differential scattering cross section on a nucleus N, and the

[25]The local velocity distribution $f_\oplus(\vec{v})$ can be re-expressed as $f_{\rm gal}(\vec{v}+\vec{v}_\oplus(t)+\vec{v}_\odot)$, where $f_{\rm gal}$ is the galactic velocity distribution, and where $\vec{v}_\oplus$ and $\vec{v}_\odot$ respectively denote the velocity of the Earth around the Sun, and that of the Sun around the Galactic Center. Note that $f_{\rm gal}(v' > v_{\rm esc} = 533^{+54}_{-41}{\rm km\ s^{-1}}) = 0$ [53].

minimum velocity needed to observe a recoil. In addition, v_{min} can be expressed as a function of the threshold energy E_{thr} :

$$v_{\text{min}} = \sqrt{\frac{m_N\ E_{\text{thr}}}{2\mu_N^2}}, \tag{1.45}$$

where m_N and μ_N respectively denote the mass of a nucleus N and the reduced mass of the DM-nucleus system. Conversely, we have

$$E_R = \frac{q^2}{2m_N} \sim \frac{\mu_N^2 v^2}{m_N}, \tag{1.46}$$

where q denotes the momentum transferred to the nucleus, and v the velocity of the incoming DM particle. The summation over N in Eq. (1.44) is relevant when a detector uses more than one type of target material. Below the escape velocity v_{esc}, the distribution $f(\vec{v})$ is often assumed to follow a Maxwell-Boltzmann distribution,[26] and beyond, $f(\vec{v})$ is simply set to zero. As for the cross section σ_N, it may generally be split into two pieces:

$$\frac{d\sigma_N}{dE_R} = \frac{m_N}{2\mu_N^2\ v^2} \cdot (\sigma_{N,0}^{\text{SI}}\ F_{\text{SI}}^2(E_R) + \sigma_{N,0}^{\text{SD}}\ F_{\text{SD}}^2(E_R)) \tag{1.47}$$

where $\sigma_{N,0}^{\text{SI}}$ and $\sigma_{N,0}^{\text{SD}}$ are, respectively, the *spin-independent* (SI) and *spin-dependent* (SD) cross-sections at zero momentum transfer. The F functions are form-factor corrections. They take into account the fact that, as the momentum transfer increases, the scattering amplitude of the individual nucleons do not add up in phase anymore. In other words, the form factors F encode the incoherent response of the nucleus.

The expression for the cross-sections can further be simplified if they do not depend on velocity. The first of them is then given by:

$$\sigma_{N,0}^{\text{SI}} = \sigma_p \cdot \frac{\mu_N^2}{\mu_p^2} \cdot \left[Z \cdot f^p + (A - Z) \cdot f^n\right]^2, \tag{1.48}$$

whereas the second encodes the part which depends on the total spin J_N carried by the nucleus,

$$\sigma_{N,0}^{\text{SD}} = \frac{32}{\pi}\mu_N^2 \cdot G_F^2 \cdot \left[a_p \cdot \langle S^p \rangle + a_n \cdot \langle S^n \rangle\right]^2 \cdot \frac{J_N + 1}{J_N}. \tag{1.49}$$

In the above expressions, $f^{p,n}$ denote the contribution of protons and neutrons to the DM coupling, μ_p the reduced proton-DM mass, A the atomic mass number and Z the number of protons in the nucleus. As for the $a_{p,n}$ and G_F coefficients, they respectively denote the proton (neutron) couplings and the Fermi coupling constant. $\langle S^{p,n} \rangle$ denote the expectation value of the spin of the protons and neutrons. Assuming isospin conservation, *i.e.* $f_p \approx f_n$, the SI cross section grows as the square of the atomic number A_N. Besides this, Eq. (1.49) tells us that target materials with an even number

[26] Deviations from this assumption are motivated by simulations, and their impact on direct detection are addressed in the literature, see *e.g.* Refs. [54, 55, 56].

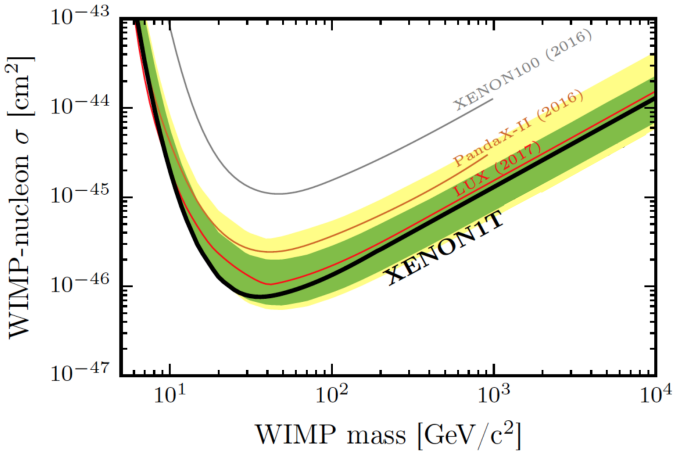

Figure 1.12: Upper limits at the 90 % CL on the spin-independent DM-nucleon scattering cross section as a function of the DM particle mass. The very recent results from XENON1T are presented in black, together with their 1 and 2-σ sensitivity bands (green and yellow, respectively). For comparison, recent limits from competitors are also presented. Results from PANDA-X II (2016) [57], XENON100 (2016) [58] and LUX (2017) [59] are respectively shown in brown, gray and red. Figure (slightly adapted) from [60].

of nucleons cannot probe SD cross sections. The SD cross-sections are typically smaller than the SI ones by a factor of A_N^2, which is why the corresponding limits on the former are a lot looser than those on the latter. Depending on the theoretical model, the predicted DM-nucleus interaction—and hence the cross section—may be classified as SD, SI, or both.

Experimental results As already mentioned, different experiments typically use different target materials. To make the comparison of their respective results easier and as fair as possible, the cross sections are reported for a single nucleon, proton or neutron. We present them for the spin-independent case in Fig. 1.12, and for the spin-dependent case in Fig. 1.13. The presence of a DM-induced signal is either tested by looking for distinctive features in the energy spectrum, for the annual modulation of the event rate as the Earth orbits around the Sun or for a directional dependence of the signal—for those detectors who have the technology necessary to reconstruct the recoil track. Modulation is induced by the change in the relative velocity of the detector with respect to the DM halo, and the corresponding maximal event rates are expected on June 2$^{\text{nd}}$ of each year. As you can see from Fig. 1.14, the residual rates measured by DAMA/NaI and DAMA/LIBRA (the successor of DAMA/NaI) seem to be in concordance with that date for over 14 cycles, bringing the significance of this modulation detection to 9.3σ [61]. Quite strangely, no other experiment has confirmed these results[27] and, for the most recent ones, even exclude the parameter space

[27] There have been weaker hints by CDMS-II but they have disappeared with the next generation of the experiment, SUPERCDMS [62]. The COGENT Collaboration also reports a mild evidence (2.2σ) for an annual modulation [63].

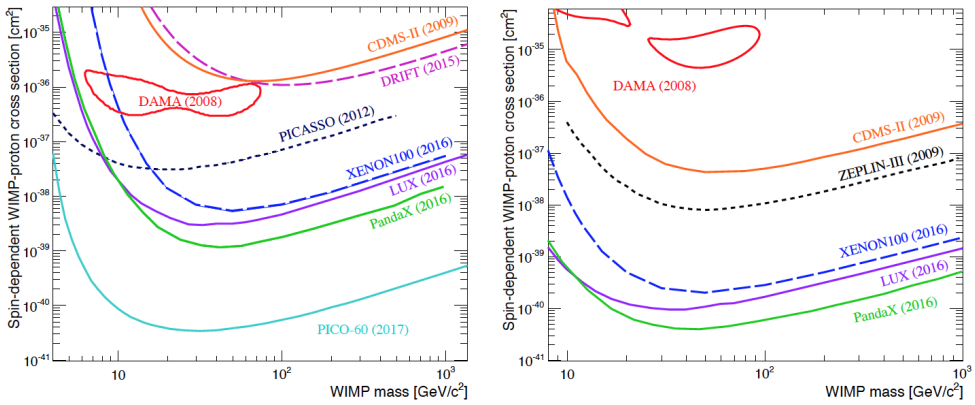

Figure 1.13: Cocktail of signal hints and upper limits on the spin-dependent DM-proton scattering cross section from various experiments. The contour regions favoured by DAMA are visible in the upper left corners. In the left (right) subfigure, a pure proton (neutron) coupling is assumed. More details on each of the limits can be found in the reference [389] cited in [52], from where this figure was taken.

favoured by DAMA (see Fig. 1.13). Other projects using a similar technology as that of DAMA are currently being pursued to independently check this result, notably at the South Pole under what is called the DM-ICE project. If the DAMA modulation happens to come from a seasonal variation effect, the opposite modulation should be seen in the Southern hemisphere. The DM-ICE Collaboration has released its first search for an annual modulation, and found that the data was consistent with no modulation, providing constraints in the DM mass versus cross section parameter space [64]. The DAMA contour regions are not excluded yet by DM-ICE, but projected sensitivities show that they will be tested with the next planned detector (see Fig. 5 in [64]). Last, "directional" studies come down to finding a forward-backward asymmetry in the recoils, which are preferably expected from the Cygnus Constellation if induced by DM particles. An in-depth discussion of all the aspects related to the direct detection of particle DM is presented in Ref. [52].

Before moving on to LHC searches, we note that the scattering of DM particles off the target's electrons is also a possibility worth being studied. The difference with a DM-nucleus scattering resides in the range of recoil energies probed. According to Eq. (1.46), the recoil energy decreases as the DM particle mass decreases. Since the threshold of the detector is non-zero (typically at the keV scale), there exists a mass under which it—the detector—is no more sensitive to the nuclear recoils. The exact value of this mass varies with different target materials, but we can give the rough estimate that this happens below $m_{\mathrm{DM}} \sim 1$ GeV.[28] The situation is different for electronic recoils where all of the kinetic energy can be available for the electron, with the consequence that a lower range of DM masses is made accessible. The main types of material used to detect electronic recoils consist of semi-conductors and scintillators. A premiere discussion of the subject can be found in Ref. [65].

[28] This effect is also behind the rise of the limits around 10 GeV (see Figs. 1.12 and 1.13).

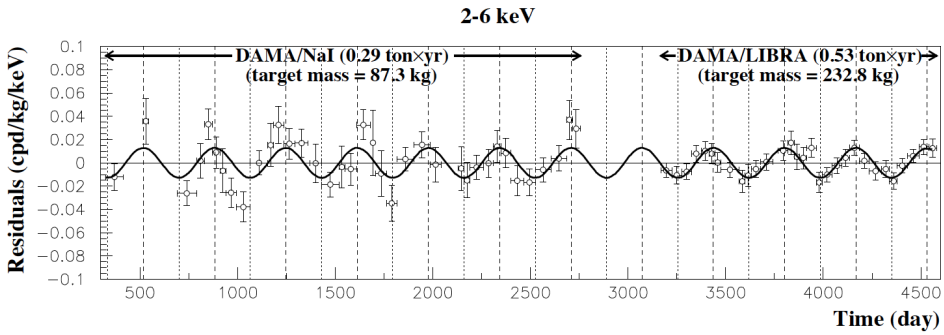

Figure 1.14: Residual rates measured by DAMA/LIBRA and DAMA/NaI. The continuous curve corresponds to the expectation from DM-induced recoils, and shows an oscillatory behaviour because of our motion around the Sun. The dashed (dotted) vertical lines correspond to the time of the year when we expect the DM-induced signal at its maximum (minimum). A periodicity of 1 year is visible and holds for over 10 cycles. From [61].

1.5.2 LHC Searches

Generalities The production of DM in particle accelerators is an alternative[29] to the detection of those DM particles which have accumulated locally and cosmologically, and whose presence is tested through direct (Sec. 1.5.1), indirect (Sec. 1.5.3), and gravitational (Sec. 1.2) detection techniques. We have seen that particle DM was at most weakly interacting under the SM gauge group but could, more generally, interact with the SM via new BSM interactions. DM particles may therefore be produced in pairs in the collisions of SM particles, like those taking place at the LHC. From there, two strategies may be adopted.

The first consists in the detection of missing energy. Indeed, if DM particles leave the detector, they behave like neutrinos by not depositing energy. At the LHC, where the longitudinal momentum of the incoming partons is not known, the escape of DM out of the detector—remember that DM is constrained to be long-lived—is signalled through missing *transverse* energy $\not{E}_T$. It is interesting to search for DM by collecting samples of mono-X events, where X represents a jet, a photon, a lepton, the SM scalar boson, etc., because momentum is obviously missing under this criterion [66].

Alternatively, if the DM particles are not produced within final states but as internal legs of Feynman diagrams, one could look for deviations from the SM prediction of the distribution of certain variables. Significant excesses or dips would indicate the presence of new physics processes taking place in the collision, possibly involving DM.[30] For instance, the hint of a di-photon excess at 750 GeV [67, 68] has generated a

[29] Beware that if the discovery of a DM particle were to happen at colliders, we would still need to check by other means whether or not it is the cosmological DM. In particular, the complementarity with the two other detection techniques shall be exploited.

[30] To do this, a dedicated statistical analysis is needed in order to confront the experimental data to the DM model and judge if the latter gives a satisfactory fit.

lot of excitement among the community, and DM interpretations of the excess have proliferated around it. Another example, relevant for low mass DM candidates (< 60 GeV) consists in the study of the invisible decay width of the SM scalar boson [69].

1.5.3 Indirect Detection

Generalities The idea behind *indirect* detection is *not* to detect the DM particles themselves, or their interaction within a detector, but rather to detect *anomalies* in the cosmic ray fluxes that would be attributable to their decays or annihilations. For instance, if the DM particle is a thermal relic, you would naturally expect some of the annihilation processes that took place at freeze-out to continue happening later on. Obviously, just after freeze-out, we know that DM cannnot keep up annihilating because the expansion of the Universe "wins". But as structures form, these annihilations may happen again—because encounters are made possible again—, potentially giving rise today to large fluxes of particles from places where the DM density is high. This is because the event rate depends on the *square* of the density, as *two* particles are needed to annihilate. In the case of decaying DM and direct detection, structures also increase the event rate in the detector, but less efficiently since it is "only" proportional to the density. Places like the Galactic Center, the core of the Sun, that of the Earth, and Dwarf spheroidal galaxies are interesting targets for indirect detection, as they likely hide a lot of DM in them. By applying indirect detection techniques to a target like the Sun or the Earth, it is also possible to probe the $(m_{\rm DM}, \sigma_N)$ parameter space, more commonly probed by direct detection experiments—poetic, isn't it?. The explanation comes from the fact that, under some assumptions about the target, the annihilation rate (which is a function of the annihilation cross-section $\sigma_{\rm ann}$) may be related to the capture rate (which is a function of the scattering cross-section σ_N).

In the following two chapters, we will study the decay of particle DM within the effective approach. In particular, we will be interested in stable products like photons, neutrinos, anti-protons and positrons. In order to make reliable predictions of what the DM-induced fluxes of these particles look like at Earth, it is important to understand how they propagate away from their production site. The treatment is different depending on whether the particle is charged or whether it is neutral.

Charged particles Charged particles feel the presence of galactic magnetic fields whose influence needs to be taken into account. The corresponding effects are encoded in the CR transport equation [70]. We do not believe it necessary here to show it in its full extent—the general expression is a bit lengthy—, but let us say that it consists in a differential equation that describes the evolution of the density $f(\vec{x}, E, t)$ of a given CR species in terms of particle injections (= source terms), diffusions, convections, diffusive re-accelerations, energy losses, energy gains, and losses by fragmentations and decays. The source term takes into account the injection of primaries in the interstellar medium (by, *e.g.*, a supernova explosion or DM decay), spallation processes and contributions from the decay of other species. Diffusion and convection are respectively caused by the scattering of CRs on the irregularities of the magnetic fields and by the presence of galactic winds of particles generated from the stellar activity within the Galaxy. Diffusive reacceleration processes are described by a diffusion in *momentum* space caused by the scattering of CRs on moving magnetic

turbulences. The importance of one term on the other depends on the CR species under consideration.

Under the steady-state assumption, and modelling the galaxy as a superposition of

- a thick cylinder of height $2L$ which embeds the magnetic turbulences;
- and a thin cylinder (or disk) which contains the gas and the stars and is sandwiched within the thick cylinder,

we can simplify the CR transport equation inside of the galaxy to the following expression,

$$\partial_z(V_C f) - K(E,\vec{x})\Delta f + \partial_E\left(b^{\rm loss}(E,\vec{x})f - K_{EE}(E,\vec{x})\partial_E f\right) = q(E,\vec{x},t), \qquad (1.50)$$

where V_C is the velocity of the galactic wind which wipes the CRs away from the disc (in the z direction), K is the diffusion coefficient, $b^{\rm loss}$ parametrizes the energy losses and K_{EE} the energy gains. The source term q is on the RHS of the equation. To ease the resolution of Eq. (1.50), the explicit dependence of K on position is usually ignored, and the following parametrisation is adopted: $K = K_0(E/\text{GeV})^\delta$. Also, the diffusive reacceleration coefficient K_{EE} can be related to the diffusion coefficient K through: $K_{EE} = 2/9\ V_a^2 E^2\beta^4/K(E)$, where V_a represents the drift velocity of the scattering centres and $\beta \equiv v/c$ is the velocity of the CR particle in units of c.

When solving Eq. (1.50), the common approach is to set the function f to zero on the boundary of the thick cylinder and outside. Obviously, this approach does not do justice to reality and could be relaxed if a more involved treatment is desired. The Green method may be used to solve Eq. (1.50) (see *e.g.* Ref. [71]), meaning that the solution can be written as a convolution of the source function q with the Green functions of the problem $I(E,E_s,\vec{x})$.[31] The energy of the particle at the source–*i.e.* at its production site—is denoted by E_s and that eventually observed at location $\vec{x}$ is denoted by E. In terms of the differential flux (in units of $\text{m}^{-2}\text{s}^{-1}\text{sr}^{-1}\text{GeV}^{-1}$),

$$\frac{d\Phi}{dEd\Omega} \equiv \frac{vf}{4\pi}, \qquad (1.51)$$

and taking DM as a source, we have

$$\frac{d\Phi_{i,\rm ann}}{dEd\Omega}(E,\vec{x},t) = \frac{v}{8\pi}\left(\frac{\rho(\vec{x})}{m_{\rm DM}}\right)^2 \langle\sigma_{\rm ann}v\rangle_{\rm tot}\sum_F BR_F\int_E^{m_{\rm DM}} dE_s \frac{dN_{F\to i}(E_s)}{dE} I(E,E_s,\vec{x}) \qquad (1.52)$$

in the case of an annihilation, and

$$\frac{d\Phi_{i,\rm dec}}{dEd\Omega}(E,\vec{x},t) = \frac{v}{4\pi}\left(\frac{\rho(\vec{x})}{m_{\rm DM}}\right) \Gamma_{\rm tot}\sum_F BR_F\int_E^{m_{\rm DM}/2} dE_s \frac{dN_{F\to i}(E_s)}{dE} I(E,E_s,\vec{x}) \qquad (1.53)$$

[31] We are making a small short-cut here, as in reality, this function $I(E,E_s,\vec{x})$ has already the halo integral of the "true" Green function in it.

in the case of a decaying DM. The i subscript refers to the CR species of interest and the sum over F simply reflects the fact that, in general, several decay/annihilation channels F might be available and that each of these channels may contribute to the total flux of i. The BR_F factor denotes the branching ratio of channel F. As for $\langle\sigma_{\rm ann}v\rangle_{\rm tot}$ and $\Gamma_{\rm tot}$, they respectively denote the total velocity-averaged annihilation cross-section and total decay width (= inverse lifetime $\tau_{\rm DM}$). $dN_{F\to i}/dE$ is the multiplicity spectrum of i given the F final state. Note that Eq. (1.52) holds for a self-conjugate DM particle,[32] and that it is given anywhere in the galaxy. In order to obtain the corresponding flux at the location of the Earth, we replace $\vec{x}$ by $r_\odot\ \vec{u_r}$ in cylindrical coordinates.

Codes dedicated to the resolution of Eq. (1.50) are available and documented online, like GALPROP [70], PICARD [72], DRAGON2 [73], and HELMOD [74]—the latter focuses on the effects of solar modulation. If you are specifically interested in DM, a shortcut may be done by using the PPPC notebooks from Cirelli *et al.*[75] who actually used GALPROP to derive the halo integrals $I(E, E_s, \vec{x})$, and provide them in the form of ready-to-use tables and interpolating functions.

The parameters used in the CR transport equation (like V_C, V_a, L and δ) can be inferred from the ratio of secondary to primary CR abundances. By primary, we mean those CR species present at the site of acceleration and which are injected into the interstellar medium, and by secondary, we mean those species that are produced by the primaries' reactions onto the ISM as they propagate. This is why the ratios of primary to secondary elements are a probe of the propagation parameters in our Galaxy. The boron-to-carbon ratio B/C is precisely measured and therefore the most convenient one to estimate the propagation parameters [76]. Obviously, the errors of measure imply that there is not just a single set of parameters that is compatible with the B/C ratio. Choices of parameters that lead to a maximum (minimum) flux of electrons, positrons, anti-protons, or anti-deuterons at Earth are referred to as the MAX (MIN) parametrization. The MED parametrization refers to the set of parameters which fits best the B/C ratio. Note that the MIN, MED and MAX configurations are not the same whether you are interested in electrons/positrons, or whether you look at anti-protons and anti-deuterons (see Table 1.3). This is simply because these particles do not obey the exact same limit of the transport equation (*e.g.*, the energy loss terms are negligible for a heavy particle like the proton). In the following two chapters, and unless stated otherwise, whenever we need to assume a propagation model we systematically take the MIN configuration, so as to remain as conservative as possible with our limit estimates.

Neutral particles For photons and neutrinos, which are at the core of all the works presented in this thesis, the story is a lot easier since they propagate along straight

[32] If this is not the case, an extra-factor 1/2 must be added. This factor is easily understood by the fact that, if the DM population is equally split into particles and antiparticles, there are twice less particles to possibly annihilate with—in comparison with the case where DM is self-conjugate.

Model	δ	K_0 [kpc^2/Myr]	δ	K_0 [kpc^2/Myr]	V_C[km/s]	V_a [km/s]	L [kpc]
MIN	0.55	0.00595	0.85	0.0016	13.5	22.4	1
MED	0.70	0.0112	0.70	0.0112	12	52.9	4
MAX	0.46	0.0765	0.46	0.0765	5	117.6	15

Table 1.3: Summary of the MIN, MED and MAX propagation parameters in our Galaxy. The parameters for the propagation of electrons and positrons are presented to the left of the table (columns 2 and 3), while those applicable to (anti-) protons are presented to the right (columns 4–7). The last column is valid for both electrons/positrons and (anti-)protons. Adapted from [71] and [77].

trajectories without being affected by magnetic fields.[33] For both of them, the total flux at Earth may be decomposed into a galactic and an extra-galactic contribution. The former is not isotropic since we are not located at the center of our Galaxy. This angular dependence is in principle parametrized with two angles (*e.g.* the galactic latitude b and longitude l), but as we only assume spherically symmetric halos in the works of this thesis, it is enough for us to keep track of the angle ψ formed by the neutrino or the photon event with the GC. The extra-galactic contribution may further be split into isotropic and non-isotropic parts, which we discuss below.

The expression of the differential fluxes in units of $\mathrm{m}^{-2}\mathrm{s}^{-1}\mathrm{sr}^{-1}\mathrm{GeV}^{-1}$ for both decaying and annihilating DM are given herebelow. The i subscript refers to the photon or the neutrino, E is its energy, and ψ its direction—with respect to the GC. We stress again that in expressing $\dfrac{d\Phi_{\text{i, ann, gal}}}{dE\, d\Omega}(E,\Omega)$ and $\dfrac{d\Phi_{\text{i, ann, x-gal}}}{dE\, d\Omega}$, the DM particle was assumed to be self-conjugate, and that an extra factor of $1/2$ must be added to Eqs. (1.54) and (1.59) if this is not the case. One more thing worth highlighting is the fact that neutrinos oscillate, which must in principle be taken into account since neutrino detectors do not see the three flavours with the same efficiency. The practical details of this will be discussed in Chap. 6.

- **Galactic** flux:

$$\frac{d\Phi_{\text{i, ann, gal}}}{dE\, d\Omega}(E,\Omega) = \frac{1}{8\pi m_{\text{DM}}^2}\langle\sigma_{\text{ann}}v\rangle_{\text{tot}}\sum_F \frac{dN_{F\to i}}{dE}\int_{\text{l.o.s.}} ds\; \rho_{\text{DM}}^2(r(s,\psi)) \quad (1.54)$$

$$\frac{d\Phi_{\text{i, dec, gal}}}{dE\, d\Omega}(E,\Omega) = \frac{\Gamma_{\text{tot}}}{4\pi m_{\text{DM}}}\sum_F \frac{dN_{F\to i}}{dE}\int_{\text{l.o.s.}} ds\; \rho_{\text{DM}}(r(s,\psi)) \quad (1.55)$$

  Because the density halo profiles depend explicitly on the distance r from the GC, we need to know how to map r to the variable used in the line-of-sight (l.o.s.) integral and the angle ψ. This is made possible through the following expression:

$$r = \sqrt{r_\odot^2 + s^2 - 2rs\cos\psi}. \quad (1.56)$$

[33] Assuming that the neutrino is also massless, it is more correct to state that they propagate along the geodesics.

In practice, the contribution of the galactic DM halo may be ignored above $r_{\rm max} = 40$ kpc, meaning that the l.o.s. integral may be truncated when $s \geqslant \sqrt{r_{\rm max}^2 - r_\odot^2 + r_\odot^2 \cos^2\psi} + r_\odot \cos\psi$. Just as for Eq. (1.44), we can easily identify in Eqs. (1.54) and (1.55) the pieces which are solely related to astrophysics and to particles physics. The astrophysics is sometimes gathered in a so-called *J-factor*, defined as

$$J(\psi) = \int_{\rm l.o.s.} ds\, \rho^2(s,\psi), \tag{1.57}$$

in the case of an annihilation, and as

$$J(\psi) = \int_{\rm l.o.s.} ds\, \rho(s,\psi) \tag{1.58}$$

in the case of a decay.

- **Extra-galactic** flux: The extra-galactic emission may itself be split into two categories: resolved and unresolved sources. In the former case, it is enough to have a model of the DM distribution within the object and apply Eqs. (1.54) and (1.55) in a cone of opening angle $d\Omega$ corresponding to the angular size of the object. In the second case, the contribution of each source adds up, forming what is called the extra-galactic *diffuse* background. This diffuse extra-galactic flux can be estimated with the following expressions:

$$\frac{d\Phi_{\rm i,\,ann,\,x\text{-}gal}}{dE_i\, d\Omega}(E_i) = \frac{c\,\langle\sigma_{\rm ann} v\rangle_{\rm tot} (\Omega_{\rm DM}\rho_c)^2}{8\pi m_{\rm DM}^2} \int_0^\infty dz\, \frac{e^{-\tau_i^{\rm depth}(E_i,z)}(1+z)^3\zeta(z)}{H(z)}\, \frac{dN_i}{dE}\Big|_{E=E_i(1+z)}, \tag{1.59}$$

and

$$\frac{d\Phi_{\rm i,\,dec,\,x\text{-}gal}}{dE_i\, d\Omega}(E_i) = \frac{c\,\Omega_{\rm DM}\rho_c\,\Gamma_{\rm tot}}{4\pi m_{\rm DM}} \int_0^\infty dz\, \frac{e^{-\tau_i^{\rm depth}(E_i,z)}}{H(z)}\, \frac{dN_i}{dE}\Big|_{E=E_i(1+z)}, \tag{1.60}$$

where c is the speed of light in vacuum, and $H(z)$ is the Hubble expansion rate at redshift z. If several final states F are available, you can easily generalize Eqs. (1.59) and (1.60) in the same way as is done in Eqs. (1.54) and (1.55). As you can see from the integration, the extra-galactic flux receives contributions from all redshifts. These contributions are weighted by some geometrical factors coming from cosmology—because expansion has a dilution and redshifting effect—, and are worth being computed as long as $E(1+z) \leqslant m_{\rm DM}$ (annihilation) or $E(1+z) \leqslant m_{\rm DM}/2$ (decay).[34] Note also that, in comparison with dN/dE, the extra-galactic spectra migrate towards lower energies (redshifting). The optical depth $\tau_i^{\rm depth}$, which characterizes the level of absorption as a particle travels in the intergalactic medium, cannot be neglected for photons and exponentially reduces the integrand of Eqs. (1.59–1.60) with increasing redshift [75]. In contrast, neutrinos do not get absorbed and, practically, we set their optical depth to zero [78].

[34] Beyond the corresponding redshift, $dN(E(1+z))/dE$ returns zero, allowing to truncate the integral.

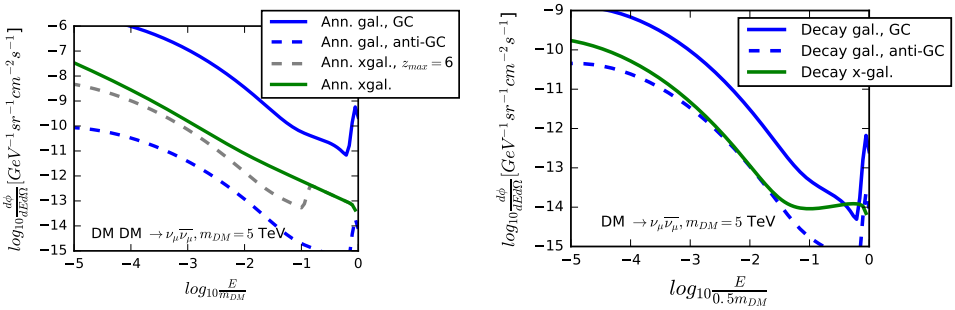

Figure 1.15: Comparison of the galactic and extra-galactic fluxes induced by a monochromatic spectrum at the source as a function of the energy E, in the direction of the GC and of the anti-GC, and assuming that DM is distributed according to the NFW profile (see Eq. (1.16)). The final state here is $\nu_\mu \overline{\nu_\mu}$ with $m_{\rm DM} = 5$ TeV, and the dN/dE spectra has been taken from the PPPC [75]. The annihilating (decaying) DM scenario is presented in the left (right) panel. Galactic (Extra-galactic) contributions to the flux are shown in blue (green). For the galactic flux, we differentiate the contributions from the GC (continuous) and anti-GC (dashed). The gray curve in the left plot is obtained by truncating the redshift integral to $z_{max} = 6$. The lifetime τ and velocity-averaged annihilation cross-section are respectively set to 10^{28}s and 10^{-23}GeV/cm^3, and the branching ratio of $DM(DM) \to \nu_\mu \overline{\nu_\mu}$ is set to 1.

You will notice that in the case of annihilating DM, the integrand depends moreover on the function $\boldsymbol{\zeta(z)}$, which is a measure of how much the DM has **clumped** into structures at a given redshift z (more clumping means a higher annihilation rate). This function, which basically denotes a *clumpiness* or *boost* factor, can be estimated on the basis of numerical simulations. A first estimation may consist in taking the combination

$$\frac{(1+z)^3 \zeta(z)}{(\Omega_\Lambda + \Omega_{m,0}(1+z)^3)^{1/2}} \simeq 10^6 \tag{1.61}$$

until redshift $z = 6$ [79].

Naively, one may expect that the diffuse extra-galactic contribution is irrelevant, but this is actually not *always* true.[35] We show in Fig. 1.15 that, depending on the direction you look at, this contribution may constitute a sizeable fraction of the galactic flux. We show this with the energy distribution of a few decay and annihilation channels, and for a couple of selected directions (the GC and the anti-GC).

Anomalies The first of the anomalies observed over the past decade consisted of an unexpected excess in the positron fraction spectrum. In the usual picture, both positrons and electrons can be produced from the spallation reactions of hadronic

[35] It is of course "fine" to neglect the extra-galactic flux in the sense that you would not get a wrong limit on the DM parameters (*e.g.* on the lifetime), but you would just end up with a weaker (= conservative) estimate of the limit.

CRs on the interstellar medium (secondary production), but only electrons receive a contribution from primary production processes (supernova remnants) [80]. If this picture is true, positrons should be more present at low energies while primaries—here, the electrons—would make up most of the flux at higher energies. In this way, the positron fraction spectrum defined as the ratio $\Phi_{e^+}/(\Phi_{e^+} + \Phi_{e^-})$, where Φ_i is the flux of i particles, is expected to smoothly decrease with respect to energy. Several experiments [81, 82, 83, 84, 85] have observed the puzzling rise of this ratio, as well as an excess in the combined flux $\Phi_{e^+} + \Phi_{e^-}$, clearly indicating that extra sources of primary positrons are absent from the models.

Whether this rise in the positron fraction is an evidence for the injection in the ISM of primary positrons by the DM is very debatable, as a purely astrophysical interpretation of the anomaly is possible if pulsars are encoded in the astrophysical model. A primary flux of electrons and positrons can be accelerated in the magnetosphere of pulsars through a mechanism known as spin-down emission. As they do so, they gather around the pulsar and are then released within the interstellar medium when the nebula disrupts. Di Mauro *et al.* have studied this option [80] as well as the addition of DM in the picture [86].[36] Their best-fit configurations to the AMS-02 data at the 1 and 2σ levels are presented in Fig. 1.16 for a few choices of leptonic (left) and hadronic (right) annihilation channels. In the upper row, the limits obtained at the 2σ CL by the study of the corresponding fluxes of photons with the FERMI data are displayed in the same color. The continuous curves are conservative estimates of the limit that Bringmann *et al.* derived in [87], by taking a cored profile and ignoring the effect of substructures. The dashed curves are optimistic estimates from [88]. Tension is noticeable for all the channels tested except the electronic and muonic ones. The lower row displays the different contributions to the $\Phi_{e^+}/(\Phi_{e^+} + \Phi_{e^-})$ spectrum—secondaries, DM induced, pulsars—and their sum (black). Ignoring possible tensions with γ-ray data, the positron fraction energy spectrum can both be reproduced with more (right) or less (left) DM—conversely, less or more positron injection by pulsars.

Besides possible tensions with the gamma-ray spectrum that must be kept under surveillance, a flux of anti-protons might as well be generated by the DM scenarios proposed to resolve the positron anomaly. The anti-proton data being very well described by the astrophysical backgrounds (see Fig. 1.17), this leaves very little room for new contributions—even astrophysical—, in particular those coming from the hadronic decays/annihilations of the DM particle. This is why you hear sometimes that *leptophilic* scenarios are attractive. Even so, care should be taken, as electroweak corrections may generate anti-protons and hence create tension in some regions of the parameter space [89].

1.5.4 The Golden Channels

By now, it should sound familiar that, in any type of analysis, searching for a signal first comes down to a good understanding and modelling of the backgrounds.[37] If

[36] Because pulsars are known to exist, the DM is assumption is not included on its own, but rather added on top of the pulsar component.

[37] For us, *background* refers to everything that is *not* DM induced.

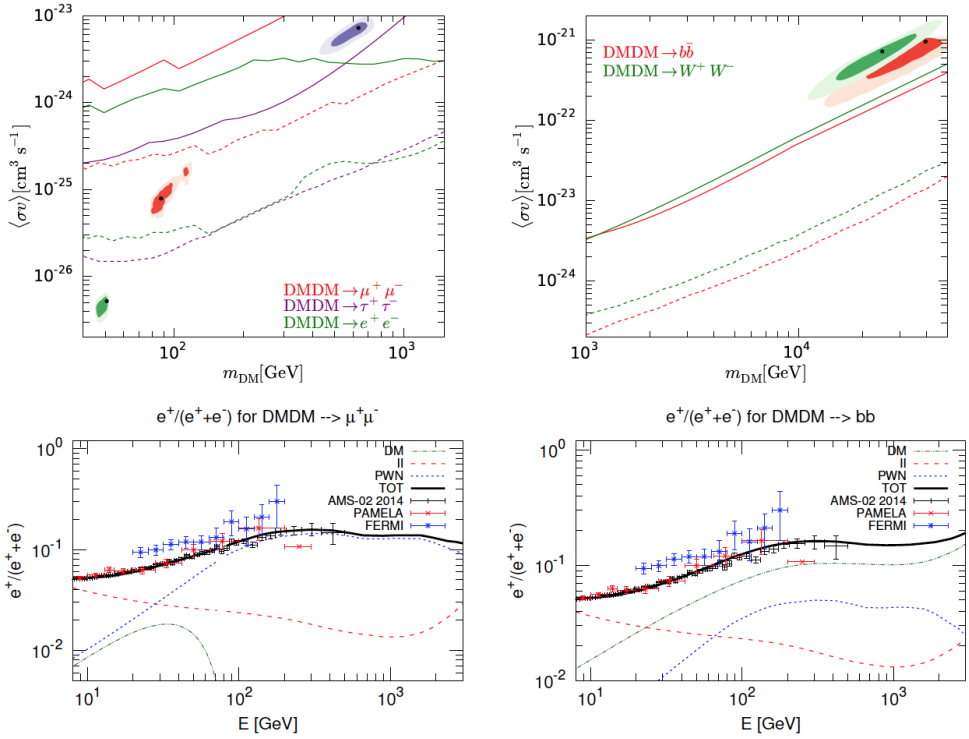

Figure 1.16: In the upper left panel, the best-fit regions to the recent AMS-02 data in the $(m_{\rm DM}, \langle\sigma v\rangle)$ parameter space are given for a selection of channels: e^+e^- (green), $\mu^+\mu^-$ (red), and $\tau^+\tau^-$ (purple). The 1σ and 2σ contours are respectively depicted by a darker and a clearer color. In the upper right panel, these contours are given for the $b\bar{b}$ (red) and W^+W^- (green) channels. Estimates of the 95 % CL limits on $\langle\sigma v\rangle$ as a function of mass are given by the continuous (conservative estimates) [87] and dashed curves (optimistic estimates) [88]. The lower row of panels shows the positron ratio energy spectra associated to the $\mu^+\mu^-$ (left) and $b\bar{b}$ (right) annihilation channels exposed above, together with the astrophysical contributions (usual secondaries and pulsar wind nebulae). Data points come from FERMI (blue), PAMELA (red) and AMS-02 (black). Their references can be found in [86], where the figure was taken from.

this is not the case, it is easy to draw the wrong conclusions and claim the presence of a signal when in fact there is none. Above $\sim$ 1 GeV, the energy spectra of the photon and neutrino backgrounds are smoothly distributed.[38] This absence of sharp features, intuitively understood as the consequence of the fact that astrophysical processes involve first and foremost violent shocks and acceleration of particles, is a true godsend for it makes supra-GeV **monochromatic** neutrinos and photons incarnate the

[38] Below $\sim$ 1 GeV, the quantum nature of the transition levels of molecules and atoms are responsible for the presence of absorption and emission lines in the photon spectrum. Neutrino transition lines do no exist, but above 1 GeV you get rid of most of the background sources—including the solar neutrinos which display a few cutoffs—, basically remaining with the atmospherical ones.

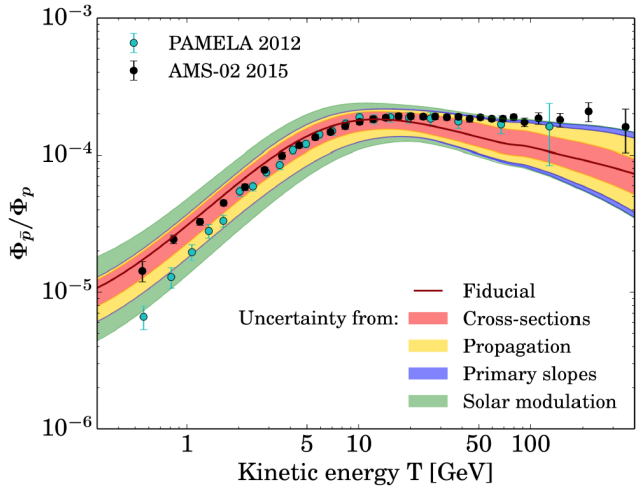

Figure 1.17: Antiproton-to-proton ratio measured by PAMELA (2012) [90] and AMS-02 (2015) [91]. The uncertainty on the predicted secondaries are encapsulated in bands, and each source of uncertainty is given in a different color (see legend on the figure). For some parameter choices, the total width of these bands can be narrowed within the error bars. The continuous curve corresponds to reference values used in [92], where the figure was taken from.

"smoking guns" of particle DM.

In the literature, there have been claims that lines had been observed in the photon spectrum at 3.5 keV [93], 511 keV [94] and 130 GeV [95, 96]. These observations have opened the door to DM interpretations of the signals, but unfortunately for us, none of them has been conclusive in theses terms.

- The analysis of Bringmann *et al.* [95], who were the first to suggest the presence of a spectral feature around the GC in the context of Internal Bremsstrahlung signatures, was soon complemented by that of Weniger [96] who, under the assumption of DM annihilations into a pair of photons, found a local significance of 4.6σ at $m_{\rm DM} \sim 130$ GeV. After taking into account the *look-elsewhere* effect,[39] this significance was actually reduced to 3.2σ. On its side, the FERMI-LAT Collaboration reprocessed the data with updated calibrations of the instrument [97] and found a hint for a line around 133 GeV. However, it had a much lower significance: 3.3σ locally, which translated to a global value of 1.5σ. The 130 GeV excess, which has now faded away for the reasons just exposed, is *not* to be confused with the excess that has been reported by other groups near the GC (see, *e.g.*, [98, 99, 100]), and which is present at a few GeVs (*non*-monochromatic). According to the FERMI-LAT Collaboration [101], that excess seems hardly consistent with a DM origin but is still under investigation. This is in part due to the extension of the excess along the galactic plane—where a

[39] We comment more on this effect in Chap. 6.

DM signal is not expected—but it obviously does not prevent the Collaboration from providing limits in the $(m_{\rm DM}, \langle\sigma v\rangle)$ parameter space (see their figure 29).

- The 511 keV line emission from the Galaxy has been observed for over four decades [94] but has been measured with high accuracy only recently, thanks to the INTEGRAL detector [102]. To this day, it is still unclear what could produce this line, but many sources other than DM could potentially contribute to a line at that energy—*e.g.* positronium decays in the Galaxy, and β^+-decay of unstable nuclei in stars [103]—, making the DM interpretation a very touchy one.

- As for the 3.5 keV line, there has been a lot of debate on whether it resulted from a new transition line (see footnote 38) or whether DM could be made responsible for it. The analysis of the few high-resolution data that the HITOMI instrument has been able to collect before its tragic dead shows that it is inconsistent with the line observed by Bulbul *et al.*, and that there is likely no line anywhere around 3.5 keV [104]. To definitely settle the situation, we will unfortunately have to wait until another high-resolution detector is sent into orbit to take more data, but in my opinion, it does take some imagination to see a line in the X-ray spectrum presented in Ref. [93].

At the theoretical level, photon and neutrino lines are expected from the decays and annihilations of non-relativistic DM with two particles in the final state (among them, at least one γ or one ν).[40] More broadly, other categories of sharp signatures exist, with the box-shaped [107] and Internal Bremsstrahlung [108, 109, 110] spectra as main ambassadors—they involve more particles in the final state. That they may also be qualified as smoking guns of the DM comes from the presence of sharp edges that, like the lines, have no astrophysical counterpart beyond the GeV scale.

At the experimental level, though, a broadening of the aforementioned features is unavoidable—making them look like bumps in the data—and the challenge is to have a detector with good enough energy-reconstruction skills. In the case of the FERMI and HESS instruments, that reach an energy resolution of about 10–15 % [111, 112],[41] the limits on the line feature are quite impressive, as depicted in Fig. 1.18. For DM annihilations (left figure), thermal cross sections ($\langle\sigma v\rangle \sim 3\cdot 10^{-26}\text{cm}^3/s$) have already been probed in a large region of the parameter space, and for decaying DM (right figure), the level of sensitivity on the inverse decay width can be about 10 orders of magnitude above the age of the Universe τ_U. Note that these limits are several orders of magnitude better than those holding on a typical γ-ray continuum, reflecting the mere fact that a line feature is nothing like the expected backgrounds. In the case of neutrino telescopes, like ICECUBE and ANTARES, the resolution potential highly depends on the sample under consideration. As already said, all neutrinos do not behave the same way, and the estimation of energy can be optimized through the choice of some specific types of events (see Fig. 13 in Ref. [115]), even if this is usually not as good in comparison with gamma-ray telescopes. We show in Fig. 1.19 a summary of the most recent searches for neutrino lines performed by Collaborations between ~ 30 GeV and 10^5 GeV, which covers the range of masses that our analyses have focused on.

[40] A popular example involving the two lines is that of the gravitino decay [105, 106].

[41] The exact value is obviously energy-dependent, but we quote this as a benchmark.

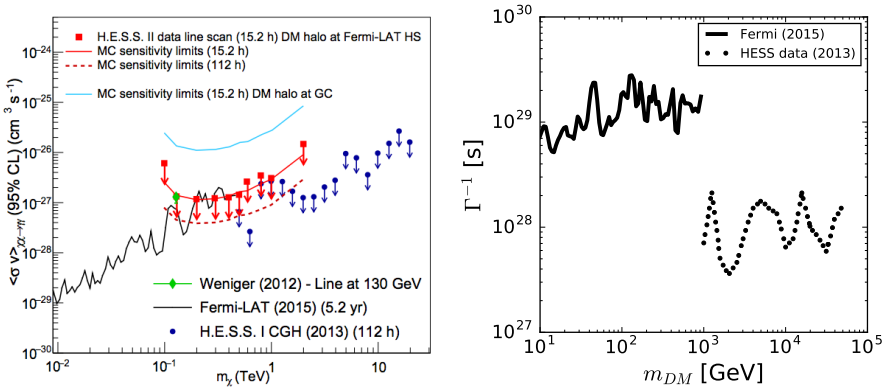

Figure 1.18: *Left:* 95 % CL limits on $\langle\sigma v\rangle_{\gamma\gamma}$, the DM annihilation cross section into two photons, as a function of the DM mass (m_χ in the figure). The black curve and the blue arrows respectively give the limits obtained by the Fermi-Lat (2015) [111] and Hess (2013) [112] Collaborations. The most recent limits obtained by Hess (2016) [113] are given by the red arrows. The curves in clear blue, continuous red and dashed red give the sensitivities of Hess derived with, respectively, a 15.2-hour observation of the GC, 15.2 and 112 hours of observation of the halo. The green dot is placed where Weniger had suspected a line. Figure taken from [113] and see unmentioned references therein. *Right:* 95 % CL limits on $\tau_{\nu\gamma}$, the inverse DM decay width with one photon in the final state, as a function of the DM mass $m_{\rm DM}$. The continuous and dotted curves respectively denote the limits derived by the Fermi-LAT Collaboration [111] and by M. Gustafsson *et al.* Ref. [114], who used the limit on the flux ϕ provided by Hess in [112].

We note the presence in the literature of recent alternative limit estimates on $\langle\sigma v\rangle_{\nu\overline{\nu}}$ based on the continuum of photons radiated by the $\nu\overline{\nu}$ final state [119]. These limits are however no more competitive with neutrino Collaboration estimates, which is why we do not show them in Fig. 1.19. It could however be interesting to reconsider them once Cta is in operation and provides its sensitivity estimates.

Be prepared to see some of these limits quite often in the following chapters, as we will derive some of our own with other methods and a number of discussions will follow from their comparisons.

Before moving on to the next chapter, let us add that the worldwide development of Gton Cherenkov detectors during the last decade has propelled neutrinos to the fore, making the complementarity of neutrino *and* gamma-ray data a reality. We will see this statement at work through some of the projects exposed in this thesis which—you may have guessed it by this time—is for the most part about neutrino and gamma line searches.

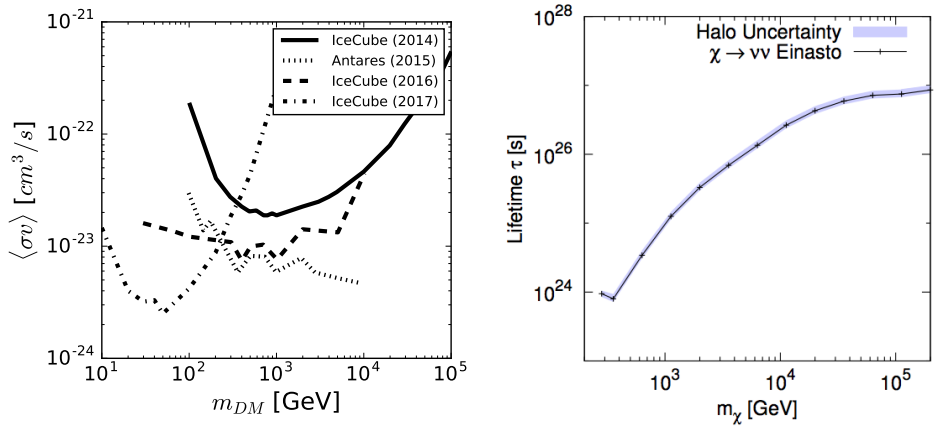

Figure 1.19: *Left:* 90 % CL Limits on $\langle \sigma v \rangle_{\nu\overline{\nu}}$ from neutrino data. The continuous, dashed, and dotted-dashed curves come from official IceCube analyses, respectively in 2014 [116], 2016 [228], and 2017 [120]. The dotted curve comes from the Antares Collaboration [117]. *Right:* 90 % CL Limits on $\tau_{\nu\gamma}$. The latest and best limits that we could find and that were published by a Collaboration are from IceCube (2011), see Ref. [118].

Part II

CHAPTER 2

Mono-energetic photons from millicharged DM decay

In the previous chapter, we have extensively exposed the gravitational evidence for the existence of DM. We have moreover assumed that DM comes in the form of particles, exposed the constraints holding on potential candidates, and exhibited the experimental efforts set for a detection. We have particularly focused our attention on indirect detection and by doing so, we have identified that the smoking-gun signatures of DM consisted in the observation of mono-energetic fluxes of neutrinos and photons—to put it simply, γ-ray and ν lines.

Experimentally, the potential presence of a γ-ray line in the photon spectrum is closely supervised. The current "leaders" in the field are essentially the Hess and Fermi-LAT Collaborations, but the arrival of new telescopes on the market (ground based and satellites) is all the more exciting for they will allow to probe the photon spectrum with further enhanced sensitivity to potential lines. Generally speaking, mono-energetic photons can be emitted through the (co-)annihilation or decay of DM particles. As explained in Sec. 1.3.3, the latter are electrically neutral or millicharged at the most, which means, in the first case, that a γ-line emission would only proceed through the loop of a charged particle, and in the second, that the emission could moreover directly come from millicharged particles. Assuming that particle DM has a thermal history and freezes out, and given the current experimental sensitivities, it is then unlikely for the annihilation scenario to produce **observable γ lines**. The reason behind this statement is the strong suppression of the corresponding partial cross section—either because of the loop or the millicharge—with respect to the total cross section which is *directly constrained* by the relic density $\Omega_{\rm DM}$. On the other hand, the decay scenario leaves us more room to play.

We investigate in this chapter the possibility to induce observable γ-ray lines from the *decay* of *millicharged* DM particles—the case of neutral DM had already been considered in the literature. After a short motivation, Sec. 2.2 introduces to the reader the different millicharge generation mechanisms available. We then expose in Sec. 2.3 the effective theory of this decay and finally discuss the phenomenology in the last section. This chapter strongly bases itself on the work presented in Ref. [121].

2.1 Motivation

Before we come to discussing the two main mechanisms of millicharge generation, let us consider for a moment the motivation and assumptions behind our will to *effectively* study the decays of particle DM and the corresponding phenomenology.

The experimental constraints holding on γ-lines show that these decays *must* be slow (remember Fig. 1.18). We therefore assume that the stability of particle DM is due to an accidental symmetry, like in the case of proton decay. The motivation behind this assumption comes from the fact that an accidental symmetry may naturally be broken by the underlying theory at the UV scale $\Lambda_{\rm UV}$ and that, in the low energy regime, the corresponding decay widths are naturally suppressed by a certain power of $\Lambda_{\rm UV}$. Given the fact that we restrain ourselves to DM masses below 100 TeV, and that the decay width into a γ-line is constrained to be smaller than $10^{-27}\mathrm{s}^{-1}$, $\Lambda_{\rm UV}$ must be larger than 10^{12} GeV if you are considering a dimension 6 operator. This clearly shows the existence of a separation of scales—that is not obvious in the annihilation scenario—and justifies the use of an effective approach.

As already explained in Sec. 1.4.2, by writing out the list of effective operators relative to a class of processes—here, the slow decays of millicharged DM—[1]you avoid the need to make any assumption on the UV completion behind. In this respect, this approach is model-independent and permits to capture within a finite set of operators all the possibly relevant physics in the low energy regime of the theory. Moreover, this language allows for a systematization of the analysis. We will restrict ourselves to effective operators of dimension six (and less).

The phenomenology of each operator goes beyond the mere γ-line emission—which we guarantee by construction. For instance, the gauge invariant nature of the operators *necessarily* predicts decay channels where the emission of a photon is replaced by that of a Z boson (as soon as $m_{\rm DM} > m_Z$ is verified). In turn, that Z boson induces the emission of CRs ($\overline{p}$, γ, e^+, ...) which are looked for and constrained by other measurements. The amount of CRs emitted along with the γ-line is **predictable** for each effective operator, giving us the ranges of branching ratios that we can expect from the UV physics for all the decay channels available. With this knowledge, it is possible to derive constraints on the DM decay width $\Gamma_{\rm tot}$ based on the continuum emissions and confront them to those directly inferred from the γ-line emission. From there, and given an experimental conjecture, we discuss how a distinction among the different effective operators emerges, allowing for the extraction of some properties of particle DM.

As a last remark, let us add that the connection of a photon with a *millicharged* particle is necessarily realised through the insertion of covariant derivatives in our effective operators. This is why, in the two millicharge generation mechanisms that

[1]The possibility to generate an observable γ-ray line from the decay of millicharged DM particles had never been investigated in the literature, probably because one would naively think that this line is strongly suppressed with respect to other induced signals as it involves the millicharge. However, we will show that there exist specific scenarios where this argument does not hold.

we are about to discuss, we are mainly interested in the general expression of the corresponding covariant derivatives. We will start by considering the case of a fermionic DM particle, and will discuss the scalar and vector cases at the end of this chapter.

2.2 Millicharge generation mechanisms

We discuss in this section two main frameworks for the generation of a millicharge. Because of the abelian nature of $U(1)_Y$, it would also be possible to simply postulate that the particle has a hypercharge Y such that $T_3 + Y/2$ is a small number. However, the appeal of the two mechanisms that we are about to expose resides in the fact that the millicharge generation is here a dynamical process. Both scenarios involve the extension of the SM gauge group by an extra $U(1)'$, and millicharges come into the picture as the mere consequence of a small mixing of the SM hypercharge gauge boson with the extra $U(1)'$ gauge boson.

2.2.1 Massless scenario: millicharge from kinetic mixing

The extension of the SM gauge group by an extra $U(1)'$ makes it possible to add the following renormalizable operator to the lagrangian [122, 123]:

$$\mathcal{L} \ni -\frac{\varepsilon}{2} F_{Y\mu\nu} F'^{\mu\nu} \,, \tag{2.1}$$

where $F_{Y\mu\nu}$ and $F'_{\mu\nu}$ respectively denote the field strength tensors of $U(1)_Y$ and $U(1)'$. As you can see, this term is nothing but a non-canonical kinetic mixing term between the corresponding gauge bosons. It can be gotten rid of by applying the following non-unitary transformation:

$$\begin{pmatrix} A'_\mu \\ B'_\mu \\ W'_\mu \end{pmatrix} = \begin{pmatrix} 1 & \epsilon & 0 \\ 0 & \sqrt{1-\epsilon^2} & 0 \\ 0 & 0 & 1 \end{pmatrix} \begin{pmatrix} A_\mu \\ B_\mu \\ W_\mu \end{pmatrix} \tag{2.2}$$

where the $U(1)'$, $U(1)_Y$ and $SU(2)_L$ gauge bosons are respectively denoted by A_μ, B_μ and W_μ (the last two had already been introduced in Sec. 1.4.1). The apostrophe in the LHS of the equation denotes the new basis thusly obtained. In this new basis, the kinetic term associated to the abelian sector is canonical:

$$\mathcal{L} \ni -\frac{1}{4} A'_{\mu\nu} A'^{\mu\nu} - \frac{1}{4} B'_{\mu\nu} B'^{\mu\nu}. \tag{2.3}$$

If the $U(1)'$ is unbroken, as we assume here, it is possible to further work on a redefinition of the fields A'_μ and B'_μ through a unitary transformation:

$$\begin{pmatrix} A^{\gamma'}_\mu \\ A^{\gamma}_\mu \\ Z_\mu \end{pmatrix} = \begin{pmatrix} 1 & 0 & 0 \\ 0 & \cos\theta_\epsilon & \sin\theta_\epsilon \\ 0 & -\sin\theta_\epsilon & \cos\theta_\epsilon \end{pmatrix} \begin{pmatrix} A'_\mu \\ B'_\mu \\ W'_\mu \end{pmatrix}, \tag{2.4}$$

where $\tan\theta_\epsilon = \tan\theta_W / \sqrt{1-\epsilon^2}$.[2] The reason for this redefinition is that two gauge bosons of the theory have remained massless, and therefore there is some arbitrariness

[2] The Weinberg angle θ_W is defined in the SM through the relation: $\tan\theta_W = g_Y/g$. In the following, we will work at the first non-trivial order. It is therefore enough for us to use the approximation $\tan\theta_\epsilon \simeq \tan\theta_W$.

in the definition of these fields. We make the convenient choice—from our point of view—to work in the basis where we can exclusively assign one gauge boson to the Q' generator, while the other one is free to couple through the $Q_{\rm SM} \equiv T_3 + Y/2$ and Q' charges. In the $(A_\mu^{\gamma'}, A_\mu^\gamma, Z_\mu)$ basis, and after the electroweak symmetry breaking has taken place, the covariant derivative becomes:

$$\begin{aligned} D_\mu = \partial_\mu &+ ig(T^1 W_\mu^1 + T^2 W_\mu^2) \\ &+ iA_\mu^\gamma \left(\frac{eQ\cos(\theta_\epsilon)}{\cos\theta_W\sqrt{1-\epsilon^2}} - \frac{g'Q'\epsilon\cos\theta_\epsilon}{\sqrt{1-\epsilon^2}}\right) \\ &+ iZ_\mu \left(gT^3\cos\theta_\epsilon - g_Y\frac{Y}{2}\frac{\sin\theta_\epsilon}{\sqrt{1-\epsilon^2}} + \frac{g'Q'\epsilon\sin\theta_\epsilon}{\sqrt{1-\epsilon^2}}\right) \\ &+ iA_\mu^{\gamma'} g'Q' \,. \end{aligned} \tag{2.5}$$

From this expression, we see that a field with charges T_3, Y, and Q' couples to the photon field A_μ^γ with a charge $Q_{em} = (Q_{\rm SM} - g'Q'\,\epsilon/g_Y)e'$, where $e' = g_Y\cos\theta_\epsilon/\sqrt{1-\epsilon^2}$ (the "new" electronic charge).[3] In particular, a field that originally starts with $Q_{\rm SM} = 0$ acquires a millicharge

$$Q_{em} = -(\epsilon g'Q'/g_Y)e'. \tag{2.6}$$

We correctly recover all the usual SM expressions in the limit $\epsilon \to 0$.

As we have seen in Sec. 1.3.3, the experimental constraints are generally set on the millicharge Q_{em} rather than directly on ϵ.[4] A value of $\epsilon \simeq 1$ is therefore not excluded, in which case there would be some tension with our remark presented in footnote 2. However, ϵ is generally and legitimately expected to be smaller than one. For instance, if we consider that the thermal relic abundance of the DM is only provided by the annihilation into dark photons, we obtain a constraint on $Q'^2\alpha' \equiv Q'^2 g'^2/4\pi$ as a function of $m_{\rm DM}$ which, together with Eq. (1.27), gives $\epsilon^2 \lesssim 10^{-6}$ and justifies our approximation.

2.2.2 Massive scenario: millicharge from the Stueckelberg mechanism

We show in Appendix A.2 that if the $U(1)'$ symmetry is spontaneously broken, a kinetic mixing interaction cannot induce a millicharge for an "originally" neutral field. This is fortunately not the last card that we can play. The Stueckelberg mechanism allows to have a *massive* gauge boson *without* having to break the corresponding gauge symmetry. The idea behind this mechanism is to add an extra scalar Φ to the model so that you have the degrees of freedom needed to give mass to new gauge bosons. Besides, to make the two sectors talk to each other and generate a mixing, the scalar is chosen such that it couples to both of them (in our case, $U(1)_Y$ and $U(1)'$). We proceed as in Ref. [124] by considering the $U(1)'$ Stueckelberg extension of the SM. Because they are quite lengthy, the details related to the Stueckelberg lagrangian and the rotation performed to reach the mass eigenstate basis are presented in Appendix

[3] The subscript *em* simply refers to the "electromagnetism" group $U(1)_{em}$.

[4] See Figs. 1.8 and 1.9. Beware that in those figures, ϵ actually denotes the ratio of a new particle's charge to the electronic charge, *not* the kinetic mixing parameter introduced in Eq. (2.1).

A.3. The covariant derivative—which is the object that we have the most interest in—ends up reading:

$$\begin{aligned} D_\mu \;=\; & \partial_\mu + iZ'_\mu \big(g'Q'(c_\psi c_\phi - s_\psi s_\theta s_\phi) - gT^3 c_\theta s_\psi \\ & +\; g_Y \tfrac{Y}{2}(c_\psi s_\phi + s_\theta c_\phi s_\psi)\big) \\ & +\; iZ_\mu \big(g'Q'(-s_\psi c_\phi - c_\psi s_\theta s_\phi) - gT^3 c_\theta c_\psi \\ & +\; g_Y \tfrac{Y}{2}(-s_\psi s_\phi + s_\theta c_\phi c_\psi)\big) \\ & +\; iA^\gamma_\mu \big(-g'Q' c_\theta s_\phi + gT^3 s_\theta + g_Y \tfrac{Y}{2} c_\theta c_\phi\big) \\ & +\; igT^1 W^1_\mu + igT^2 W^2_\mu \,, \end{aligned} \tag{2.7}$$

where c and s stand for sine and cosine. The angles ϕ, θ and ψ are defined through the following expressions,

$$\tan\phi = \frac{M_2}{M_1}, \quad \tan\theta = \frac{g_Y}{g}\cos\phi, \quad \text{and} \quad \tan\psi = \frac{\tan\theta\tan\phi M_{\mathrm{W}}^2}{\cos\theta(M_{\mathrm{Z}'}^2 - (1+\tan^2\theta)M_{\mathrm{W}}^2)}, \tag{2.8}$$

where M_1 and M_2 respectively correspond to the "bare" masses of the $U(1)'$ and $U(1)_Y$ gauge bosons [124]. You can easily guess in Eq. (2.7) the expression of the electric charge:

$$Q_{em} = (-g'/g_Y Q' \tan\phi + Q_{SM})e', \tag{2.9}$$

where $e' = g g_Y \cos\phi / \sqrt{g^2 + g_Y^2 \cos^2\phi}$. An originally neutral field acquires in this way a charge $Q_{em} = -Q' \tan\phi \, g'/g_Y \, e'$.

With the Z-mass and Lep data measurements at our disposal, it is possible to constrain the mass eigenvalues predicted by the Stueckelberg mechanism in the gauge sector. Their expressions depending on the parameters presented above (see $M_\pm$ in Appendix A.3), we have $\tan\phi \lesssim 0.04$ [125] and thereby justify the approximation of small ϕ used in the following.

2.3 Effective operators

Assuming particle DM to be a fermion, which we denote by Ψ_{DM}, the Lorentz-invariant structure of the Lagrangian imposes the presence of a second fermionic field Ψ in the decay. In addition, exactly **two particles** are required in the final state of this decay (in order for the photons to be **monochromatic**). By construction, this means that the following decay channel

$$\Psi_{\mathrm{DM}} \to \Psi\gamma \tag{2.10}$$

is the only way that Ψ_{DM} can emit mono-energetic photons. Under our assumption that Ψ_{DM} has a millicharge, the field Ψ necessarily carries that same millicharge. We will not specify the exact nature of Ψ—*e.g.* whether it is a Dirac or Majorana particle—but bear in mind that it could potentially be a SM neutrino.[5] We moreover assume that $m_\Psi \ll m_{\mathrm{DM}}$ so that $E_{\gamma\text{-line}} \simeq m_{\mathrm{DM}}/2$.

[5] This option is further discussed in Sec. 2.5.5.

We now come to the determination of the operators which induce the $\Psi_{\rm DM} \to \Psi\gamma$ decay. Recall that we are interested in those operators which realise the coupling to the photon through the covariant derivative of a millicharged field.[6] We find a single dimension-five operator:

$$(D_\mu D_\nu \overline{\Psi})\sigma^{\mu\nu}\Psi_{\rm DM}\,, \tag{2.11}$$

and three dimension-six operators:

$$(D_\mu D_\nu \overline{\Psi})\sigma^{\mu\nu}\Psi_{\rm DM}\Phi\,, \tag{2.12}$$

$$\overline{\Psi}\sigma^{\mu\nu}(D_\mu D_\nu \Psi_{\rm DM})\Phi\,, \tag{2.13}$$

$$(D_\mu \overline{\Psi})\sigma^{\mu\nu}(D_\nu \Psi_{\rm DM})\Phi\,, \tag{2.14}$$

where Φ can be a new field beyond the SM or simply the SM scalar doublet H. The addition of their respective hermitian conjugate is here implicit. Note the presence of $\sigma_{\mu\nu}$ which implies that the operators displaying two successive covariant derivatives on a given particle can be rewritten as a sum of operators where those covariant derivatives are replaced by the field strength tensors of each gauge boson to which the particle couples, and where each term is weighted by the corresponding gauge coupling.[7] Regarding dimension-five operators, another option would naively consist in those operators that display a covariant derivative on a scalar field, such as $\overline{\Psi}\gamma_\mu\Psi_{\rm DM}D^\mu\Phi$. This kind of operator does *not* give any radiative two-body decay as it would require the scalar field to have both a *vev* and a millicharge, and thus give mass to the photon. Similarly, operators with a $\not{D}\Psi$ or $D^2\Phi$ do not give any radiative decays, as can be seen from the corresponding equations of motion. Operators with an additional γ_5 are redundant since the operators involve different fermion fields (*i.e.* γ_5 can always be reabsorbed in the redefinition of one of the fermion fields). The dimension-six operators are equivalent *up to* one operator[8] that does not produce monochromatic photons but can give other decays—including two-body decays—, hence a different phenomenology. At the two-body decay level, the scalar field Φ of the last three operators may only intervene through its *vev*.

There is in principle an infinite choice of quantum numbers for the $\Psi_{\rm DM}$, Ψ and Φ fields, but as we consider the phenomenology of our list of effective operators, we will see how a simple picture can emerge despite of this fact.

2.4 Phenomenology

We can say of all of the operators exposed in the previous section that they have a plural phenomenology, meaning that they not only induce γ-lines but also **predictable** CR fluxes of a different nature ($e^\pm, \overline{p}, \dots$) or shape (*e.g.*, continuum emission of photons).

[6] The neutral case has been studied in Ref. [114].

[7] This basically means that such an operator can easily be produced from one-loop diagrams involving UV particles, similarly to those diagrams which generate the $F^{\mu\nu}\overline{\Psi}\sigma_{\mu\nu}\Psi'$ dipole operators. The latter are in particular relevant for the $\mu \to e\gamma$ decay, and the difference here would be that the photon is radiated by a millicharged particle instead of a charged lepton or charged gauge boson.

[8] And a total derivative term, but this one is physically irrelevant.

This means that the DM decay width Γ_{tot} may be constrained in a multi-messenger context. Used in complementarity with each other, these different sets of constraints can provide a way to discriminate the effective operators at the origin of a putative detection.

We devote this section to the evaluation—for each operator—of the branching ratios of the different decay channels available to particle DM. This allows us, in Sec. 2.5, to set limits on the DM decay width based on the corresponding estimates of the antiproton and continuum γ-ray fluxes.

2.4.1 Line *vs* continua

Given the minimal SM extensions presented in Sec. 2.2 and the effective operators of Sec. 2.3, there are at most five decay channels available to the DM particle Ψ_{DM}.[9] For clarity, these channels are listed in the first column of Tab. 2.1. We have already explained in Sec. 1.5.3 how, given a set of final states and their respective branching ratios, you could compute the differential flux of any type of CR induced by DM decays (see Eqs. (1.53), (1.55), and (1.60)). In that respect, Tab. 2.1 is all you need to estimate a given CR flux induced by a given effective operator. We give here the "generic" form of this table, but special cases will be made explicit in the following subsections. We give the analytical expression of the BRs—and hence the f_X functions—when needed.[10]

Decay channel	Branching ratio
$\gamma\psi$	Q^2_{DM}
$Z\psi$	$c^2_Z \cdot f_Z(m_{\text{DM}}, m_Z)$
$Z'\psi$	$c^2_{Z'} \cdot f_{Z'}(m_{\text{DM}}, m_Z)$
$W^+\psi^-$	$\frac{g^2}{4} c^2_W \cdot f_W(m_{\text{DM}}, m_W)$
$W^-\psi^+$	$\frac{g^2}{4} c^2_W \cdot f_W(m_{\text{DM}}, m_W)$

Table 2.1: Effective decay channels available for a millicharged DM fermion (first column). The branching ratio of each channel is presented in the second column modulo a *global common* factor. The couplings $c_{Z,Z',W}$ can be read out from the covariant derivatives presented in Eqs. (2.5) and (2.7), and are also given in Eqs. (2.15)–(2.17). The analytical expressions of the $f_X(m_{\text{DM}}, m_X)$ functions depend on the specific $SU(2)_L$ multiplet to which the covariant derivative applies. In the cases that we will cover, this function is equal to one unless specifically stated otherwise. The millicharge Q_{DM} is explicitly given for the kinetic mixing and Stueckelberg scenarios in Eqs. (2.6) and (2.9), respectively. See text and Appendix A.1 for further details and particular expressions.

In order to be as conservative as possible with our CR flux estimates and thusly with our upper limit on the total DM decay width Γ_{tot}—which is easily converted to

[9] In this chapter, we restrict ourselves to the consideration of 2-body decay channels. The addition of 3-body decays in the picture is discussed in Chapter 3.

[10] These functions are set to zero if $m_{\text{DM}} < m_X$. When $m_{\text{DM}} \gg m_{Z,Z',W}$, they are always equal to unity except for the operator of Eq. (2.14), see Sec. 2.4.5 and Appendix A.1.

a limit on the γ-ray line emission using Tab. 2.1—, we use here the MIN propagation configuration. We also study the $SU(2)_L$ representations with the least amount of CRs emitted with respect to the monochromatic emission.[11]

The general expression of the Z coupling is readable from Eqs. (2.5)–(2.7):

$$c_Z = \frac{gT_3}{\cos(\theta_\epsilon)} + \frac{g'Q'\epsilon\sin(\theta_\epsilon)}{\sqrt{1-\epsilon^2}} \quad \text{in the kinetic mixing scenario}, \tag{2.15}$$

$$c_Z = -g'Q'(s_\psi c_\phi + c_\psi s_\theta s_\phi) - gT_3 c_\theta c_\psi\Big(1 + t_\theta^2(1 - \frac{t_\psi t_\phi}{s_\theta})\Big) \quad \text{in the Stueckelberg scenario}. \tag{2.16}$$

In the last expression, $t_{\theta,\phi,\psi}$ denotes the tangent of θ, ϕ, ψ (see Sec. 2.2.2 for more details). The coupling to the Z' boson is only relevant in the Stueckelberg scenario and reads:

$$c_{Z'} = -g'Q'(s_\psi s_\theta s_\phi - c_\psi c_\phi) - gT_3 s_\psi c_\theta\Big(1 + t_\theta^2(1 + \frac{t_\phi}{s_\theta t_\psi})\Big). \tag{2.17}$$

Finally, the coupling c_W to the W boson may take very different values as a function of the multiplets considered in the various operators (and the Clebsch-Gordan coefficients). As mentioned above, we consider the cases which minimize c_W and hence give a conservative limit on the DM decay width.[12]

Before coming to study each effective operator, let us stress that we will not consider the emission of CRs by the Z' boson. The latter could for example decay to pairs of non-SM particles, but even if it produced SM particles, we can still make the statement that our approach is conservative. By neglecting the contribution of the Z' to the CRs, the Stueckelberg and kinetic mixing scenarios lead to the same bounds on the decay width (at the lowest non-trivial order in ϕ and ϵ, respectively). We discuss how our results might be affected if we were not to neglect the Z' decays into SM particles at the end of Sec. 2.5.

2.4.2 $(D_\mu D_\nu \overline{\Psi})\sigma^{\mu\nu}\Psi_{\mathbf{DM}}$ effective operator

For this operator to be gauge invariant, the quantum numbers of $\Psi_{\rm DM}$ and Ψ must necessarily be the same. In particular, we have that $T_3^{\rm DM} = T_3^{\psi}$. A first important remark to make at this stage, and which is of relevance for all of the operators, is that there will always be a large[13] production of Z and/or W bosons from the two-body decays of the DM *unless* the field to which the covariant derivative applies is a singlet under $SU(2)_L \times U(1)_Y$. Assuming that this field is *not* a singlet (for instance $T_3 \neq 0$), the production of CRs is strongly boosted with respect to the γ-line emission (by the

[11] This basically amounts to consider that the derived fields live in the singlet and doublet representations. Any higher representation induces more CRs and tightens the bounds on Γ_γ, thereby lessening the chances of *observing* a γ-ray line.

[12] By "conservative", we mean that this limit cannot loosen.

[13] "Large" is here used by opposition with a production that would be suppressed by $Q_{\rm DM}^2$.

inverse of the millicharge squared). Regarding the c_W coupling, we can write for this operator that

$$c_W = a + b. \tag{2.18}$$

For an $SU(2)_L$ multiplet of dimension $n = 2\lambda + 1$, $a = 0$ if $Y_{\rm DM} = 2\lambda$ and $a = 1$ in all other cases. Similarly, $b = 0$ if $Y_{\rm DM} = -2\lambda$ and $b = 1$ in all other cases. As a result, $c_W = 0$ if and only if $a = b = 0$, which happens only if $\lambda = 0$, that is to say for a SM singlet. From this discussion, we outline three cases:

(i) Ψ_{DM} *and hence* Ψ *are SM singlets:* In this case, there is no W emission and the Z emission involves two powers of the millicharge, just as the γ-ray line production. As a result, there is no suppression by passing from the constraints on the continuum to those on the γ line. The branching ratios are presented at the lowest order in ϵ (kinetic mixing) and ϕ (Stueckelberg) in the column (i) of Tab. 2.2.[14]

(ii) $T_3^{DM} = T_3^{\Psi} = 0$ *with* Ψ_{DM}, Ψ *non-singlets:* In this case, there is production of W bosons and $a+b = 2$, giving the column (ii) in Tab. 2.2 at the lowest order in ϵ or ϕ. In order to obtain a conservative and model-independent upper bound, we have made the hypothesis that the charged components of Ψ produced together with W bosons do not yield an important contribution to CRs production. In practice, we neglect here the contribution from the $Z\psi$ as it is largely sub-dominant in comparison with that from the W-boson.

(iii) $T_3^{DM} = T_3^{\Psi} \neq 0$*:* In this case, the production of Z and W bosons is not suppressed. Here we only consider the case with $a + b = 1$ and $T_3^{\rm DM} = 1/2$, as it is the one which minimizes the CR emission. The corresponding branching ratios are presented in the column (iii) of Tab. 2.2 at the lowest order in ϵ or ϕ.

Decay channel	(i)	(ii)	(iii)
$\gamma\psi$	$Q_{\rm DM}^2$	$Q_{\rm DM}^2$	$Q_{\rm DM}^2$
$Z\psi$	$Q_{\rm DM}^2 \tan^2\theta_W$	$Q_{\rm DM}^2 \tan^2\theta_W$	$g^2/(4\cos^2\theta_W)$
$Z'\psi$			
$W^+\psi^-$	0	$g^2/2$	$g^2/4$
$W^-\psi^+$	0	$g^2/2$	$g^2/4$

Table 2.2: Same as Tab. 2.1 in the particular case of $(D_\mu D_\nu \overline{\Psi})\sigma^{\mu\nu}\Psi_{\rm DM}$. The $Z'\psi$ entry is masked on purpose because we neglect any contribution from the Z' in the Stueckelberg framework.

2.4.3 $(D_\mu D_\nu \overline{\Psi})\sigma^{\mu\nu}\Psi_{\rm DM}\Phi$ effective operator

With this operator, the relevant quantum numbers are those of Ψ. The minimal CR emission as a function of T_3^{Ψ} follows the same pattern as for the previous operator:

(i) Ψ is a SM singlet: prediction (i) of Tab. 2.2.

[14] In the case of the Stueckelberg scenario, the prediction in this column is a good approximation if $\sin\phi \ll \sin\psi$, which is what is expected if there is a big splitting between the SM gauge bosons and the Z' masses.

(ii) $T_3^\Psi = 0$ with Ψ non- singlet: prediction (ii) of Tab. 2.2.

(iii) $T_3^\Psi \neq 0$: prediction (iii) of Tab. 2.2.

2.4.4 $\overline{\Psi}\sigma^{\mu\nu}(D_\mu D_\nu \Psi_{\mathbf{DM}})\Phi$ effective operator

Now, the relevant quantum numbers are those of the DM particle:

(i) Ψ_{DM} *is a SM singlet*: prediction (i) of Tab. 2.2.

(ii) $T_3^{DM} = 0$ *with* Ψ_{DM} *non- singlet*: the CR emission is minimised when $c_W = 1/2$, giving[15] the prediction (ii) in Tab. 2.3.

(iii) $T_3^\Psi \neq 0$: the CR emission is minimised with $T_3^\Psi = 1/2$ and $c_W = 1/4$, giving the prediction (iii) in Tab. 2.3.

Decay channel	(i)	(ii)	(iii)
$\gamma\psi$	$Q_{\rm DM}^2$	$Q_{\rm DM}^2$	$Q_{\rm DM}^2$
$Z\psi$	$Q_{\rm DM}^2 \tan^2\theta_W$	$Q_{\rm DM}^2 \tan^2\theta_W$	$g^2/(4\cos^2\theta_W)$
$Z'\psi$			
$W^+\psi^-$	0	$g^2/8$	$g^2/16$
$W^-\psi^+$	0	$g^2/8$	$g^2/16$

Table 2.3: Same as Tab. 2.1 in the particular case of $\overline{\Psi}\sigma^{\mu\nu}(D_\mu D_\nu \Psi_{\rm DM})\Phi$. The $Z'\psi$ entry is masked on purpose because we neglect any contribution from the Z' in the Stueckelberg framework.

2.4.5 $(D_\mu\overline{\Psi})\sigma^{\mu\nu}(D_\nu \Psi_{\mathbf{DM}})\Phi$ effective operator

The phenomenology of this operator is more involved than that of the operators above because the dependence on the couplings of Ψ and $\Psi_{\rm DM}$ to the various gauge bosons is more complicated. Nonetheless, minimizing the CR emission requires Ψ and $\Psi_{\rm DM}$ to have the same quantum numbers, which greatly reduces the complexity of the branching ratios. In the case where both $\Psi_{\rm DM}$ and Ψ are SM singlets, the number of Z bosons radiated (at the lowest order in ϵ or ϕ) is proportional to

$$Q_{\rm DM}^2 \cdot \tan^2\theta_W \cdot \left[1 - (\frac{m_Z}{m_{\rm DM}})^2\right]^2 \left[1 + \frac{1}{2}(\frac{m_Z}{m_{\rm DM}})^2\right], \tag{2.19}$$

meaning that the γ-ray line emission is *not* suppressed with respect to the emission of CRs. In the case where $\Psi_{\rm DM}$ and Ψ are *not* SM singlets, the predictions are quite lengthy and we *only* give them for the cases where $T_3 = 0$ and $T_3 = 1/2$ in the Appendix A.1. Unlike all of the previous cases where the dependence on m_W was negligible for $m_{\rm DM} \gg m_W$, there are here terms proportional to $m_{\rm DM}/m_W$,[16] implying

[15] This minimum value of c_W is obtained in the situation where $\Psi_{\rm DM}$ is a triplet, and where Ψ and Φ are quintuplets. Any combination of smaller multiplets leads to a bigger value of c_W. For example, taking $\Psi_{\rm DM}$ as a triplet with $Y = 0$, and taking both Ψ and Φ as doublets with $Y = 1$ leads to $c_W = 2$.

[16] These terms come from the longitudinal W contribution.

a power-law dependence on $m_{\rm DM}$. This gives rise to stronger constraints on the decay width with increasing $m_{\rm DM}$ (see Fig. 2.1 in the next section).

2.5 Indirect limit estimates

Once the branching ratio of the different decay channels is known (*e.g.* Tabs. 2.2 and 2.3), it is possible to constrain the strength of a γ-ray line from the observational constraints existing on the CR continua (in our case, $\overline{p}$ and γ continuum). In the following, we will sometimes refer to these limits as *indirect limits* on the γ-ray line, in contrast to those coming from the *direct* (= dedicated) searches for a line.

2.5.1 Statistical method

The methodology used to obtain these constraints is the same as that used in Ref. [114], meaning that we take a chi-square test statistic and derive a 95% CL interval on the DM total decay width $\Gamma_{\rm tot}$ (our only free parameter in Eqs. (1.53), (1.55), and (1.60)) by requiring that:

$$\Delta\chi^2 \equiv \sum_{\text{bins } i} \frac{(\text{data}_i - \text{model}_i)^2}{\sigma_i^2} = 3.84. \tag{2.20}$$

In this equation, "model$_i$" refers to the prediction of our model (DM and background fluxes) in bin i, "data$_i$" is the flux observed in bin i, and σ_i^2 denotes the statistical and systematic errors (added in quadrature) in each bin. The data and the values of σ_i^2 are taken from Refs. [126] (antiproton flux) and [127, 128] (diffuse γ-rays, read off figure 4).

Regarding the **antiproton flux**, we have only used the data above 10 GeV so as to avoid the uncertainties related to the solar modulation effect. Beyond 10 GeV, the data is well understood from astrophysical models (see Fig. 1.17), and we take the observed data as our background (= Null) model, giving $\chi^2 = 0$ by construction.

With the **isotropic diffuse γ-ray** background, we have more room to play in the sense that there is less consensus regarding its origin. We therefore consider a slightly modified version of the test statistic presented in Eq. (2.20):

$$\Delta\chi^2_{\text{modified}} \equiv \sum_{\text{bins } i} \Theta_{\rm H}(\text{model}_i - \text{data}_i) \frac{(\text{data}_i - \text{model}_i)^2}{\sigma_i^2}, \tag{2.21}$$

where $\Theta_{\rm H}$ is the Heaviside step function. Concretely, with this version of the test statistic, we only consider the bins where the DM prediction overshoots the observation (and use it as a model in those bins).[17] This approach is clearly more conservative than that exposed above, but we will see that it does not prevent from getting better limit estimates than with the antiprotons above $m_{\rm DM} \sim 1$ TeV. We have used the diffuse γ-ray background measurement of Fermi-LAT [129] and Hess [130].[18]

[17] We model the DM-induced contribution with the extra-galactic and galactic fluxes. For the latter, we have made the conservative choice to only consider the contribution from the galactic poles, where the DM density is low.

[18] The slight change of behaviour around 1 TeV is where the crossover with the constraints from $\overline{p}$ data happens.

2.5.2 Results

Fig. 2.1 displays the indirect limits that we have obtained as a function of the DM mass $m_{\rm DM}$. In case a γ-line is observed in the near future, the utility of this figure is to show, in the twinkling of an eye, which operators remain compatible with this detection. Likewise, if a DM-induced signal is observed in CR data but not a γ-ray line, this plot tells you which operators remain compatible with the non-observation of that line.

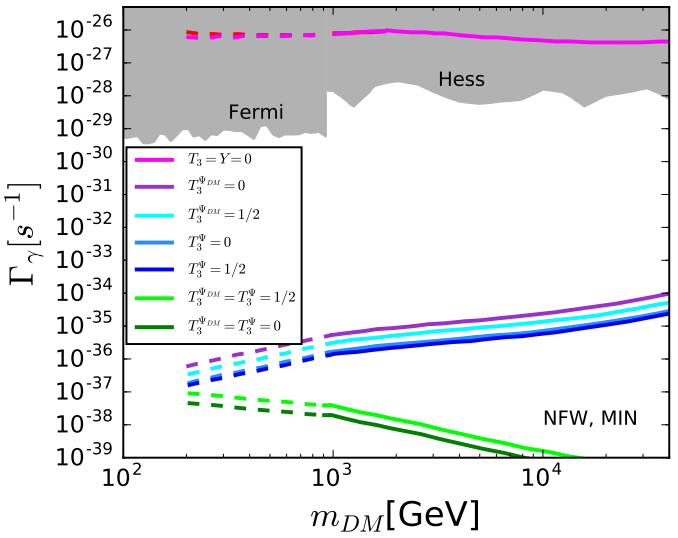

Figure 2.1: Upper limits at the 95% CL on Γ_γ, the decay rate of particle DM into monochromatic photons, as a function of the DM mass $m_{\rm DM}$. The limits computed within our work, that is to say from the CR continua, are given by the colored curves. The gray areas give the regions excluded at 95 % CL by dedicated line searches performed with Fermi-LAT [111] and Hess [112] data. For the dashed curves, we have used Pamela measurements of the $\overline{p}$ flux [126], and for the continuous curves we have used the measurements of the diffuse photon background by Fermi-LAT [127, 128]. We have considered the NFW profile for the DM density and used the Min propagation model to compute conservative estimates of the $\overline{p}$ flux [75]. By using the Max configuration, the dashed curves go down by an order of magnitude. The curve labelled with $T_3 = Y = 0$ is the (absolute) upper bound valid for almost all operators when the derived field is a SM singlet, see column (i) of Tab. 2.1. The only exception is the $D_\mu \overline{\Psi} \sigma^{\mu\nu} D_\nu \Psi_{\rm DM} \Phi$ operator with singlet derived fields, for which the bound is almost identical except at DM masses around 200 GeV (in red). The curves labelled with T_3^{Ψ} are given for the $D_\mu D_\nu \overline{\Psi} \sigma^{\mu\nu} \Psi_{\rm DM} \Phi$ and $D_\mu D_\nu \overline{\Psi} \sigma^{\mu\nu} \Psi_{\rm DM}$ operators, whereas those with $T_3^{\Psi_{\rm DM}}$ are given for $\overline{\Psi} \sigma^{\mu\nu} D_\mu D_\nu \Psi_{\rm DM} \Phi$. The two remaining curves, labelled $T_3^{\Psi_{\rm DM}} = T_3^{\Psi}$, are given for $D_\mu \overline{\Psi} \sigma^{\mu\nu} D_\nu \Psi_{\rm DM} \Phi$. All constraints hold for the kinetic mixing as well as for the Stueckelberg frameworks at first order in ϵ and ϕ.

A clear picture emerges:

- Except for the case in which the derived field is a singlet under the SM, none of the effective operators listed above—each taken individually—would be able to produce a γ-ray line strong enough to meet the current experimental sensitivities without overproducing the $\overline{p}$ and diffuse γs. In other words, as soon as the field on which the derivative applies is *not* a SM singlet, the observation of a γ-ray line would be associated to an excess of CRs 5 to 10 orders of magnitude higher than the level of sensitivity provided by Pamela or Fermi-LAT;
- The results show that the observation of a γ line **could be due to the fact that DM has a millicharge**. This observation would point towards the specific case in which the *derived* field is a singlet.[19] Thus, the minimal scenarios would either feature two singlet fermions in Eq. (2.11) or the SM scalar field together with two millicharged fermion fields of which one is a doublet (Eqs. (2.12)–(2.14));
- Note however that it is *not* possible to differentiate the mechanisms responsible for the millicharge,[20] nor the effective operators that are responsible for a decay;
- The prediction (i) in Tab. 2.2 is generic when the derivative acts on a singlet field (same for all the operators).[21] This is the prediction from which we can expect the most monochromatic photons, and it provides in this regard an "absolute" bound on Γ_γ. Modulo higher-order corrections in ϵ or ϕ, this bound is—unfortunately—the same as that presented for singlets in Ref. [114] in the context of a neutral DM particle.

We have already explained that when the field that is derived is *not* a SM singlet, we only consider the multiplet configurations that give a conservative estimate of the CR fluxes. These conservative estimates are identical for $D_\mu D_\nu \overline{\Psi}\sigma^{\mu\nu}\Psi_{\rm DM}$ and $D_\mu D_\nu \overline{\Psi}\sigma^{\mu\nu}\Psi_{\rm DM}\Phi$, and they differ by less than one order of magnitude for $\overline{\Psi}\sigma^{\mu\nu} D_\mu D_\nu \Psi_{\rm DM}\Phi$—that is to say within the uncertainty coming from the propagation models. The only operator with a very different behaviour is $D_\mu \overline{\Psi}\sigma^{\mu\nu} D_\nu \Psi_{DM}\Phi$, and this is because of its dependence of the branching ratios on the DM mass (see Eq. (2.19) and Appendix A.1). Not only do these bounds exhibit a different behaviour as a function of the DM mass (stronger with increasing $m_{\rm DM}$), they also differ above 2 TeV by more than two orders of magnitude. Therefore, if the experimental sensitivity to a line were (unrealistically!) improved by several orders of magnitude, it would in principle be possible to discriminate this particular effective operator from those where the derived field is not a SM singlet.

2.5.3 Extra emission from the Z'

In the Stueckelberg scenario, the contribution of the Z' to the emission of CRs—if kinematically allowed—has been neglected on purpose. However, by considering the decay of the Z' we get even more stringent bounds on the DM decay width. In order

[19] Beware that this does *not* necessarily mean that the DM is a singlet, nor the accompanying scalar field.

[20] Going beyond the first order in ϵ or ϕ would not help neither because these correction would be drown into other uncertainties (astrophysical, DM profiles, etc.).

[21] Except a mild difference with the operator in Eq. (2.14).

to have an idea of how large this effect could be, assume that the Z' mainly decays into a $b\bar{b}$ pair—which produces a lot of CRs—, and that $g'Q' = 1$. If the derived field is *not* a SM singlet, the limits are about two orders of magnitude stronger than what has been presented. This is easily understood from the fact that the Z' would produce a similar amount of CRs in comparison to a Z or W boson, but at the same time $g'Q' = 1$ is stronger that the weak coupling by 1 order of magnitude. If, instead, the derived field *is* a SM singlet, the relative branching ratios (line *vs* CRs) does not depend on $g'Q'$. Yet, the coupling to the monochromatic photon is suppressed by $\sin\phi$ and, modulo a common factor, the branching ratio of the decay into the line and into the Z' are respectively given by $\cos^2\theta \sin^2\phi$ and ~ 1 (at leading order). The ϕ angle being constrained by the Z-width measurement at LEP [131],

$$\sin\phi \lesssim 0.04, \tag{2.22}$$

it means that the bound of scenario (i) in Tab. 2.2 is improved by 3–4 orders of magnitude in this case. The observation of a γ-ray line with an intensity around the present experimental sensitivity would therefore probe this scenario (see Fig. 2.1).

2.5.4 Rapid decays

Thus far, we have derived constraints on the intensity of a γ-ray line from CR emissions. In this process, the coupling to the invisible photon has not been taken into account for the latter does not induce any CR flux in the visible sector (by definition). However, if the "dark charge" $g'Q'$ is large, you may want to start worrying about the total decay width (or lifetime) of particle DM. The decay into $\Psi\gamma'$ is naturally faster than that into $\Psi\gamma$ by a factor of ϵ^{-2}. Therefore, we have to make sure that the DM lifetime is greater than the age of the Universe:

$$\Gamma^{-1}(\Psi_{\rm DM} \to \Psi\gamma') \gtrsim \tau_U \ . \tag{2.23}$$

By doing so—this requires to assume a value of $g'Q'$—, and using the CMB bound on the millicharge presented in Eq. (1.27), we obtain the limits on Γ_γ presented in Fig. 2.2. Clearly, with a large value of $g'Q'$, considering the lifetime is competitive (with respect to the direct line searches), whereas smaller values are basically irrelevant. Unless the Z' is heavy enough for $\Psi_{\rm DM} \to \Psi Z'$ to be kinematically forbidden, this consideration also applies in the context of the Stueckelberg scenario.

2.5.5 $\Psi_{\rm DM} \to \gamma\nu$

We can legitimately ask ourselves what would happen if the Ψ particle accompanying the photon in the decay of a millicharged DM particle were a SM neutrino. It should be clear now from Sec. 2.5.2 that having a neutrino as a partner in the decay does not allow any of the operators in Eqs. (2.11), (2.12) and (2.14) to induce an *observable* γ-line in the $\mathcal{O}(100 - \text{few}\,10^4)$ GeV DM mass range (strong Z/W emissions). The only operator left seems to be the one in Eq. (2.13) as the neutrino doublet is there *not* derived and the DM field could simply be a singlet. However, the scalar field Φ must take a *vev* in order to leave room for 2-body decays, meaning that the DM field must carry the same millicharge as the neutrino. That charge—of the neutrino—is even more constrained than for a particle that is, say, at the GeV scale ($q_\nu \lesssim 2 \times 10^{-14} e$, see

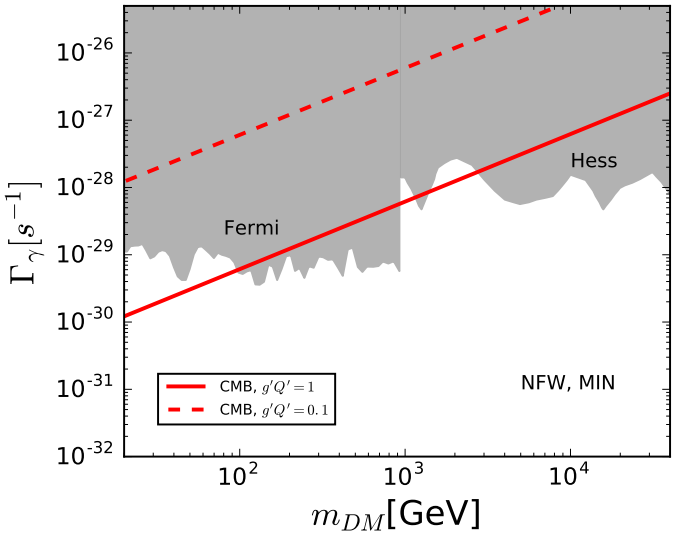

Figure 2.2: Limits on the decay width of a fermionic DM with a γ-ray line in the final state as a function of $m_{\rm DM}$, taking various values of the dark charge $g'Q'$ and imposing that $\Gamma^{-1}(\Psi_{\rm DM} \to \psi\gamma') \gtrsim \tau_U$. We have considered the limit on the millicharge coming from the CMB, that is to say Eq. (1.27). The "direct" upper limits at the 95% CL from Fermi and Hess are the same as in Fig. 2.1.

Fig. 1.8), further enhancing the indirect limits that we have obtained above on Γ_γ. For these reasons, a line observed at the present sensitivities with an energy above the Z mass could not be attributed to a millicharged DM decaying into a neutrino and a photon through any of the operators under study.

We can nonetheless ask ourselves whether or not it would be possible to observe this line at lower masses, where the production of Z/W bosons in the final state is kinematically impossible. In this case, the off-shell production of these bosons and their subsequent decays must be supervised for they can lead to small DM lifetimes (shorter than the age of the Universe) and/or too many CRs. Assuming that a γ line must result from a two-body decay with inverse decay width $\Gamma_\gamma^{-1} \sim 10^{26-30}$ sec (= to be *observable*), it is easy to see that the three-body inverse decay width from, say, $\Psi_{\rm DM} \to 3\nu$ is shorter than the age of the Universe unless

$$m_{\rm DM} < 35\ {\rm MeV} \cdot \left(\frac{10^{28}\,{\rm sec}}{\tau_\gamma}\right)^{1/4}. \tag{2.24}$$

This limit on $m_{\rm DM}$ is stronger than those coming from other Z-decay modes, to the exception of $\Psi_{\rm DM} \to \nu e^+ e^-$ which gives

$$m_{\rm DM} < 2\, m_e \tag{2.25}$$

in order to avoid the overproduction of 511 keV photons in the galactic center.[22]

[22]The limit on the corresponding decay width with a DM mass below ~ 35 MeV is given by $\Gamma(\Psi_{\rm DM} \to \nu e^+ e^-) < 10^{-26}\, s^{-1} \cdot (m_{\rm DM}/{\rm MeV})$ [132, 133].

2.6 Scalar and Vector DM

It is also possible to construct effective operators leading to the emission of a γ-ray line from the decay of a scalar or vector DM particle. Due to the angular momentum conservation, a scalar DM particle cannot decay to a scalar and a photon and we only need to consider a decay into a photon and another massive spin-one particle—which necessarily carries the same millicharge as particle DM. On the form, the operators that allow the decay of a scalar DM particle into a vector and a photon also hold for a vector DM particle decaying into a scalar and a photon as you only need to redefine which field is the DM field. Beware though that a vector DM particle can *also* decay into a photon and another vector particle.

In the case of a "scalar-vector-photon" effective vertex, we find one dimension-five operator:

$$F^A_{\mu\nu} F^{A\mu\nu} \Phi \,, \tag{2.26}$$

and two dimension-six operators:

$$F^A_{\mu\nu} F^{A\mu\nu} \Phi \Phi' \,, \tag{2.27}$$

$$F^A_{\mu\nu} D^\mu \Phi D^\nu \Phi' \,. \tag{2.28}$$

The Φ and Φ' fields denote scalar representations, while $F^A_{\mu\nu}$ denotes the fields strength tensor of the non-abelian gauge group to which the millicharged vector is associated. The DM field can either be one of the scalar or vector particles.[23] In the latter case, it is "hidden" in a covariant derivative or a non-abelian[24] field strength tensor. The photon can show up in one of the $F^A_{\mu\nu}$ field strengths through gauge boson mixing. This would *e.g.* occur if, on top of a kinetic mixing between the hypercharge and $U(1)'$ gauge bosons, the symmetry breaking scheme induces a mixing between the $U(1)'$ gauge boson and those of the new non-abelian group.

The absence of (isolated) covariant derivatives in Eqs. (2.26)–(2.28) is a consequence of the use of the equations of motion and the rotation away of non-canonical kinetic terms. Note that operator (2.28) is equivalent to operator (2.27) up to terms that do not produce monochromatic photons but do contribute to the CR continua. This is why we separately list them.

Based on our experience with the millicharged fermion DM decay scenario, we comment now on the phenomenology of the millicharged scalar and vector DM decays. For the two operators of Eqs. (2.26) and (2.27), the emission of a Z boson is always proportional to the square of the millicharge, even if the scalars are not singlets under the SM. The reason is that the Z boson, like the photon, can only come—in

[23] Regarding the possibility for a vector DM particle to decay into a photon and *another* vector particle, we could think of operators which only involve the $F^A_{\mu\nu}$ field strength tensors (*e.g.*, $F^A_{\mu\nu} F^{A\mu\rho} F^{A\nu}_{\rho}$), and where a photon is inserted in the tensors through a gauge boson mixing mechanism. We however did not find any simple realisation of this, which is why this option is not further considered.

[24] A necessary condition for the vector DM to acquire a millicharge is to be a complex field. For this reason, it is associated to a non-abelian gauge group.

these two operators—from a field strength tensor (not from a covariant derivative). This means that the prediction (i) of Tab. 2.2 is still valid, even if the scalars are not SM singlets.[25] The "absolute" bound (the top red curve in Fig. 2.1) is, as in the fermionic case, saturated under the assumption that there is no CRs produced from the Z' decay (Stueckelberg case, if kinematically allowed). As for the operator of Eq. (2.28), the production of Z and W may not be suppressed by the millicharge if the scalars are non-SM singlets. Its phenomenology is therefore also similar to that of the fermion operators.

2.7 What should you take away from this chapter?

This chapter has been dedicated to the study of millicharged DM particle decays involving the production of mono-energetic gamma-rays in the final state, and has addressed the question of whether or not this class of scenarios could be responsible, in a "multi-messenger context", for the potential observation of gamma-ray lines in the near future.

To answer this question, we have relied on the EFT framework. This approach was justified by the fact that dedicated gamma-ray line searches *already* probe large suppression scales, typically giving—in the case of > 100 GeV millicharged particle decays—$\Lambda \gtrsim 10^{12}(10^{18})$ GeV for dimension-six(five) operators.

After reviewing the different millicharge generation mechanisms at hand (Sec. 2.2), we have developed in Secs. 2.3 and 2.6 the list of effective operators that (at least) induced the class of decays above-mentioned (with a focus on fermionic DM candidates). It turns out that this list was very restrictive. In each case, we have determined conservative estimates of the cosmic-ray fluxes accompanying the emission of mono-energetic photons ($\overline{p}$, continuum of γ rays) and, given the experimental constraints on these fluxes, new complementary sets of constraints on the DM decay width were obtained (see Fig. 2.1). We have focused on the $100\text{GeV} - 50\text{TeV}$ DM mass range, and the outcome was that, whenever an operator involved the action of a covariant derivative on a non-singlet field, the limits on the DM decay width were at least 6 orders of magnitude stronger than those obtained in the context of dedicated line searches. This is understandable from the fact that the gamma-ray line emission through a covariant derivative is *always* suppressed by the square of the millicharge, as opposed to the emission of cosmic rays—when the derived field is *not* a singlet.

In terms of the question phrased hereabove, the conclusion of this work—where we assume particle DM to be millicharged and metastable—is that a putative $\gtrsim 100$ GeV gamma-ray line discovery around the present levels of sensitivity would specifically point to those effective operators involving the covariant derivative of singlet fields. In other words, we have shown that the discovery of a γ-ray line could be due to the fact that DM is millicharged.

[25] This statement holds up to corrections in $m_Z^2/m_{Z'}^2$ for $m_{Z'} > m_Z$.

CHAPTER 3

Mono-energetic photons *and* neutrinos from neutral DM decay

Within the previous chapter, we have been interested in the possibility for particle DM to be millicharged and have at least one decay channel that involves the production of a mono-energetic photon. We acknowledge that we have but little commented on the nature of ψ, the partner of the mono-energetic photon. The reader will be reassured to know that we redeem ourselves in this chapter by considering the particular case where $\psi = \nu$. This is certainly one of the most exciting scenarios of DM decay since it opens the door to **multi**-messenger **line** searches.

The fact that neutrino line searches have just started gaining in interest in the past few years has obviously to do with the youth of the field of neutrino astronomy. Nonetheless, the sensitivity improvements of detectors like IceCube and Antares are encouraging and the ability that they have in probing the sky beyond the TeV scale is a clear advantage over γ-ray astronomy. With the analysis presented in Chapter 6—which we performed after a public data release by the IceCube Collaboration—, we explicitly see this statement at work in the context of the searches for spectral features in the neutrino and gamma-ray sky. Given the fact that similar sensitivities were found in some region of the parameter space that we probe, this was the opportunity for us to again adopt the EFT approach and perform a systematic study of the DM decays into $\gamma\nu$ in order to see what were the prospects to observe the two lines in a near future. The cases of neutral and millicharged particle DM will separately be considered. The work presented in this chapter has been published under Ref. [134].

3.1 Motivation

Back in 2014, the IceCube Collaboration released a data sample of neutrinos (>100 GeV) along with the backgrounds' distributions and differential effective areas [3]. With this in hand, an analysis could be performed by any outsider of the Collaboration and we seized this opportunity to search for DM-induced sharp features in this sample (this is the subject of Chapter 6). What we did show was a large improvement of the constraints holding on the flux of monochromatic neutrinos in comparison to the latest official limits by the Collaboration.[1] We have in particular shown, for the DM decay scenario, the existence of a range of DM masses where the dedicated γ-ray line searches with Hess data [112, 114] reach a comparable level of sensitivity than that which we have obtained on neutrino lines (see Fig. 3.1, from $\sim$ 10 to 50 TeV). Within this range, which interestingly allows for thermally produced DM candidates, this opens the way to a potential "**double smoking gun**" evidence of the DM particle, that is to say the observation of both γ- and ν-lines of similar intensities and energies.

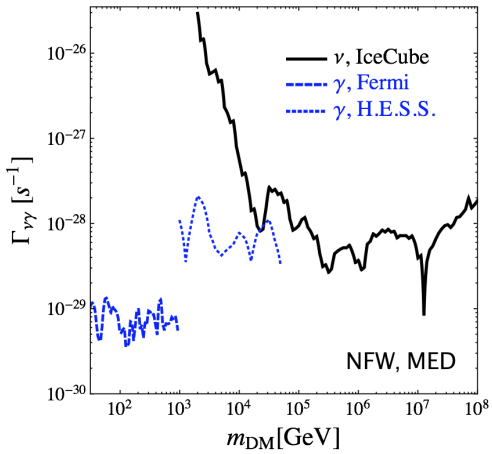

Figure 3.1: 95 % CL limits on $\Gamma(\text{DM} \to \gamma\nu) \equiv \Gamma_{\nu\gamma}$ from Fermi-LAT (2015, dashed blue line) [111], Hess (2013, dotted blue) [112, 114], and those derived in Chapter 6 where we have used a public data sample of IceCube (2014, solid black)[139]. In the DM mass range from 10 to 50 TeV, the constraints on the two types of lines are within the same order of magnitude. This means that models predicting similar gamma-ray and neutrino line intensities can be tested in that region.

At the theoretical level, these two lines can be produced from:[2]

- different annihilations channels;
- different decay channels;

[1] Apart from us, and at that time, a few other groups had studied this possibility but in the very high energy part of the spectrum [135, 136, 137].

[2] We do not consider any mixture of these scenarios.

- the same *decay* into a $\nu\gamma$ final state (not possible with an annihilation or requires co-annihilations).[3]

Along the first two scenarios, the γ and ν lines could largely differ in terms of energy and intensity.[4] The observation of correlated lines would likely indicate that they come from the same process, potentially pointing towards the existence of decaying DM fermions.[5] We therefore choose to study the latter of the three scenarios. By the end of this chapter, we will show that the observational discovery of a "double smoking gun" could be around the corner in some specific cases. We start off by considering the neutral DM scenario in depth and comment on the millicharged option towards the end of this chapter.

As in Chapter 2, the plan is to consider the whole list of lowest-dimensional operators and analyse their respective phenomenology. A main difference with the analysis in Chap. 2 is that we will include the 3-body decay channels induced by the effective operators. More specifically, we will include the phenomenology of those 3-body decay channels that "happen to" dominate the DM decay width at high mass. Even if this means that the $\gamma\nu$ decay channel can be subleading, the 3-body processes also give interesting features in the photon and neutrino spectra, similar to those obtained in the context of internal Bremsstrahlung (IB) processes. These **line-like** features can **also be looked for** (as explicitly done in Chapter 6) and may as well constitute a probe of the DM particle. In parallel, all of the operators that we are about to list lead to the emission of a featureless continuum of CRs, from which we can derive complementary sets of constraints on the DM decay width. This approach was already adopted in Chapter 2.

3.2 Effective operators—Neutral DM

To investigate what are the proportions of monochromatic photons, neutrinos and CRs that we can expect within the $\Psi_{\rm DM} \to \gamma\nu$ scenario, we use the effective approach. As in Chapter 2, the motivation for using it is clear: the cosmological timescales required for the DM lifetime can naturally be explained in the framework of an accidental global symmetry at low energies that is broken by some new UV physics.

Up to dimension 6, and assuming that the DM particle is neutral and has spin 0, 1/2 or 1, it has been shown in Ref. [114] that there exists a limited list of operator

[3]Other scenarios where γ and ν line-like signals appear with a similar intensity and same energy are still possible. For example, in multicomponent DM annihilation scenarios two distinct DM particles do not need to form a bosonic state (as annihilating conjugated particles) and could thus lead to a $\gamma + \nu$ annihilation final state. Double line-like signals might also arise from 3-body final states, such as from $\nu\bar{\nu}\gamma$ annihilation or decay processes. We will not consider these more elaborate cases here.

[4]Note that there is always a minimum degree of correlation: a decay into $\nu\nu$ induces a (suppressed) decay into $\gamma\gamma$ at the two-loop level (or at the one-loop level if there is an associated l^+l^- channel), and *vice versa*.

[5]We do not mean by this that a same decay *always* predicts similar intensities. A couple of counterexamples can *e.g.* be found in the context of millicharged DM (see Sec. 3.7).

structures leading to γ-lines.[6] Only eight of these operator structures also lead to a neutrino line via the $\gamma + \nu$ decay channel. Two of them are of dimension 5

$$\mathcal{O}^{(5)Y} \equiv \overline{L}\sigma_{\mu\nu}\Psi_{\rm DM}F_Y^{\mu\nu}, \quad \Psi_{\rm DM} = (2,-1) \tag{3.1}$$
$$\mathcal{O}^{(5)L} \equiv \overline{L}\sigma_{\mu\nu}\Psi_{\rm DM}F_L^{\mu\nu}, \quad \Psi_{\rm DM} = (2/4,-1) \tag{3.2}$$

and 6 are of dimension 6

$$\mathcal{O}^{1Y} \equiv \overline{L}\sigma_{\mu\nu}\Psi_{\rm DM}F_Y^{\mu\nu}\phi, \quad \Psi_{\rm DM}\cdot\phi = (2,-1) \tag{3.3}$$
$$\mathcal{O}^{1L} \equiv \overline{L}\sigma_{\mu\nu}\Psi_{\rm DM}F_L^{\mu\nu}\phi, \quad \Psi_{\rm DM}\cdot\phi = (2\oplus 4,-1) \tag{3.4}$$
$$\mathcal{O}^{2Y} \equiv D_\mu\overline{L}\gamma_\nu\Psi_{\rm DM}F_Y^{\mu\nu}, \quad \Psi_{\rm DM} = (2,-1) \tag{3.5}$$
$$\mathcal{O}^{2L} \equiv D_\mu\overline{L}\gamma_\nu\Psi_{\rm DM}F_L^{\mu\nu}, \quad \Psi_{\rm DM} = (2/4,-1) \tag{3.6}$$
$$\mathcal{O}^{3Y} \equiv \overline{L}\gamma_\mu D_\nu\Psi_{\rm DM}F_Y^{\mu\nu}, \quad \Psi_{\rm DM} = (2,-1) \tag{3.7}$$
$$\mathcal{O}^{3L} \equiv \overline{L}\gamma_\mu D_\nu\Psi_{\rm DM}F_L^{\mu\nu}, \quad \Psi_{\rm DM} = (2/4,-1) \tag{3.8}$$

In the above list, L represents a lepton doublet $L \equiv (\nu_L, l_L^-)^T$ of e, μ or τ flavor and $F_{Y,L}^{\mu\nu}$ represent the field strength tensors of the $U(1)_Y$ and $SU(2)_L$ gauge fields. The (n, Y) labels (last column) denote the dimension n and hypercharge Y that a given field (or field combination) must have under the $SU(2)_L \times U(1)_Y$ group in order to build gauge invariants. As in Chap. 2, whenever we refer to the contribution of an operator, we always mean the contribution of this operator *and* that of its hermitian conjugate.[7] We also assume the operators to be flavour *democratic* (= flavour universal), but the results are marginally affected by another choice.

Apart from the DM field, almost all of the operator structures given above only involve SM fields. The two exceptions to this statement are the operator structures of Eqs. (3.3)–(3.4): they involve a scalar field ϕ which does *not* have to be the SM scalar doublet field H. By considering only SM fields and taking into account all the possible DM multiplets up to the 5-plets and a complete set of $SU(2)_L$ index contractions, the 8 operator *structures*[8] above lead to 25 different effective operators, which we list in Table 3.1.

We end up with three linearly independent invariants in the case of the dimension 5 operators in Eqs. (3.1)–(3.2) and 6 linearly independent invariants in the case of the dimension 6 operators in Eqs. (3.5)–(3.8). The operators involving a scalar field in Eqs. (3.3)–(3.4) lead to 9 invariants when $\phi = H$ (where $\Psi_{\rm DM}$ is hyperchargeless)

$$\mathcal{O}_H^{1Y} \equiv \overline{L}\sigma_{\mu\nu}\Psi_{\rm DM}F_Y^{\mu\nu}H, \; \Psi_{\rm DM} = (1/3,0) \tag{3.9}$$
$$\mathcal{O}_H^{1L} \equiv \overline{L}\sigma_{\mu\nu}\Psi_{\rm DM}F_L^{\mu\nu}H, \; \Psi_{\rm DM} = (1/3_{a,\not{b},c,d,e,f}/5,0) \tag{3.10}$$

and to 7 invariants when $\phi = \widetilde{H} \equiv i\sigma_2 H^*$ (where $\Psi_{\rm DM}$ has $Y = -2$)

$$\mathcal{O}_{\widetilde{H}}^{1Y} \equiv \overline{L}\sigma_{\mu\nu}\Psi_{\rm DM}F_Y^{\mu\nu}\widetilde{H}, \; \Psi_{\rm DM} = (3,-2) \tag{3.11}$$
$$\mathcal{O}_{\widetilde{H}}^{1L} \equiv \overline{L}\sigma_{\mu\nu}\Psi_{\rm DM}F_L^{\mu\nu}\widetilde{H}, \; \Psi_{\rm DM} = (3_{\not{a},b,c,d,e,f}/5,-2). \tag{3.12}$$

[6] See Ref. [138] for a list of operators leading to monochromatic neutrinos.

[7] That is, on top of the $\Psi_{\rm DM}$ decay channels, the hermitian conjugated operator induces the $\overline{\Psi_{\rm DM}}$ decay to the conjugated final states (with identical BRs).

[8] Actually 10 if you separately consider H and $\widetilde{H}$.

Operator Structure	DM field (*n-plet*, Y)	Fields contract. (*n-plet*)	*Operator*
$\overline{L}\sigma^{\mu\nu}\Psi_{\rm DM}B_{\mu\nu}$	$(2,-1)$		$\mathcal{O}^{(5)Y}_{\text{2-let}}$
$\overline{L}\sigma^{\mu\nu}\Psi_{\rm DM}W_{\mu\nu}$	$(2,-1)$		$\mathcal{O}^{(5)L}_{\text{2-let}}$
	$(4,-1)$		$\mathcal{O}^{(5)L}_{\text{4-let}}$
$\overline{L}\sigma^{\mu\nu}\Psi_{\rm DM}B_{\mu\nu}H$	$(1,0)$		$\mathcal{O}^{1Y}_{H,\text{1-let}}$
	$(3,0)$		$\mathcal{O}^{1Y}_{H,\text{3-let}}$
$\overline{L}\sigma^{\mu\nu}\Psi_{\rm DM}W_{\mu\nu}H$	$(1,0)$		$\mathcal{O}^{1L}_{H,\text{1-let}}$
	$(3,0)$	a: $(\overline{L}H)=1$	$\mathcal{O}^{1L,a}_{H,\text{3-let}}$
	$(3,0)$	c: $(\Psi_{\rm DM}H)=2$	$\mathcal{O}^{1L,c}_{H,\text{3-let}}$
	$(3,0)$	d: $(\Psi_{\rm DM}H)=4$	$\mathcal{O}^{1L,d}_{H,\text{3-let}}$
	$(3,0)$	e: $(\overline{L}\Psi_{\rm DM})=2$	$\mathcal{O}^{1L,e}_{H,\text{3-let}}$
	$(3,0)$	f: $(\overline{L}\Psi_{\rm DM})=4$	$\mathcal{O}^{1L,f}_{H,\text{3-let}}$
	$(5,0)$		$\mathcal{O}^{1L}_{H,\text{5-let)}}$
$\overline{L}\sigma^{\mu\nu}\Psi_{\rm DM}B_{\mu\nu}\widetilde{H}$	$(3,-2)$		$\mathcal{O}^{1Y}_{\widetilde{H},\text{3-let}}$
$\overline{L}\sigma^{\mu\nu}\Psi_{\rm DM}W_{\mu\nu}\widetilde{H}$	$(3,-2)$	b: $(\overline{L}\widetilde{H})=3$	$\mathcal{O}^{1L,b}_{\widetilde{H},\text{3-let}}$
	$(3,-2)$	c: $(\Psi_{\rm DM}\widetilde{H})=2$	$\mathcal{O}^{1L,c}_{\widetilde{H},\text{3-let}}$
	$(3,-2)$	d: $(\Psi_{\rm DM}\widetilde{H})=4$	$\mathcal{O}^{1L,d}_{\widetilde{H},\text{3-let}}$
	$(3,-2)$	e: $(\overline{L}\Psi_{\rm DM})=2$	$\mathcal{O}^{1L,e}_{\widetilde{H},\text{3-let}}$
	$(3,-2)$	f: $(\overline{L}\Psi_{\rm DM})=4$	$\mathcal{O}^{1L,f}_{\widetilde{H},\text{3-let}}$
	$(5,-2)$		$\mathcal{O}^{1L}_{\widetilde{H},\text{5-let}}$
$D_\mu\overline{L}\gamma_\nu\Psi_{\rm DM}B_{\mu\nu}$	$(2,-1)$		$\mathcal{O}^{2Y}_{\text{2-let}}$
$D_\mu\overline{L}\gamma_\nu\Psi_{\rm DM}W_{\mu\nu}$	$(2,-1)$		$\mathcal{O}^{2L}_{\text{2-let}}$
	$(4,-1)$		$\mathcal{O}^{2L}_{\text{4-let}}$
$\overline{L}\gamma_\mu D_\nu\Psi_{\rm DM}B_{\mu\nu}$	$(2,-1)$		$\mathcal{O}^{3Y}_{\text{2-let}}$
$\overline{L}\gamma_\mu D_\nu\Psi_{\rm DM}W_{\mu\nu}$	$(2,-1)$		$\mathcal{O}^{3L}_{\text{2-let}}$
	$(4,-1)$		$\mathcal{O}^{3L}_{\text{4-let}}$

Table 3.1: The ten possible effective operator *structures*, involving only SM fields (apart from the DM particle), leading to the $\Psi_{\rm DM}\to\gamma\nu$ decay (1st column) with their allowed DM multiplets (2nd column) and possible $SU(2)_L$ index contractions—if not unique—of the fields in the operator (3rd column). The last column labels the 25 resulting effective operators (the DM multiplet, contraction choice and included scalar field are specified in the label's indices).

Here, H denotes the SM scalar doublet with hypercharge $Y=-1$, *i.e.* $H=(H^0,H^-)$ with $H^0=(v+h+ia_0)/\sqrt{2}$, $v=174$ GeV and $m_h=125$ GeV. As indicated by the subscripts $\{a,b,c,d,e,f\}$, for both $\mathcal{O}^{1L}_H$ and $\mathcal{O}^{1L}_{\widetilde{H}}$ there are various possible structures when $\Psi_{\rm DM}$ is a triplet because various contractions between the $SU(2)_L$ indices of the fields are possible. The six operator setups $3_{a,b,c,d,e,f}$ respectively correspond to the cases where H and L form a singlet or a triplet, where $\Psi_{\rm DM}$ and H form a doublet or a quadruplet and where the $\Psi_{\rm DM}$ and L form a doublet or a quadruplet (and

correspondingly for the two remaining fields in the operator).[9] Note that for $\mathcal{O}^{1L}_{H,\text{3-let}}$ ($\mathcal{O}^{1L}_{\widetilde{H},\text{3-let}}$) the b (a) case does not lead to a DM decay into $\gamma\nu$ and is therefore excluded from the list. We indicate this by crossing out the b and a subscripts in Eqs. (3.10) and (3.12), respectively.

Note that, in the most minimal setups, DM particles with $Y \neq 0$ can strongly be constrained by direct DM searches due to that Z-bosons mediate direct interactions with nuclei. Various mechanisms can be invoked to avoid this, *e.g.* the existence of mass splittings within an $SU(2)$ DM multiplet or an appropriate mixing of the DM field with a pure SM singlet.

3.3 Phenomenology of the 2-body decays

3.3.1 Multiple neutrino lines

Gauge invariance is manifest in the effective operator language, implying that any of the listed effective operators necessarily predicts—besides the decay channel into $\gamma\nu$—the existence of a decay channel into $Z\nu$. If kinematically allowed, that is to say if $m_{\rm DM} > m_Z$, this additional decay channel is the source of a continuum of CRs from the subsequent decays of the Z boson (see Sec. 3.3.2), but not only. It also induces a second neutrino-line in the spectrum at

$$E_\nu = \frac{m_{\rm DM}}{2}\left(1 - \frac{m_Z^2}{m_{\rm DM}^2}\right). \tag{3.13}$$

When the effective operator involves the $F_Y^{\mu\nu}$ field strength tensor, the intensity of this lower-energy neutrino line is $\tan^2\theta_W \simeq 0.3$ times that of the neutrino line produced at $E_\nu = m_{\rm DM}/2$ (= the one associated to the $\gamma\nu$ final state). With the $F_L^{\mu\nu}$ field strength tensor, this number changes to $\tan^{-2}\theta_W \simeq 3.3$.[10] Given the finite experimental resolutions, the two neutrino lines can be viewed as one single effective bump at $E_\nu \sim m_{\rm DM}/2$. For a typical 10% energy resolution, this happens as soon as $m_{\rm DM} \gtrsim 300$ GeV (see Eq. (3.13)). In this case, the relative intensity $R_{\nu/\gamma}$ of the ν-line *versus* that of the γ-line (at the source) is augmented

$$R_{\nu/\gamma} = \frac{1}{\cos^2\theta_W} \simeq 1.3\,, \tag{3.14}$$

and

$$R_{\nu/\gamma} = \frac{1}{\sin^2\theta_W} \simeq 4.3\,, \tag{3.15}$$

assuming that the operator contains the $F_Y^{\mu\nu}$ and $F_L^{\mu\nu}$ field strengths, respectively. At high DM masses, all of our operators necessarily give the monochromatic γ and

[9] Only two out of these six invariant contractions are linearly independent (they can all be written as linear combinations of the invariants obtained with, *e.g.*, $\Psi_{\rm DM}\cdot\phi$ being a 2-let and a 4-let), but we study all these setups because they could in principle be induced by the mediation of different heavy multiplets

[10] Note that the gamma and neutrino lines which are centered at $E_\nu = m_{\rm DM}/2$ share the same intensity (at the source).

ν lines in one of these proportions, and hence the field strength that is contained in the active operator could in principle be experimentally distinguished. In practice, nevertheless, this might not always be that simple. If several operators are induced by the UV physics, they will all contribute and, in some cases, interfere. In fact, a contribution from several operators *is* expected in many cases but not mandatory. Models with operators involving only one type of field strength up to dimension 6 can be found, like in the minimal DM scenario (see section 3.6 below). Unless particular destructive interferences take place among several operators with the two types of field strengths, a measured ratio $R_{\nu/\gamma}$ of order of a few would constitute a strong indication for a single $\gamma\nu$ decay channel scenario (but not a proof), whereas larger values would constitute a strong indication for separate channel scenarios—annihilation and/or decay. A value of $R_{\nu/\gamma}$ smaller than 1 would definitely require a scenario with separate decay channels.[11]

3.3.2 Secondary CR emission

Besides producing monochromatic fluxes of photons and neutrinos, the emission of a continuum of CRs is expected from νZ and, in some cases, from the $W^{\pm}l_L^{\mp}$ decay channel(s). For the dimension 5 and 6 operators above, this has already been analysed at length in Ref. [114]. As explained in Chapter 2, each operator leads to well-defined branching ratios. The 25 operators presented above in Tab. 3.1 end up giving 5 different "phenomenological outcomes" that we call A, C, D, E and F. The branching ratios involved in each of these outcomes are given in Table 3.2.

Decay channel	A	C	D	E	F
$\gamma\psi$	$\cos^2\theta_W$	$\sin^2\theta_W$	$\sin^2\theta_W$	$\sin^2\theta_W$	$\sin^2\theta_W$
$Z\psi$	$\sin^2\theta_W$	$\cos^2\theta_W$	$\cos^2\theta_W$	$\cos^2\theta_W$	$\cos^2\theta_W$
$W^+\psi^-$	0	0	1/4	1	9/4
$W^-\psi^+$	0	0	1/4	1	9/4

Table 3.2: Effective 2-body decay channels available (first column) and branching ratios in the different outcomes A, C, D, E, and F, modulo a *common* factor proper to each case. See text for further details.

These branching ratio predictions hold when the DM dominantly decays into 2-body final states. Given a DM field representation (column 1), Table 3.3 matches each one of the 25 operators presented in Tab. 3.1 to one of the 5 phenomenological outcomes A, C, D, E, and F. Given a total decay width Γ_{tot}, the A outcome gives the least amount of CRs and is only obtained with the operators that involve the F_Y field strength. The C, D, E and F outcomes are obtained with the operators involving the F_L field strength.

[11] If the lines come from the same decay, then for each mono-energetic γ-ray produced, there is at least one mono-energetic ν produced at the same energy, meaning that $R_{\nu/\gamma}$ is a least equal to one.

DM field n-plet,	Y	Operator	Prediction
1	0	$\mathcal{O}_H^{1Y}$	A
		$\mathcal{O}_H^{1L}$	E
2	-1	$\mathcal{O}^{(5)Y}$, $\mathcal{O}^{2Y}$, $\mathcal{O}^{3Y}$	A
		$\mathcal{O}^{(5)L}$, $\mathcal{O}^{2L}$, $\mathcal{O}^{3L}$	E
3	0	$\mathcal{O}_H^{1Y}$	A
		$\mathcal{O}_H^{1L,a}$	C
		$\mathcal{O}_H^{1L,d}$, $\mathcal{O}_H^{1L,f}$	D
		$\mathcal{O}_H^{1L,c}$, $\mathcal{O}_H^{1L,e}$	E
3	-2	$\mathcal{O}_{\tilde{H}}^{1Y}$	A
		$\mathcal{O}_{\tilde{H}}^{1L,e}$	C
		$\mathcal{O}_{\tilde{H}}^{1L,b}$, $\mathcal{O}_{\tilde{H}}^{1L,d}$	D
		$\mathcal{O}_{\tilde{H}}^{1L,c}$	E
		$\mathcal{O}_{\tilde{H}}^{1L,f}$	F
4	-1	$\mathcal{O}^{(5)L}$, $\mathcal{O}^{2L}$, $\mathcal{O}^{3L}$	D
5	0	$\mathcal{O}_H^{1L}$	D
5	-2	$\mathcal{O}_{\tilde{H}}^{1L}$	D

Table 3.3: Predicted phenomenology of the possible DM setups from all the effective operators that give the $\Psi_{\rm DM} \to \gamma\nu$ decays. The operators are defined in Table 3.1 (omitting their "DM n-plet" index since we give it in the 1st column). These are the predictions from DM decays into 2-body final states. For DM masses above $\sim$ 4 TeV, the predictions from the operators including a H or $\tilde{H}$ field are modified by 3-body decays, see Sec. 3.4.

3.3.3 Results

We show in Fig. 3.2 the limits on the decay width $\Gamma_{\nu\gamma}$ that we have obtained according to the prescription outlined in Sec. 2.5.1. The antiproton (continuum photon) constraints give the best limit for $m_{\rm DM}$ below (above) $\sim$ 5 TeV. Besides using Fermi-LAT data [140], we have also used the Hess telescope data (up to 25 TeV) [112]. In practice, when considering only 2-body final states, the constraints inferred from the Fermi-LAT data are always stronger than those derived from the Hess data measurements.

For the operators of Eqs. (3.1)–(3.2) and (3.5)–(3.8), these bounds are valid up to the contribution of decays with 3 or more bodies in the final state. These extra 3-body contributions can safely be neglected because the branching ratios of these channels are suppressed by the phase space. For the operators of (3.3)–(3.4) (and hence Eqs. (3.9)–(3.12)) these bounds are also reliable unless $m_{\rm DM} \gg v_\phi$, where v_ϕ is the vacuum expectation value of the ϕ field (see Sec. 3.4). We have included the electroweak corrections in the computation of the continuum energy spectrum of gamma-rays and antiprotons from DM decays. The small dips around $m_{\rm DM} \simeq 2$ TeV come from a hardening of the photon spectrum (due to these EW corrections) which, moreover, coincides with a drop in the measured isotropic γ-ray flux.

For the operators with an F_Y tensor (A curve), the "direct" limits on $\Gamma_{\gamma\nu}$ are stronger than those derived from the associated CRs by a factor of about 10 to 100 in

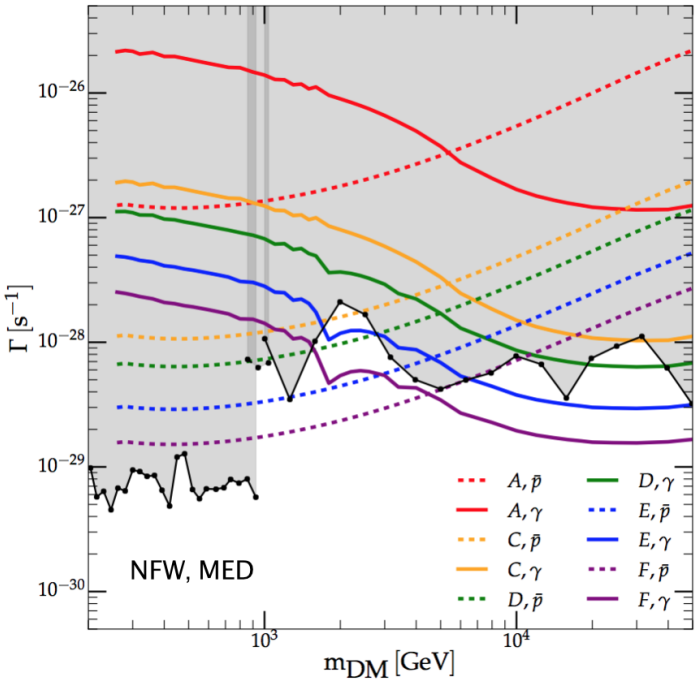

Figure 3.2: 95% CL limits on the DM decay rate to monochromatic gamma-ray lines. Excluded regions from direct line searches [111, 112, 114] (grey regions) as well as the indirect upper bounds derived from the associated CR emission each operator unavoidably induces (colored dotted curves are constraints from antiproton data [126], and solid curves from gamma-ray data [140]). Shown are the bounds we get for the A, C, D, E, and F scenarios given in Table 3.2 when the 2-body DM decays are included. These cases apply to the various possibilities of operators and DM multiplets according to Tabs. 3.1 and 3.3, as explained in the text.

the DM mass range of 1 TeV to 50 TeV. For the operators with an F_L tensor, *i.e.* the curves C to F in Fig. 3.2, the indirect constraints (at the 2-body decay level) are competitive with the dedicated line searches (within a factor of 10) as soon as $m_{\mathrm{DM}} \gtrsim 1$ TeV. For these operators, there are also real further possibilities to make a distinction between them (as opposed to $\mathcal{O}^{(5)Y}$, $\mathcal{O}^{2Y}$, $\mathcal{O}^{3Y}$, $\mathcal{O}_H^{2Y}$ and $\mathcal{O}_{\widetilde{H}}^{2Y}$ which all lead to the same curve A at the 2-body level).

As a last comment, let us add that depending on the UV completion we might end up with different linear combinations of operators (when more than one is available for a given DM field). However, this generally requires a careful tuning of the possible interferences to significantly alter the individual predictions of each operator [141].

3.4 Phenomenology of the 3-body decays

3.4.1 General considerations

For the operator structures in Eqs. (3.3) and (3.4) we find that, in addition to the 2-body decays of particle DM, the 3-body decay processes involving the scalar field ϕ *must* also be taken into account. The reason behind this statement is that the BRs of the former are proportional to v_ϕ^2, while the BRs of the latter are proportional to $m_{\rm DM}^2$. More specifically, the 3- to 2-body decay width ratio scales as $\sim m_{\rm DM}^2/64\pi^2 v_\phi^2$.

If ϕ is the SM scalar doublet, as in Eqs. (3.9)–(3.12), then the 3-body decays start dominating the decay width when $m_{\rm DM} \gtrsim 4$ TeV. In this case, after replacing the Goldstone bosons by their corresponding longitudinal gauge bosons (in the unitary gauge), we get the following list of possible 3-body decays:

$$\begin{aligned}
\Psi_{\rm DM} \to & \nu\gamma h, & \nu\gamma Z_L, & & l\gamma W_L,\\
& \nu Z h, & \nu Z Z_L, & & l Z W_L,\\
& l W h, & l W Z_L, & & \nu W W_L.
\end{aligned}$$

Above 4 TeV, it is a good approximation to calculate these 3-body decays in the electroweak unbroken phase (that is to say the $\Psi_{\rm DM} \to \nu W_3 H^0, l W_3 H^+, \nu W H^+$, and $l W H^0$ decay processes), and then use the equivalence theorem to relate them to the corresponding processes in the broken phase.

Different multiplets which used to give the same list of BRs at the 2-body decay level do not necessarily lead to the same BRs for the 3-body decays. In order to see the typical ranges of BRs predicted at the 3-body decay level, we consider the following 4 operators with $\phi = H$—and as a consequence, $Y_{\rm DM} = 0$—:

$$\widetilde{A}: \quad \mathcal{O}^{1Y}_{H,1/3-\rm let} \equiv \overline{L}\sigma_{\mu\nu}\Psi^{1/3-\rm let}_{\rm DM} F_Y^{\mu\nu} H \tag{3.16}$$

$$\widetilde{C}: \quad \mathcal{O}^{1L,a}_{H,3-\rm let} \equiv \overline{L}\sigma_{\mu\nu}\Psi^{3-\rm let}_{\rm DM} F_L^{\mu\nu} H \tag{3.17}$$

$$\widetilde{D}: \quad \mathcal{O}^{1L}_{H,5-\rm let} \equiv \overline{L}\sigma_{\mu\nu}\Psi^{5-\rm let}_{\rm DM} F_L^{\mu\nu} H \tag{3.18}$$

$$\widetilde{E}: \quad \mathcal{O}^{1L}_{H,1-\rm let} \equiv \overline{L}\sigma_{\mu\nu}\Psi^{1-\rm let}_{\rm DM} F_L^{\mu\nu} H \tag{3.19}$$

In the first case, $\Psi_{\rm DM}$ is a singlet (1-let) *or* a triplet (3-let).[12] In the subsequent cases, $\Psi_{\rm DM}$ is a triplet (3-let, with $\overline{L}$ and H forming a singlet), quintuplet (5-let) and singlet (1-let), respectively. As already indicated, we denote the corresponding phenomenological outcomes as $\widetilde{A}$, $\widetilde{C}$, $\widetilde{D}$ and $\widetilde{E}$, in analogy with the notation used at the 2-body decay level in Tab. 3.2. The "tilde" is added to stress the relevance of the 3-body decay channels at high mass.

[12] They give the same invariants, which is why we have grouped them.

Decay Channel	Operator			
	F_Y	F_L		
	$\widetilde{A}$ (1/3-let)	$\widetilde{E}$ (1-let)	$\widetilde{C}$ (3-let)	$\widetilde{D}$ (5-let)
$\nu\gamma$	$4\cos^2\theta_W$	$4\sin^2\theta_W$	$4\sin^2\theta_W$	$4\sin^2\theta_W$
νZ	$4\sin^2\theta_W$	$4\cos^2\theta_W$	$4\cos^2\theta_W$	$4\cos^2\theta_W$
lW	0	8	0	2
$\nu\gamma h$	$\cos^2\theta_W$	$\sin^2\theta_W$	$\sin^2\theta_W$	$\sin^2\theta_W$
$\nu\gamma Z_L$	$\cos^2\theta_W$	$\sin^2\theta_W$	$\sin^2\theta_W$	$\sin^2\theta_W$
$l\gamma W_L$	$2\cos^2\theta_W$	$2\sin^2\theta_W$	$2\sin^2\theta_W$	$2\sin^2\theta_W$
$\nu Z h$	$\sin^2\theta_W$	$\cos^2\theta_W$	$\cos^2\theta_W$	$\cos^2\theta_W$
$\nu Z Z_L$	$\sin^2\theta_W$	$\cos^2\theta_W$	$\cos^2\theta_W$	$\cos^2\theta_W$
lZW_L	$2\sin^2\theta_W$	$2\cos^2\theta_W$	$2\cos^2\theta_W$	$2\cos^2\theta_W$
lWh	0	2	0	1/2
lWZ_L	0	2	0	1/2
νWW_L	0	4	0	1

Table 3.4: Branching ratios of the 3-body processes induced by the operators of Eqs. (3.16)–(3.19), up to the factors given in Eqs. (3.20) and (3.21). The correspondence with the $\widetilde{A}$, $\widetilde{C}$, $\widetilde{D}$, and $\widetilde{E}$ scenarios is also expressed in those equations.

The BRs are given in Tab. 3.4 up to the following normalization factors

$$\frac{c\,(64\pi^2 v^2)}{m_{\rm DM}^2 + 64\pi^2 v^2} \quad \text{for the 2-body decay channels,} \tag{3.20}$$

$$\frac{c\,m_{\rm DM}^2}{m_{\rm DM}^2 + 64\pi^2 v^2} \quad \text{for the 3-body decay channels,} \tag{3.21}$$

where c is a constant equal to $1/4$, $1/4$, $1/6$, and $1/12$ respectively.

3.4.2 Additional spectral features

Besides bringing extra sources of CRs—which we discuss in Sec. 3.4.4—, the 3-body decays involving a scalar field bring extra features in the photon and neutrino spectra. To discuss them, we conveniently define the following decay widths:

$$\Gamma_\gamma^{2b} \equiv \Gamma_{\nu\gamma}, \tag{3.22}$$

$$\Gamma_\nu^{2b} \equiv \Gamma_{\nu\gamma} + \Gamma_{\nu Z}, \tag{3.23}$$

$$\Gamma_\gamma^{3b} \equiv \Gamma_{\nu\gamma h} + \Gamma_{\nu\gamma Z_L} + \Gamma_{l\gamma W_L}\,, \tag{3.24}$$

$$\Gamma_\nu^{3b} \equiv \Gamma_{\nu\gamma h} + \Gamma_{\nu\gamma Z_L} + \Gamma_{\nu Z_L h} + \Gamma_{\nu Z_L Z} + \Gamma_{\nu W_L W}\,, \tag{3.25}$$

as they embody the intensity of the line(-like) features at different levels.

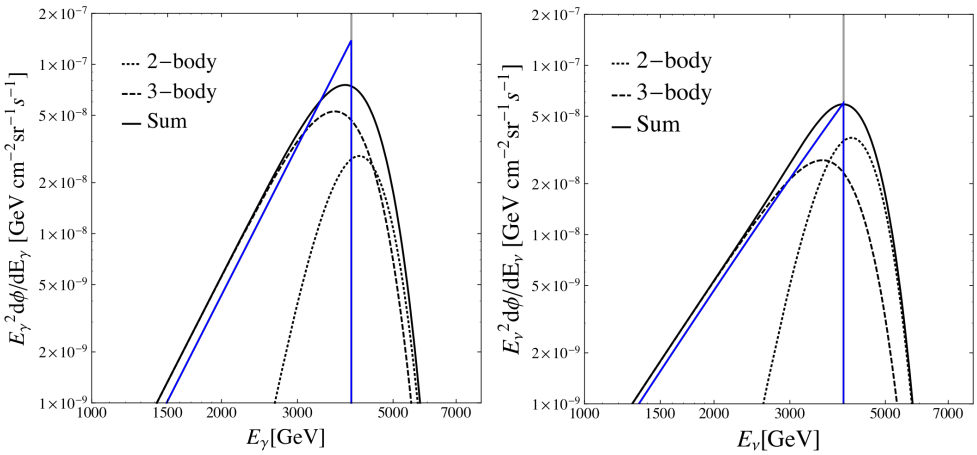

Figure 3.3: Primary photon (left) and neutrino (right) energy spectra obtained for the operator $O^{1Y}_{H,1/3-\text{let}}$ in Eq. (3.16) for an 8 TeV DM particle with a lifetime of 10^{28} s. The contributions from the 2-body $\gamma\nu$ (grey) and 3-body IB (blue) channels are shown. The corresponding smeared spectra by a gaussian energy resolution of 15% (according to Eq. (3.29)) and their sum are also shown (dotted, dashed and black curve, respectively).

The extra hard contribution to the **primary photon flux**[13] is proportional to Γ^{3b}_γ and similar to that coming from IB processes. It has a rapidly increasing energy spectrum that peaks at the kinematic cutoff $E_\gamma = m_{\rm DM}/2$ (up to $\mathcal{O}(m_h^2/m_{\rm DM}^2)$ corrections),[14] for

$$\frac{dN}{dE_\gamma} = \frac{64}{m_{\rm DM}} \left(\frac{E_\gamma}{m_{\rm DM}}\right)^3 \Theta_{\rm H}\left(\frac{m_{\rm DM}}{2} - E_\gamma\right). \tag{3.26}$$

We show in Fig. 3.3 the characteristic (primary) differential flux $d\phi/dE_\gamma$ induced at the 2 and 3-body decay levels. We have considered for this example the operator of Eq. (3.16) with $m_{\rm DM} = 8$ TeV and a total decay width $\Gamma_{\rm tot} = 10^{-28}$ s^{-1}. The effect of the detector's finite resolution are modelled by a Gaussian with a 15% standard deviation and corresponds to the smeared spectra (dotted and dashed).

The extra hard contribution to the **primary neutrino flux** is proportional to Γ^{3b}_ν and

$$\frac{dN}{dE_\nu} = \frac{32}{m_{\rm DM}}\left(1 - \frac{2E_\nu}{3m_{\rm DM}}\right)\left(\frac{E_\nu}{m_{\rm DM}}\right)^2 \Theta_{\rm H}\left(\frac{m_{\rm DM}}{2} - E_\nu\right). \tag{3.27}$$

[13] In the following, we will refer to a particle as being "primary" if it is directly produced from one of the local effective operators. If it is produced subsequently, we call it "secondary". This definition is slightly different from that given in Sec. 1.5.3.

[14] Line and IB spectral features can show up together in many frameworks (*e.g.* [142, 143, 144, 145]) from one-loop 2-body and tree-level 3-body radiative annihilations. We wish to emphasize here that for the operators of Eqs. (3.3) and (3.4), these features appear at the *same* coupling and loop order (the only difference is that it is either the scalar field or its *vev* which come into play).

This spectrum is less peaked than that of Eq. (3.26) but still displays a rise and a kinematical cutoff at $E_\nu = m_{\rm DM}/2$. In that respect, it is "sharp enough" in comparison with the featureless and decreasing astrophysical backgrounds of neutrinos. Figure 3.3 (right) shows the primary neutrino flux that is obtained at the 3-body decay level for a DM mass of 8 TeV and a 15% energy resolution. As can be seen by comparing it with the photon spectrum (left), this one is basically as sharp because it undergoes the *same* kind of kinematical cutoff.

3.4.3 Re-interpretation of the line searches

A proper determination of the constraints which hold on $\Gamma_{\rm tot}$ in the presence of the spectra that we have just seen in Sec. 3.4.2 would in principle require dedicated analyses, where all of the spectrum (2-body *and* 3-body contributions) is incorporated in the fits to the data. In the absence of such analyses, we can nevertheless derive approximate bounds on $\Gamma_{\rm tot}$ by estimating the respective contribution of the monochromatic and line-like fluxes in the energy bin around $m_{\rm DM}/2$. The reason for this is that the last bin can be considered as the most relevant to determine the limit since it is where (most of) the DM-induced bump lies. To do so, we define the relative intensity of the two contributions within the bin of edges $E_{\rm min} = \frac{m_{\rm DM}}{2}(1 - r_E)$ and $E_{\rm max} = \frac{m_{\rm DM}}{2}(1 + r_E)$ as

$$f_{\gamma,\nu} = \frac{\displaystyle\int_{\rm bin} dE' \int dE \, \frac{dN^{3b}_{\gamma,\nu}}{dE} \, K(E', E)}{\displaystyle\int_{\rm bin} dE' \int dE \, \frac{dN^{2b}_{\gamma,\nu}}{dE} \, K(E', E)}, \tag{3.28}$$

where $dN^{ib}_{\gamma,\nu}/dE$ is the energy spectrum of the primary photons/neutrinos produced in an i-body decay, and E' the reconstructed energy. For the detector response, we assume a Gaussian function

$$K(E', E) = \frac{1}{r_E E \sqrt{2\pi}} e^{-\frac{1}{2}\left(\frac{E-E'}{r_E E}\right)^2}. \tag{3.29}$$

With this setup, the numerator of Eq. (3.28) depends on the detector resolution r_E, while the denominator stays fixed to 68%. For a typical value $r_E = 15\%$, we get $f_\gamma = 0.57$ and $f_\nu = 0.44$. The behaviour of $f_{\gamma,\nu}$ as a function of r_E is plotted in Fig. 3.4.

Assuming, as already said, that the experimental limits dedicated to monochromatic line searches are driven by the bin in which the DM signal prediction is the highest, these same limits can be re-interpreted as limits on the combination $\Gamma^{2b}_\gamma + f_\gamma \cdot \Gamma^{3b}_\gamma$, where f_γ has been defined in Eq. (3.28). Given the fact that the BRs are known, these limits can easily be re-translated into a limit on any other partial decay rate (as done in Fig. 3.5), and in particular on Γ^{2b}_γ (dotted-dashed curve). That these limits on Γ^{2b}_γ drop at large $m_{\rm DM}$ is not surprising given the smaller and smaller 2-body BRs (see Eq. (3.20)).

3.4.4 Secondary CR emission—Results

As already said above, for the operators involving the SM scalar field H, the 3-body-decay-induced fluxes dominate if $m_{\rm DM} \gtrsim 4$ TeV. As a result, these channels

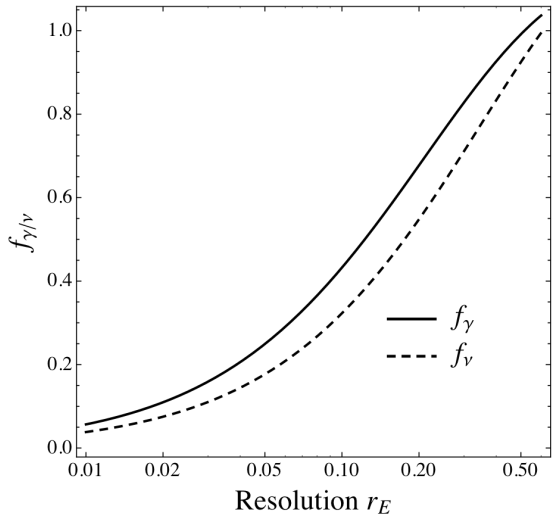

Figure 3.4: *Solid line* (f_γ): the ratio between the number of prompt photons in 3-body decays and prompt photons in 2-body decays in an energy window $(m_{\rm DM}/2)(1 \pm r_E)$. *Dashed line* ($f_\nu$): same ratio, but for neutrinos. The $f_{\gamma,\nu}$ factors are analytically defined in Eq. (3.28). The 3-body γ and ν energy spectra are given in Eq. (3.26) and (3.27), respectively.

are expected to considerably increase the amount of low energy CRs, and hence to considerably strengthen the associated bounds on monochromatic line signals from these operators. For illustration, we show in Fig. 3.6 the secondary photon spectrum corresponding to the $\widetilde{A}$ scenario of Eq. (3.16) together with the line-like signal.

We show in Fig. 3.7 the bounds deduced from the continuum of gamma-rays ($\widetilde{A}$ and $\widetilde{E}$ scenarios, left and right respectively) on the γ line (*i.e.* on Γ_γ^{2b}), on the decay width into a line-like signal (*i.e.* $\Gamma_\gamma^{2b} + \Gamma_\gamma^{3b}$) and on the quantity that is actually being probed with pure monochromatic line-searches, that is to say $\Gamma_\gamma^{2b} + f_\gamma \Gamma_\gamma^{3b}$ (with $f_\gamma = 0.57$). For the antiproton constraints we only show the bounds on $\Gamma_\gamma^{2b} + f_\gamma \Gamma_\gamma^{3b}$. This figure can be compared with Fig. 3.2, which was obtained in the previous section limiting ourselves to 2-body decays.

As expected, these new bounds are more stringent than those obtained at the 2-body decay level at high values of $m_{\rm DM}$. Assuming an experimental sensitivity improvement of $\sim$ one order of magnitude, what you see from these figures is that the prospects for observing the pure γ-line part (in the two specific scenarios $\widetilde{A}$ and $\widetilde{E}$) is low as soon as $m_{\rm DM} \gtrsim 10$ TeV. The observation of an "IB-like" feature consistent with CR measurements is however possible, at least up to $E_\gamma \sim 50$ TeV.

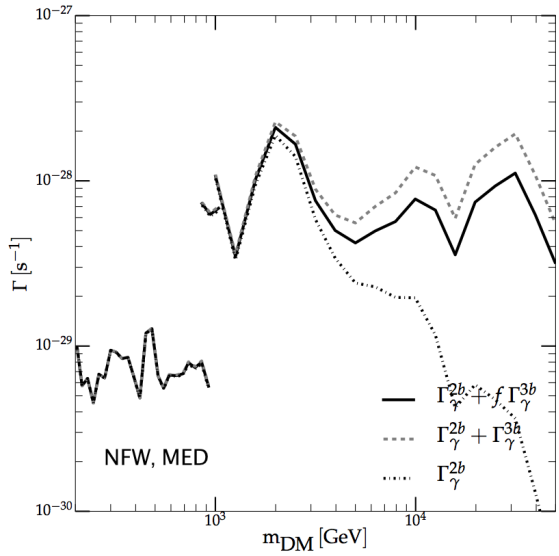

Figure 3.5: Solid black lines: 95% CL limits on the intensity of a γ-line from Fermi-LAT (below $\sim$1 TeV) and Hess (above $\sim$1 TeV). These bounds are now reinterpreted as bounds on $\Gamma_\gamma^{2b} + f_\gamma \cdot \Gamma_\gamma^{3b}$ with $f_\gamma \simeq 0.43$ for Fermi-LAT and $f_\gamma \simeq 0.57$ for Hess. As the ratios of the various partial decay widths are totally fixed by the value of $m_{\rm DM}$ for a given operator, these bounds can be translated into bounds on other partial widths. As an example we show the bounds induced on the 2-body decay width $\Gamma_\gamma^{2b} = \Gamma_{\gamma\nu}$ and on the total radiative decay width $\Gamma_\gamma = \Gamma_\gamma^{2b} + \Gamma_\gamma^{3b}$, for the operators of Eqs. (3.3) and (3.4) with ϕ the SM scalar doublet. These bounds turn out to be identical for all the cases considered in Tab. 3.4. However, the bounds on the total DM decay rate $\Gamma_{\rm tot}$ depend on the operator, and we do not show them here.

3.5 Double smoking gun prospects

With all the discussions made above, we can now focus on the prospects for observing both a neutrino and a gamma-ray line-like feature within the $\Psi_{\rm DM} \to \gamma\nu$ decay scenario.

To do so, we have summarized in Fig. 3.8 the limits on γ-ray (left) and ν (right) line-like signals. The dedicated line searches performed by the Fermi [111] and Hess [112, 114] Collaborations and those obtained in Chapter 6 correspond to the grey regions (95 % CL exclusion regions). As for the colored curves, they are deduced from the constraints on the γ and $\overline{p}$ continua induced by the effective operators. When these deduced limits are weaker than those from the dedicated line searches, they fall into the grey regions. When this happens, the interpretation is that you *could* find a line signal (if it exists at the edge of the experimental sensitivity) without being in conflict with other constraints. The bounds on Γ_γ^{2b} considering only 2-body decays are presented in dashed and those on $\Gamma_\gamma^{2b} + f_\gamma \Gamma_\gamma^{3b}$—the quantity that is more correctly probed in the scenarios with relevant 3-body decays—are given by the solid (color) curves.

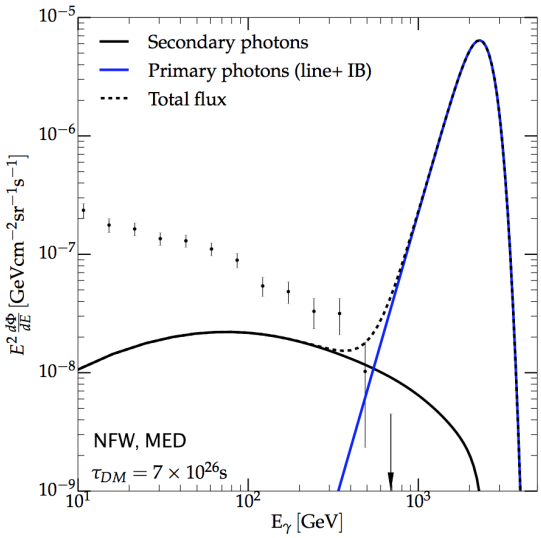

Figure 3.6: Photon flux obtained in the $\widetilde{A}$ scenario of the operator of Eq. (3.16), for $m_{\rm DM} = 5$ TeV, $r_E = 15\%$ and a DM lifetime of 7×10^{26} s. The line-like energy spectrum (blue), and the continuum spectrum from Z, H and W_L decay at lower energies (gray), together with the sum of these contributions (dashed). Data points from Ref. [140].

The exact prospects for the detection of a "double smoking gun" depend on the operator considered. To do this, it is useful to define r_γ and r_ν as the ratios of the direct line-search limits ($\Gamma^{\rm limit}_{\nu,\gamma}$) to the indirect CR constraints on a line signal ($\Gamma^{\rm CR-limit}_{\nu,\gamma}$) in each effective operator setup:

$$r_{\nu,\gamma} = \frac{\Gamma^{\rm limit}_{\nu,\gamma}}{\Gamma^{\rm CR-limit}_{\nu,\gamma}}. \tag{3.30}$$

These ratios can directly be read off from Figs. 3.8.a and 3.8.b and their interpretation is straightforward:

- If, for a given operator, the associated CR constraint on the line signal is more stringent than those from direct searches of ν and γ lines, then both r_ν and r_γ are larger than 1. In this case, to detect both a ν and γ line-like feature and stay compatible with the *current* CR constraints, both sensitivities must be improved by factors larger than r_γ and r_ν, respectively. This situation applies in particular to the $\widetilde{E}$ case, except at the lowest DM masses where $r_\gamma < 1$.
- If instead r_γ is smaller than 1 and $r_\gamma < r_\nu$, then the γ-line feature could be just below present sensitivity, whereas a detection of the associated neutrino line feature would require that the neutrino sensitivities improve by more than a factor r_ν/r_γ.
- Similarly, if r_ν is smaller than 1 and $r_\nu < r_\gamma$, it means that the neutrino line could be somewhere just below the corresponding sensitivity and the gamma-line sensitivity would require an improvement by at least a factor r_γ/r_ν to become observable for that operator prediction.

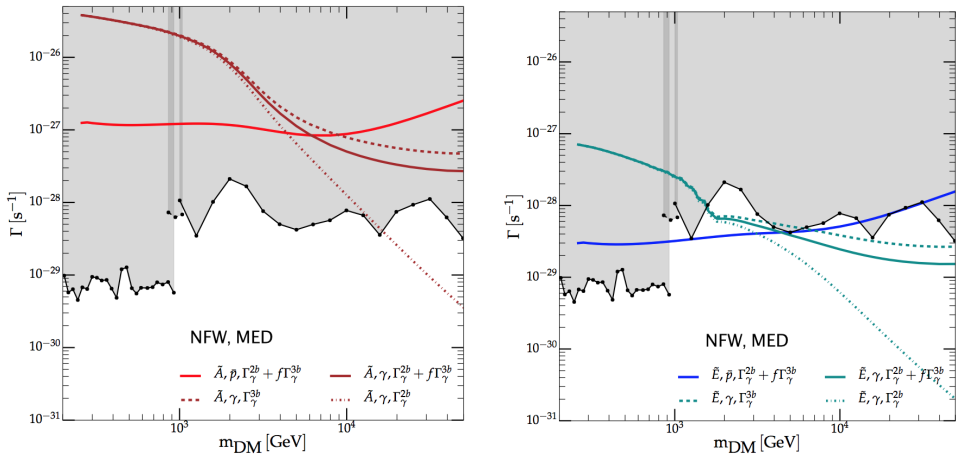

(a) $\widetilde{A}$ case (F_Y) ***(b)*** $\widetilde{E}$ case (F_L)

Figure 3.7: 95 % CL upper limits on decay rates into a gamma-ray line-like signal. The "direct" line searches give the grey regions (excluded), while the colored lines are the indirect limits on the line-like signal. *Left panel:* Red solid curves present the limits on $\Gamma_\gamma^{2b} + f_\gamma \cdot \Gamma_\gamma^{3b}$ (with $f_\gamma = 0.57$) derived by imposing that the associated CR prediction $\widetilde{A}$ in Eq. (3.16) does not overshoot Pamela antiproton data (light red) or Fermi-LAT isotropic gamma-ray background data (solid dark-red). *Right panel:* The same as the left panel (solid blue and solid cyan curve, respectively), but for the prediction $\widetilde{E}$ of the operator in Eq. (3.19). We also give the limits on the decay width $\Gamma_\gamma^{2b} + \Gamma_\gamma^{3b}$ and on Γ_γ^{2b} (using the BRs from Table 3.4 for these two operators).

To get a little more practice, we propose to further quantify this discussion within a few examples:

- **$\widetilde{E}$ case** (solid blue): both r_γ and r_ν always larger than ~ 1 when $m_{\mathrm{DM}} \gtrsim 1$ TeV. For example, at $m_{\mathrm{DM}} = 10$ TeV, one has $r_\gamma = 3$ and $r_\nu = 5$, meaning that the sensitivities to a γ-line and ν-line respectively need to be improved by a factor 3 and 5 to have a chance to observe the two lines. A putative future observation of a photon or neutrino line with higher intensities could not stem from the operators giving prediction $\widetilde{E}$.

- **A case** (red dashed): could be on the verge of giving a double-line signal. For, say, $m_{\mathrm{DM}} \simeq 30$ TeV, this case gives $r_\gamma \sim r_\nu \sim 1/10 < 1$ and the associated CR signal would be at least 10 times smaller than what is probed today. For the same DM particle mass, $m_{\mathrm{DM}} \simeq 30$ TeV, the C and D cases (orange and green dashed lines) have instead $r_\gamma \sim r_\nu \sim 1$ and an observation of both a double-line signal and the associated photon continuum flux could be around the corner.

- **$\widetilde{A}$ case** (red solid): gives $r_\gamma \simeq 1/8$ and $r_\nu \simeq 3$ at $m_{\mathrm{DM}} = 3$ TeV. This means that a photon line signal can be present just below the current sensitivity, but the neutrino-line sensitivity is required to improve by a factor $r_\nu/r_\gamma \simeq 24$ (to

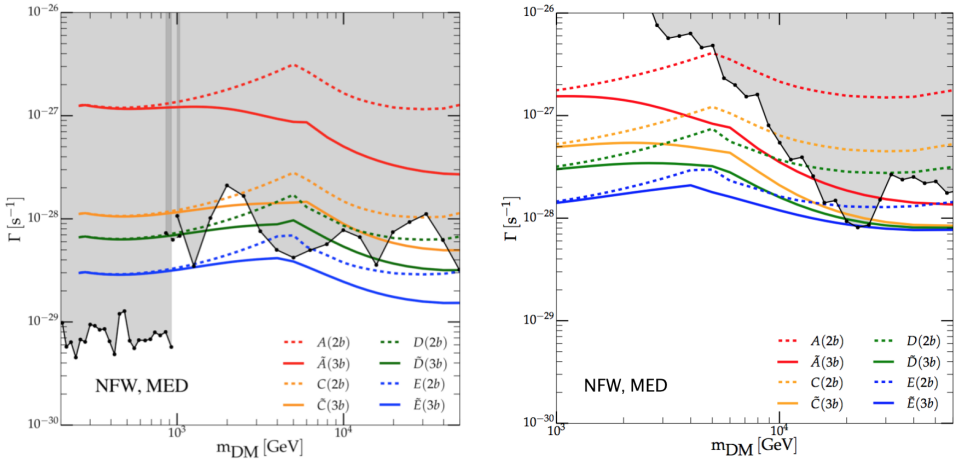

(a) Constraints on γ line-like signals ***(b)*** Constraints on ν line-like signals

Figure 3.8: Summary of the 95% CL limits on the line-like signals of the various effective operators. *Left panel:* limits on gamma-ray line-like signals (as in Fig. 3.2 and 3.7). *Right panel:* limits on neutrino line-like signals. Dashed colored lines: the CR induced bounds on a line-like signal from operators with DM decays into 2-body final states. These operators and their predictions can be found in Tables 3.1 and 3.3. Solid colored lines: same as dashed curves, but for the operators with relevant DM decays into 2- *and* 3-body final states. These colored limits are on $\Gamma^{2b}_{\gamma,\nu} + f_{\gamma,\nu} \cdot \Gamma^{3b}_{\gamma,\nu}$ for the CR predictions $\tilde{A}$, $\tilde{C}$, $\tilde{D}$ and $\tilde{E}$ (the operators of Eqs. (3.16)–(3.19)) with $f_\gamma = 0.57$ and $f_\nu = 0.44$ (15% energy resolution assumed in Hess and IceCube, respectively). To discuss the "double smoking gun" prospects, these limits should be compared to the direct gamma- and neutrino line-search limits (grey exclusion regions).

see the corresponding neutrino line). This also means that the observation of a neutrino-line with a stronger intensity would rule out this setup.

Alternatively, we can present the required constraints on the suppression scale Λ. At $m_{\rm DM} = 1$ TeV, the scales that are probed in this way are typically around 10^{16} GeV (dimension-5 operators) and 10^{30} GeV (dimension-6 operators). We refer the interested reader to Appendix B.1 (many figures involved).

All in all, what we conclude from Fig. 3.8 is that a realistic sensitivity improvement of the dedicated neutrino and gamma-ray line searches by a factor of ten *does allow* for many potential observations of the *double smoking-gun evidence* of particle DM.

3.6 The example of a minimal DM quintuplet

As an explicit example, let us take a fermion quintuplet with $Y_{\rm DM} = 0$ [146]. This "minimal" DM candidate is known to be accidentally stable—as it linearly couples to SM fields *only* starting from dimension 6 effective operators—and to have a mass fixed to $m_{\rm DM} = 9.6$ TeV by the relic density constraint [147]. The minimal DM scenario is

in tension with the constraints on the production of γ-line through DM annihilation [148, 149] but not totally excluded (because of the uncertainties on the DM halo profile). By decaying, this candidate could *only* produce a γ-line and a ν-line through the effective operator in Eq. (3.18),

$$\widetilde{D}: \qquad \mathcal{O}^{L1}_{H,5-\text{let}} \equiv \qquad \overline{L}\sigma_{\mu\nu}\Psi^{5-\text{let}}_{\text{DM}}F^{\mu\nu}_{L}H. \tag{3.31}$$

Therefore, the ratio of the pure monochromatic neutrinos to pure monochromatic photons from 2-body decays is fixed to:

$$R_{\nu/\gamma} \equiv \; n_\nu/n_\gamma \simeq 4.3. \tag{3.32}$$

However, since the operator in Eq.(3.31) involves the SM scalar doublet, we know that the 3-body contributions dominate the decay width for $m_{\text{DM}} \gtrsim 4$ TeV—and in particular new line-like features appear. The relative branching ratios of the nine main decay channels are given in the quintuplet column of Tab. 3.4.

In Fig. 3.8, our bounds on the line-like photon and neutrino features are given by the solid green lines. For $m_{\text{DM}} = 9.6$ TeV, the HESS limits—which we should reinterpret as limits on $\Gamma^{2b}_\gamma + f_\gamma \cdot \Gamma^{3b}_\gamma$ with $f_\gamma \simeq 0.57$—reach a level of sensitivity similar to those from the continuum (solid green curve in Fig. 3.8.a). For neutrinos, the "dedicated" limits are a factor $r_\nu \simeq 2$ weaker (solid green curve in Fig. 3.8.b). Therefore, if a neutrino or gamma line were to be observed just below the current sensitivities, the CR continuum signal of quintuplet DM should also be within reach. In that sense, the simultaneous observation of a ν line, a γ line and an excess of CRs would **strongly hint to the quintuplet nature of particle DM**.

3.7 Millicharged DM

So far, we have assumed that particle DM was electrically neutral. However, it is perfectly possible to give it a small electric "millicharge", as seen at length in Chapter 2. If so, a new set of operators must be added to Eqs. (3.1)–(3.8). They involve covariant derivatives acting on millicharged fermion fields:

$$D_\mu D_\nu \overline{L}\sigma^{\mu\nu}\Psi_{\text{DM}} \tag{3.33}$$
$$D_\mu D_\nu \overline{L}\sigma^{\mu\nu}\Psi_{\text{DM}}\phi \tag{3.34}$$
$$\overline{L}\sigma^{\mu\nu} D_\mu D_\nu \Psi_{\text{DM}}\phi \tag{3.35}$$
$$D_\mu \overline{L}\sigma^{\mu\nu} D_\nu \Psi_{\text{DM}}\phi \tag{3.36}$$

We have considered the phenomenology of these operators in Chapter 2, but let us recall that if the field(s) to which the covariant derivatives apply are not $SU(2)$ singlets, an observable γ-line is not of an option taking into account the largely boosted[15] decay channels involving a Z boson (and/or W boson). The single operator which escapes this statement is:

$$\widetilde{A}: \qquad \overline{L}\sigma^{\mu\nu} D_\mu D_\nu \Psi_{\text{DM}}\phi, \tag{3.35}$$

[15] By the inverse of the millicharge squared.

with $\Psi_{\rm DM}$ a $SU(2)_L$ singlet and, interestingly, ϕ having the same quantum numbers as the SM scalar doublet H.

It is interesting to note that the ν-line signal can be generated with a strong intensity. Indeed, unlike the $\nu\gamma$ and νZ decay channels, the $\nu\gamma'$ (kinetic mixing) and $\nu Z'$ (Stueckelberg, if kinematically allowed) decay channels are not suppressed by the millicharge of particle DM. Given the experimental bounds on the existence of millicharged particles (see Sec. 1.3.3), these scenarios would lead to a ν line intensity much larger than that of the corresponding γ line (we are speaking here of many orders of magnitude!).

The only way to evade the latter statement is therefore to impose the following two additional conditions:

(i) the millicharge originates from the Stueckelberg mechanism (massive scenario),

(ii) $m_{Z'} > m_{\rm DM}$ (to forbid the $\nu Z'$ decay channel).

In that case, and taking $\phi = H$, we find the $\widetilde{A}$ phenomenological outcome (red solid curves in Fig. 3.7).

3.8 Comments on the astrophysics

Before closing this chapter, we would like to add that we have also assessed the Inverse Compton contribution from CMB photons scattering off DM induced electrons and positrons (see, *e.g.*, [150]). This contribution is however found to have a marginal effect on the limits (at most a factor 2, and only for DM masses above 10 TeV in the F case) and was therefore not included in our plots. Recently, it has been emphasized that various astrophysical sources of photons, including blazars, can explain most of the continuum photon spectrum [88]. If true, this leads to stronger continuum photon constraints on DM decay. Imposing that the DM induced flux cannot exceed the difference between the observed flux and the astrophysical contribution (given in Fig. 1 of Ref. [88][16]), the constraints presented in Fig. 3.2 improve by a factor of 2.

Our choice of the MED propagation setup for the anti-protons [77] was based on the preliminary AMS-02 data [151, 92] which seemed to be more favored than the MIN setup at the time this work was done—the latter setup would give 5 times weaker constraints. With the more recent AMS-02 data, we also reassessed our positron constraints (see, *e.g.*, [152]), and concluded that they are always weaker than our antiproton constraints because positrons come together with W bosons, which themselves produce antiprotons in quantity.

[16] To be conservative, we take the lower edge of the blue band given in the upper left panel of this figure.

3.9 What should you take away from this chapter?

This chapter was dedicated to the study of DM particle decays involving the simultaneous production of mono-energetic gamma-rays and mono-energetic neutrinos in the same 2-body decay, and has addressed the question of whether or not this class of scenarios could be responsible, in the near future and in a "multi-messenger context", for a potential observation of gamma-ray and neutrino lines around the *same* energy. This discussion was mainly motivated by the results obtained in Chapter 6, where we show the possibility for γ-ray and neutrino telescopes to reach comparable sensitivity levels on the DM decay width in a certain range of DM masses.

For similar reasons to those that were invoked in Chapter 2, we have again relied on the EFT framework to address this question. We have studied the phenomenology of the effective operators associated to those decays, both under the assumption of neutral and millicharged DM particles (Secs. 3.2 and 3.7, respectively). For the effective operators involving a scalar field ϕ, we have highlighted the importance of 3-body decay processes as they induce non-negligible—and sometimes dominant—contributions to the different cosmic-ray fluxes when $m_{\rm DM} \gtrsim$ TeV (Sec. 3.4.2). These contributions affect the low-energy continua, such as those of $\overline{p}$'s and γ-rays, thereby hardening the constraints on the DM decay width (this is what causes the departure of the continuous curve from the dashed curve in Figs. 3.8(a) and 3.8(b)). Regarding the γ-ray and neutrino fluxes, the three-body decay processes also induce *new* line-like features which are predominant at high DM masses ($\gtrsim 10$ TeV). We have commented on a possible way of re-interpreting dedicated line searches in that case.

As explained in Sec. 3.5 and Appendix B.1, the outcome of this analysis—in terms of the question phrased above—is that we *can* highlight the 10–50 TeV DM mass region as a region where it is possible, in some scenarios, to find gamma-ray and neutrino lines in a near future—what we refer to as the "double smoking gun discovery" of DM—without being in tension with CR data measurements.

Part III

CHAPTER 4

Principles of Neutrino Detection

"I turned my attention for a while to gamma ray astronomy and soon began the first in a continous series of experiments at the Savannah River site to study the properties of the neutrino."

— Frederick Reines

The experimental discovery of the neutrino in 1956 [153] marked the end of a 26-year-long quest for the particle hitherto postulated by W. Pauli [154]. More importantly, it opened the door to the frenzied development of new experimental techniques aiming at bringing to light the properties of this particle. Today, neutrinos are known to be leptons coming in three flavours that oscillate among one another, to have at least two light massive eigenstates and to have weak interactions. In spite of all the efforts, their very nature—whether they are Dirac or Majorana—, the origin of their mass and its connection to BSM physics are still blurry and under scrutiny. Nevertheless, the above-mentioned properties sufficed to soon realise that neutrinos are excellent messengers, if not ideal. Because they are light, they travel fast and do not get trapped by gravitational wells as they propagate. They also do not carry any electrical charge, which means that magnetic fields do not bend their trajectories, making neutrino astronomy possible. Lastly, because of the weak nature of their interactions, neutrino propagation (in space) is negligibly affected by diffusion and absorption, giving access to environments that "regular" astronomy cannot probe whatsoever.

However, what has been depicted so far as qualities *before* reaching the detector inevitably becomes unpleasant when it comes to make a detection. This is why huge detectors are crucial to build satisfying volumes of data. "Cheap" options consist in instrumenting huge volumes of a naturally abundant material, like water and ice. Because the following two chapters are dedicated to analyses of IceCube data, we will focus on the latter. Neutrino interactions with the ice produce optical, radio and acoustic radiation, via, respectively, the Cherenkov [155], the Askaryan [156] and the thermo-acoustic effects [157]. These radiations can be searched for using different techniques, and examples of detectors include IceCube, Arianna [158] and Spats [159]. It is worth noting that the search for Cherenkov light is well suited for neutrino energies up to 10^{17} eV, while the other two techniques are well suited for higher energies because of the higher attenuation lengths involved. We discuss in this chapter the principles of neutrino detection, with a strong emphasis on the Cherenkov effect detection with IceCube.

4.1 Neutrino interactions

The detection of any kind of particle calls for the production of measurable signals. In essence, these signals are the result of perturbations of the medium caused by the passage of charged particles (*e.g.*, ionization, nuclear excitation, ...). For a neutral particle to be detected, it is thus vital that its interactions with the medium produce charged particles. Fortunately enough, (anti)neutrino-electron and (anti)neutrino-nucleus scattering processes fulfilling this condition do exist. They can be referred to as charged current (CC) or neutral current (NC) interactions, depending on whether the exchanged vector boson is electrically charged ($W^{\pm}$ bosons) or neutral (Z^0 boson). Tree-level Feynman diagrams of (anti)neutrino-electron and (anti)neutrino-nucleus scatterings are depicted in Figs. 4.1 and 4.2, respectively, and typical corresponding cross sections are presented in Figs. 4.3a and 4.3b as a function of the neutrino energy E_ν. In the collisions with matter (*i.e.* atoms), neutrino-nuclei scatterings are generally stronger than neutrino-electron scatterings [160, 161].[1] The one exception is around $E_\nu = 6.3$ PeV, where the processes $\overline{\nu}_e e \to \overline{\nu}_l l$ with $l = e, \mu, \tau$ and $\overline{\nu}_e e \to \textit{hadrons}$ are resonantly enhanced [162].

Detectors like IceCube aim at collecting the Cherenkov light produced by all the charged daughter particles of the (anti)neutrino-ice interaction. How this light is radiated and what are its properties is discussed in the following section.

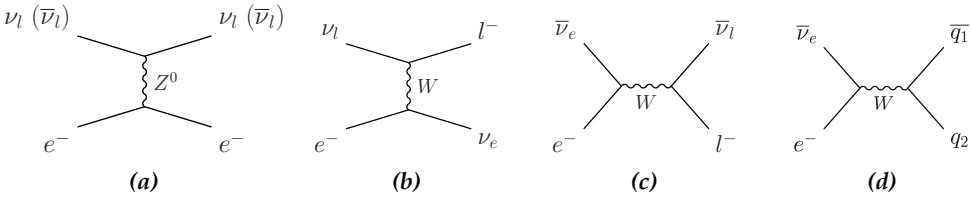

Figure 4.1: Neutrino- and antineutrino-electron scattering diagrams. (a) Z-boson (exchange) in the t-channel. (b) W-boson (exchange) in the t-channel. (c) W-boson (exchange) in the s-channel with leptonic decay. (d) W-boson (exchange) in the s-channel with hadronic decay. In the rest frame of the electron, both (c) and (d) display the Glashow resonance when the anti-neutrino has an energy close to ~ 6.3 PeV.

Figure 4.2: Neutrino-nucleon and antineutrino-nucleon scattering diagrams. (a) NC exchange in the t-channel. (b) Charged current exchange in the t-channel.

[1] This is because the latter are proportional to the mass of the electron.

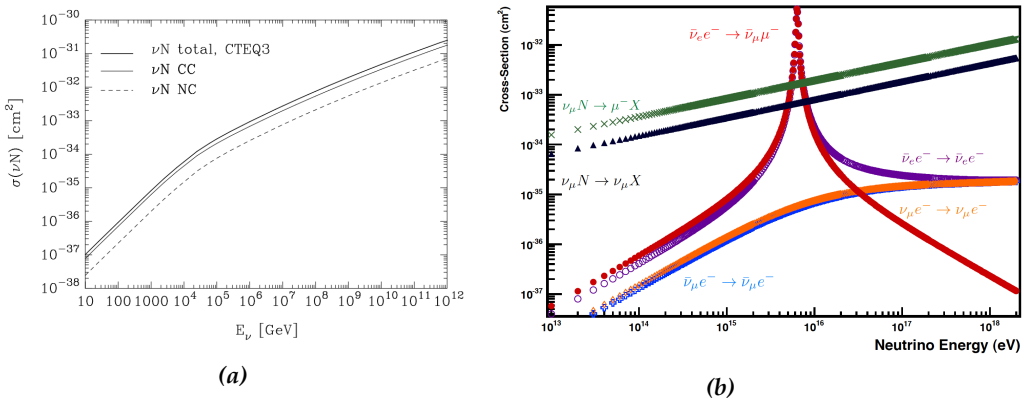

(a) ***(b)***

Figure 4.3: Neutrino-electron and neutrino-nucleon scattering cross sections as a function of the (anti)neutrino energy E_ν in the frame where the electron is at rest. (a) 10 GeV $< E_\nu < 10^{12}$ GeV. The dashed, thin and thick lines respectively correspond to $\sigma(\nu\mathcal{N} \to \nu + \text{anything})$, $\sigma(\nu\mathcal{N} \to \mu^- + \text{anything})$ and their sum. Figure taken from [160], where an analogous curve in the case of anti-neutrinos can be found. (b) $E_\nu > 10^4$ GeV. The Glashow resonance is easily identified at ~ 6.3 PeV. The process(es) used to produce each curve are referred in the figure. From [161].

4.2 Cherenkov radiation

Let us denote by c_{medium} the speed of light in a given medium. The Cherenkov effect is the phenomenon by which any charged particle moving in this medium with velocity $v > c_{\text{medium}}$ induces radiation. The effect can be understood as follows. The charged particle produces an electric field and as it passes by electrons—which are naturally present in the medium—, it accelerates them. Therefore, each of the accelerated electrons emits a spherical electromagnetic wave. Then, and as illustrated in Fig. 4.4, if the velocity of the passing charged particle is greater than the speed of the waves—that is to say $v > c_{\text{medium}}$—,the individual fronts of the waves may interfere constructively, forming a shock wave moving in a specific direction with respect to the direction of motion of the passing particle. This is characterized by the Cherenkov angle θ_C, with

$$\cos\theta_C = \frac{c_{\text{medium}}}{v} = \frac{1}{\beta n(\omega)}, \tag{4.1}$$

and where $n(\omega)$ is the *refractive index* of the medium (which is possibly dispersive, hence the dependence on the angular frequency ω). In the case of ice, $n \approx 1.33$, making $\theta_C \approx 41^\circ$ for highly relativistic particles.

The Cherenkov radiation is thus the electromagnetic equivalent of a sonic boom. It is a collective effect and must not be confused with braking radiation (see below). The latter can happen in parallel to Cherenkov radiation, and can *even* take place in vacuum!

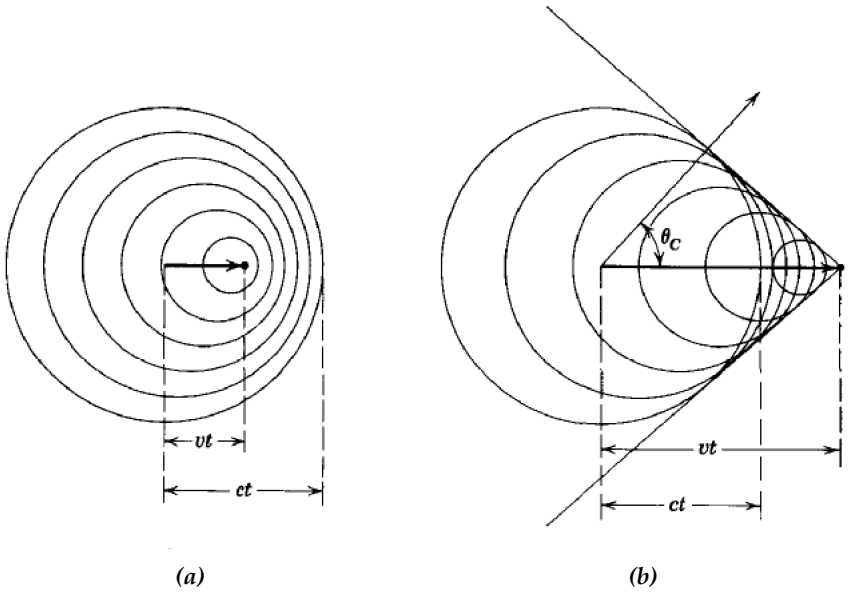

Figure 4.4: Illustration of the Cherenkov light emission for a charged particle moving with velocity (a) $v < c_{\text{medium}}$ and (b): $v > c_{\text{medium}}$. c_{medium} is presented as c in the figures. From [163].

The amount of Cherenkov photons radiated per unit length and frequency is given by [163]:

$$\frac{d^2N}{dxd\omega} = \frac{e^2\omega}{c^2_{\text{medium}}}\left(1 - \frac{1}{\beta^2 n^2(\omega)}\right), \tag{4.2}$$

where e is the electron charge. The dependence on ω of Eqs. (4.1) and (4.2) simply means that, if the medium is dispersive, photons of different frequencies are emitted along different cones and in different proportions. At a given frequency ω, the measurement of the Cherenkov angle θ_C informs on the energy of the charged particle. Note that the condition $v > c_{\text{medium}}$ defines a minimum energy E_{min} under which the Cherenkov radiation is not possible—whether E is the original energy of the particle when it was produced, or the result of many energy loss processes (see next section). With m denoting the mass of the particle, E_{min} is given by the following expression:

$$E_{\text{min}} = \frac{mc^2}{\sqrt{1 - \frac{1}{n^2(w)}}}. \tag{4.3}$$

4.3 Energy losses

Besides inducing the radiation of Cherenkov light as they propagate, the charged particles produced by the (anti)neutrino-ice interactions also loose energy via other processes. A number of different processes can be responsible for this:

– **Ionization**, the process by which electrons are knocked out of their atom. It involves elastic scatterings of charged particles off atomic electrons. Ionization

happens when the energy transferred to a given electron is greater than its binding energy;

– **Bremsstrahlung**, a.k.a. braking radiation, which consists in the emission of energetic photons by a decelerating charged particle. In the case of IceCube, the deceleration is simply due to interactions with the ice. Energetic photons quickly loose their energy in matter by producing pairs of electrons and positrons. In turn, the latter interact with the ice, decelerate, produce braking radiation and so on. The result is the production of a chain of daughter particles with less and less energy—which is why at some point the chain stops—, known as electromagnetic "cascade" or "shower" (see Fig. 4.5). Obviously, this type of cascade can also be initiated by a high-energy electron;

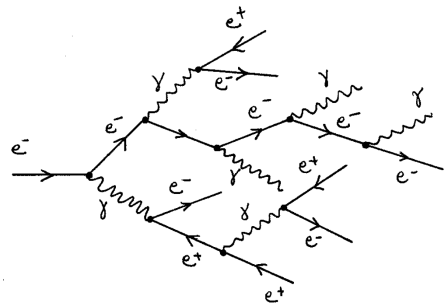

Figure 4.5: Development of an electromagnetic shower initiated by an electron. Each vertex hides an interaction with the medium.

– e^+e^- **pair production**;

– **Inelastic photo-nuclear interactions**;

– **Decay**. In this case, the daughter particles carry on the energy losses mentioned above.

As we discuss below, leptons of different flavours are not at all affected by the same processes, nor do they loose the same amounts of energy (in proportion to their original energy), giving rise to a few characteristic patterns of light emission.

4.3.1 Electron energy losses

In the case of electrons, energy losses are mainly due to ionization and braking radiation. Moreover, above $E_c = 78.60$ MeV (76.50 for positrons) [164],[2] ionization becomes irrelevant and leaves Bremsstrahlung as the only source of losses. The radiation length X_0 of electrons in ice is of about ~ 40 cm [165], and characterizes the length over which an electron typically looses $1/e$ of its energy. In terms of the

[2]This energy where there is a transition of dominant processes is referred to as the "critical energy".

length of a cascade, this leads to a logarithmic dependence on the energy of the (first) electron:

$$L = X_0 \cdot \frac{\ln E/E_c}{\ln 2}. \tag{4.4}$$

From this equation, we see that TeV electrons typically induce cascades of a few meters. In consequence, the Cherenkov light pattern fits in a bubbly (or spherical) shape.

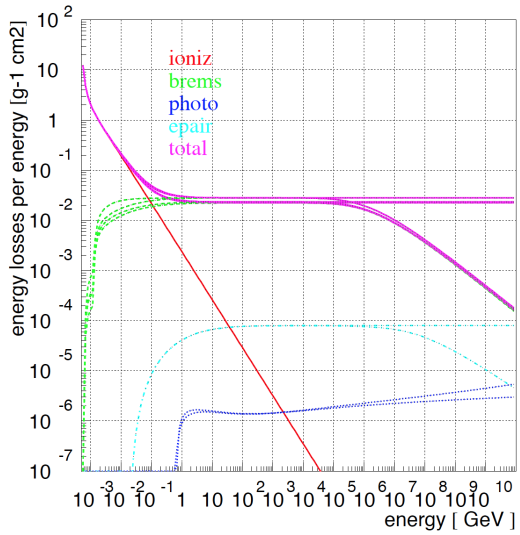

Figure 4.6: Electron energy losses from ionization (solid red), Bremsstrahlung (dashed green), photo-nuclear interactions (dotted blue), e^+e^- pair productions (dashed-dotted cyan) and decay (solid magenta). The lower magenta curves have Landau–Pomeranchuk–Migdal corrections included in their calculation [166]. From [167].

4.3.2 Muon energy losses

In this case, ionization, Bremsstrahlung, photo-nuclear interactions and pair production have to be taken into account. The muon lifetime is large enough to neglect its decay, see Fig. 4.7. Between 20 and 10^{11} GeV (which covers the range of energies that we consider in our analyses), the losses, as a function of energy, can be approximated by an (almost) constant contribution coming from the ionization together with an (almost) linear contribution embedding the other three processes. That is,

$$-\left\langle \frac{\mathrm{dE}_\mu}{\mathrm{dx}} \right\rangle \approx \mathrm{a}(\mathrm{E}_\mu) + \mathrm{b}(\mathrm{E}_\mu)\,\mathrm{E}_\mu, \tag{4.5}$$

where a and b mildly depend on the muon energy E_μ. A good choice is to take $\mathrm{a} = 0.268\mathrm{GeV m}^{-1}$ and $b = 4.70 \times 10^{-3}\mathrm{m}^{-1}$ [167]. The $\langle\ \rangle$ sign is there to remind that all processes but ionization are stochastic and the losses were thus quantified after taking averages over some large enough dx. With Eq. (4.5) at hand, it is easy to see

that it takes a long distance before a muon looses a significant fraction of its original energy. Indeed, solving Eq. (4.5) gives:

$$\mathrm{E}_\mu(x) \approx e^{-bx}\,(E_0 + a/b)\,, \tag{4.6}$$

with E_0 the energy of the muon as it enters in contact with the ice. The mean range of a muon can then be approximated as

$$\mathrm{R}_\mu \approx \frac{1}{b}\ln\left(1 + E_0\frac{b}{a}\right). \tag{4.7}$$

For example, 100, 10^3 and 10^4 GeV muons stop after travelling $\sim 215, 620$, and 1100 m in the ice, respectively. These distances are way longer than those inferred for electrons. The typical light pattern induced by a muon event is thus the result of a succession of showers (induced by Bremsstrahlung, photo-nuclear interactions and pair production processes) that are much smaller in size than the muon range, and therefore takes the form of a cylinder. On a scale like IceCube's, this cylinder looks like a track. Whether or not the muon has lost all its energy within the instrumented volume of IceCube may lead to further classification: *e.g.*, fully contained event, starting event, through-going muon, and stopping events.

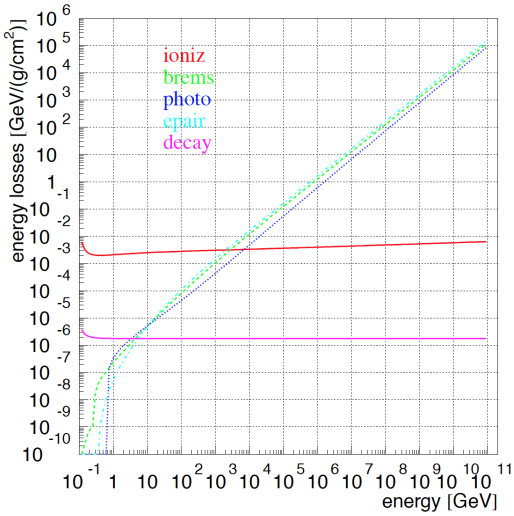

Figure 4.7: Muon energy losses. Color and line code as in Fig. 4.6. From [167].

4.3.3 Tau energy losses

Here, the relevant processes are: ionization, photo-nuclear interactions, pair production and, most importantly, decay. The decay length X_{dec} of a particle with lifetime T being

$$\frac{\beta}{\sqrt{1-\beta^2}}cT, \tag{4.8}$$

it is easy to see that, over the range of energies probed by IceCube, the decay length of the τ lepton significantly varies[3]: about 5 cm at 1 TeV and 500 m at 10 PeV. As a consequence, the light deposition pattern involves a first shower—(anti)neutrino-ice interaction—followed by a track of length $\sim X_{\rm dec}$—τ propagation—and possibly a second shower—τ decay—if the event stops in the ice/matter. Depending on $X_{\rm dec}$ ($\leftrightarrow E_\tau$), the detector may or may not resolve the track-like light emission pattern, leading to specific morphologies (see Fig. 4.9). It is worth noting that, at a given energy, τ-tracks are thinner than μ-tracks. This is because τ energy losses are comparatively less important (as is seen by comparing figures 4.7 and 4.8). This feature can serve as a criteria to identify ν_τ-induced events [168].

4.3.4 Hadrons

We have seen in Figs. 4.1 and 4.2 that the inelastic interactions of neutrinos with the ice could produce jets of hadronic particles. The propagation of these particles in the detector leads to a "hadronic" cascade, of which the development and the light yield differs from those of electromagnetic showers. The reason for these differences comes from the fact that more neutral particles (besides photons) are produced in hadronic cascades, and that the threshold for higher-mass charged particles to emit Cherenkov light is typically higher (see Eq. (4.3)), making $E > E_{\rm min}$ less often satisfied. The production of neutral pions does however lead—through their decays into photons—to the production of electromagnetic sub-cascades, and a possible treatment is to see hadronic cascades as electromagnetic ones, and apply a correction factor to the detected energy [170].

4.4 Neutrino Oscillations

As mentioned in the introduction of this chapter, neutrinos are leptons. Like any other fermion, they are represented in the Lagrangian by a mathematical object called "spinor". The spinor representation of the Lorentz group being completely reducible, such an object can be split into different physical states/objects that transform independently under the Lorentz group: in this case, the **L** (for *Left-handed*) and **R** (for *Right-handed*) representations. In the original formulation of the standard model, all fermions but neutrinos are assigned two chiral counterparts, arbitrarily making neutrinos massless.[4] Building up neutrino mass terms can be done in several ways (we refer the reader to [171] for a review), and is intimately linked with the neutrino oscillation phenomenon, on which we focus below.

[3] In comparison with the (typical) sensors' separation distance, see Sec. 5.1.

[4] In other words, neutrinos cannot have a Dirac mass—unlike all the other SM fermions. Furthermore, they cannot have a Majorana mass term in this framework due to the SM gauge invariance. In a BSM framework, they could however acquire a mass after the EW symmetry breaking.

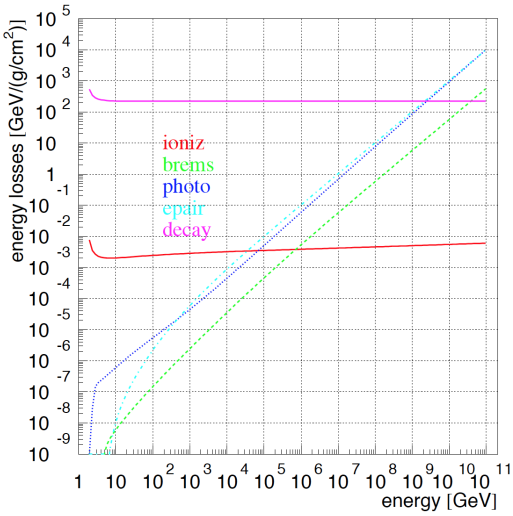

Figure 4.8: Tau energy losses. Color and line code as in Fig. 4.6. From [167].

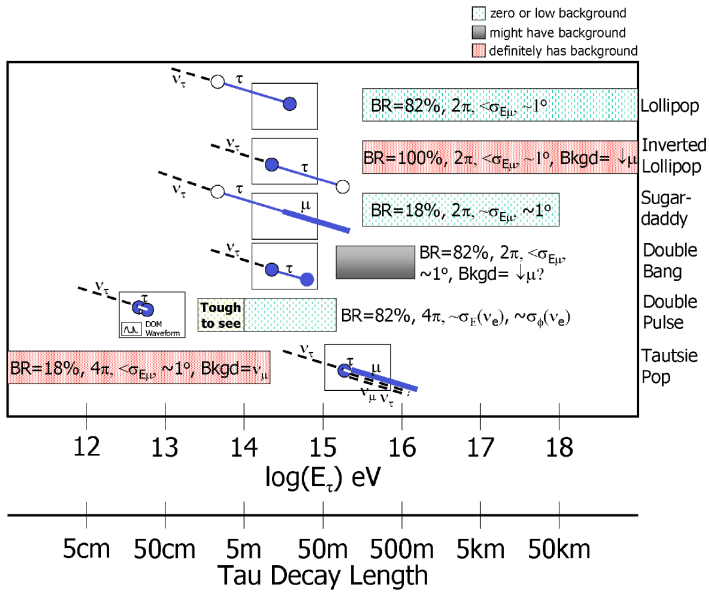

Figure 4.9: Summary of τ-induced topologies accessible to IceCube and their fancy name. From [169].

4.4.1 In vacuum

Suppose we start with three stable flavour eigenstates $\{|\nu_{\alpha=e,\mu,\tau}\rangle\}$ and their anti-particles.[5] The corresponding mass matrix cooked up by a theoretician is generally non-diagonal

$$\mathcal{M}_\nu = \begin{pmatrix} M_{ee} & M_{e\mu} & M_{e\tau} \\ M_{\mu e} & M_{\mu\mu} & M_{\mu\tau} \\ M_{\tau e} & M_{\tau\mu} & M_{\tau\tau} \end{pmatrix}. \tag{4.9}$$

If neutrino masses are of the Majorana type, this matrix can be diagonalized by a single unitary transformation U.[6] Flavour and mass eigenstates (= those carrying a latin index) are then related in the following ways:

$$|\nu_{\alpha,L}\rangle \equiv \sum_{i=1,2,3} U_{\alpha i} |\nu_{i,L}\rangle. \tag{4.10}$$

The matrix U is referred to as the PMNS matrix (after Pontecorvo, Maki, Nakagawa and Sakata [172]) and is conveniently parametrized as a product of matrices:

$$U = \begin{pmatrix} 1 & 0 & 0 \\ 0 & c_{23} & s_{23} \\ 0 & -s_{23} & c_{23} \end{pmatrix} \begin{pmatrix} c_{13} & 0 & s_{13}e^{-i\delta} \\ 0 & 1 & 0 \\ -s_{13}e^{i\delta} & 0 & c_{13} \end{pmatrix} \begin{pmatrix} c_{12} & s_{12} & 0 \\ -s_{12} & c_{12} & 0 \\ 0 & 0 & 1 \end{pmatrix} \begin{pmatrix} e^{i\alpha_1} & 0 & 0 \\ 0 & e^{i\alpha_2} & 0 \\ 0 & 0 & 1 \end{pmatrix}, \tag{4.11}$$

where c_{ij} and s_{ij} refer to $\cos\theta_{ij}$ and $\sin\theta_{ij}$, respectively. The θ_{ij}'s are called the *mixing angles*, δ is called the Dirac phase and α_1 and α_2 are Majorana phases. Both Dirac and Majorana phases are CP-violating phases (the last matrix in Eq. (4.11) only needs to be considered in the Majorana case). The fact that flavour and mass eigenstates are related by a non-trivial transformation, as soon as $\mathcal{M}_\nu$ is non-diagonal, is called *neutrino mixing* and also happens in the quark sector.

With this is mind, we can now introduce oscillations. Since interactions with matter produce flavour eigenstates, let us start off at the source with a neutrino of flavour α and momentum $\boldsymbol{p}$. According to Eq. (4.10), this state corresponds to a given superposition of the physical mass eigenstates with same momentum $\boldsymbol{p}$. However, assuming different mass eigenvalues, the eigenstates $|\nu_i\rangle$ do not propagate in phase, resulting in time-dependent projections of $|\nu_\alpha\rangle$ on $|\nu_i\rangle$'s. Therefore, it is possible for a state $|\nu_\alpha\rangle$ to transition—that is, to oscillate—to a state $|\nu_\beta\rangle$ where β may differ from α. Denoting by $|\nu_\alpha(t)\rangle$ what has become of the original $|\nu_\alpha\rangle$ after propagating during a time t in vacuum, *i.e.*

$$|\nu_\alpha(t)\rangle = \sum_j e^{-iE_j t} |\nu_j\rangle, \tag{4.12}$$

the probability for this process to happen is simply given by:

$$P_{\alpha\to\beta} = |\langle\nu_\beta|\nu_\alpha(t)\rangle|^2, \tag{4.13}$$

[5] The case of unstable particles and/or more than three families is considered in the literature.

[6] If they are of the Dirac type, this transformation is bi-unitary, meaning that another matrix $V \neq U$ is needed to describe the transformation of the right neutrinos.

where

$$\langle \nu_\beta | \nu_\alpha(t) \rangle = \sum_j e^{-iE_j t} U_{\alpha j} U^*_{\beta j} \ . \tag{4.14}$$

Assuming extremely relativistic neutrinos, and replacing t by the distance travelled L (recall that $c \equiv 1$), Eq. (4.13) gives:

$$P_{\alpha \to \beta}(E, L) = \sum_{k,j} U^*_{\alpha k} U_{\beta k} U_{\alpha j} U^*_{\beta j} e^{-i \frac{\Delta_{kj}}{2E} L}, \tag{4.15}$$

with $\Delta_{kj} \equiv m_k^2 - m_j^2$. From Eq. (4.15), it becomes clear that oscillations can take place if and only if at least one mass eigenvalue is different than the others. This, in particular, requires at least one massive state.

At the experimental level, the so-called Solar Neutrino Problem [173] appeared in the late 1960s but was not understood for a long time, nor interpreted as a sign of neutrino oscillations. Neutrino oscillation was then established on strong grounds by the Super-Kamiokande Collaboration, that observed the disappearance of high-energy atmospheric ν_μ [174]. This was the first in a series of results pointing towards the existence of neutrino masses.

The value of the mixing angles in vacuum θ_{ij} and of the Δ_{ij} are summarized in Tab. 4.1. Note that we have made the choice to restrict to the Normal Ordering scheme.

Parameter	Best-fit value $\pm 1\sigma$
$\sin^2 \theta_{12}$	$0.306^{+0.012}_{-0.012}$
$\sin^2 \theta_{23}$	$0.441^{+0.027}_{-0.021}$
$\sin^2 \theta_{13}$	$0.02166^{+0.00075}_{-0.00075}$
$\frac{\Delta^2_{21}}{10^{-5}\ \mathrm{eV}^2}$	$7.50^{0.19}_{-0.17}$
$\frac{\Delta^2_{31}}{10^{-3}\ \mathrm{eV}^2}$	$2.524^{+0.039}_{-0.040}$

Table 4.1: Best-fit values of some of the three-flavour oscillation parameters together with their 1σ allowed range, assuming a normal mass hierarchy. Adapted from [175].

4.4.2 In matter

So far, we have considered neutrino propagation in vacuum. The introduction of a medium through which neutrinos can propagate slightly changes this picture. Indeed, since matter has electrons, an electronic neutrino can interact (elastically) with matter—unlike ν'_μs and ν'_τs. This leads to an effective potential for the electronic neutrino that is different than for the other two flavours. In comparison with the

propagation in vacuum (Sec. 4.4.1), this leads in particular to different neutrino mixings and masses. Named after Mikheyev, Smirnov, and Wolfenstein [176, 177], the MSW effect can even, under specific conditions, be responsible for maximal mixing while the corresponding mixing angles in vacuum are negligible.

A **word of caution** should now be added. Because of neutrino-matter interactions, neutrino absorption effects (which correspond to inelastic processes) should also be considered. They lead to a non-unitary evolution of the neutrino beams which, coupled to oscillations, requires a more complicated treatment than considered above. In a tiny nutshell, it consists in correcting the unitary evolution by an exponential decay whose argument goes like the inverse of the neutrino absorption length weighted over the three flavours (see [178] for further details). In our analyses, matter will refer to both the Earth atmosphere and the Earth itself (if the neutrino comes from below the horizon). In these specific media, oscillations are effective below 100 GeV, while absorption starts being significant above 50 TeV. The two effects do not overlap and we will therefore take them into account by simply multiplying their respective probabilities of occurring and reweighing our neutrino fluxes with that number (see Sec. 7.2.2).

CHAPTER 5

The IceCube Neutrino Observatory

Neutrinos are naturally expected from a wide variety of sources and span over no less than twenty decades of energy. At the higher end of the neutrino energy spectrum, beyond the reach of any man-made reactor or accelerator, atmospheric and extra-terrestrial neutrinos provide—together with other high energy cosmic rays—the unvaluable insights into the *terra barbaria* of very high energy physics.

The idea of fishing high-energy neutrinos dates back to the early years of experimental neutrino physics. In order to test the quadratic behaviour of neutrino cross sections at high energies—as predicted by the four-fermion theory—, M.A. Markov proposed in 1960 to collect atmospheric neutrino data samples by building an underwater Cherenkov telescope [180]. Over the course of time, the technique has been extended to underground detectors (which consist of water-filled tanks buried in the rock), under-ice detectors, and serves today various scientific purposes, such as the identification and study of extra-terrestrial neutrino sources. The searches for monochromatic neutrinos at IceCube presented in Chapters 6 and 7 fit in this context: their observation would be a clean and unequivocal indicator of the existence of DM particles in our Universe.

Ice-fishing for neutrinos was first developed in Antarctica with the Amanda neutrino telescope [182]. The successful deployment and operation of the latter served as a proof of concept to build the IceCube Neutrino Observatory, the direct successor of Amanda and first gigaton neutrino detector ever. The Observatory, located about one kilometer away from the geographical South Pole, consists of arrays of Cherenkov light detectors deployed deep in and at the surface of the Antarctic ice cap.

This chapter is dedicated to a review of the main components of the IceCube Neutrino Observatory and how the magic happens as they interact with each other to produce discrete event samples from a very large amount of signals. Future possible plans to build a super-observatory at the South Pole are also presented at the end of the chapter.

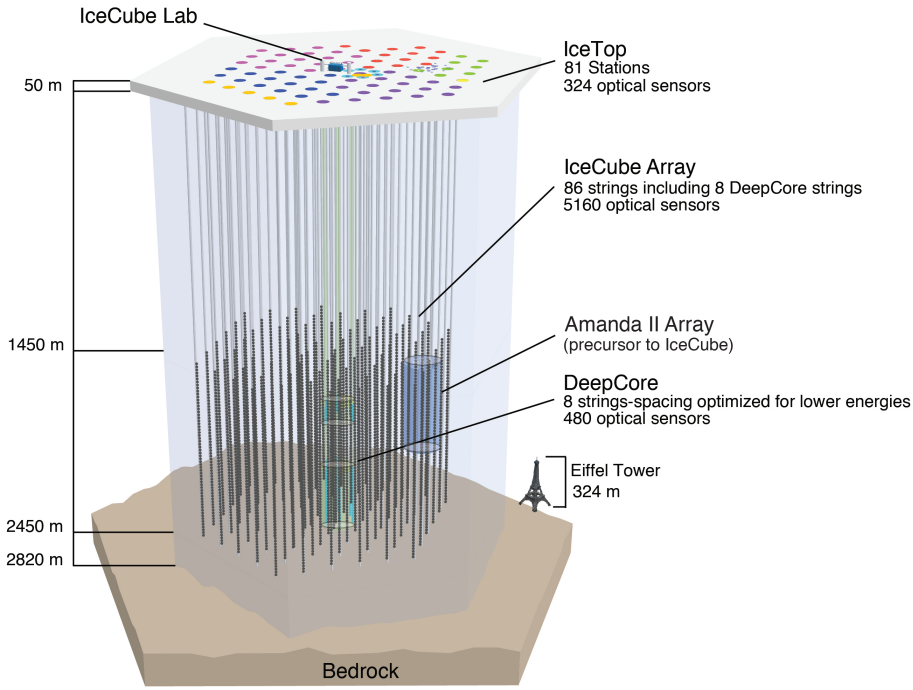

Figure 5.1: Artistic view of the IceCube Neutrino Observatory. Credit: IceCube Collaboration.

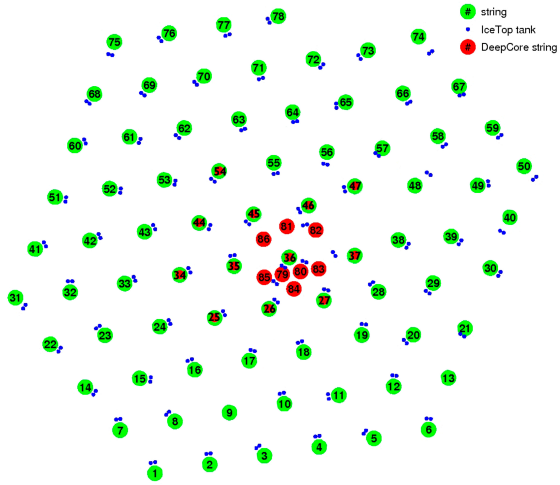

Figure 5.2: Layout of the sensor arrays at the IceCube Observatory. *Green*: IceCube strings. *Red*: DeepCore strings. *Green* and *red*: IceCube strings that can be used in an extended definition of DeepCore. *Blue*: IceTop tanks. Credit: IceCube Collaboration.

5.1 The sensor arrays

The IceCube detector principally consists of an array of Cherenkov light detectors deployed in the Antarctic ice, called In-Ice, and of a superficial array, called IceTop. Both InIce and IceTop fit in a triangular grid pattern (see Fig. 5.1), respectively instrumenting about 1 km^3 of ultra-clear ice and an area of about 1 km^2.

5.1.1 In-Ice

The In-Ice array consists itself of two sub-arrays. The first one, commonly referred to as the IceCube array, is made of 78 vertical strings evenly separated by a distance of 125 m. On each of these strings, 60 Digital Optical Modules (DOMs) are spread between 1,450 and 2,450 m of depth with a constant vertical separation of 17 m. This configuration allows to be sensitive to neutrinos with energies down to ∼100 GeV and up to 100 EeV. The second sub-array is known as the DeepCore detector. It is located in the inner bottom part of IceCube (1760 to 2450 m deep) and has a denser configuration: 8 vertical strings separated by a distance of ∼ 70 m, and a DOM vertical separation of, respectively, 7 and 10 m below and above the *dust layer*. This layer is characterized by a less transparent ice at depths of 1850 to 2107 m (see Fig. 5.4) and has therefore been intentionally avoided when deploying the DeepCore DOMs. The DeepCore configuration lowers the threshold of neutrino energies that can lead to detectable events down to ∼ 10 GeV. Beware that, from analysis to analysis, the definition of DeepCore may be extended: it may include up to 12 of the innermost strings of the IceCube array (green-red circles in Fig. 5.2).

In total, the In-Ice array is made of 5,160 DOMs which are shielded from air showers by more than one kilometer of ice. The DOMs have been deployed string by string into 2.5 km-deep water-filled holes which were bored using hot-water jets. After deployment, and after the water refroze, the DOMs have become stuck in the ice, making any future replacement impossible. The reliability goal originally targeted by the Collaboration was a 90 % DOM survival after 15 years. It has been shown that a significantly better achievement was made in reality, and that DOM losses were mostly caused by deployment [181].

A couple of future extensions of the In-Ice array have been proposed and are discussed in Sec. 5.5. Note on Fig. 5.1 the presence of the Amanda array within IceCube.[1] The local coordinate system is presented in Appendix C.1.

5.1.2 IceTop

On top of the In-Ice array—no pun intended—there is IceTop. It consists of 162 ice-filled tanks scattered in pairs over the ice surface (blue circles in Fig. 5.2). Two tanks of the same station are spaced by about 10 m, and the corresponding 81 pairs are placed about 25 meters away from the onset of 81 In-Ice strings. In addition to be filled with 90 cm of ice, each tank contains two downward-facing DOMs which collect

[1] The Amanda detector had actually been part of IceCube for two years, but was decommissioned in 2009 [183].

the Cherenkov light of down-going charged particles that interact with the ice placed in the tank. These particles (mostly muons at zero altitude) are part of the air showers produced by cosmic rays when they hit the nuclei present in our atmosphere. An obvious goal of IceTop is to study these cosmic rays and their composition, but IceTop is also used as a calibration tool for IceCube and may be used to veto atmospheric muons that reach the In-Ice array (see Sec. 4.3.2).

In order to minimize the build up of drifting snow—precipitations are low at the South Pole—, the tanks were installed in trenches so that the top of a tank after installation would initially coincide with the surface. Despite this precaution, the snow has constantly been accumulating over the IceTop stations. Because sweeping it out is not an efficient solution on the long term, the build up must be taken into account in order to correctly reconstruct air showers. A first solution consists in simulating the attenuation factor at each station but it is also proposed to use acoustic sensors in order to have in-situ measurement of the column depth of snow accumulated at each site.[2]

5.2 The Ice

The calibration of the detector is at the core of event reconstruction and simulation. In particular, measurements of the South Pole ice properties take an important *rôle* in this process. We have seen that the In-Ice array was equipped with 5,160 eyes[3] constantly staring in the dark and ready to catch optical Cherenkov photons. Yet, to reconstruct an event,[4] these Cherenkov photons who constitute the only tangible information to the detector must be propagated back to their emission point, requiring an accurate knowledge of the ice properties. The same requirement holds for the opposite approach, that is, simulating neutrino or muon events and propagating optical Cherenkov photons from their point of emission to the sensors.

The South Pole ice is probably the purest that we know of on Earth [185]. Moreover, at the depths where the In-Ice strings are found, it is highly transparent to light. This is because the pressures involved at these depths are high enough to have compressed any air bubble introduced when the ice layers formed and incorporate it—over a long period of time—into the structure of the ice. Quite fortunately, these structures have an index of refraction similar to that of pure ice. Contrariwise, the ice that has refrozen in the boreholes do display residual bubbles and, besides being sources of uncertainties, affect light propagation. This is also the case with the dust deposited by the winds through the ages, as they cannot be gotten rid of by any physical mechanism. Light propagation can be described in terms of three main parameters: an absorption coefficient, a scattering coefficient, and the angular distribution of the outgoing photon at each scattering point. These parameters additionally depend on

[2] Because the stations have not all been deployed around the same time, they need their own measurement of the snow column depth. For instance, tanks deployed in the latest seasons have accumulated less snow.

[3] Ignoring the dead ones.

[4] By "event", we mean here the original neutrino or muon event.

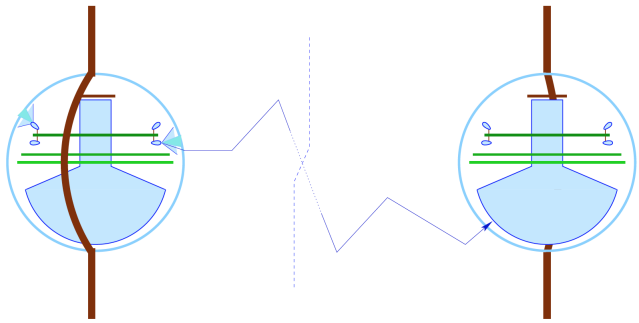

Figure 5.3: Illustration of the ice calibration using a flasher board. A LED in the left DOM flashes out photons which are then recorded by a neighbouring DOM. This step is repeated with all the DOMs in one string, and the data on all the neighbouring DOMs collected. From [184].

depth[5] and some of them also depend on the wavelength of the photon. To model these dependences, a few more parameters are necessary. The last two ice-models introduced by IceCube are SPICE-Lea[6] (the most recent one) [187] and SPICE-Mie[7] [184]. The latter uses a total of six parameters while SPICE-Lea introduces three more parameters (*i.e.* 9 in total) in order to account for a possible azimuthal dependence of the scattering. The development of SPICE-Lea was actually motivated by the observation of an azimuthal asymmetry [187]. For both models, the parameters are obtained from a global fit to *in-situ* measurements.

These measurements were performed using artificial light emitters, a technique already used by the Amanda Collaboration [185]. In the case of IceCube, the light sources consist of LED flashers. Each DOM hosts a flasher board with 12 LEDs (see Figs.5.3 and 5.5,): six of them are horizontally placed on the board, while the other six are tilted at a 48° angle with respect to the board. As explained in [184], the LEDs on a given string (in that case, string 63) were programmed to flash out light which was then recorded on the nearest and next-to-nearest strings, as illustrated in Fig.5.3. This set of data, to which the ice-model was fit, is called the *flasher run data*. The absorption and scattering coefficients at 400 nm resulting from the fit are presented in Fig. 5.4 (top and bottom, respectively), for both SPICE-Mie (blue) and SPICE-Lea (black). The gray band corresponds to the systematic uncertainties with SPICE-Mie. In both subfigures, the *dust layer* is easily recognized at 2000 m of depth (massive peak). Note the global decrease of both the absorption and scattering coefficients as a function of depth, which clearly highlights the fact that the ice is becoming clearer and clearer. Lastly, the right axes give the average absorption (top) and scattering (bottom) lengths, defined as the inverse of the corresponding coefficient on the left axis. Note

[5]Because of the existence of a gradient of temperature in the ice cap, depth can be traded for temperature and vice-versa [186].

[6]South Pole ICE with λ_e and a, where λ_e defines the new likelihood of the model and where a stands for *anisotropy*.

[7]South Pole ICE with Mie scattering.

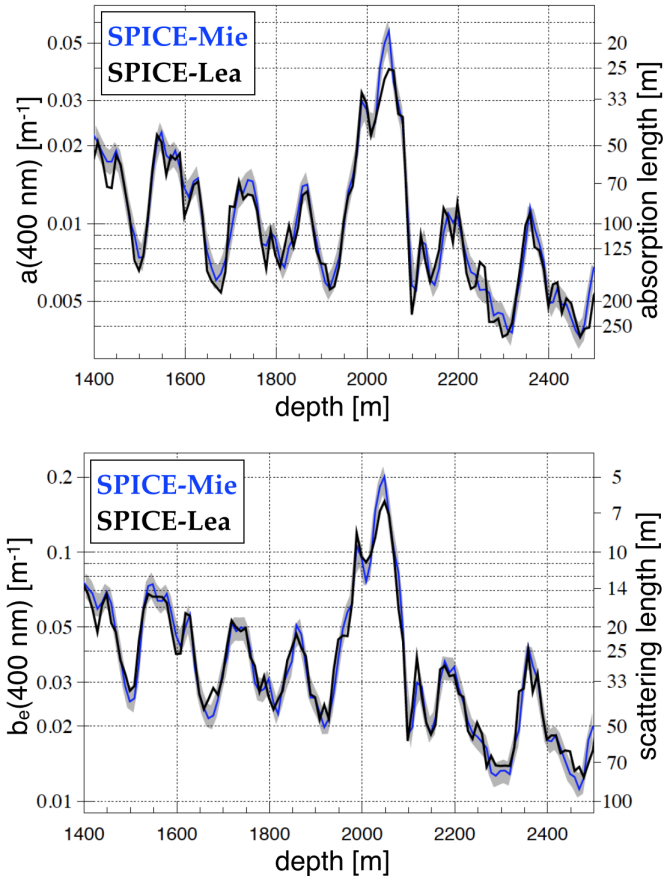

Figure 5.4: Absorption (top) and scattering (bottom) parameters at the South Pole as a function of depth. The corresponding lengths are found on the right axes. The solid blue (black) line gives the output of a global fit of the SPICE-Mie (SPICE-Lea) model to the LED flasher data. The gray band around the SPICE-Mie results give an estimate of the systematic uncertainties. In comparison to SPICE-Mie (the older version of the two models), SPICE-lea encodes the anisotropic propagation of photons at a given depth. Further details can be found in [184]. Figure taken from [187].

that, with the absorption length scale involved, the choice of a DOM separation of $\mathcal{O}(100\text{m})$ at IceCube makes sense.

5.3 Data Acquisition

In this section, we propose to review some of the key components and features of the IceCube data acquisition system (DAQ). As any other DAQ, that of IceCube provides solutions for the detection, capture, digitization and filtration of signals, as well as for their transfer from one place (of the Observatory) to the other. The IceCube DAQ architecture has nonetheless a very distinctive feature: it is decentralized. That means that, in order to meet the high-accuracy standards set for timestamping and saving information from 5000+ sensors spread over a cubic-kilometer of ice, a number of tests and tasks—like digitization—are locally performed on the freshly collected signals. Only then is the data gathered at the surface—in what is called the *counting house*—for further and deeper analysis.

5.3.1 The Digital Optical Modules

The Digital Optical Modules are the eyes of IceCube and its most fundamental unit. Each module consists of a pressure-safe vessel containing a 10-inch downward-facing Hamamatsu photomultiplier tube (PMT) that transforms (the) Cherenkov light into measurable electric signals via the photoelectric effect [188]. In addition, a DOM is also equipped with :

- on-board electronics that take care of digitizing (and storing) signals (the DOM MainBoard);
- a power supply;
- a clock for accurate local time-stamping;
- communication hardware;
- a LED Flasher Board which is used for calibration purposes;

and is designed to act autonomously, as required by the decentralized architecture of the DAQ. The main components of a DOM are illustrated in Fig. 5.5.

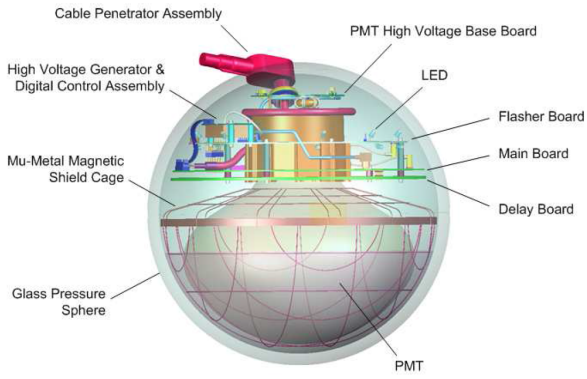

Figure 5.5: Schematic view of an IceCube DOM and its main components. More details on some of these components are provided in the text. From [189].

The PMT

A PMT is a sort of bulb in which you find a photocathode at one side, an anode at the other, and a succession of dynodes in between, as illustrated in Fig. 5.6. A PMT at IceCube has its photocathode grounded and a tension that highly increases as we successively move from dynode to dynode in the direction of the anode (about 2 kV at the anode). To guarantee mechanical support and provide optical coupling to the glass sphere, a gel is used. Also, in order to minimize the effects of the Earth's magnetic field on the propagation of charged particles inside the PMT, the latter is surrounded by a shield cage.

The operating principle of a PMT is the following. When a photon first hits the photocathode, an electron may be kicked off (photoelectric effect). The probability that it happens is not necessarily one and, moreover, depends on the energy of the photon. This is known as the quantum efficiency. The PMTs provided by the Hamamatsu Photonics company for IceCube are sensitive to the 300 nm–650 nm range of wavelengths and have an efficiency distribution which peaks around 390 nm (25 % for "regular" IceCube DOMs and 34 % at DeepCore). When the ejection of an electron happens, the latter is accelerated towards the anode because of the high voltage. As it does so, it hits the first dynode, ejecting more electrons (secondary emission). These electrons are themselves accelerated to the next dynode, ejecting even more electrons, and so on, until the anode is reached. The result is a massive amplification of the signal that is now readable at the output of the tube. Each IceCube PMT contains 10 dynodes. Those of In-Ice are operated at gain of 10^7 while those of IceTop have a gain around 10^6. In fact, in each tank, two DOMs may as well operate at different gains, so as to cover as much as possible the dynamic range of the PMTs.

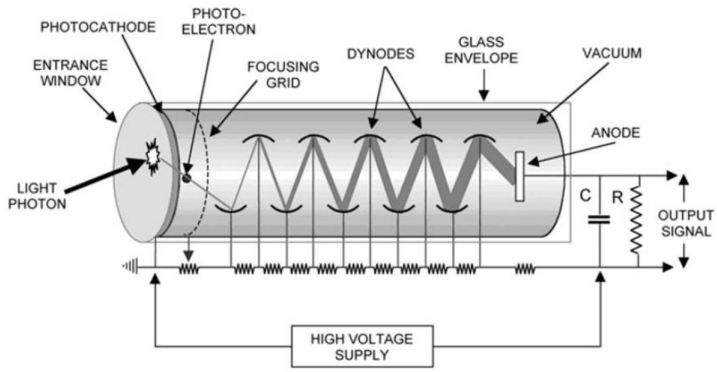

Figure 5.6: Schematic representation of a PMT and operating principle. A photon hits the photocathode and ejects a photoelectron according to the photoelectric effect. The latter is accelerated towards the first dynode, extracting more electrons. A snowball effect takes place, until the last bunch of electrons reaches the anode, creating a readable pulse at the output of the PMT. Taken from [190].

The DOM MainBoard

The PMT signals are read out by the DOM MainBoard (MB), which is where most of the DOM circuitry is found. Upon entering the MB, the output of the PMT is passed through a comparator with a programmable threshold. This threshold is measured in units of PE, the average voltage induced at the PMT anode by one single Photo-Electron at the photocathode, and it is typically set to 0.25 PE for In-Ice DOMs. In parallel, the signal is also passed through a 11.2-m long serpentine, introducing a 75 ns delay before it reaches the digitizers. This delay allows time for the comparator to find out whether or not the anode voltage has exceeded the threshold value and, if it has, to trigger the capture and digitization of the PMT waveform by the digitizers. In the last case, we say that there has been a *hit*.

The delayed signal is further split among two types of digitizing systems: the fast Analog-to-Digital Converter (fADC) and the Analog Transient Waveform Digitizer (ATWD). The fADC and the ATWD respectively collect 256 and 128 samples of 10-bit data at a sampling rate of 40 and 300 Mega Samples Per Second (MSPS). The PMT waveforms can thus be finely sampled using the ATWD (3.3 ns per sample), but are only read for 427 ns. For its part, the fADC coarsely samples the waveforms (25 ns per sample) but has a capture window of $6.4\ \mu s$, which is particularly relevant to follow long-lasting signals. Note that the output of the PMT is continuously sampled by the fADC.

The digital conversion of a hit may be carried out in low and high resolution, depending on the length of the waveform and the coincidence with other hits (see below). When a hit is saved in low resolution, it means that it is only attributed a time stamp and a very abbreviated version of the fADC output called the *coarse charge stamp*. The latter encodes only three samples from the fADC output: the sample with the highest count among the first 16 samples, the one directly before and that directly after. This is the way that Soft Local Coincidence (SLC) hits are digitized. As for Hard Local Coincidence (HLC) hits, they are readout in both low (= all the fADC output) and high resolution (= all the ATWD output). To reduce the dead time of a DOM, the MB contains two ATWDs: if one of them is busy processing a waveform, the other one is still available for another capture.

Local Coincidence of hits

Whether a hit receives the HLC or the SLC flag depends on local coincidence (LC). As mentioned later in Sec. 5.3.2, each DOM can directly communicate with its neighbours. These neighbours can in turn propagate the information to the next-to-nearest neighbours, and so on. In particular, when a DOM "fires", it sends out an LC tag, meaning that it saw a hit. If at least one of the four closest neighbours fires within an interval of 1 μs, the hit receives the HLC tag. Otherwise, the hit is considered as isolated and receives the SLC flag.

The purpose of the LC check is to reduce with a simple test, and at an early stage of the DAQ, both the noise—most likely, isolated hits are not produced by neutrinos or muons—and the data flux. The noise corresponds to the hits observed by a DOM when in fact there was no light in the ice. Its origin consists in the *dark noise* of the PMT

and a contribution that is not fully understood but may be due to the radioactivity of some of the materials used, spontaneous scintillation, etc. Because the dark noise embeds temperature-dependent processes, it has a variable rate as a function of depth. On average, this rate is around 500 Hz for the regular IceCube DOMs and 780 Hz for the DeepCore DOMs (higher quantum efficiency).

5.3.2 On the way to Level 2

Cabling

The operability of the IceCube Observatory as a whole relies on an intricate network of cables. Not only does this network provide power to the different building blocks of the detector, it also makes communication and data-sending from and to 5000+ sensors possible. Each string of DOMs is served by one cable in which 20 quads are found. Each quad consists of two pairs of twisted wires and may serve up to four DOMs.[8] Each surface-to-DOM cable has 30 breakouts whence three pairs of wires realise two DOM-cable connections. Three pairs of wires enter a DOM via the Cable Penetrator Assembly (see Figs. 5.5 and 5.7). Two of them are used for the LC checks with adjacent DOMs (see above); the third one is used to send data to the surface. There, a junction box is dedicated to the collection of all the cables from both IceTop tanks and that of the corresponding string. They are merged into one cable which realises then the connection to the DOMHubs which are computers located in the IceCube Laboratory (ICL). A schematic representation of the cabling associated to one string is found in the left panel of Fig. 5.7.

After the LC checks, the digitized hit data are sent to the ICL via the cabling network just portrayed. Those hits carrying the HLC flag go through a first battery of tests—the triggers—, after which discrete physics events are build and filtered so as to leave as much of the background aside.

Triggering

IceCube uses 5 types of triggers. Each of them is defined on specific subsets of arrays (In-Ice, IceTop, DeepCore, etc.), and they have their own settings which may be redefined up to once a year. The trigger algorithms run in parallel and look for a certain number of HLC hits clustered in time. Some of them also look for spatial coincidences (see Table 5.1). At the end of the process, all the triggers that have fired are merged into a Global Trigger. The readout window of the latter is defined as the union of all the individual readout windows of the triggers who have fired, plus some interval before and after. All the SLC and HLC hits falling in this "global readout" window are saved together as one event.

The Simple Multiple Trigger (SMT) is the most basic trigger used at IceCube. It looks for a predefined number N (or more) of HLC hits within a sliding time window of several microseconds. When the condition is met, a slightly extended readout

[8] In order to minimize weight and costs, two adjacent InIce DOMs share the same pair of wires. The surface hardware being subject to less constraints, this is not the case for IceTop DOMs (each of them is connected to the network via a single pair of wires).

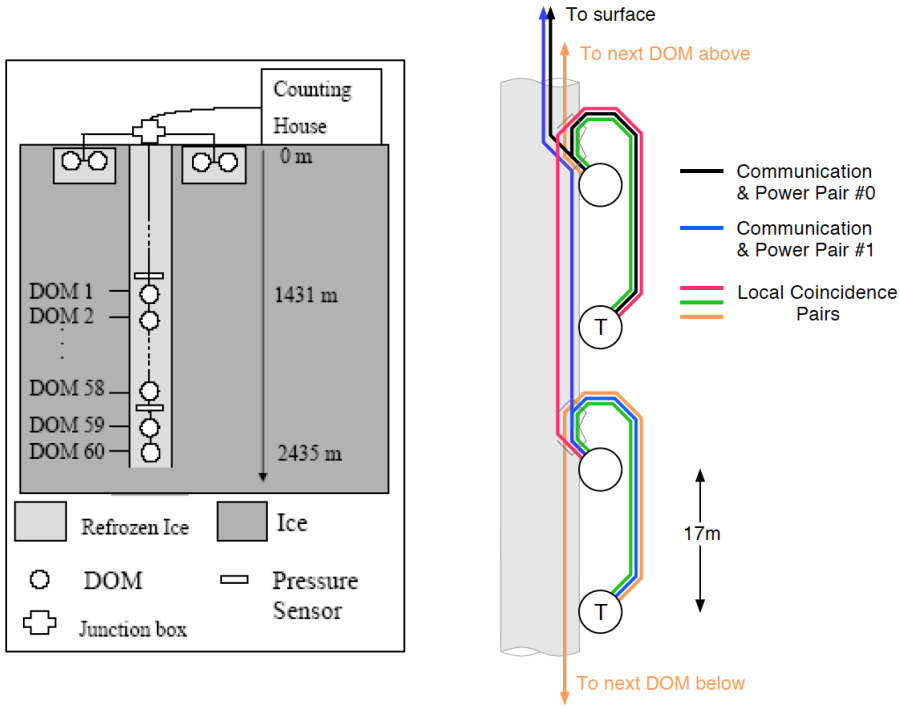

Figure 5.7: Left: Schematic view of an IceCube string and two associated tanks. From [189]. Right: Schematic of the cable connections at four DOM locations. The wires used for power and communication with the surface are shared among two pairs of DOMs. The wires dedicated to the direct communication between neighbouring DOMs are also depicted. From [191].

window is defined around the cluster of HLC hits just found. The value of N and the width of the sliding window take a different value depending on the sub-array under consideration. They are presented, as of 2016, in Table 5.1. **The Volume Trigger** defines, in addition to a sliding time window, a spatial window—more precisely, a cylinder—around DOMs. Similarly to the SMT, the Volume Trigger looks for a given multiplicity of hits within these two windows (spatial and temporal). Again, the specific value of the different parameters depend on the sub-array to which the DOM belongs. This trigger also fires if a certain multiplicity of hits is observed, regardless of the spatial clustering. **The String Trigger** looks for coincidences of HLC hits on the given DOM string. As for the last two types of triggers, called **SLOP** and **FRT**, they are used in very specific studies (magnetic monopole searches and DOM noise studies) and we refer the reader to Ref. [191] for details.

Processing and Filtering

After the triggers, the data traffic is reduced to about 1TB/day. This is way beyond the capacities of satellite transmission. The filters at IceCube reduce the flow of data

Trigger	DOM set	N HLC hits	Window [μs]	Topology	Rate [Hz]
SMT	In-Ice	8	5	—	2100
SMT	DeepCore	3	2.5	—	250
SMT	IceTop	6	5	—	25
Volume	IceTop infill	4	1	cylinder (r = 175 m, h = 75m)	3700
Volume	In-Ice	4	0.2	cylinder (r = 175 m, h = 75m)	4
String	In-Ice	5	1.5	7 adjacent vertical DOMs	2200

Table 5.1: Parameters (as of May 2016) used in different trigger algorithms. Only those of the SMT, Volume and String triggers are presented. As you can see, different sub-arrays may use different settings. IceTop infill refers to the denser configuration of eight stations at the center of IceTop. Because the rates vary with season, the values presented should be understood as "typical values". Details on the SLOP and FRT trigggers can be found in [191], where the table was adapted from.

down to a manageable rate of about 100 GB/day.

Now that the hits are merged into distinct and discrete events, it is possible to select events on the basis of the physics that we want to do with IceCube. Over the years and depending on the physics goals, the Collaboration has developed a number of filters dedicated to the selection of specific candidates (track events, cascade events, DeepCore events, etc.). About 25 filters were available for the year 2016. Events that satisfy at least one of the filters defined for the corresponding year are kept: they typically represent 10-15 % of the events sorted out by the triggers. The latter are commonly referred to as the Level 1 data, the filtered events as the Level 2 data. It is the Level 2 sample that is made accessible for the Collaboration on a computer (cluster) at Madison, USA. At that point, the experimentalist setting up an analysis is free to choose the combination of filters that suits best the analysis' purposes. For example, the analysis presented in Chapter 7 only uses the DeepCore filter.

5.4 Event Topologies at IceCube

We have already discussed in Chapter 4 how the different types of charged particles produced by neutrino-ice interaction can loose energy as they propagate. For the record, we came to the conclusion that there were two basic Cherenkov light emission patterns: the spherical-ish pattern (when the outgoing charged lepton quickly looses all its energy), and the the cylindrical-ish pattern (when the outgoing lepton travels long distances in the detector). With the inter-string and inter-DOM scales involved at IceCube, and given the typical attenuation length of light in ice, observing these patterns is not a problem (see Figs. 5.8 and 5.9).

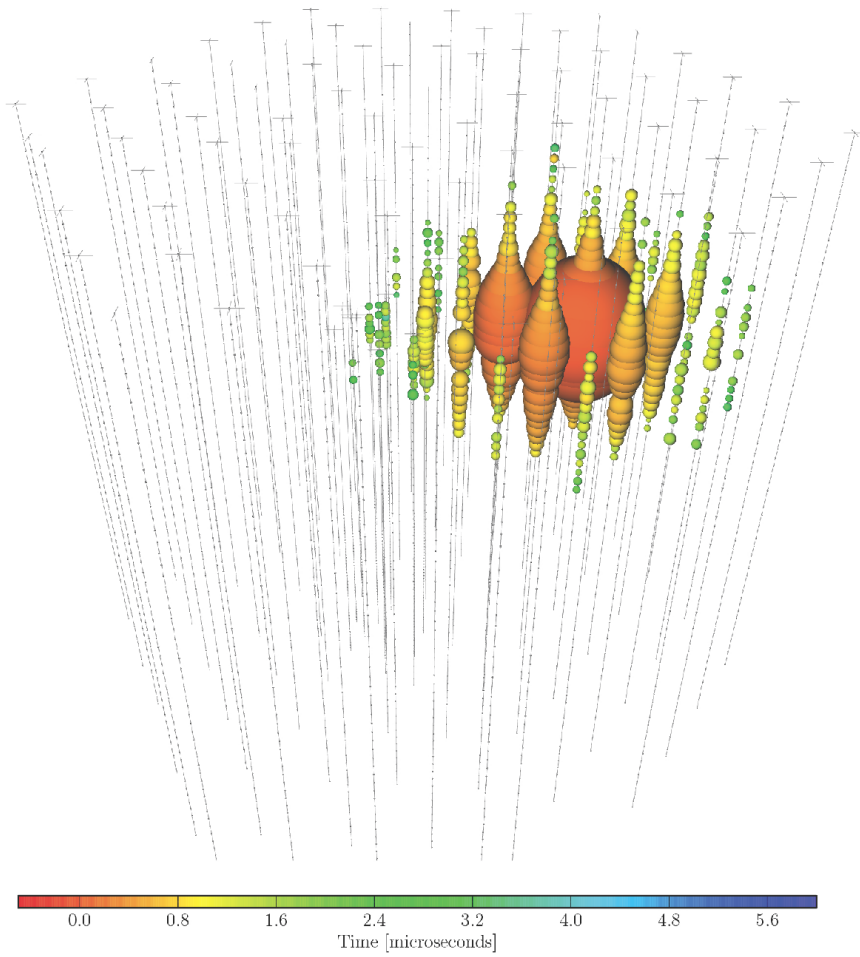

Figure 5.8: Meet Bert! With an estimated energy of 1.04 PeV, it is one of the highest-energy neutrino events ever detected at IceCube. It has the topology of a shower and was observed on 09-Aug-2011. The DOM size on the figure corresponds to the intensity of the light signal observed. Note that the shower is extending outwards, as indicated by the color code (= time). Credit: The IceCube Collaboration.

5.5 Future arrays at the South Pole

5.5.1 Cherenkov light detection

By now, it should sound familiar to the reader that IceCube is the world's largest neutrino detector. Even so, he should also be aware that proposals to extend IceCube in the mid and long terms do exist. These proposed extensions seek the improvement

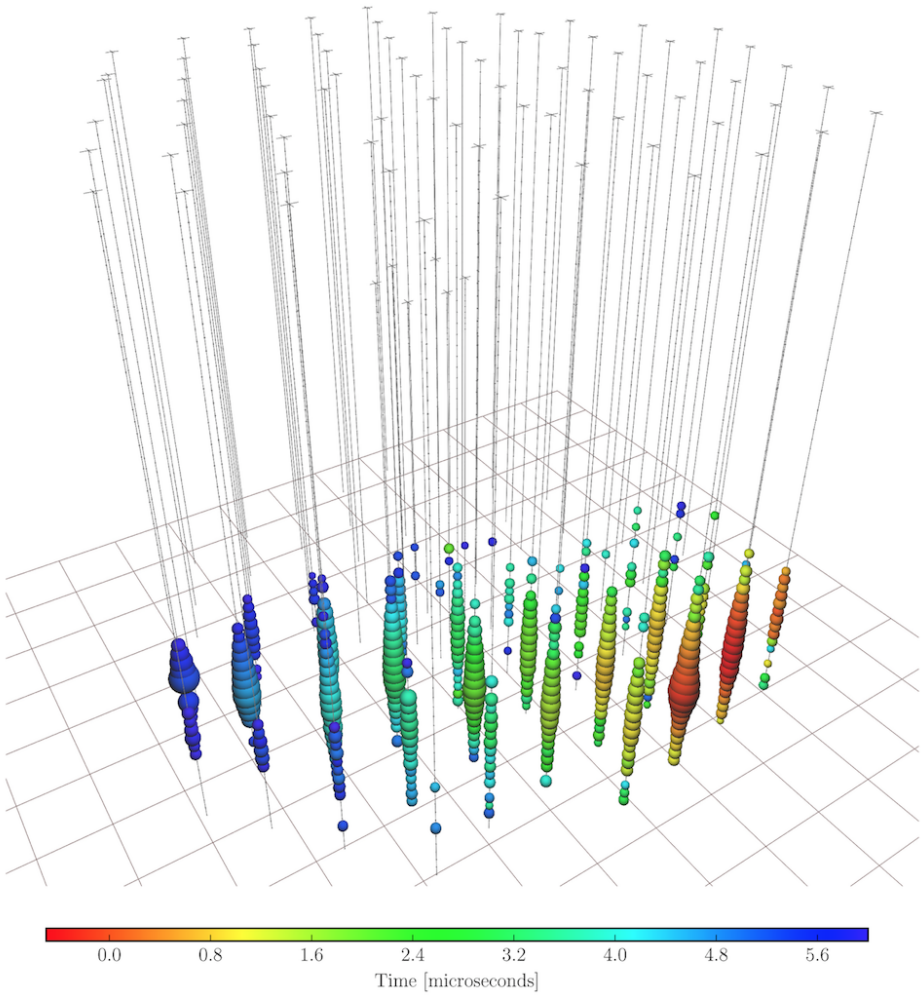

Figure 5.9: High-energy track event at IceCube. This event was observed on 28-Oct-10 and the neutrino energy estimated to 880 TeV. The charged lepton propagates from right to left, as indicated by the color code. Credit: The IceCube Collaboration.

of the sensitivity of the detector towards the lower and higher ends of the energy range that is currently probed.

Pingu[9] is a proposed low-energy extension of IceCube [192]. It will consist of 26 vertical strings placed in the inner bottom part of the IceCube detector (below the *dust layer*), and will occupy a volume about the same as DeepCore with the difference of a higher density of strings coupled to a higher density of DOMs on a given string (192 DOMs vertically distributed over about 300 m). Because its configuration lowers the threshold of the detector to a few GeV, the Pingu sub-array will be key in many

[9]Precision IceCube Next Generation Upgrade.

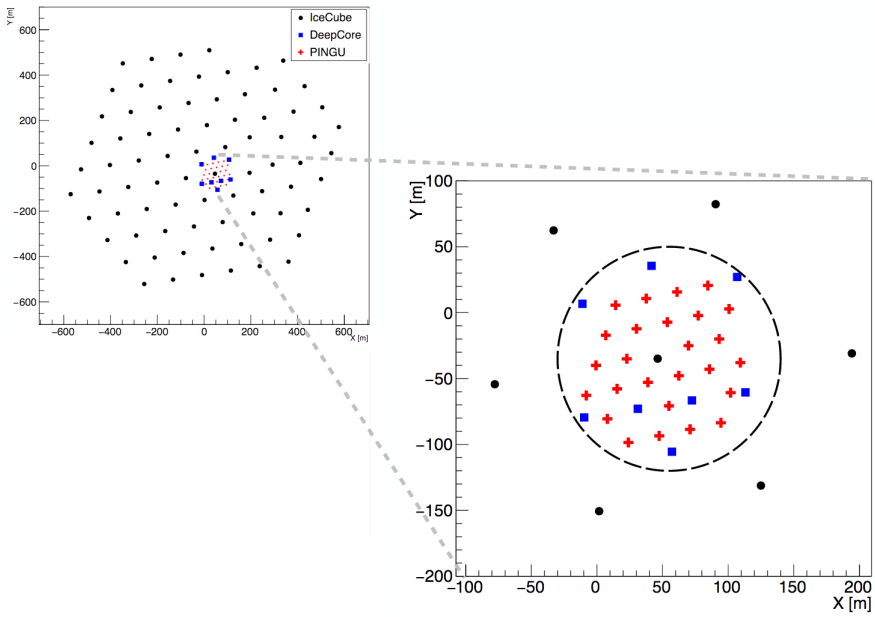

Figure 5.10: Proposed layout of PINGU, the low energy extension of ICECUBE. To have an idea of the relative scale of the different sub-arrays, the figure on the left shows all the strings of the INICE detector. The location of the ICECUBE, DEEPCORE and proposed PINGU strings are respectively shown in black (circles), blue (squares) and red (+). PINGU will lay at the very inner bottom part of ICECUBE, below the *dust layer* (not shown in the figure), and will instrument about 5 MTon of very clear ice. From [192].

low-energy related studies, such as those on solar neutrinos, neutrino oscillations (parameters) and on the neutrino mass hierarchy.

ICECUBE-GEN2 will extend the instrumented volume by a factor of about 10 [224]. Similar costs to those previously needed for ICECUBE are foreseen because of a ~ 10 times sparser array of strings. The array will also be about 250 m thicker (vertically) than the current km-deep INICE. The final layout of this detector is not settled yet, as analyses are still ongoing [224, 225]. In any case, the sparsening of the strings should improve the sensitivity of the detector to neutrino energies up to 10^9 GeV, thereby contributing to the study of *very* high-energy particle physics.

5.5.2 Hybrid detection

Besides the aforementioned extensions which are proper to the realm of Cherenkov astronomy at the South Pole, other techniques are currently being developed and may lead in the future to a massive super-observatory there. As briefly mentioned in Chapter 4, high-energy neutrinos interacting in a dense medium can produce three types of detectable signals: Cherenkov light, radio and acoustic waves. The first of these types of signals having been discussed at length in Sec. 4.2, we think it useful

here to add a few words about the last two. In comparison to Cherenkov light signals, they involve higher attenuation lengths, hence giving the opportunity to test the very high energy end of the neutrino spectrum where, who knows, the DM particle may reside.

Radiowave detection

At the core of radio wave emission by high-energy neutrino interactions, we actually find both the Cherenkov [155] and the Askaryan effects [156]. Recall that the first of them consists in the emission of a constructive electromagnetic wave front caused by the quick de-excitation of atoms when the medium is traversed by a superluminal charged particle. The radiation due to a single charged particle happens in the optical and UV ranges and we generically call it "Cherenkov light". Yet, neutrino interactions are not all about single charged particles. As we have seen in Sec. 4.3, they also generate a lot of e^+e^- pairs. Each lepton in these pairs will individually radiate as long as its $\beta > 1/n$. If the pairs are quickly produced and contained in a small region—small with respect to the wavelength λ of the radiation—, the individual radiations of each type of particle (electrons *vs* positrons) may add up coherently. Nonetheless, if the net charge of the cascade were zero, the radiation associated to the entire shower (positively *and* negatively charged particles) would cancel out. As pointed out by G.A. Askaryan [156], this is not the case as the shower ends up carrying an excess of negative charges. This effect, named after Askaryan, is easily understood as a consequence of the facts that:

- electrons can be kicked off their atoms by photon and electron scattering processes;
- positrons can annihilate with the medium's electrons.

The charge asymmetry is typically around 20-30 % at ultra-high energies and is the reason why a longwave radiation from electromagnetic showers is possible. Both *microwave* and *radio* Cherenkov light may be expected. Note that, at radio frequencies, a Cherenkov angle of 56° is predicted (instead of the 41° quoted in Sec. 4.2 in the case of optical light). The radiowave detector currently being developed at the South Pole is the Askaryan Radio Array (ARA), with the plan of covering an area of 100 km^2. A much bigger competitor named ARIANNA is being build on the Ross Ice shelf. Its sensors will spread over 1000 km^2 and will have the particularity to use the ice-water interface as a mirror to detect down-going radio waves.

Acoustic wave detection

Acoustic wave detection bases itself on the thermo-acoustic effect [157]. The idea behind this mechanism is that neutrino-induced particle cascades deposit energy in the medium and locally heat it. There, the increase in temperature expands or contracts the medium,[10] causing a pressure pulse to propagate. The intensity of the pulse is proportional to the acceleration of the expansion (or contraction) of the heated volume. In addition, the propagation of the pulse takes place perpendicularly to the axis

[10] Some materials may have a negative thermal expansion coefficient, but this is not the case for water nor ice.

of the shower.

The South Pole Acoustic Test Setup (SPATS) is the instrument currently dedicated to the development of acoustic wave detection at the South Pole. It consists of four strings deployed up to a depth of 500 m in four boreholes belonging to the InIce array of the IceCube Observatory. SPATS has been designed to investigate the properties of the South Pole ice (like the attenuation length and the sound speed) and the possibility to further perform acoustic neutrino astronomy there. A recent study has measured that the attenuation length was around 300 m, much lower than theoretical predictions (about 1 km) [159]. Nonetheless, as in the case of radiowave detection, this length still allows a larger separation of the sensors, thereby reducing the costs to build a large-scale array.

CHAPTER 6

A search for neutrino spectral features induced by DM at IceCube

Now that the reader has had an in-depth introduction to the principles of neutrino detection and to the operation of the IceCube detector, we will spend a couple of chapters discussing how, with the events collected, DM-induced smoking guns can properly be searched for.

Unlike with γ-ray lines, the fact *is* that there is but little appropriate treatment in the literature when it comes to searching for the annihilation or decay modes of particle DM that involve the production of sharp features in the neutrino spectrum. A close look at official Collaborations' analyses of the $\nu\bar{\nu}$ channel reveals that the majority of them actually consist in angular distribution analyses. We do not mean to say that this approach is "bad"—it *does* have its pros—but we want to point out that the most logical strategy to adopt when it comes to unveiling a specific signal that *you know* has a spectral feature in it should be to—at least—include spectral information (instead of integrating it out and making yourself blind to it).

While we do agree that angular studies have their reasons to be (very good angular reconstruction skills with some subclasses of events, generally enough statistics to produce smooth angular PDFs, annihilation *vs* decay discrimination possible based on the profile of a signal), the potential discovery of a spectral feature—through a dedicated search—would have a lot more to tell about the *Particle Physics* of DM rather than its astrophysical properties. A straightforward example is the location of the sharp feature, which is generally a direct probe of the DM mass (or half of it).

It is in this perspective that we review here the dedicated and careful study that we have performed a few years ago on a public data sample of the IceCube Collaboration. To our knowledge, this was the **first** analysis in the literature looking at the detailed spectral shape of neutrino events. We start with a presentation of the sample, explain how the signal events are modelled, and then present a first set of quick and easy limit estimates. After this, we discuss our dedicated statistical analysis based on the log-likelihood ratio method, the results of which have motivated the third chapter of this thesis. We consider the less popular scenario of DM decay, and the results obtained in the 1–100 TeV energy range did put an end to a long period of no update. They improved the latest official IceCube limit estimates (back then, see Fig. 1.19) by about one order of magnitude and are still competitive with more recent limit estimates [193]. This work has been published in Ref. [139].

6.1 Sample

The sample used throughout this chapter has been released by the IceCube Collaboration in late 2014 and consists of 2 years of neutrino events collected from 2010 to 2012 [3].[1] The energy range covered by this data release goes from 100 GeV to 10^8 GeV. Twenty energy bins have been considered within this range and $N_{\rm tot} = 383$ events detected in total (tracks *and* cascades in the approximate proportion of 1:3). We denote the number of events in each energy bin i by $N^i_{\rm obs}$ and show the corresponding distribution in Fig. 6.1. Notice that the statistics are fairly limited, which is why we do not expect the systematic uncertainties to dominate over the statistical uncertainties.

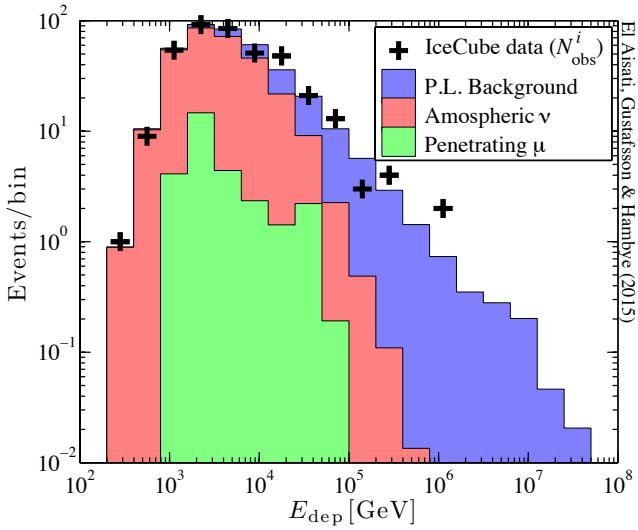

Figure 6.1: Observed deposited energy spectrum from the whole sky (black +). The colored regions show the expected backgrounds: the contribution from the atmospheric muons and neutrinos are respectively depicted in green (bottom) and red (middle); the contribution from astrophysical neutrinos (best-fit of a power-law modelling, see Eq. (6.1)) is depicted in blue (top). The data is taken from Ref. [3].

The background distributions come from specialized event generators (Corsika for the atmospheric muons [196, 197], NuGen [198] and Genie [199] for the neutrinos). We will not discuss the functioning principles of these generators here but a few more words will be added in the next chapter.[2] The existence of an extra-terrestrial flux of neutrinos is clear from the figure, and to observe it was one of the main reasons—if not *the* main reason—for building a GTon detector like IceCube at the South Pole.

[1] It is also known as the Medium-Energy Starting Events (Mese) sample.

[2] For the project presented in Chapter 7, we had—among others—to filter the simulated background events *ourselves*. This is why we will take the time to add few pieces of information regarding these generators there.

Even if the origin of this flux is yet to be confirmed, common sense tells us that a contribution from "regular astrophysical sources"[3] *is* expected since neutrinos are a natural by-product of the processes behind the production of cosmic rays. Like for photons, the expected behaviour of this astrophysical flux is that of a power-law. When we need to model the astrophysical contribution, we will assume (as in Ref. [3]) that it consists of an isotropic flux with a *single* power-law in the energy spectrum, and that it carries equal parts of each flavor as well as of neutrinos and anti-neutrinos. More specifically, we will use the following expression:

$$\frac{\mathrm{d}\Phi_{\mathrm{astro}}}{\mathrm{d}E_\nu \mathrm{d}\Omega} = 3 \times 10^{-18} \times \Phi_0 \left(\frac{E_\nu}{E_0}\right)^{-\gamma}, \tag{6.1}$$

where $E_0 = 10^5$ GeV. This kind of spectrum can *e.g.* be expected from active galactic nuclei and star-burst galaxies with $2.0 \lesssim \gamma \lesssim 2.6$ [200, 201]. The best-fit values obtained in Ref. [3] are $\gamma = 2.46 \pm 0.12$ and $\Phi_0 = 2.06^{+0.35}_{-0.26}$ GeV^{-1}cm^{-2}sr^{-1}s^{-1}, and these are the values which have been used to produce the blue region in Fig. 6.1. For your information, a Pearson's χ^2 test [202] of the fit presented in that figure gives a p-value of 0.42 after a set of 10^5 pseudo-experiments has been considered.[4] The interpretation of this number should be that the upper edge of the blue region already gives a good fit to the observations. We will later use it as our NULL model for generating pseudo-experiments. You will however notice the presence of a few intriguing excesses, in particular around $\sim$ 50–100 TeV and $\sim$ 1 PeV. They are present to this day in the 6 years of data taken with the complete ICECUBE detector [203]. To address them, it has been proposed to use two different power laws—different normalisation and spectral index— so that the softer one would take care of the low-energy excess, while the harder one would take care of the PeV excess. A soft component might however induce some tension with γ-ray observations (see for instance Refs. [204, 205]).

In our fits and limit estimates, we will stick to maximum one astrophysical component (with the same parametrization as that used in Eq. (6.1)) and will consider the addition of a DM-induced distribution of events N^i_{DM}. We discuss in the next section how N^i_{DM} is modelled.

6.2 Modelling a signal

Given a neutrino flux $\mathcal{F}$—whether it be an atmospheric, astrophysical or DM-induced flux like presented in Sec. 1.5.3—, the differential number of expected events in the ICECUBE detector is simply obtained from a convolution with the detector's instrument

[3] We use this terminology by opposition to a DM contribution.

[4] A direct assumption of a χ^2 distribution with $N_{\mathrm{bin}} - 5 = 15$ d.o.f would have given a p-value of 0.63. Because of low statistics (in some bins), this assumption is not necessarily valid and we have generated 10^5 Poisson-distributed data realisations. All the fits to the pseudo-data were done with an adjustable single power-law astrophysical component $N^i_{\mathrm{astro}}(\Phi_0, \gamma)$ together with freely normalized atmospheric backgrounds. In Ref. [3], the goodness-of-fit p-value was found to be 0.2 for this model, but there three observables were considered for the fits (not only the reconstructed deposited energy, but also the directional and track property information).

response. We therefore start with the following expression:

$$\frac{\mathrm{d}N_\alpha}{\mathrm{d}E_\nu \mathrm{d}\Omega \mathrm{d}E' \mathrm{d}\cos\theta' \mathrm{d}\phi'} = \frac{\mathrm{d}\mathcal{F}\alpha}{\mathrm{d}E_\nu \mathrm{d}\Omega} \mathcal{E}_\alpha D_{\mathrm{eff},\alpha}, \tag{6.2}$$

where E', θ' and ϕ' respectively denote the events' reconstructed—*i.e.* observed—energy, zenith and azimuth angles at IceCube. As already explained in Sec. 1.5.3 in the context of DM-induced fluxes, E and Ω respectively track the *true* energy and *true* angular distributions. The index $\alpha \in \{e, \mu, \tau, \overline{e}, \overline{\mu}, \overline{\tau}\}$ is introduced to keep track of the flavor composition of the incoming flux at the *surface* of the Earth, and whether this flux consists of neutrinos and/or anti-neutrinos.

The DM-induced flux $\mathcal{F}^{\mathrm{DM}}$ has a galactic and extra-galactic contributions, which we respectively denote by Φ_{gal} and $\Phi_{\text{x-gal}}$ (see Eqs. (1.54)–(1.55) and (1.59)–(1.60)). Recall that the latter of these two fluxes is isotropic (and cosmologically redshifted), while the former is Ω-dependent (but not redshifted).[5] When we consider the scenario where particle DM decays, we take these *two* contributions into account (unless stated otherwise). In the other scenario (annihilation), we will *only* consider the galactic contribution. The reason for this "asymmetrical" choice is that the modelling of the clumping factor $\zeta(z)$, which only affects the flux resulting from DM annihilations, is highly model-dependent and we wish not to address this here.

The exposure $\mathcal{E}_\alpha$ is given by the product of the effective area $A_{\mathrm{eff},\alpha}(E_\nu, \theta, \phi)$ and exposure time T (= 641 days for the sample under consideration).[6] The angle of an event relative to the zenith is expressed as $\theta(b, l) = \arccos(\widehat{z}_{IC} \cdot \widehat{s})$, where $\widehat{s}(b, l)$ is a unit-vector giving the direction of this event. The zenith $\widehat{z}_{IC}$ at IceCube is located, in Galactic coordinates, at $b_{IC} = -27.4^\circ$ and $l_{IC} = 303^\circ$ (see Appendix C.1 for a representation of the local coordinate system).

A neutrino coming from the direction (θ, ϕ) with true energy E_ν at the *surface* of Earth is reconstructed with an (deposited) energy E' at a direction (θ', ϕ'). The probability distribution associated to this reconstruction is called the dispersion function $D^\alpha_{\mathrm{eff}}(E', \theta', \phi'; E_\nu, \theta(b, l, t), \phi(b, l, t))$.[7] The instrument response function $(A_{\mathrm{eff}} D_{\mathrm{eff}})_\alpha$ available in [194] is *binned*: it has been pre-integrated over all ϕ and ϕ', as well as over a selection of bins in the θ, θ' E and E' spaces.[8] It is worth noticing here that separate instrument response functions are available for each neutrino and anti-neutrino flavor—e, μ, τ—, and that they all show a strong dependence on θ_{IC}—the zenith angle measured at IceCube—due to the energy losses and absorption effects in the Earth starting from $E_\nu \sim 50$ TeV (see Sec. 4.4.2).

The differential number of observed neutrinos (with respect to the reconstructed

[5] In particular, neutrino lines are redshifted.

[6] We make the approximation that A_{eff} is independent on the azimuth angle $\phi(b, l, t)$ and that the response of the detector has no explicit time dependence.

[7] D^α_{eff} is usually normalized such that its integration over E', $\cos\theta'$ and ϕ' gives 1.

[8] The effective areas provided in Ref. [194] are also summed over all interaction channels.

variables) is given by

$$\frac{\mathrm{d}N_\alpha^i}{\mathrm{d}E'_\nu d\Omega'} = \int_{\Delta_i E} \mathrm{d}E \int_{4\pi} \mathrm{d}\Omega \, \frac{\mathrm{d}N_\alpha}{\mathrm{d}E_\nu \mathrm{d}\Omega \mathrm{d}E' \mathrm{d}\Omega'}, \tag{6.3}$$

where we integrate E over the energy bins $\Delta_i E$ used in Ref. [194].

Because the supplemental material to the sample in Ref. [3] provides no data on $\phi'(t)$ and only a northern/southern hemisphere separation in θ', we also integrate over all ϕ' and θ' (*i.e.* $\Delta\theta'(t)$ and $\Delta\phi'(t)$ include the whole sky). After taking into account all the possible flavour contributions to the flux, we can finally integrate the differential number of neutrinos with respect to the reconstructed energy E' to obtain, in each bin i, the observed number of DM-induced events $N_{\rm DM}^i$:[9]

$$N_{\rm DM}^i(m_{\rm DM}, \tau_{\rm DM} \text{ or } \langle\sigma_{\rm ann}\rangle) = \int_{\Delta E'} \mathrm{d}E' \int_{\Delta\theta'(t)} \mathrm{d}\cos\theta' \int_{\Delta\phi'(t)} \mathrm{d}\phi' \sum_{\alpha=\substack{e,\mu,\tau,\\ \overline{e},\overline{\mu},\overline{\tau}}} P_\alpha \frac{\mathrm{d}N_\alpha^i}{\mathrm{d}E'_\nu \mathrm{d}\Omega'}. \tag{6.4}$$

Whether you have a dependence on $\tau_{\rm DM}$ or $\langle\sigma_{\rm ann}v\rangle_{\rm tot}$ in the above expression depends on the DM scenario that is originally assumed.

The flavor composition P_α of the incoming neutrino flux at the surface of the Earth is set by the neutrino mixing probabilities. Using the expressions that we have obtained in Sec. 4.4.1 in the limit of long baseline oscillations ($L \gg E_\nu/\Delta m_\nu^2$), and using the mixing angles presented in Table 4.1, we have:

$$\begin{aligned} P(\nu_e \leftrightarrow \nu_e) &= 0.551, \quad P(\nu_e \leftrightarrow \nu_\mu) = 0.273 \\ P(\nu_e \leftrightarrow \nu_\tau) &= 0.176, \quad P(\nu_\mu \leftrightarrow \nu_\mu) = 0.351 \\ P(\nu_\mu \leftrightarrow \nu_\tau) &= 0.377, \quad P(\nu_\tau \leftrightarrow \nu_\tau) = 0.447. \end{aligned}$$

A pure flavor state β produced at the source gives $P_\alpha = P(\beta \leftrightarrow \alpha)$ in Eq. (6.4). We show in Appendix D.1 that, depending on the flavor of the neutrinos emitted, the bounds on the DM inverse decay width vary by less than a factor of two. We also show there that the particle/anti-particle content of the flux induces slightly more important variations. For the plots presented in this chapter, we will systematically present the case of a democratic flavour composition (*i.e.* $P_\alpha = 1/6 \ \forall \ \alpha$).

You can find in Fig. 6.2 an explicit example of $\{N_{\rm DM}^i\}$ that we have computed in the case of 100 TeV monochromatic neutrinos produced by the decays of particle DM (*i.e.* DM $\to \nu + X$, where X is any state with negligible mass and no signal contribution in IceCube), assuming equal parts of ν and $\overline{\nu}$ and a "democratic" flavor composition.

6.3 Robust limit estimates

Now that we know how to estimate $N_{\rm DM}^i$ in any circumstance, we can put quick and easy robust bounds in the $(m_{\rm DM}, \tau_{\rm DM})$ or $(\langle\sigma_{\rm ann}v\rangle)_{\rm tot}$ parameter spaces.

[9] We purposely make a fixation on **DM**-induced events, but keep in mind that this expression is used in the same way with any other flux of neutrinos $\mathcal{F}$ (*e.g.* the astrophysical flux in Eq. (6.1)).

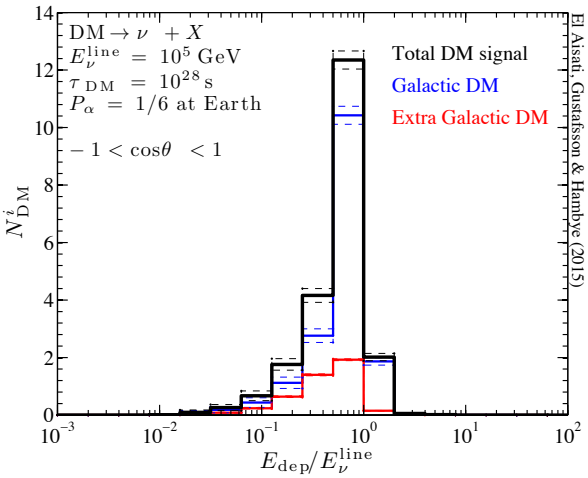

Figure 6.2: Deposited-energy ($E_{\rm dep}$) spectrum for DM decay into monochromatic neutrinos of energy $E_\nu^{\rm line} = 10^5$ GeV. The normalization of the signal corresponds to a DM particle with $m_{\rm DM} = 2 \times 10^5$ GeV and lifetime $\tau_{\rm DM} = 10^{28}$s. A democratic neutrino flavor mixture and equal parts of ν and $\overline{\nu}$ in the flux reaching the surface of the Earth are assumed. The plot shows the total number of events (black curve) after integration over the whole sky and after including propagation effects through the Earth. The galactic contribution (dominant, blue) and the extragalactic DM contribution (red) are also separately shown. The dashed curves enclose the effective area uncertainty range. This range has been obtained by propagating and adding in quadrature the uncertainties presented in [194]. The energy binning is the same as in Fig. 6.1.

We follow the Neyman construction of a confidence interval [206] and start by defining an upper limit $N^i_{\rm limit}$ on the number of Poisson-distributed events in each bin i through the following equation:

$$\sum_{k=0}^{N^i_{\rm obs}} \frac{(N^i_{\rm limit})^k}{k!} e^{-N^i_{\rm limit}} = 1 - q, \tag{6.5}$$

where q represents the confidence level (CL) on this limit. We will systematically work at the $q = 95\,\%$ CL.

To simplify this first approach and still remain conservative, we decide in *this* section to only include the atmospheric backgrounds. The sum of their central values in each bin is represented by the upper edge of the red region in Fig. 6.1, and we scale down these backgrounds to their 2-σ lower edges,[10] so that $N^i_{\rm bkg} = 0.538 N^i_\mu + 0.938 N^i_\nu$. Note that $N^i_{\rm bkg} \leqslant N^i_{\rm limit}$ is always fulfilled in this data set.[11] This being said, we define the lower (upper) bound on the DM lifetime (annihilation cross section) by asking for

[10] The 1-σ uncertainties of the penetrating muon and atmospheric neutrinos are read from Table 1 in Ref. [3].

[11] A violation of this inequality would have been interpreted as an artifact of fixing the

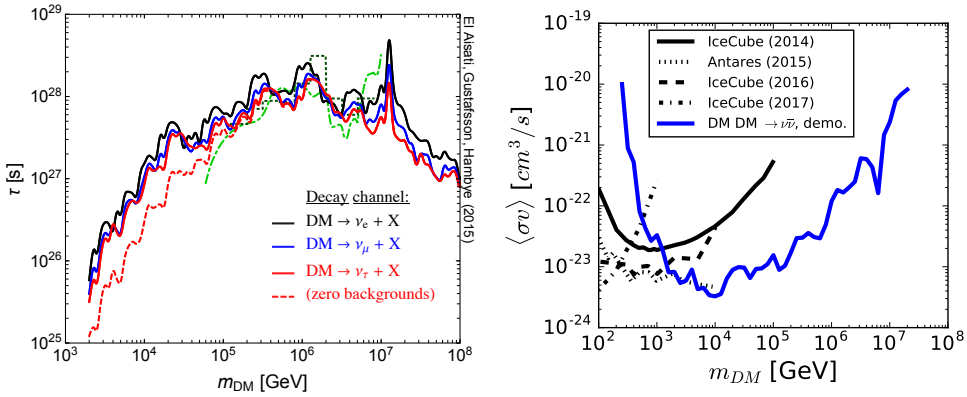

(a) Decaying DM ***(b)*** Annihilating DM

Figure 6.3: *Left*: 95 % CL limits on the inverse decay width of particle DM and on its annihilation cross section assuming monochromatic neutrinos in the final state (galactic contributions only). Solid (black, blue and red) curves are for DM decay or annihilation into pure neutrino flavor states (ν_e, ν_μ and ν_τ, respectively) at production—which, after propagation to Earth, are no longer pure flavor states. The companion final state X in DM(DM) $\to \nu_\alpha + X$ is assumed to be light compared to the DM particle mass $m_{\rm DM}$. The dashed red curve shows the limit for DM $\to \nu_\tau + X$ if no atmospheric background subtraction is made. For comparison, we show the limits on the lifetime derived by Rott, Kohri and Park [136] (90 % CL, green dotted curve) as well as Esmaili, Kang and Serpico [137] (90 % CL, green dashed-dotted curve) who analysed the 3-years high-energy data set from Ref. [2]. Equal parts of ν and $\overline{\nu}$ are assumed for the DM signals. *Right*: Same as Fig. 1.19, with the addition of our "robust" limit estimate (95 % CL), obtained according to Eq. (6.7), and assuming a flavour-democratic composition.

$N^i_{\rm DM} + N^i_{\rm bkg}$ not to overshoot the limit $N^i_{\rm limit}$ in any energy bin i. In other words, for a given spectrum $\{N^i_{\rm DM}(m_{\rm DM}, \tau_{\rm DM}$ or $\langle\sigma_{\rm ann}v\rangle_{\rm tot}\}$, we have

$$\tau_{\rm limit} = \min\{\tau_{\rm DM} \in \mathbb{R}^+ | \forall i : N^i_{\rm DM} + N^i_{\rm bkg} \leqslant N^i_{\rm limit}\} \quad \text{(decay)}\,, \tag{6.6}$$

or

$$\langle\sigma_{\rm ann}\rangle_{\rm tot,\,limit} = \max\{\langle\sigma_{\rm ann}v\rangle_{\rm tot} \in \mathbb{R}^+ | \forall i : N^i_{\rm DM} + N^i_{\rm bkg} \leqslant N^i_{\rm limit}\} \quad \text{(annihilation)}\,. \tag{6.7}$$

We give in Fig. 6.3 the 95 % CL constraints obtained on $\tau_{\rm DM}$ and $\langle\sigma_{\rm ann}v\rangle_{\rm tot}$ according to this prescription, and assuming a monochromatic neutrino line in the final state. We show in Fig. 6.3(a) different cases: pure e, μ and τ flavours with equal parts of neutrinos and anti-neutrinos. For the sake of illustration, we also show the limits if zero background is assumed (thin dashed curve), although this is unrealistically conservative. The limits that we have obtained in the case of a decay are compared to those of Refs. [136] and [137]. In the case of an annihilation, they have been compared to recent Collaboration estimates [116, 228, 120, 117]. The peaks at $m_{\rm DM} = 6.3$ PeV

background—whereas it should be associated with a certain uncertainty—, or as a large downward statistical fluctuation in the data.

(annihilation) and $m_{\rm DM} = 12.6$ PeV (decay) are easily recognizable: they come from the Glashow resonance of 6.3 PeV electronic anti-neutrinos annihilating on electrons in the ice (see Sec. 4.1).

6.4 Improved statistical analysis

Before constraining the properties of particle DM, the priority should first be to search for a signal in the data (which we did not do in the past section). This section is devoted to discussing how we do this in a more involved statistical framework, namely by studying the **profile log-likelihood** of the energy spectrum, and by taking into account energy dispersion effects.[12] Once this is done—spoiler: no significant signal will be found—, we turn to the derivation of improved sets of limits.

6.4.1 Search for a line signal

Method We construct a test statistic by comparing the maximum log-likelihood of the background model to that obtained under the hypothesis of a DM-induced line signal on top of the background [210]. More specifically, to study how the addition of a signal improves the fit, we evaluate

$$\mathrm{TS} \equiv 2 \ln \frac{\mathcal{L}(n_{\rm sig} = n_{\rm sig,best})}{\mathcal{L}(n_{\rm sig} = 0)} \geqslant 0 \,, \tag{6.8}$$

where the Poisson likelihood function is given by

$$\mathcal{L} = \prod_{\text{bins } i} \frac{(N^i_{\rm model})^{N^i_{\rm obs}}}{N^i_{\rm obs}!} e^{-N^i_{\rm model}}, \tag{6.9}$$

and depends on $n_{\rm sig}$ through $N^i_{\rm model}$. Indeed, $N^i_{\rm model}$ comes from the superposition of the backgrounds' contribution and that of the signal:

$$N^i_{\rm model}(n_{\rm sig}, n_{1,2,3}, \Phi_0, \gamma) = n_{\rm sig} N^i_{\rm DM}(m_{\rm DM}, \tau_0) + n_1 N^i_\mu + n_2 N^i_\nu + n_3 N^i_{\rm astro}(\gamma, \Phi_0). \tag{6.10}$$

In Eq. (6.8), the three backgrounds' normalizations $n_{1,2,3}$ and the astrophysical power-law spectral index γ are set to their respective best-fit value (largest likelihood) for each choice of a signal amplitude $n_{\rm sig}$ (*profile* likelihood). We respectively set the normalizations within $N^i_{\rm DM}$ and $N^i_{\rm astro}$ to the (arbitrary) reference points $\tau_0 = 10^{28}$ s or $\langle \sigma_{\rm ann} v \rangle_{\rm tot} = 10^{23} \mathrm{cm}^3/s$ and $\Phi_0 = 2.06$ GeV^{-1}cm^{-2}sr^{-1}s^{-1}. Our best-fit background-alone model (*i.e.* maximum likelihood under the assumption that $n_{\rm sig} = 0$) has $n_1 = 1.36, n_2 = 0.85, n_3 = 1.12$ and $\gamma = 2.62$ in Eq. (6.10). This background model is plotted in Fig. 6.6 and differs from that presented in Fig. 6.1 which, by definition, uses $n_1 = n_2 = n_3 = 1$ and $\gamma = 2.46$.

For each TS determination, we use the full energy range of data. The TS should asymptotically follow a $\frac{1}{2}\delta(\mathrm{TS}) + \frac{1}{2}\chi^2(\mathrm{TS})$ distribution (Chernoff theorem [211]).[13]

[12] The method is similar to, *e.g.*, the Fermi-LAT gamma-ray line search in Ref. [97], briefly summarized in [207].

[13] We constrain all the signal contributions to be non-negative, otherwise we would have cited the Wilks theorem [212].

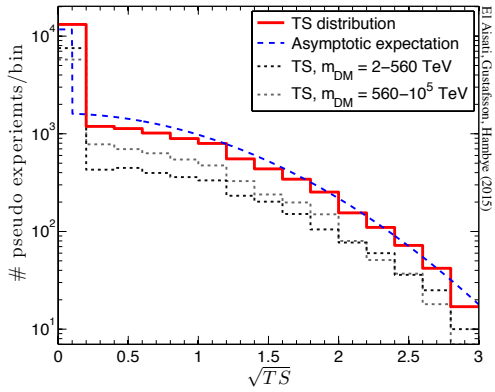

Figure 6.4: Collective TS distribution from 2.02×10^4 monochromatic neutrino line searches (at our 101 used DM masses) in MC generated pseudo data from our NULL background model assumption. The data follows well a $\frac{1}{2}\delta(\mathrm{TS}) + \frac{1}{2}\chi^2(\mathrm{TS})$ distribution (shown by the dashed blue line after multiplication by 2.02×10^4). Dotted grey curves show the TS distribution from $m_{\mathrm{DM}} < 560$ TeV (dark grey) and $m_{\mathrm{DM}} > 560$ TeV (light grey) line searches separately.

Because of low statistics, this behaviour is not guaranteed and we perform 2.02×10^4 Monte Carlo (MC) experiments to verify it. For *each* DM mass tested, we find good agreement between the TS distribution thusly obtained and the asymptotically expected distribution. Figure 6.4 illustrates this with the *collective*[14] TS distribution of our pseudo data realisations generated from the NULL hypothesis.

Results We tested DM masses from 2 TeV to 100 PeV in steps of 5 % in $\log_{10} E_{\mathrm{line}}$ and checked the various flavor and neutrino/anti-neutrino compositions presented in the figures below and in Appendix D.1. No significant line signal was found in this sample. The maximal TS was 2.9—corresponding to a significance of $\sqrt{\mathrm{TS}} \simeq 1.7\ \sigma$—and occurred for a line of pure ν_e at Earth and a DM mass of 45 TeV. In Fig. 6.5, we show a representative plot of the significances as a function of the DM mass (solid red curve) in the case of a democratic flavor composition and equal parts of ν and $\overline{\nu}$ at the source. In this particular setup, the maximal significance is $\sqrt{\mathrm{TS}} \simeq 1.5\ \sigma$ for $m_{\mathrm{DM}} = 44.8$ TeV and $\tau_{\mathrm{DM}} = 1.0 \times 10^{28}$ s. We note that the second largest TS peak, with $\sqrt{\mathrm{TS}} \simeq 1.3\,\sigma$ (for $m_{\mathrm{DM}} = 2.52$ PeV and $\tau_{\mathrm{DM}} = 3.9 \times 10^{28}$ s), is due to the few neutrino events at ~ 1 PeV energies for which a DM origin has been speculated [138, 213, 214, 215, 195, 216, 217, 218, 136, 137, 219, 220, 221].[15]

For the sake of illustration, we show in Fig. 6.6 our best-fit DM spectrum as well as our best line signal at ~ 1 PeV. We have also calculated the TS of the "robust" limits presented in Sec. 6.3 with a minor correction to account for a democratic flavor composition of the DM signal (dashed black in Fig. 6.5). Except at the lowest masses, the

[14] "Collective" means here that we have merged the distributions obtained at different masses.

[15] One more supra-PeV event is seen now in the six-year sample (around 2 PeV) [203].

"robust" limits always have TS values larger than 2.71 (which justifies the terminology that we have adopted). They go below $\sqrt{\text{TS}} = \sqrt{2.71} = 1.65$ at the lowest DM masses because their derivation assumes fixed background contributions—while the profile log-likelihood setup allows for a free normalization of all the backgrounds. At the lowest masses, it did happen that our best-fits prefer lower atmospheric background contribution compared to the fixed NULL model in Fig. 6.1 (upper edge of the blue region).

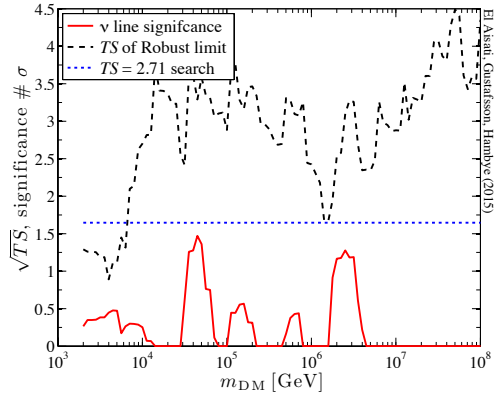

Figure 6.5: Local fit significance of a monochromatic line from DM decays *vs* $m_{\rm DM}$ (solid red curve). For comparison, we also evaluate the TS of the signals at our "robust" limits (black dashed). The blue dotted line is where we have set the threshold for the 95 % CL limit estimates (TS $= 2.71$). We assume a democratic flavor composition and equal parts of ν and $\overline{\nu}$ at the surface of the Earth.

6.4.2 Look-elsewhere effect

The reader should realise that all of the significances that we quote must be understood as **local** significances—that is to say at the *specific* value of the DM mass considered—and that, by addressing our original question "Is there a signal anywhere in the $[1\text{TeV}, 50\text{PeV}]$ energy range?", those significances actually decrease. This effect is commonly known in Statistics as the problem of **Multiple Comparisons**, and as the *look-elsewhere* effect in Particle Physics. It can be summarized as the fact that, by running a series of simultaneous tests at different energies, each of which having a probability α_{local} of making a false detection,[16] you end up with a higher probability of making a wrong detection over the whole range of energies, $\alpha_{\text{global}} > \alpha_{\text{local}}$.

As an example, let us consider the largest $\sqrt{\text{TS}}$ that we have observed, that is to say a local significance of 1.7σ. This number corresponds to a local p-value of 0.089. From MC experiments, we have determined that the global effective number of trials is about 20 for the monochromatic line search.[17] Assuming that the tests are

[16] This is known as the type I error of the test.

[17] This number can also be reproduced with the following rule of thumb [222]: trial number $\simeq \frac{1}{3} \times \frac{\text{energy range}}{\text{energy resolution}} \times \text{significance} \sim 20$.

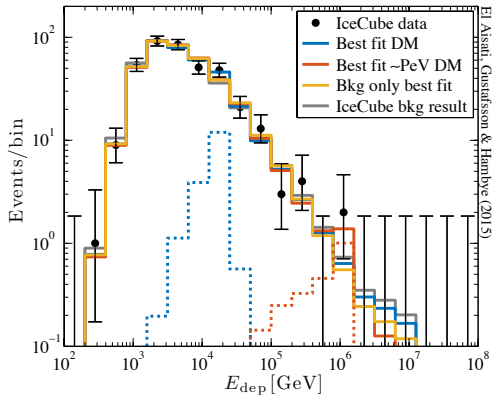

Figure 6.6: Observed deposited-energy spectra compared to: our best-fit model with a decaying DM particle with $m_{\rm DM} = 44.8$ TeV (blue, the DM contribution is in blue-dotted); our secondly best-fit model with a DM particle mass of 2.52 PeV (red, and red-dotted for the DM contribution); our best-fit background-only model (orange); and the IceCube Collaboration's best-fit background model (grey) [3]. We have systematically assumed a democratic flavor composition and equal parts of ν and $\overline{\nu}$ at the surface of the Earth. The significance the two DM signals is less than $1.5\,\sigma$.

independent, you get the following global p-value:

$$p_{\rm global} = 1 - (1 - p_{\rm local})^{20}, \tag{6.11}$$

which actually reduces the significance to $\sim 0.2\sigma$ (globally).

6.4.3 Limits on a line signal

With no significant line detected, we can now derive stringent limits on the DM decay or annihilation rate into a monochromatic neutrino line. We set our 95 % CL upper limits on $n_{\rm sig}$[18] by requiring that the profiled likelihood $\mathcal{L}(n_{\rm sig})$ leads at most to a TS of 2.71 when compared to the maximum value $\mathcal{L}(n_{\rm sig} = n_{\rm sig,best})$.[19] The limits derived in this way are shown in Fig. 6.7, where we also indicate by a thin red line the 99.9 % CL limit (TS = 5.41). It turns out that this method improves the lifetime constraints by *up to* a factor 5 compared to the simple approach used in Sec. 6.3. An improvement was anticipated partly because of the implementation of the astrophysical background. Again, all these limits are obtained assuming a democratic flavor composition and equal parts of ν and $\overline{\nu}$, so that $P_\alpha = 1/6$. Other variants are presented in Appendix D.1.

We also compare in Fig. 6.7 the observed limits with the expected sensitivity. For data with low statistics, large fluctuations can naturally appear between different data realisations and this comparison becomes particularly relevant. We have generated 200 MC data sets from the Null hypothesis at each DM mass and repeated

[18] This upper limit on $n_{\rm sig}$ is easily converted into a limit on $\tau_{\rm DM}$ or $\langle\sigma_{\rm ann} v\rangle_{\rm tot}$ according to the scenario under consideration.

[19] In Sec. 6.4.4, we verify that this method has the statistically correct 95 % coverage.

every single time the procedure explained in the previous paragraph. As a result, a distribution of limits is produced at each mass. The expected 68 % (yellow) and 95 % (green) containment bands of the limits are shown together with the median expectation (dashed black curve). A straightforward propagation of the effective areas uncertainties induces a rescaling of the limits of 30 % at the most, confirming our expectation that the statistical uncertainties should dominate.

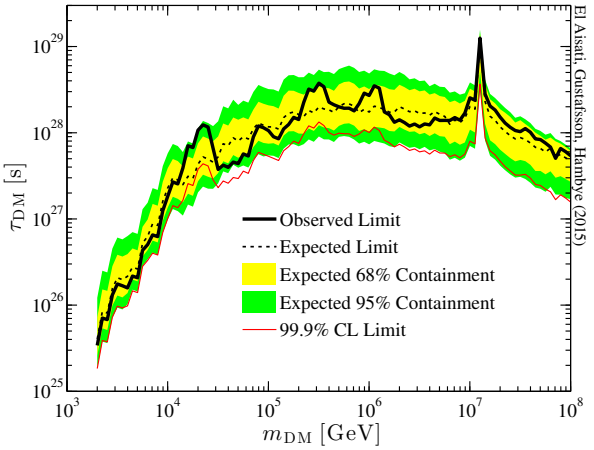

Figure 6.7: 95 % CL lifetime limits (solid curve) on the DM particle decay lifetime into monochromatic neutrino. Expected sensitivity reach (dashed curve) and its 68 % (yellow) and 95 % (green) containment bands are also shown. The thin red line shows shows the 99.9% CL limits. For the incoming neutrino flux, a democratic flavor composition and equal parts of ν and $\overline{\nu}$ is assumed at the surface of the Earth.

You will notice that the level of sensitivity that we have derived in the decaying DM scenario reaches competitive values in comparison to the latest official estimates by the IceCube Collaboration [118, 193] and those of other groups [136, 137] (see Fig. 6.8). Starting from $m_{\rm DM} \sim 10$ TeV, this statement is also true if we take into account the sensitivity reach of γ-ray telescopes [111, 112, 114]. This observation is far from innocuous and a **whole chapter** of this thesis has been dedicated to the discussion of possible implications, namely the chances to see a "double-barreled smoking gun" from DM decays in the near future. You are kindly referred to Chapter 3 if you want to read more on this. This paragraph constitutes the main conclusion of this chapter. You can see the next two sections as refined discussions.

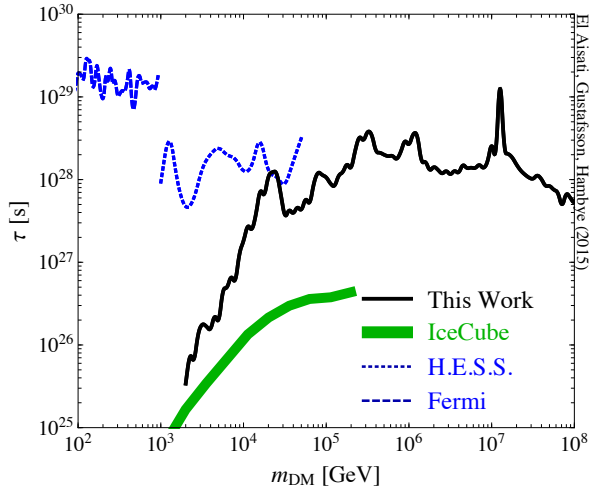

Figure 6.8: Comparison of the 95 % CL lifetime limits on $\Gamma_{\nu\gamma}$ from several groups. From Fermi-LAT [111] (blue, dashed) and H.E.S.S. [112, 114] (blue, dotted) using gamma-ray data compared to the neutrino line bounds derived in this study (solid black) as well as previous IceCube limits [118], that were obtained with 22 strings of the detector and a livetime of 276 days. Note that a more recent limit from the IceCube Collaboration has recently been presented (2016), and is slightly better than our estimates—closely following its behaviour—as it uses the 6-year extension of the Mese sample [223].

6.4.4 Coverage probability

We have claimed throughout this chapter that our limit estimates were given at the 95 % CL, meaning that the probability to reject the presence of a signal when in fact there is one is set to 0.05 (type I error). However, a discrepancy between this claimed value and the *actual* probability of wrongly excluding a signal may arise if, for some reason, some of the assumptions behind the likelihood method were not met.

To investigate the *actual* coverage probability of our analysis, we have simulated 10^5 MC realisations of a DM line signal on top of the Null hypothesis, looking at 101 DM masses between 2 TeV and 200 PeV. The monochromatic neutrino lines were randomly given a signal strength $n_{\rm sig}$ between one order of magnitude larger or smaller than the derived limit $n^{\rm IC}_{\rm sig,\,limit}$, and we repeated the likelihood procedure exposed above for each one of these realisations. The corresponding limit estimate $n^{95\,\%\,\rm CL}_{\rm sig,\,limit}$ and TS were then stored to produce Fig. 6.9.

The interpretation of that figure is simple: the horizontal line separates the region of the plot where the signal was wrongly rejected (top, $n_{\rm sig}/n^{95\,\%\,\rm CL}_{\rm sig,\,limit} > 1$) from the region where the confidence interval correctly keeps it (bottom, $n_{\rm sig}/n^{95\,\%\,\rm CL}_{\rm sig,\,limit} < 1$). For signal normalisations larger than the limits that we have derived from the IceCube data ($n_{\rm sig}/n^{\rm IC}_{\rm sig,\,limit} > 1$), we find a coverage of 93 %, which is in rather good agreement with our stated 95 % CL. For $n_{\rm sig}/n^{\rm IC}_{\rm sig,\,limit} < 1$, the statistical coverage reaches

99 %, meaning that our statistical analysis provides there a *safe* overcoverage—this is expected for low signal strengths. For the sake of visibility, we only show in Fig. 6.9 the output of the first 10100 MC realisations and color-code each of them with the corresponding TS value. Also, we assigned points with $\sqrt{\mathrm{TS}} > 6$ a value of 6.

6.4.5 Constraints on other line-like signals

The methods described in Secs. 6.4.1 and 6.4.3 are general in the sense that the presence of *any* signal in the sample can be tested to see if it significantly improves the fits. This is in particular true for the category of line-like spectra. In practice, we will parametrize them as a single power-law with exponent n. For the decay scenario, we use:[20]

$$\frac{\mathrm{d}N}{\mathrm{d}E} = \frac{2^{n+1}(n+1)}{m_{\mathrm{DM}}} \left(\frac{E}{m_{\mathrm{DM}}}\right)^n \Theta_{\mathrm{H}}(m_{\mathrm{DM}} - 2E)\,, \tag{6.12}$$

where the sharp spectral cut-off at $E = m_{\mathrm{DM}}/2$ is parametrized by the unit step function $\Theta_{\mathrm{H}}(m_{\mathrm{DM}} - 2E)$. This expression works as a good proxy for several physical scenarios: it appears in the cases of DM decay into three-body final states induced by effective operators (where $n \approx 2-3$, see Chapter 3) or when DM particles decay into an intermediate state which, for instance, promptly decays into neutrinos to form a "box-shaped" spectrum (in that case, $n = 0$) [107]. For *gamma-ray* signals, final state radiation and internal bremsstrahlung processes give spectra of this form too (with $n \approx 0 - 3$ [108, 109, 110]).

The spectra in Eq. (6.12) are normalized so as to give one neutrino in the final state.[21] We derive limits for the cases with $n = 0, 1, 3$ and compare them with the pure monochromatic line signal limit in Fig. 6.10. Quite obviously, the softer the spectrum, the less stringent the limit.

[20] Equivalent spectra can be obtained for the annihilation scenario with the simple substitution $m_{\mathrm{DM}} \to 2m_{\mathrm{DM}}$.

[21] This can easily be corrected if there are actually more, like in the case of the box spectrum (four neutrinos in the final state).

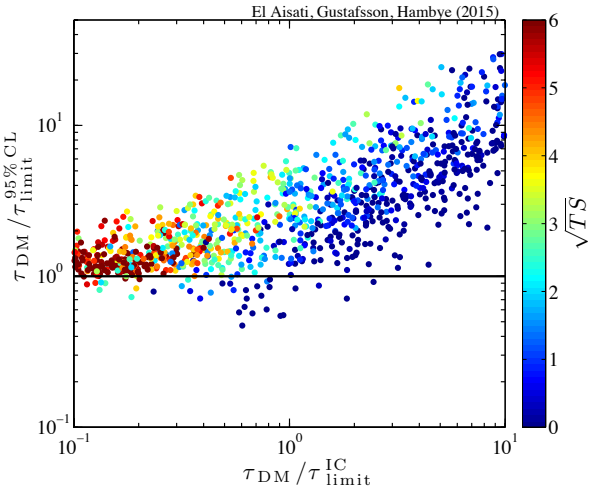

Figure 6.9: Comparison of the 95 % CL lower limit $\tau^{95\,\%\,\mathrm{CL}}_{\mathrm{limit}}$ to the true DM lifetime value τ_{DM} for a set of 100 MC realisations (for each 101 DM masses tested between 2 TeV and 200 PeV). Each realisation is from a model with a DM particle lifetime τ_{DM} randomly drawn between 0.1 and 10 times the lifetime limit derived from the IceCube data $\tau^{\mathrm{IC}}_{\mathrm{limit}}$. The color of each point gives the significance $\sqrt{\mathrm{TS}}$—*i.e.* the number of standard deviations σ—of the injected DM model. Points above the solid horizontal line represent realisations where the lower lifetime limit covers the true injected value. For the DM signals, a democratic flavor composition and equal parts of ν and $\overline{\nu}$ were assumed at the surface of the Earth.

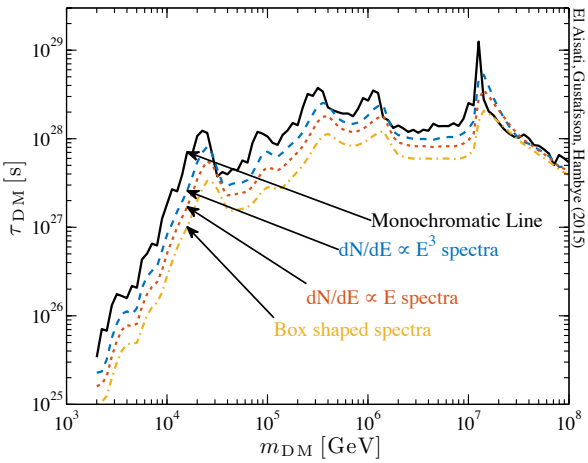

Figure 6.10: 95 % CL lifetime limits on various neutrino line-like signals from DM decay: monochromatic line, internal Bremsstrahlung ($dN/dE_\nu \propto E_\nu$ and $\propto E_\nu^3$) and box-like spectrum (dN/dE_ν = constant). Democratic flavor composition and equal parts of ν and $\overline{\nu}$ are assumed after propagation to the surface of the Earth.

6.5 What should you take away from this chapter?

This chapter was dedicated to a search for DM-induced signals in the MESE sample developed by the ICECUBE Collaboration. Instead of looking at the angular distribution of the data, the search consisted in studying its energy distribution so that the potential presence of line(-like) features—who constitute the clear signs of the DM existence and capture interesting aspects of the Particle Physics of DM—could be highlighted. This type of searches, quite unpopular with neutrino data, has shown to be particularly effective for γ-lines.

The statistical method used to conduct the search consisted in studying the log-likelihood ratio of the NULL hypothesis and a selection of alternative hypotheses. By alternative *hypotheses*, we mean that we have scanned a large range of masses (from 100 GeV to 10^8 GeV) and tested for several DM decay channels. There was no clear evidence in the data for any of the tested signals (Sec. 6.4.1). We have therefore derived sensitivity estimates on the basis of the behaviour of the profiled likelihood (Sec. 6.4.3). Our findings were very encouraging, especially regarding the scenario of DM decay: the results were up to more than an order of magnitude better than the latest official limits from the ICECUBE Collaboration—at the time—, and clearly show the possibility to have competitive—or better—sensitivity estimates in comparison with gamma-ray line(-like) searches in some region of the parameter space (in this case $\gtrsim 10$ TeV). This means that a neutrino line could be discovered before a gamma-ray line, and also means that it could be possible to test out models that involve the two types of lines with a similar energy, and see if a "double detection" could be around the corner. This result has in particular motivated the work presented in Chapter 3.

CHAPTER 7

A search for neutrino spectral features induced by DM at DeepCore

Even if we have enormously learned from the study presented in Chapter 6, the uninformed reader has actually been given *but* a foretaste of what analysing the IceCube data was supposed to look like from A to Z. We have mainly relied on ready-to-use event distributions and effective areas, and these ingredients were very handy for the outsiders that we were. However, they have constrained us in some aspects of the analysis, like the knowledge—and potential investigation—of angular distributions.

By the end of 2015, we became aware of a one-year cascade sample that had been developed a little earlier during the PhD thesis of Henric Taavola, a previous IceCube member [227, 228]. His cascade sample had the nice feature that it contained events seen with the DeepCore detector, and therefore allowed to probe the presence of spectral features at small DM masses (as low as $m_{\mathrm{DM}} \sim 10$ GeV), unlike the Mese sample (see Chapter 6). We ended up writing a proposal to the Collaboration so that we could have access to and work on this newer sample as *associate members*. Besides being able to go down in DM masses, the appeal of this project was the possibility to increase the statistics involved by constructing a 5-year sample, to work on an event-by-event basis, to have the freedom to choose whether or not to include angular informations in the fits (especially interesting for a DM annihilation), and to work on a sample involving little atmospheric muon background.

Besides processing 5 years of data (*i.e.* from 2012 to 2016), we have also processed $\sim$ 100 times more simulation files than Henric did to avoid as much as possible suffering from low-statistics PDFs. We have reused a great part of his original processing scripts and updated them so that they could handle post-2011 files (in particular, the new filters and newer software). We will not further comment on this aspect here, but let us mention that a considerable time was dedicated to debugging, something which—to make a confession—we did not expect in these proportions.

As we outline the data selection procedure and its optimisation, which have basically been arranged by Henric, most of the care will consist in checking that the data and the simulations behave as in 2011—in other words, that the original cuts still make sense for 2012+. Beware that our approach will differ at the final stage of the data selection as we keep a feature-oriented perspective.

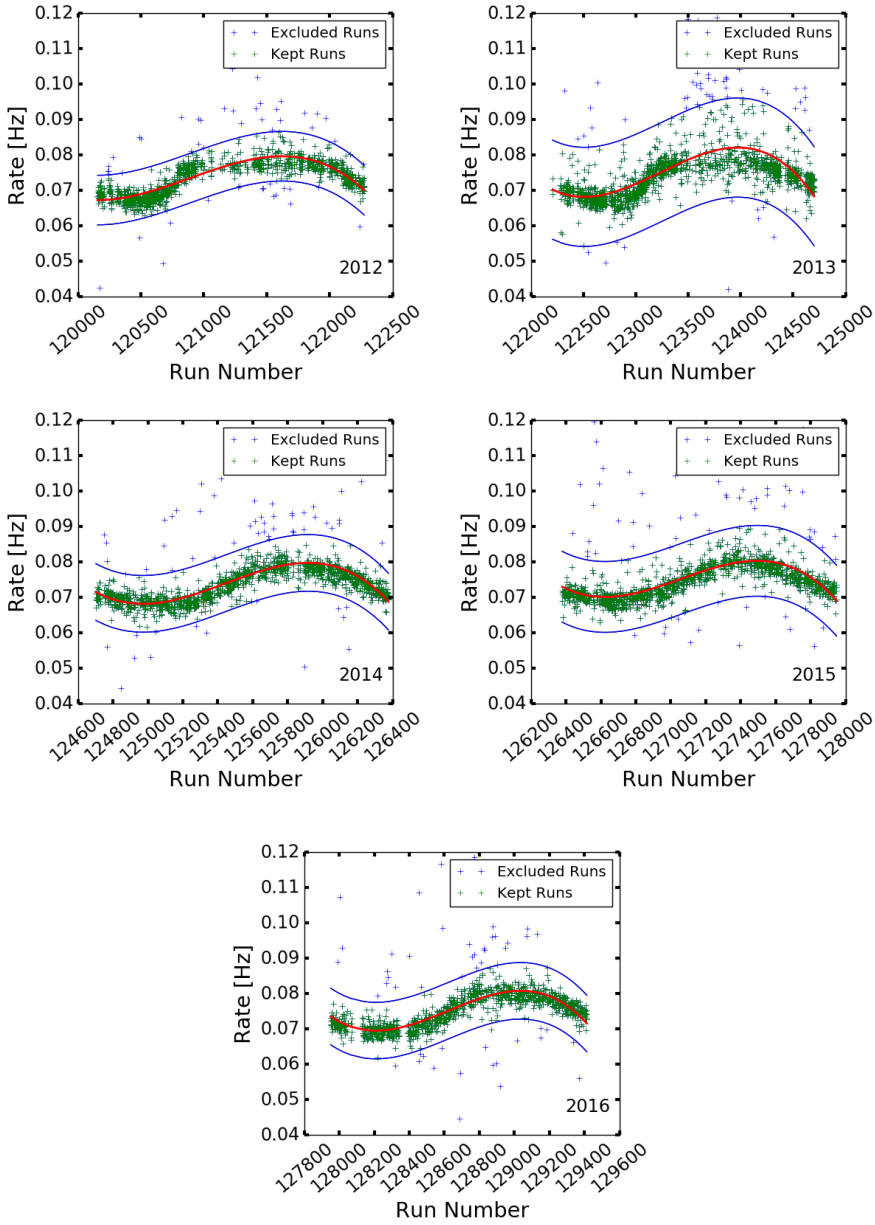

Figure 7.1: Observed rate of events at LEVEL 3 as a function of run number ($\propto$ time). Different subfigures correspond to different years (see bottom right). The runs to the far left of the x-axis correspond to the earliest runs in an "ICECUBE year", which typically starts around the month of May. The seasonal variation is clearly visible, with more (less) events observed during the austral summer (winter). As explained in the text, this effect is directly correlated with the density variations in the atmosphere. The red curve corresponds to a cubic regression fit—giving a general behaviour—and the region delimited by the blue curves corresponds to a 95 % containment band around that fit. The runs falling outside of the blue edges have been removed.

We start off this chapter with a presentation of the data sample and of the simulations. The data selection is then exposed, and we finally discuss the sensitivity of our analysis. Beware that, because the unblinding of this analysis is in progress, we will *not* show *observed* limits at any point. These and the work that is about to be exposed, will be submitted for publication together with the IceCube Collaboration.

7.1 The Data

We use in this chapter the data collected from the 15th of May 2012 to the 11th of May 2017 with the IceCube detector in its 86-string configuration. As explained in Sec. 5.3.2, this data is passed through triggers and online filters at the South Pole and is therefore available at Madison as Level 2 data. It is organized in *runs* of 8 hours, each of which is assigned a number, as well as the label "good" (= can be used) or "bad" (= can not be used). For instance, test runs and runs during which lots of DOMs were simply not working receive the "bad" tag.[1] Besides looking for good runs, we have removed those runs which displayed an event rate much higher or much lower than the observed general tendency. This removal is illustrated in Fig. 7.1.[2]

The existence of a periodic variation of the rates is obvious in Fig. 7.1. This modulation coincides with the seasonal variation of the temperature in the atmosphere. To understand why, recall that [229]:

- among the products of the cosmic-ray interactions with the nuclei present in the atmosphere, muons are the most abundant at the sea level and also the most penetrating ones (neutrinos aside);
- the propagation of pions and kaons down the atmosphere is a competition between interactions with the nuclei in the atmosphere—which produce other pions and kaons of lower energy—and decay—from which the muons are mainly created.

Since the atmosphere at the South Pole is warmer and less dense during the austral summer, pions and kaons find less targets to collide with—probabilistically speaking—, getting more time to decay. As a consequence, more muons trigger IceCube in that period of the year. Conversely, there are less muons reaching the ground during the austral winter because the atmosphere is denser, making collisions more likely for the pions and kaons. This effect is clearly observed in Fig. 7.1.

Unless stated otherwise, let us stress that all the plots in this chapter consider a fraction of $\sim 0.7\%$ of the real data—what we will refer to as our *burnsample*. Typically, the reason for using a burnsample as we go on with the filtering procedure and the definition of cuts is that we do not want to (even unconsciously) bias any of the choices that we make. We also use the burnsample to "control" the quality of the simulations that we use, in the sense that, since we know that the data is dominated by the

[1] This information is available in a series of files in the data warehouse at Madison.

[2] You may notice that the rates on the y-axis are "small": this is because we have sorted the runs according to this criterion once at Level 3 (see Secs. 7.3.2 and 7.3.3). In comparison, the trigger rate of the IceCube detector is around 2.5 kHz.

atmospheric backgrounds at the earliest stages of the analysis. In other words, to make sure that we understand our simulations well—they will be central to the extraction of the sensitivity of our analysis in Sec. 7.4—, we will systematically compare the distribution of all the variables that we use at different levels of the analysis with those of the burnsample.

7.2 Data simulation

Again, data simulations will be useful for two things: checking that we actually understand the data—that we know to be background-dominated until late in the analysis—and getting the probability density functions (PDFs) needed for the actual DM analysis. In our case, these PDFs will consist in the reconstructed energy and angular distributions (with respect to the GC) of the atmospheric background and DM-induced events.

As far as this thesis is concerned, we want to make it clear that we have *not* generated the simulation events ourselves but have rather relied on the Level 2 files *already provided* at the data warehouse in Madison. We however believe it useful to add a few words on how they are produced.

The simulation of an event is basically split into four tasks which are performed individually by different MC programs. These tasks consist in: particle generation, particle propagation, photon propagation, and detector response generation.

7.2.1 Event Generators

The generation of **muon events** is done with Corsika [196],[3] which is a code that simulates the air showers produced by the collision of cosmic rays onto the nuclei present in the terrestrial atmosphere. Corsika tracks the propagation in the atmosphere of all the particles participating to the shower until they decay, interact with a nucleon or reach the ground level. A slightly modified version of Corsika called dCorsika has been developed at IceCube for a suitable use with the IceCube software [197].

In order to generate showers, dCorsika needs to be fed a cosmic-ray composition and an energy spectrum. The most popular models used at IceCube are the Polygonato model by Hörandel [230] and the 5-component model [231]. They are both typically given an energy spectrum going like $\sim E^{-2.6}$ as an input, but the main difference resides in the fact the first of these models treats all of the elements up to Fe, while the second only takes into account the 5 most abundant elements (H, He, N, Al, and Fe). In practice, the Polygonato model does not describe our data very well—especially "normalisation-wise"—[4] and the 5-component model cannot even be considered as a "realistic" one. Thankfully, it is possible to reweigh the individual simulation events to any other flux model of our choice and we opted for the GaisserH3a flux model by T. Gaisser [231], as it gives a better description of our data. To take into account the

[3] COsmic Ray SImulation for KAscades.

[4] With our sample, we have noticed a discrepancy of about 20 %.

Sample	Energy range	Type
11499	LE	baseline
11808	LE	baseline
11865	LE	baseline
11905	LE	baseline
11926	LE	baseline
11937	HE	baseline
11943	LE	baseline
12268	LE	baseline
12161	LE	baseline
12025	LE + HE	baseline
12388	LE	baseline

Table 7.1: CORSIKA samples used in the analysis. The identification number of the sample is reported in the first column, and the range of energy considered for the primaries in the second column (LE $\equiv$ [600 GeV $-$ 10^5GeV], HE $\equiv$ [10^5GeV $-$ 10^{11}GeV]). The third column says whether the sample was used as a baseline or for the estimation of systematic uncertainties.

fact that multiple muon events may come from the same shower,[5] we have also used the DIPLOPIAWEIGHT correction weight. The CORSIKA baseline samples used in this analysis are presented in Tab. 7.1 together with the energy range that they consider for the primary particles.

The **neutrino events** are generated with NUGEN [198][6] and GENIE [199]. At ICECUBE, the latter is typically used to represent low-energy neutrinos ($\lesssim$ 190 GeV) and the former to represent neutrinos beyond 100 GeV.[7] To make the transition as smooth as possible, we have defined as a transition region the energy range from 190 to 195 GeV, and corrected the weight of each NUGEN (GENIE) event by a linearly increasing (decreasing) function in that range. At 190 GeV and 195 GeV, the value of this function is respectively given by 0 and 1 when the event comes from the NUGEN generator (1 and 0 in the case of GENIE). The behaviour of these corrections is illustrated in Fig. 7.2.

As with dCORSIKA, these generators use a non-physical neutrino flux model as an input. The atmospheric neutrino event distributions are obtained by reweighing simulation events to the Honda (2006) flux [232] using the NEWNUFLUX library [233]. Likewise, the distribution of DM-induced events are obtained by reweighing those same simulations to the DM-induced neutrino flux. Because it has extensively been

[5] This is especially true for down-going muons.

[6] Neutrino-Generator.

[7] To avoid a loss of statistics at high energies (typically $\gtrsim$ 1 TeV) and have the smoothest PDFs possible for our DM analysis in Sec. 7.4, we have systematically taken NUGEN files generated with a flux $\propto E^{-1}$, as this was the hardest spectrum that we could find.

done, we specifically discuss how we assign weights to neutrino events in Sec. 7.2.2.

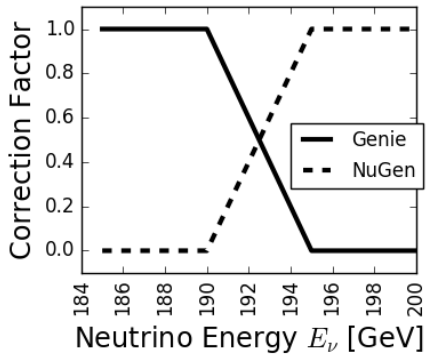

Figure 7.2: Correction factor applied to the weight of a neutrino event with an energy in the range $190 - 195$ GeV, depending on whether this neutrino comes from the NuGen or Genie generator. Outside of this range, we *either* only keep events coming from Genie ($E_\nu < 190$ GeV) or from NuGeN ($E_\nu > 195$ GeV).

Before moving on, let us stress again why it is important for us to have a good understanding of the backgrounds (and why we therefore have processed many simulation files). The main difference with the analysis of Henric [227, 228] is that we do not just aim at studying the angular distribution of events with respect to the GC,[8] but also want to include spectral information[9] into the fits and have smooth estimates of the corresponding *2-dimensional* distributions (or PDFs). Since the detector's response is isotropic with respect to azimuth (over a long period of time), Henric was able for his analysis to produce smooth estimates of the distribution of events—again, only in terms of the angle ψ—"simply" by scrambling those events with respect to their azimuth and reassigning them the corresponding new ψ. For our 2-dimensional PDFs, this procedure would only smooth the behaviour of the PDFs with respect to ψ but not the energy.[10] This is why simulations (atmospheric muons, atmospheric neutrinos, DM-induced neutrinos) are mandatory for us and we will rely on them until the end of this chapter.

7.2.2 Reweighing Neutrino Events

In order to avoid wasting time and energy by generating massive amounts of unsuccessful neutrino events,[11] the interaction probability of any event coming out of a generator is artificially set to 1. As a consequence, each simulation event needs to be

[8] To see how ψ is defined in terms of azimuth and zenith, see Appendix C.1.

[9] In other words, the reconstructed energy.

[10] The response of the detector is not uniform with respect to energy, which is why we cannot play the same smoothing trick.

[11] "Unsuccessful" in the sense that these neutrinos would fail interacting in or around the detector.

reweighed afterwards by the total interaction probablity $P_{\text{tot, int}}$ so as to correctly reproduce the reality. Besides, the fact that the generation spectrum is set to an arbitrary function (typically $\propto E^{-\gamma}$ with $\gamma = 1$ or 2) and *not* to the flux of interest (atmospheric flux or specific DM-induced flux) also needs to be corrected for. In that perspective, each event is assigned a specific weight, called OneWeight, defined as:

$$\text{OneWeight} = \left(\frac{P_{\text{tot, int}}}{E^{-\gamma}}\right) \int_{E_{\text{min}}}^{E_{\text{max}}} E'^{-\gamma} dE' \cdot A \cdot \Omega, \tag{7.1}$$

where E_{min} and E_{max} give the range in which the neutrino energies are generated, A denotes the generation surface, and Ω the generation solid angle. OneWeight is given in units of GeV cm^2 sr and, as you can see, encodes practical parameters of the simulation which the user does not necessarily need to know. The fact that you divide by $E^{-\gamma}$ in Eq. (7.1) can be seen as "bringing back the generation spectrum to a flat one". Given an ensemble of N generation events and your favourite flux model $\mathcal{F}$ of neutrinos and anti-neutrinos at the surface of the Earth, a single MC event i corresponds to a rate

$$w_i = \frac{\text{OneWeight}}{N} \times \frac{d\mathcal{F}(E_\nu, \Omega_\nu)}{dE_\nu \Omega_\nu} \tag{7.2}$$

of "physical" events in the detector.[12] Note that the effect of Earth absorption is already taken into account in $P_{\text{tot, int}}$. The impact of the neutrino oscillations through the Earth on w_i is however estimated separately, see the NuCraft package [179].

7.2.3 Propagation and Detector Response

The propagation of muons and photons is respectively handled with the Mmc [234][13] and Ppc [235][14] codes, both developed by IceCube. The detector response is simulated by building in each DOM the PMT waveform associated to the photons who have reached it (output of Ppc) and simulating the DOM response. As this is done, random and correlated noise are also added. To produce the Level 2 files, the PMT outputs are then passed through the same coincidence logic (see Sec. 5.3.2), triggers and filters as those used online at the South Pole for the real data.

7.3 Data selection

As just said, all of the data and simulation files go through the very same selection procedure. Because of the high event rates initially involved, the strategy is to start with a cleaning of the events based on fast and easy reconstruction techniques, mostly involving simple geometrical variables. Once the rates are reduced, *i.e.* once Level 3 is reached, more involved and time-consuming techniques can be applied. Quite obviously, in these successive steps, care must be taken to cut away as little as possible of the signal.

[12] If the flux is expressed separately for neutrinos and anti-neutrinos, and assuming equal proportions of neutrinos and anti-neutrinos from the simulations, N must be divided by two.

[13] Muon Monte Carlo.

[14] Photon Propagation Code.

You may notice that the structure of this section is very similar to that in Ref. [227]. This choice was made to ease the comparison, as our personal contribution mainly consists in checking the stability of the procedure developed by Henric for the data samples of 2012+ and our (much more abundant) MC simulations.

7.3.1 Triggering and Filtering

We remind you that the event selection starts with the SMT3 DeepCore trigger and is followed by the DeepCore filter (see Sec. 5.3.2).[15] The **SMT3 trigger** imposes that 3 HLC hits at least are recorded in DeepCore within a time window of 2.5 μs.[16] When this happens, the time of the first HLC hit is used to define a readout window of $\pm 6\mu$s for which all recorded hits—even from non-DeepCore strings—are saved. The rate at which IceCube triggers is around $\sim$ 2.5 kHz. The *rôle* of the **DeepCore filter** is to keep those events which seem to originate from the DeepCore region, and so greatly reduces the atmospheric muon background (about a factor of 10). The way that this filter works is by defining a "center of gravity" (COG) of the N_{ch} HLC hit DOMs observed in DeepCore as:

$$\vec{x}_{\text{COG}} \equiv \frac{\sum_{i=1}^{N_{ch}} m_i \vec{x}_i}{\sum_{i=1}^{N_{ch}} m_i}, \tag{7.3}$$

where m_i and $\vec{x}_i$ respectively denote the amplitude of the hit at DOM i and the position of DOM i. From there, an average time t_{COG} is assigned to $\vec{x}_{\text{COG}}$, and both are compared to the position and time of every single hit DOM to derive a velocity. If, for more than one DOM, the velocity calculated in this way is close to the speed of light, chances are the event was a muon passing by, and the DeepCore filter therefore rejects it. The rate of events at this stage is $\sim$ 17 Hz.

To avoid a possible source of confusion in the terminology, let us clarify that we denote by "Level X variables" those variables computed at Level X-1 that are used to filter our samples from Level X-1 to Level X.

7.3.2 From Level 2 to Level 2′

This intermediate step is performed to make sure that enough DOMs on enough strings have fired so that a meaningful event reconstruction can take place. In practice, a number of at least eight hit DOMs on at least four strings is required. The rate of events is now reduced to ~ 8.5 Hz.

7.3.3 From Level 2′ to Level 3

To build the Level 3 sample, we do *not* use complicated and time-consuming reconstruction techniques yet. A series of 10 *simple* variables was selected to choose whether or not an event is worth being kept—through a straight cut—up to Level 3:

[15] In other words, the triggers and filters respectively take the Level 0 data to Level 1, and the Level 1 data to Level 2.

[16] We use an extended definition of DeepCore where the three outer strings of the In-Ice array are used as a veto region, see Fig. 5.2.

- **LineFit Speed**: this is the speed obtained by fitting a straight line (= track) through the cleaned hit map with the *improved LineFit* algorithm.[17] Cascades—which we are interested in—have a speed close to zero while track-like muon events are more likely to have a speed close to the speed of light. The cut on this variable was originally set so that events with a speed strictly larger than 0.22m/ns are removed. As you can see from Fig. 7.3, this choice still makes sense for the years that we have processed;

- **Tensor of Inertia Eigenvalue Ratio**: for this variable, the cleaned hit map of an event is represented as an ellipsoid of which the principal axes give its eigenvalues $I_{i=1,2,3}$. By defining the following ratio:

$$R_{\text{TOI}} \equiv \frac{\min(I_1, I_2, I_3)}{\sum_{i=1}^{3} I_i}, \tag{7.4}$$

  a perfectly spherical hit map would lead to $R_{\text{TOI}} = 1/3$, while elongated (= track-like) events lead to values closer to 0. Events with $R_{\text{TOI}} \geqslant 0.10$ are kept for further processing;

- **RT Veto**: this variable gives the maximum number of causally connected hits found in the veto region[18] *before* the time of the first hit observed in the cleaned hit map. The larger this number, the more likely it comes from an atmospheric muon event. We select events with a maximum of two such causally connected hits;

- **NVetoAbove**: this variable returns the number of registered hits in the veto region were registered above and before the first trigger hit of an event. We select events with maximum three of those hits;

- **COGSplitDiff**: for this variable, the cleaned list of hits is reorganised from the earliest to the latest and then split into two halves.[19] Following Eq. (7.3), each half is then attributed a COG and the distance between these two COGs defines COGSplitDiff. This distance is expected to be smaller for cascades than for tracks. We systematically reject events for which this separation is larger than 100 m;

- **COGzSplitDiff**: this variable is the same as that exposed in the previous bullet point with the difference that it has been projected onto the vertical axis (see Fig. C.1). The cut is placed at 70 m;

- **|FirstHit-COG|**: this variable corresponds to the distance between the first hit and the COG of the cleaned hit map. As you can see from Fig. 7.5, we keep events for which |FirstHit-COG| $\leqslant$ 175 m;

- **ZFirst**: gives the z coordinate of the very first hit in the cleaned hit map. We keep events with $z \leqslant 150$ m;

[17] More details on the reconstruction algorithms can be found in Sec. 5.2. of Ref. [227].

[18] Remember that we use the three outer layer of the IN-ICE array as a veto region.

[19] If the number of hits is odd, it is the "latest" half that inherits of an extra hit.

- **QR6**: this variable is defined as the ratio of the charge collected by all the DOMs during the first 600 ns of the event and the total collected charge Q_{tot}:

$$\text{QR6} = \frac{\sum_{i=0}^{i=600\text{ns}} Q_i}{Q_{\text{tot}}}. \tag{7.5}$$

  We typically expect cascade events to have a larger QR6 than track events. We systematically keep events with QR6 > 0.45;

- **FillRatio**: FillRatio is defined as the ratio of the number of DOMs in the cleaned hit map and the number of DOMs in the smallest sphere containing that cleaned hit map. According to this definition, perfectly spherical events have a FillRatio of 1, and the more elongated the event, the smaller this variable. In order to avoid cutting too much in the signal region (see Fig. 7.5), the cut is set at 0.03 (keeping everything above).

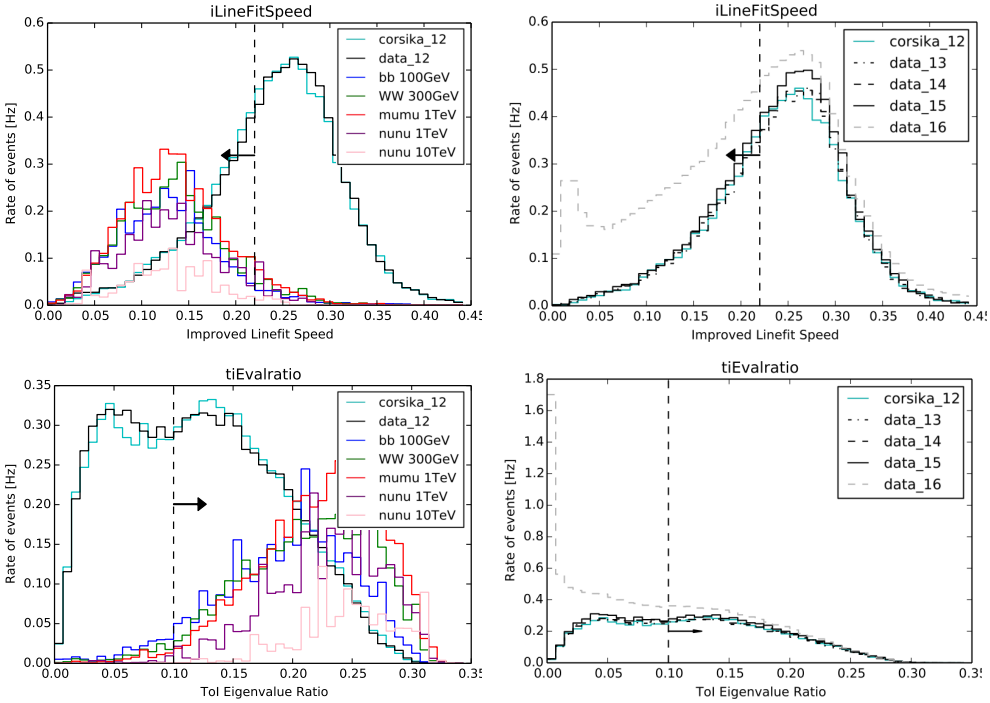

Figure 7.3: Distribution of the LEVEL 3 variables and cuts. On the left, the distribution corresponding to the neutrinos induced by the $b\bar{b}$100 GeV, WW300 GeV, $\mu^+\mu^-$1 TeV, $\nu\bar{\nu}$1 TeV and $\nu\bar{\nu}$10 TeV DM annihilation channels are respectively shown in blue, green, red, purple, and pink. The burnsample and the muon backgrounds respectively correspond to the black and cyan curves. The same variable distributions are presented on the right, but for the burnsample of subsequent years (2013–2016). The cyan curve is identical to that on the left. The vertical dashed lines and the black arrows represent the cuts. The speed in the top row is given in units of m/ns.

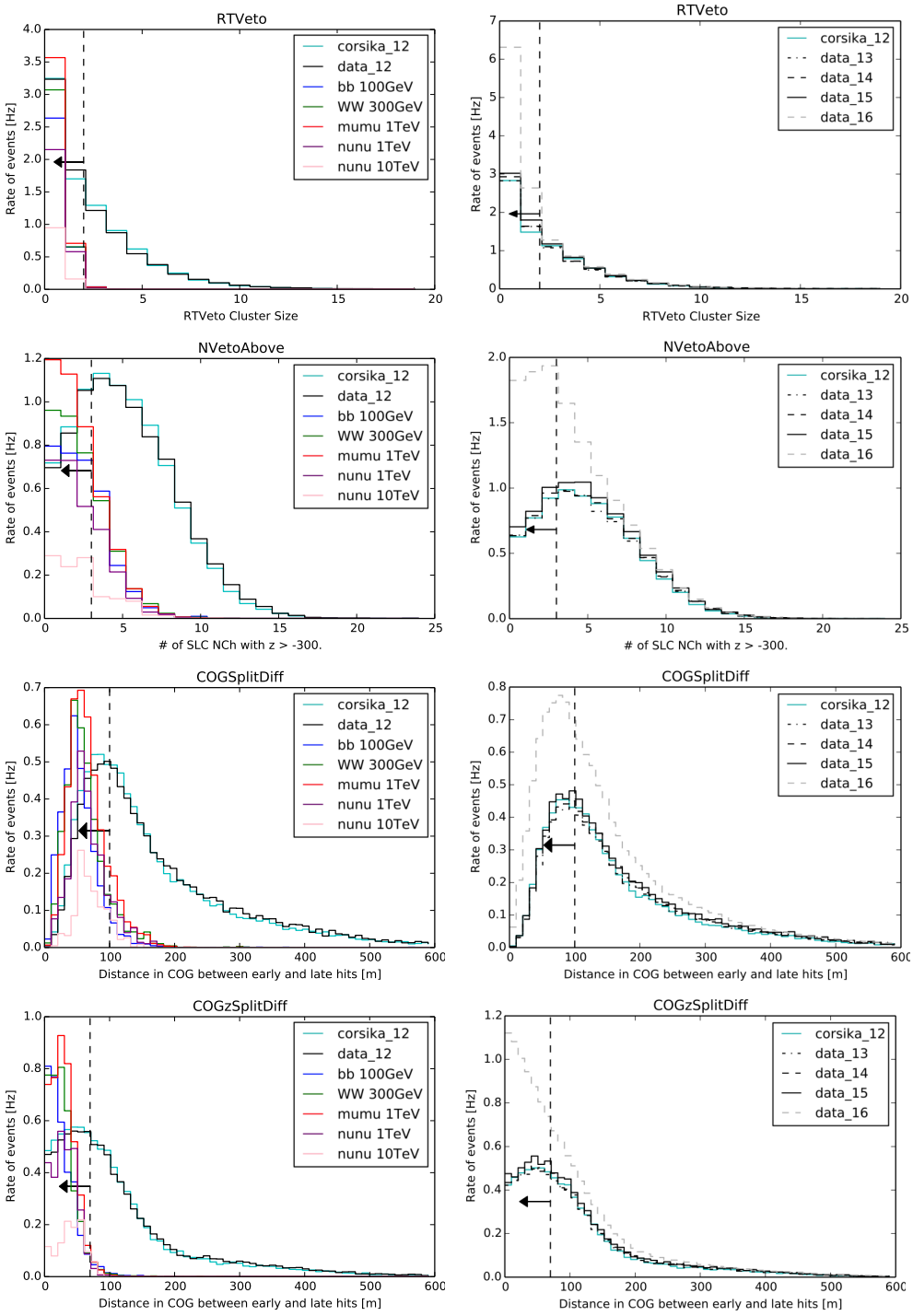

Figure 7.4: Same as Fig. 7.3, but for the variables specified at the top of each subfigure.

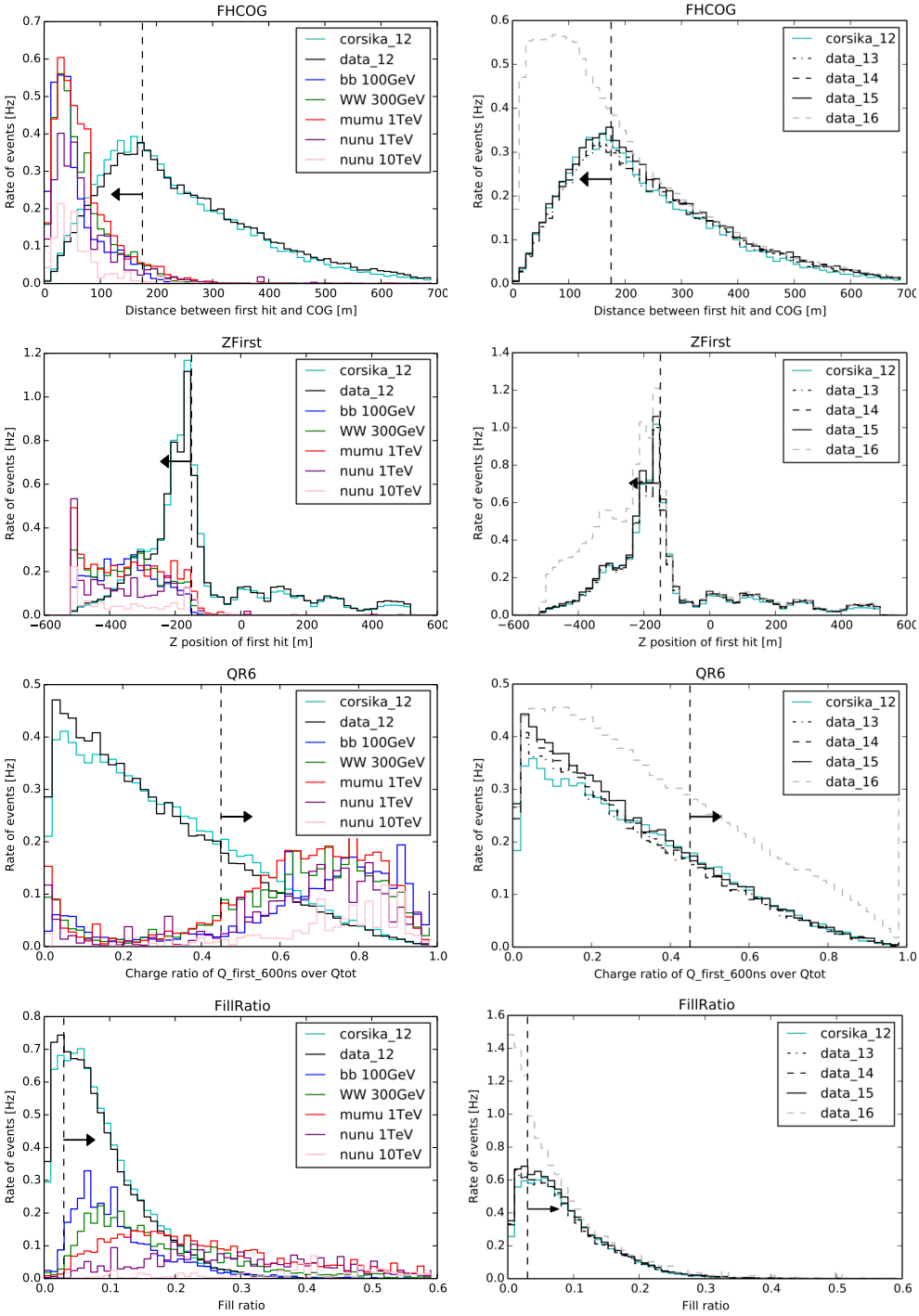

Figure 7.5: Same as Fig. 7.3, but for the variables specified at the top of each subfigure.

In comparison with year 2011 (see corresponding figures in Ref. [227]), we observe in 2012–2015 smaller event rates by a factor of about 2 to 3.[20] After discussing with other people in the Collaboration, this decrease was also typically observed in other analyses from 2011 to 2012, and originates from the update of filters and triggers that had taken place at the time. We also notice a slightly different shape for the Tensor of Inertia Eigenvalue Ratio variable, and a decrease of rates in 2016. However, none of the original cut choices was very much put into question because, precisely *after* those cuts—*i.e.* once we arrive at Level 3—, the rates as well as the shape involved for *all* the variable distributions ended up being comparable to those of 2011 (see *e.g.* Sec. 7.3.4 below). The rates of the Level 3 data (*i.e.* **after** the cuts just itemized) is around 0.07 Hz (*vs* 0.08 Hz for 2011).

7.3.4 From Level 3 to Level 4

Likelihood Reconstructions

The event rates having been reduced to only ~ 0.07 Hz, three sophisticated likelihood reconstruction algorithms are used to further the reduce the fraction of background events (in particular, track events). In a nutshell,[21] these algorithms are based on log-likelihood fits, one of which uses the infinite track hypothesis (TrackLlh) and the other two the cascade hypothesis (CascadeLlh and Monopod). Through the fits, the aim is to estimate the following set of parameters,

$$\vec{p} = (\vec{x_0}, t_0, \Omega, E_0), \tag{7.6}$$

where Ω and E_0 respectively denote the direction from which the event originates and its deposited energy. As for t_0 and $\vec{x_0}$, they respectively denote an arbitrary time and the corresponding position on the track—when the track hypothesis is used—or the time of the interaction and the corresponding vertex position—when the cascade hypothesis is used. TrackLlh and CascadeLlh both use a simplified description of the ice at IceCube. In contrast, Monopod is an improved cascade reconstruction algorithm in the sense that it uses a complete description of the ice and CascadeLlh as a seed. All of the three algorithms are run on each event, and the best-fit parameters (*e.g.* reconstructed energy, reconstructed ψ, ...) as well as the corresponding log-likelihoods are stored.[22]

Boosted Decision Trees

To classify an event as signal-like or background-like, we now resort to more complicated cuts—as opposed to the "straight cuts" used in the previous two subsections. More specifically, a specific type of machine-learning techniques known as **Boosted Decision Tree** classifiers (BDTs) is used. As depicted in Fig. 7.6, decision trees basically consist in a succession of nodes and branches that respectively represent—in our case—where the cut on some variable is placed and the possible outcomes. For this

[20] Around 8.5 Hz (see above) *vs* $\sim$ 18 Hz for 2011.

[21] More details can be found in Sec. 5.3. of Ref. [227].

[22] As we are about to see, the latter will also be used in the definition of some Level 4 variables.

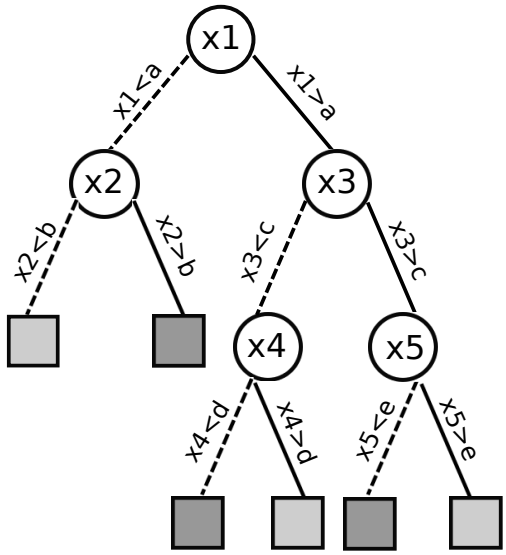

Figure 7.6: Illustration of a binary BDT. At each node of the BDT (circles), the variable with the best separation power is considered ($x1, x2, x3, \ldots$, with the corresponding cuts respectively denoted by $a, b, c, d, e, \ldots$). Nodes at the end of a tree are referred to as "leaves" and are depicted in green. For the sake of reminding that a leaf can be background-like or signal-like, we have used two shades of gray in this figure.

analysis, *binary* trees were used, meaning that only *two* possible outcomes were considered: the event variable being looked at at the node is either "greater" or "smaller" than the cut value, and passes through the corresponding branch. Nodes found at the end of a tree are referred to as *leaves*.

A decision tree is first **trained** on a sample made of known signal and background events. At each step, the variable (and the cut on that variable) with the higher separation power is considered,[23] until a leaf is reached.[24] Each leaf is then assigned a score between -1 (background-like) and $+1$ (signal-like). This score reflects the fraction of true signal events that have ended up in that leaf during training *versus* the fraction of background events. The interpretation should be that an event with a higher score than another one is more likely to be a signal event.

That a decision tree is **boosted** actually means that not one but **many** trees are considered (typically a forest of $\sim \mathcal{O}(1000)$ trees), in such a way that misclassified events (*i.e.* signal events ending up in a background leave and *vice versa*) are given more weight between the training of consecutive trees so that they can better be tackled. At the end of this process, a "boosted" tree is built by taking into account

[23] A given variable may actually be considered more than once.

[24] At a given node, branch splitting stops for one of these three reasons: either because the maximum allowed depth has been achieved—user-dependent—, because a node has reached a 100 % signal or background purity, or because it would generate leaves with poor statistics.

a weighted average of all the individual trees. In can be shown that this new tree benefits from a higher performance than any of the single trees of the forest [236].

It was also previously checked that the BDTs were **not overtrained**, *i.e.* that they do not separate signal and background events according to features that are specific to the training sample (in other words, that they are immune to statistical fluctuations).

Level 4 Variables

A set of 14 preliminary and promising variables was first selected to train the BDT. With a view to trading some of the performance for speed and easiness, this primary selection was then reduced to a set of 7 variables by progressively eliminating those variables that were used the least in the BDT and whose removal did not significantly decrease its performance. The 7 remaining variables are:

- **L3QR6**: defined in Eq. (7.5);
- **L3ZFirst**: defined in the previous subsection;
- **DeltaCOGz**: defined in the previous subsection;
- **RatioLH**: this variable corresponds to the log-ratio of the likelihoods computed by the CascadeLlh and TrackLlh reconstruction algorithms:

$$R_{\mathrm{LLH}} = \log\left(\frac{\mathcal{L}_{\mathrm{cascade}}}{\mathcal{L}_{\mathrm{track}}}\right); \tag{7.7}$$

- **RatioRLogL**: is the ratio of the reduced log-likelihood of the cascade and track hypotheses:

$$R_{\mathrm{r,\,LLH}} = \frac{(\log\mathcal{L})_{\mathrm{r,\,cascade}}}{(\log\mathcal{L})_{\mathrm{r,\,track}}}; \tag{7.8}$$

- **RhoL4**: shortest distance between the central string (string 36) and the first hit of the cleaned map;
- **TrackRLogL**: reduced log-likelihood of the TrackLlh reconstruction.

We show in Figs. 7.7 and 7.8 the distribution of these variables for the burnsample, the atmospheric muons and a selection of DM annihilation processes. As you can see, there is still a fairly good agreement between the data and the muon background at Level 3, and so we did not bother showing the atmospheric neutrino estimates yet.

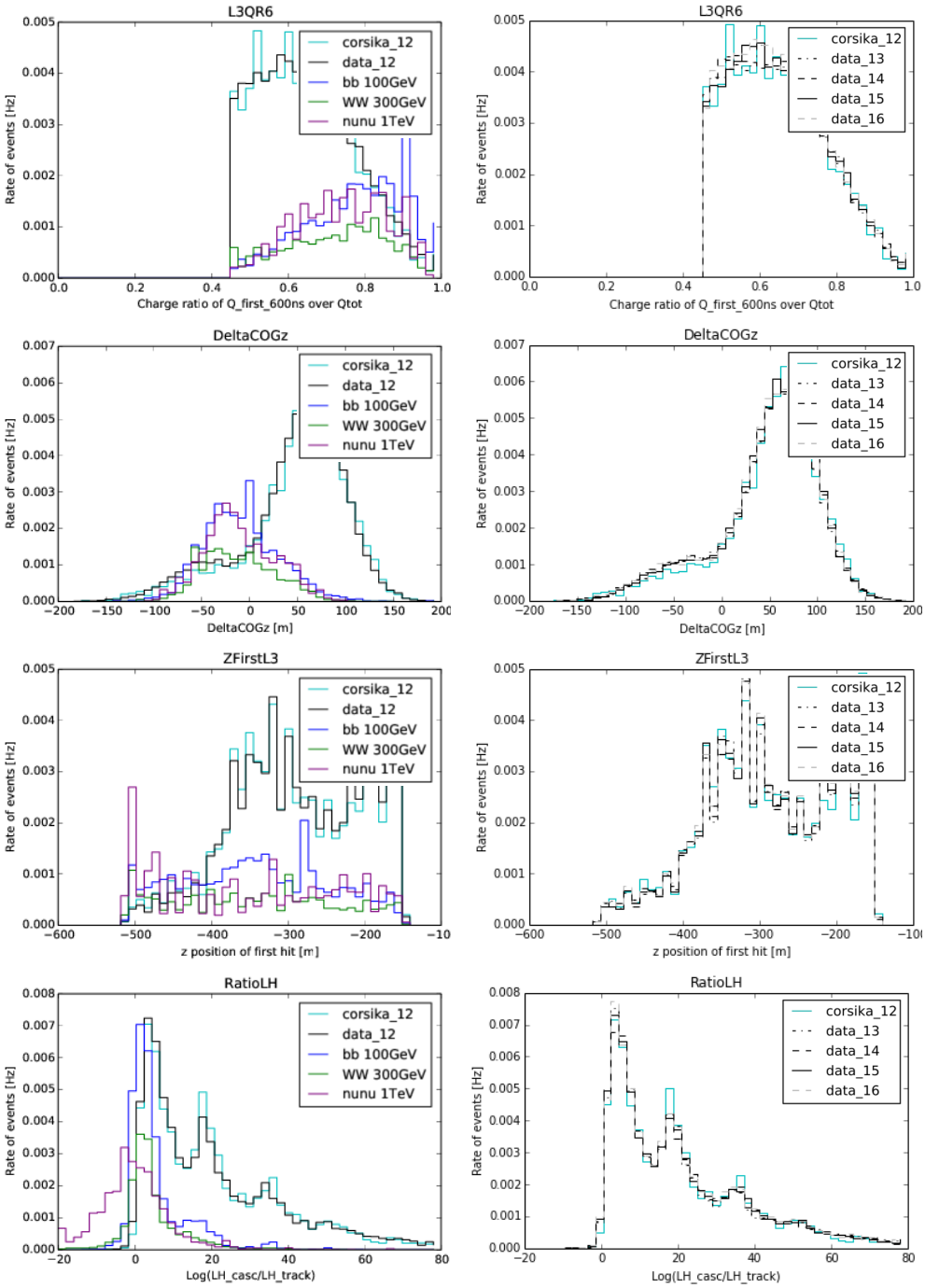

Figure 7.7: Distribution of the LEVEL 4 variables. On the left, the distribution corresponding to the neutrinos induced by the $b\bar{b}100$ GeV, $WW300$ GeV, and $\nu\bar{\nu}1$ TeV DM annihilation channels are respectively shown in blue, green, and purple. The burnsample and the muon backgrounds respectively correspond to the black and cyan curves. The same muon curves are shown on the right, together with the distributions associated to the burnsamples of the subsequent years (2013–2016).

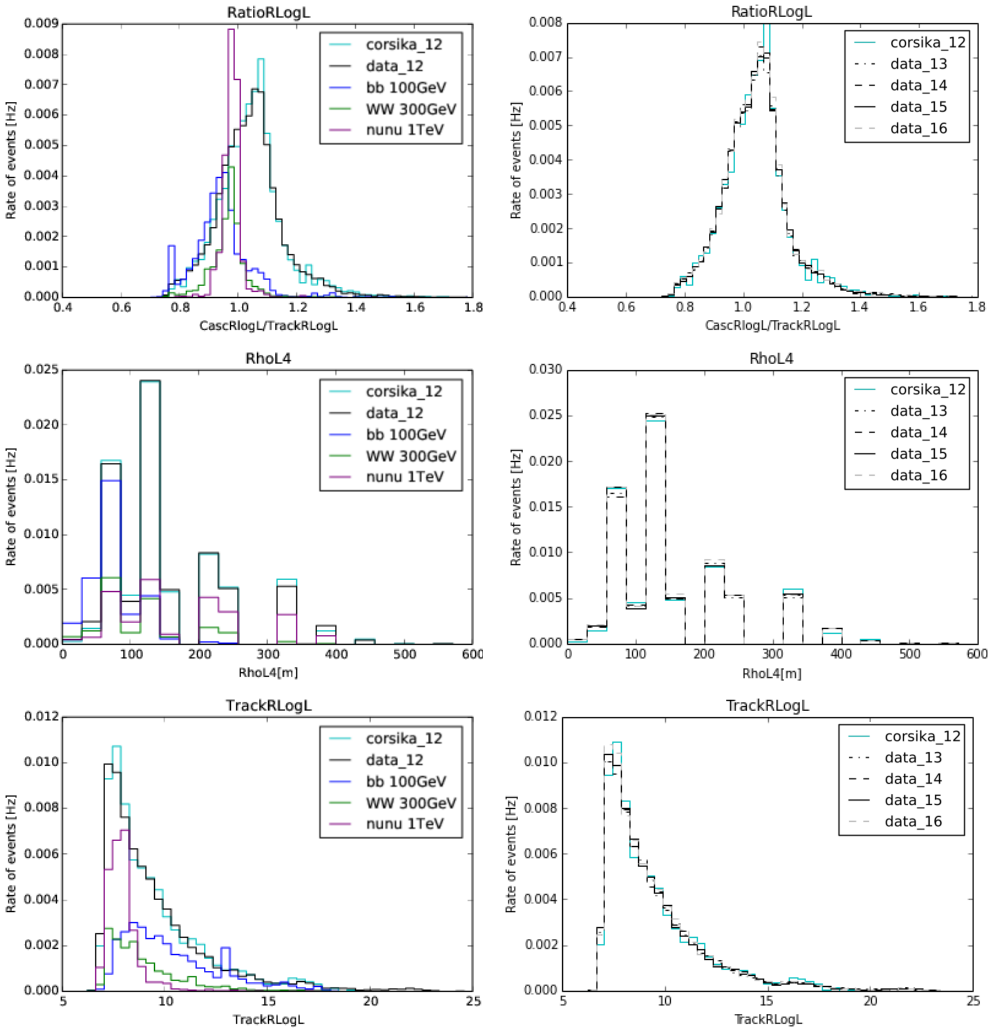

Figure 7.8: Same as Fig. 7.7, but for the variables specified at the top of each subfigure.

BDT score distributions

We will consider in Sec. 7.4 many DM-induced signals in terms of final states and masses. However, to avoid the heaviness of training a BDT for *every single* of these signals, a selection of **two** BDTs is actually used. One of them targets high-energy (HE) signals and is trained on the W^+W^- annihilation channel with $m_{\rm DM} = 300$ GeV. The other tree is trained on the $b\bar{b}$ annihilation channel with $m_{\rm DM} = 100$ GeV and thereby targets low-energy (LE) signals. Each event is passed through the two BDTs and therefore assigned two scores. The final samples will be referred to as LE or HE samples depending on whether the cut is performed on the LE or HE BDT score, respectively. The distributions of the BDT scores are presented in Figs. 7.9 and 7.10.

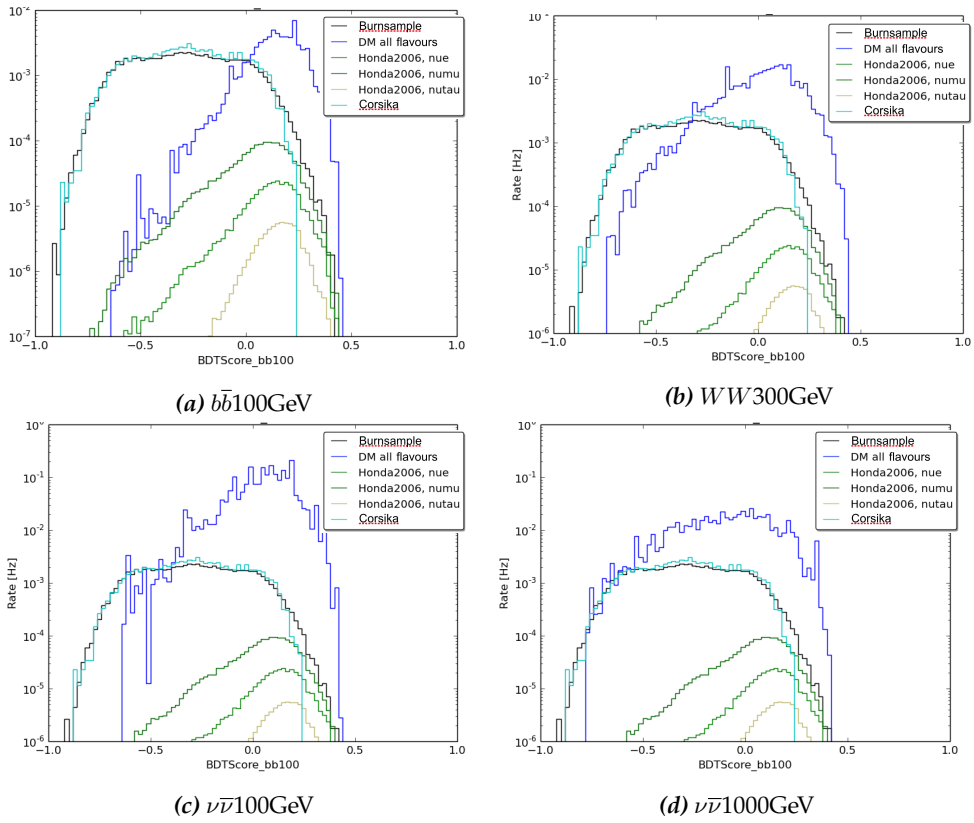

(a) $b\bar{b}$100GeV

(b) WW300GeV

(c) $\nu\bar{\nu}$100GeV

(d) $\nu\bar{\nu}$1000GeV

Figure 7.9: Score distribution obtained from the BDT trained with DM DM $\rightarrow$ $b\bar{b}$ with $m_{\rm DM} = 100$ GeV. The distribution is shown for different annihilation final states: $b\bar{b}$100 GeV, WW300 GeV, $\nu\bar{\nu}$100 GeV and $\nu\bar{\nu}$1000 GeV. The different components that are shown are: the burnsample (black), the atmospheric muons (cyan), the atmospheric neutrinos (three shades of green) and the DM-induced signal (see caption, all flavours included, blue). Notice how subdominant the contribution of atmospheric ν_τ is. This is because ν_τ's are not produced in the atmosphere, and therefore only come from oscillation effects through Earth.

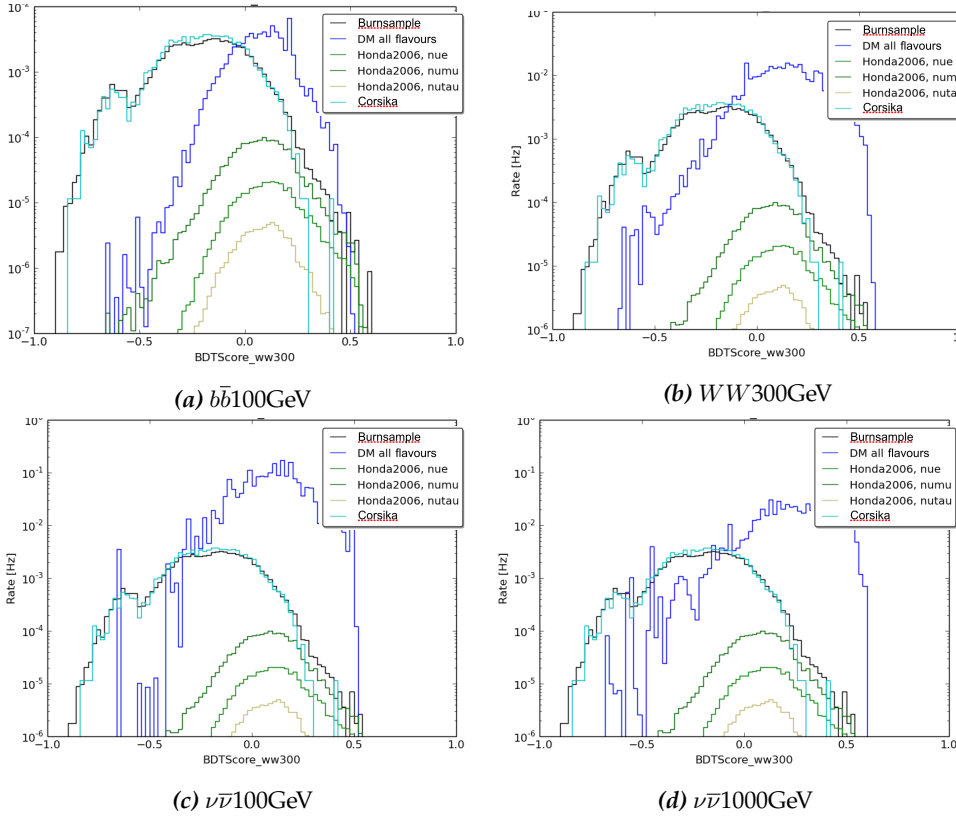

(a) $b\bar{b}$100GeV ***(b)*** WW300GeV

(c) $\nu\bar{\nu}$100GeV ***(d)*** $\nu\bar{\nu}$1000GeV

Figure 7.10: Score distribution obtained from the BDT trained with DM DM $\rightarrow$ WW with $m_{\mathrm{DM}} = 300$ GeV. Everything else is the same as in Fig. 7.9.

Optimization of the cut on the BDT score

As you can see from those two figures, BDT scoring provides a way to define a background-like region (to the left, score < 0) and a signal-like region (to the right, score > 0), thereby allowing to further enhance the signal-to-background ratio in the data by "appropriately" placing a cut somewhere around the transition region. To decide on its precise location,[25] we look for the optimum sensitivity reach by studying the behaviour of the sensitivity as a function of the cut. This procedure would be very heavy if we had to repeat it for every single signal that we plan to probe,[26] and we will therefore choose the LE and HE cuts on the basis of the following selection of eight DM scenarios:[27]

- 100 GeV DM decaying and annihilating into $b\bar{b}$;

[25] There is a trade-off between keeping enough statistics—to build relatively smooth PDFs—and *not* drowning the signal into the background.

[26] The same argument was already used to explain why we restricted ourselves to using *only* two BDTs, one optimized for the LE signals and the other for the HE ones.

[27] We systematically consider that the flavour composition induced by these channels averages out at the detector.

- 300 GeV DM decaying and annihilating into W^+W^-;
- 100 GeV DM decaying and annihilating into $\nu\overline{\nu}$;
- and 1000 GeV DM decaying and annihilating into $\nu\overline{\nu}$.

We estimate the sensitivity reach exactly as we did in Sec. 6.4: we generate a large number of fake data realisations from the background (here, 1000), and for each of these fake realisations, we profile the log-likelihood of the signal hypothesis and exclude those values of Γ_{tot} (decay) or $\langle\sigma_{\text{ann, tot}}v\rangle$ (annihilation) with a log-likellihood ratio larger than 2.71/2 (at the 95 % CL). This gives a distribution of limits, of which the median defines our sensitivity (systematically denoted by a black curve in Figs. 7.11, 7.12, 7.13 and 7.14). The containment bands are obtained by taking the appropriate percentiles of these distributions.

Two major differences with Sec. 6.4 must however be highlighted:

- the fits are performed on a 2-dimensional grid, of which the axes correspond to the reconstructed energy and reconstructed angle ψ with respect to the GC. The binning on both axes has also been chosen to optimize the sensitivity reach. After testing out a number of bin sizes, we have decided to use three—logarithmically equally spaced—bins per decade of energy (between 10 GeV and 10^5 GeV) and 30° bins for ψ (between $\psi = 0$ and $\psi = 180°$). For the few channels tested (see above), this typically gave us an improvement by a factor of two in comparison with a 1-dimensional approach (whether it be using the grid of energy E or of the angle ψ);
- we completely ignore a potential contribution of neutrino events from astrophysical sources. The reason for this simplification is that, with DeepCore, we are sensitive to low DM masses ($\lesssim \mathcal{O}(10)$ TeV), that is to say where the astrophysical flux plays little role. The backgrounds are therefore characterized by two parameters: the normalisation of the atmospheric muon flux, and that of the atmospheric neutrino flux.

Because we have not unblinded yet, we only show the *expected* sensitivity estimates—and their 68 % and 95 % containment bands—for 5 years of data taking.[28] We have however checked that the *observed* limits obtained with our burnsample were in agreement with our sensitivity estimates—for the corresponding livetime. By doing so, we have also checked that the sensitivity estimates improved by a factor corresponding to the ratio between the livetime of our 5 years of data and that of the burnsample.[29] Keep in mind that these results are still preliminary in the sense that they have not been approved yet by the Collaboration.

[28] More specifically, a livetime of 151,669,139.5 seconds.

[29] The containment bands also shrank by a similar factor, as expected.

Given the results exposed in Figs. 7.11, 7.12, 7.13 and 7.14, we choose to:

- place the cut on the LE BDT score at 0.20 in the case of DM annihilation;
- place the cut on the HE BDT score at 0.20 in the case of DM annihilation;
- place the cut on the LE BDT score at 0.20 in the case of DM decay;
- place the cut on the HE BDT score at 0.20 in the case of DM decay.

In both cases, the event rate is reduced down to $\sim 2.5 \times 10^{-4}$ Hz.

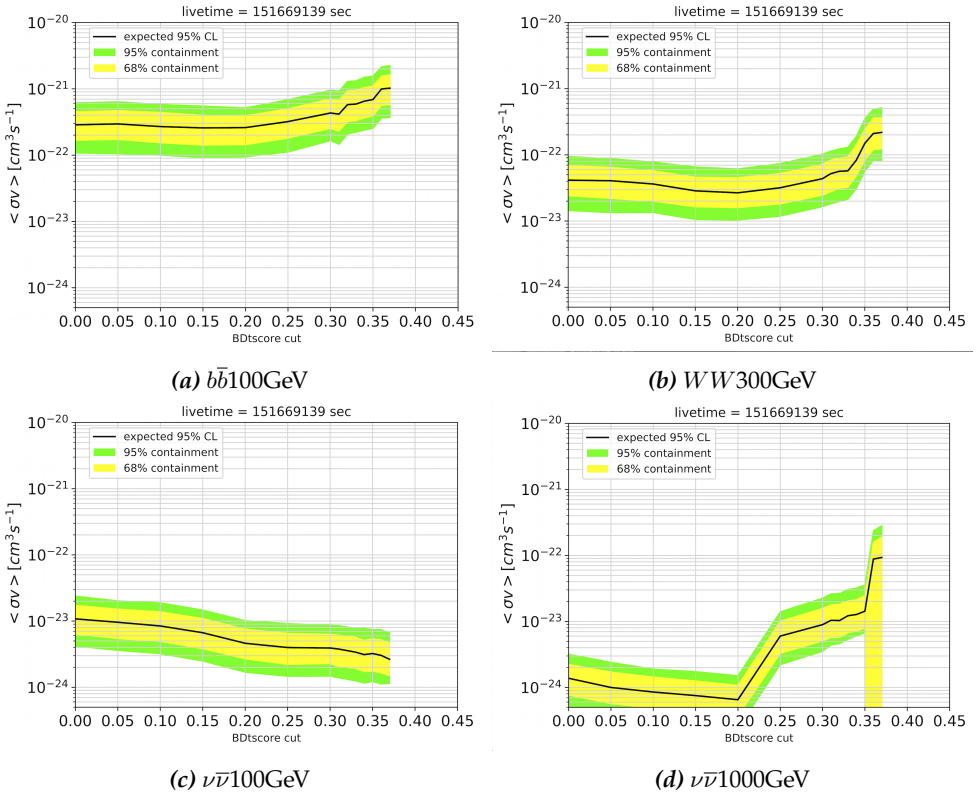

(a) $b\bar{b}$100GeV ***(b)*** WW300GeV

(c) $\nu\bar{\nu}$100GeV ***(d)*** $\nu\bar{\nu}$1000GeV

Figure 7.11: Sensitivity of the analysis to a selection of four DM annihilation channels as a function of the LE BDT score cut. The annihilation channel is referred below each subfigure. The expected sensitivity at the 95% CL is represented by the black curve (to be interpreted as an *upper* limit on $\langle \sigma_{\text{ann, tot}} v \rangle$), and the 68 % (95 %) containment band depicted in yellow (green) in the colored version, and light gray (dark gray) in the B/W version.

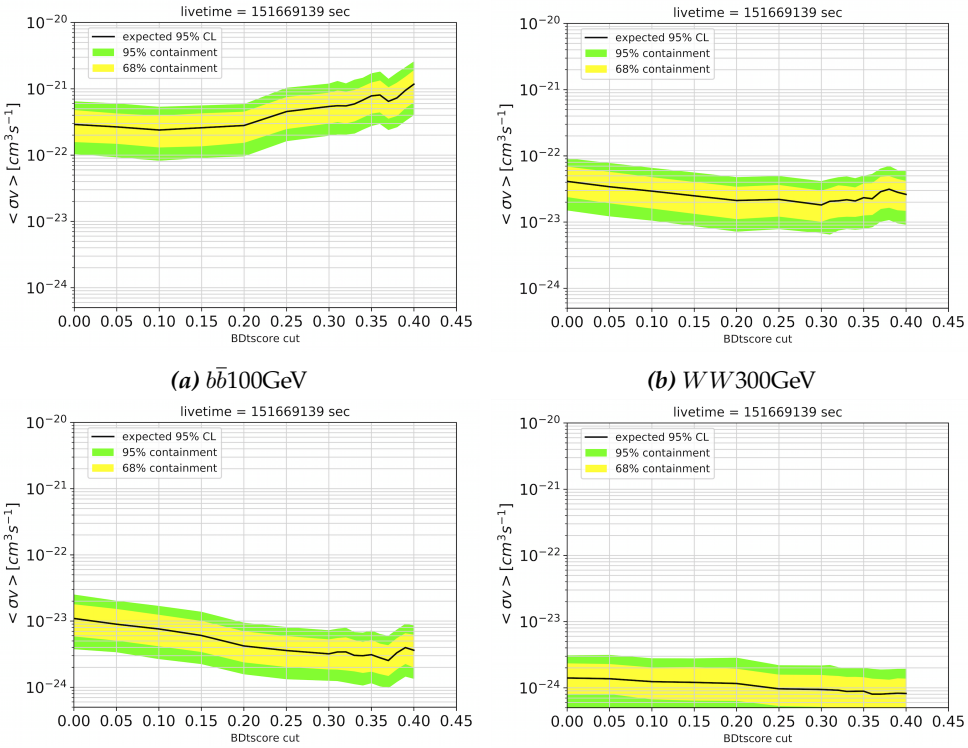

(a) $b\bar{b}$100GeV ***(b)*** WW300GeV

(c) $\nu\bar{\nu}$100GeV ***(d)*** $\nu\bar{\nu}$1000GeV

Figure 7.12: Sensitivity of the analysis to a selection of four DM annihilation channels as a function of the HE BDT score cut. The annihilation channel is referred in the upper left corner of each subfigure figure. The expected sensitivity at the 95% CL is represented by the black curve (to be interpreted as an *upper* limit on $\langle \sigma_{\text{ann, tot}} v \rangle$), and the 68 % (95 %) containment band depicted in yellow (green) in the colored version, and light gray (dark gray) in the B/W version.

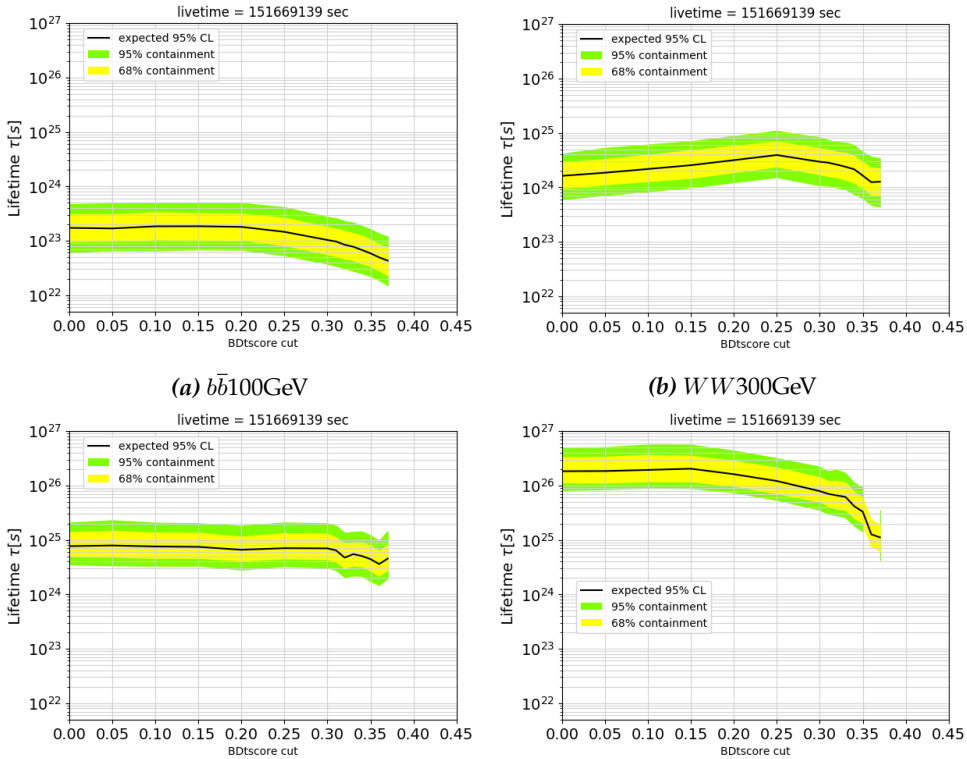

(a) $b\bar{b}$100GeV ***(b)*** WW300GeV

(c) $\nu\bar{\nu}$100GeV ***(d)*** $\nu\bar{\nu}$1000GeV

Figure 7.13: Sensitivity of the analysis to a selection of four DM decay channels as a function of the LE BDT score cut. The decay channel is referred in the upper left corner of each subfigure figure. The expected sensitivity at the 95% CL is represented by the black curve (to be interpreted as a *lower* limit on Γ_{tot}), and the 68 % (95 %) containment band depicted in yellow (green) in the colored version, and light gray (dark gray) in the B/W version.

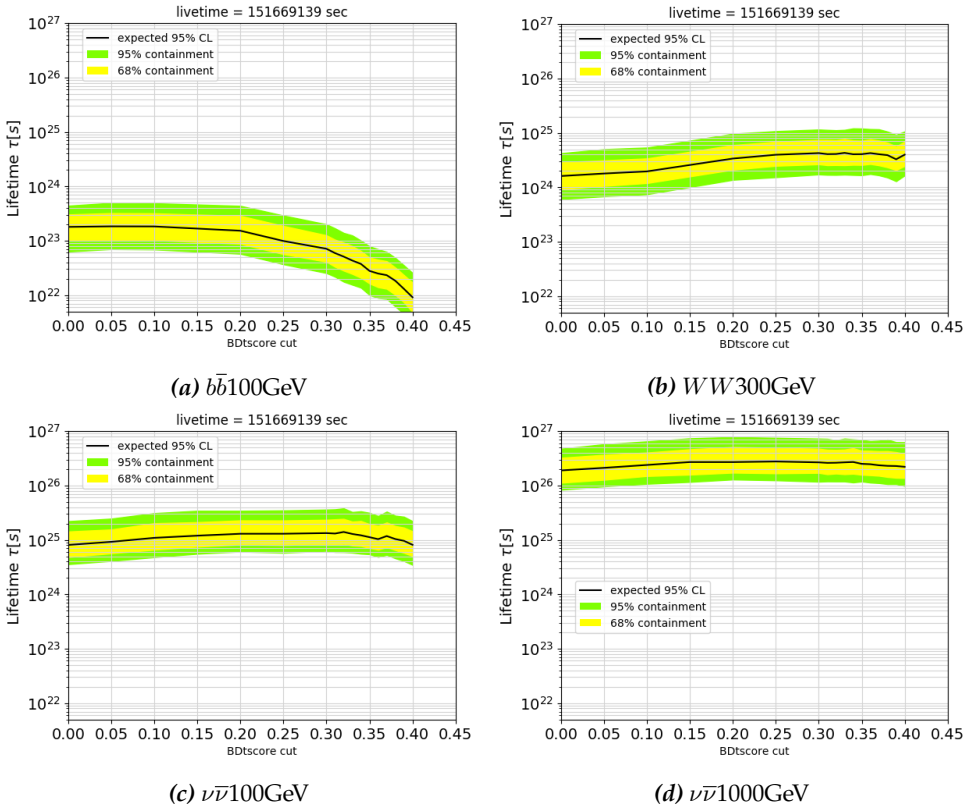

(a) $b\bar{b}$100GeV ***(b)*** WW300GeV

(c) $\nu\bar{\nu}$100GeV ***(d)*** $\nu\bar{\nu}$1000GeV

Figure 7.14: Sensitivity of the analysis to a selection of four DM decay channels as a function of the HE BDT score cut. The decay channel is referred in the upper left corner of each subfigure figure. The expected sensitivity at the 95% CL is represented by the black curve (to be interpreted as a *lower* limit on Γ_{tot}), and the 68 % (95 %) containment band depicted in yellow (green) in the colored version, and light gray (dark gray) in the B/W version.

7.4 Sensitivities

We have exposed in the previous section the basic aspects of background *vs* signal separation on the basis of a score coming out of a BDT. Where we decide to put the frontier on what is likely background and what is not was a question of optimizing the sensitivity reach. We have done so by taking into account a few specific channels at a few masses, and now that we have decided where we place the cuts on the LE and HE BDT scores (see the box on page 163), we present the sensitivity of our analysis to a selection of decay and annihilation channels as a function of the DM mass.

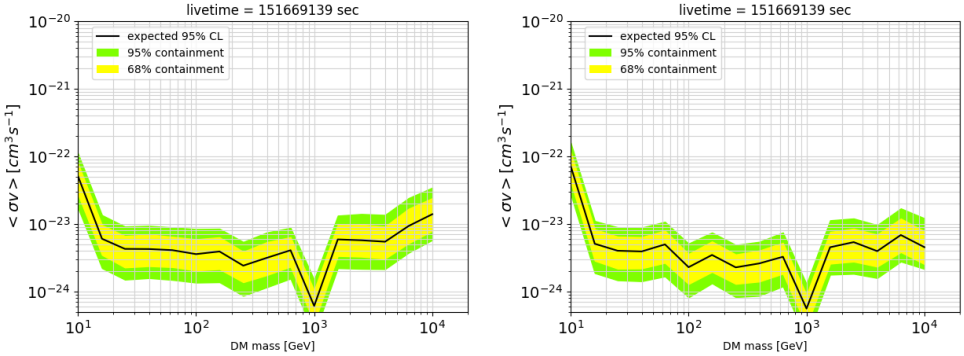

(a) $\nu\overline{\nu}$, LE ***(b)*** $\nu\overline{\nu}$, HE

Figure 7.15: Sensitivity of the analysis to DM annihilations into $\nu\overline{\nu}$ as a function of the DM mass m_{DM}. *Left*: In the case of the LE selection. *Right*: In the case of the HE selection. The peaks at 1 TeV come from heavy statistical fluctuations in the MC simulations (see text).

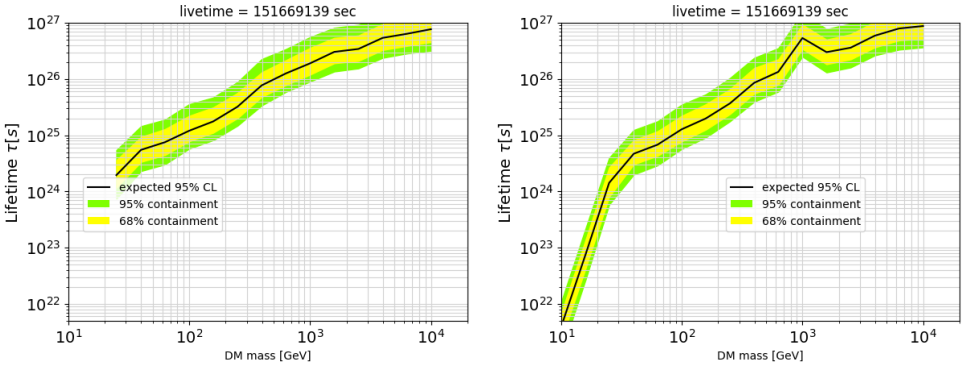

(a) $\nu\overline{\nu}$, LE ***(b)*** $\nu\overline{\nu}$, HE

Figure 7.16: Sensitivity of the analysis to DM decays into $\nu\overline{\nu}$ as a function of the DM mass m_{DM}. *Left*: In the case of the LE selection. *Right*: In the case of the HE selection.

Before we move on, we would like to comment on the peaks observed around 1 TeV. As already mentioned in the caption of Fig. 7.15, these peaks come from important statistical fluctuations in the neutrino simulations. In that sense, these features are not physical and the curves should—more correctly—be smoothly transitioning between 600 GeV and $\sim$ 2 TeV. The fluctuations of the simulations are illustrated in Fig. 7.17, where we show the reconstructed energy distributions (integrated over the whole sky) corresponding to the annihilation of 100 GeV (left) and 1000 GeV (right) DM particles into $\nu\bar{\nu}$.

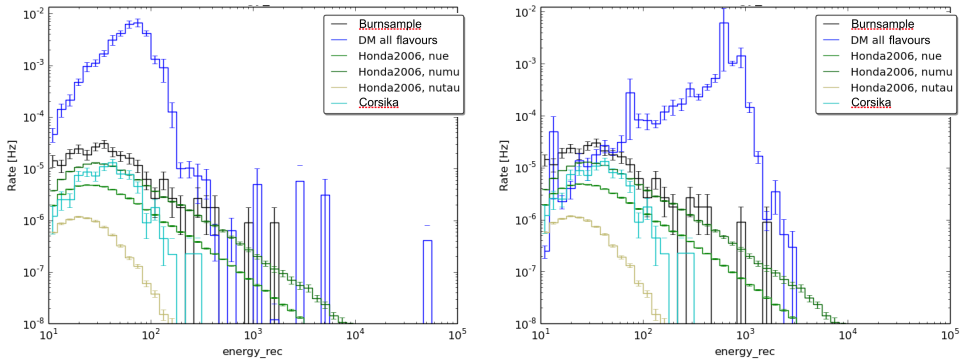

(a) $\nu\bar{\nu}$100 GeV ***(b)*** $\nu\bar{\nu}$1000 GeV

Figure 7.17: Reconstructed energy distributions in the case DMDM $\rightarrow \nu\bar{\nu}$ with $m_{\mathrm{DM}} = 100$ GeV (left) and $m_{\mathrm{DM}} = 1000$ GeV (right).

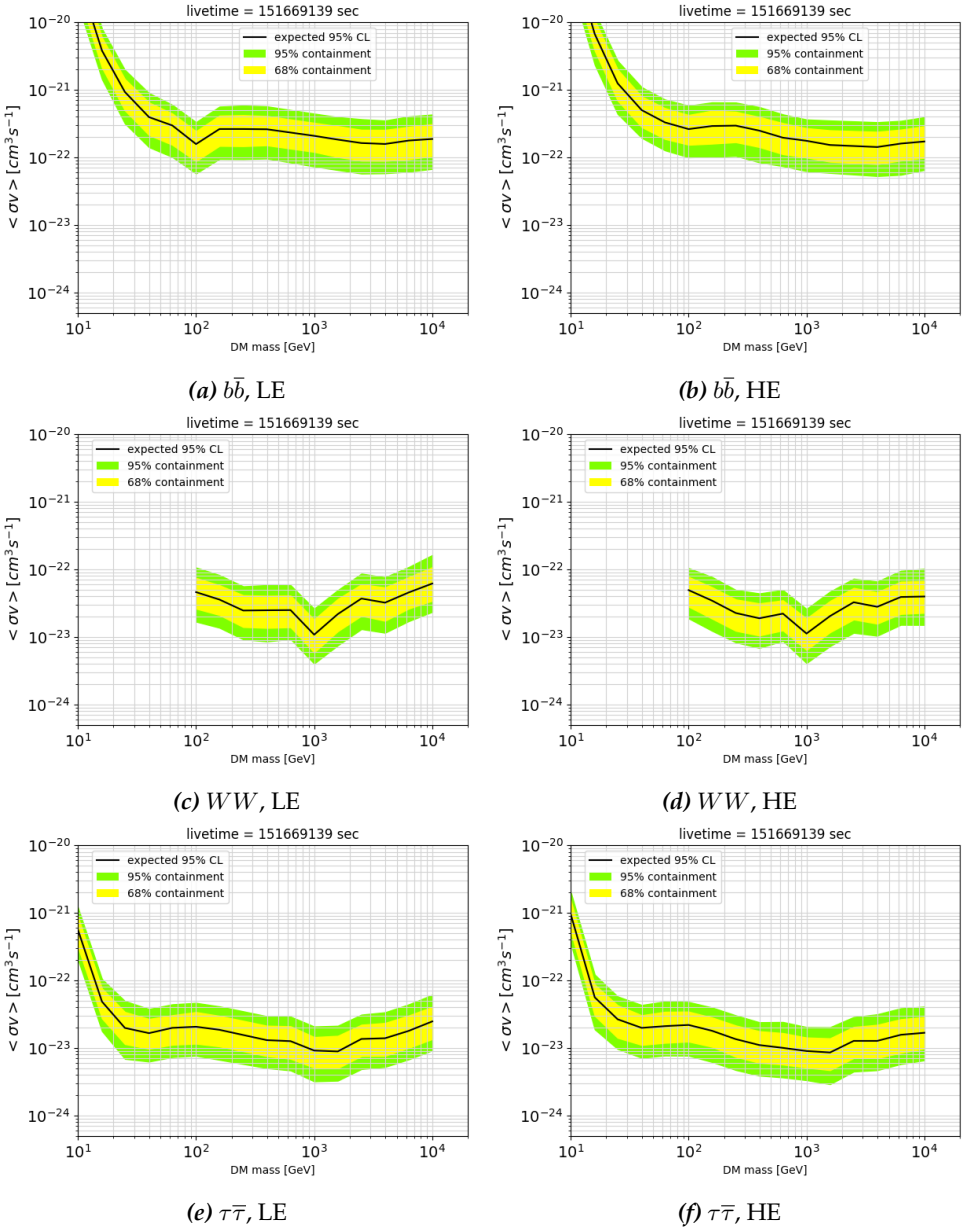

(a) $b\bar{b}$, LE ***(b)*** $b\bar{b}$, HE

(c) WW, LE ***(d)*** WW, HE

(e) $\tau\overline{\tau}$, LE ***(f)*** $\tau\overline{\tau}$, HE

Figure 7.18: Sensitivity of the analysis to DM annihilations into $b\bar{b}, WW, \tau\overline{\tau}$ as a function of the DM mass m_{DM}. *Left*: In the case of the LE selection. *Right*: In the case of the HE selection.

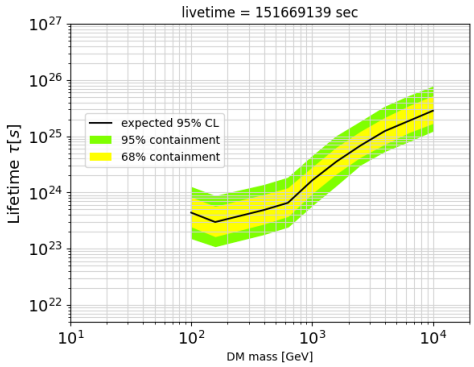

(a) $b\bar{b}$, LE

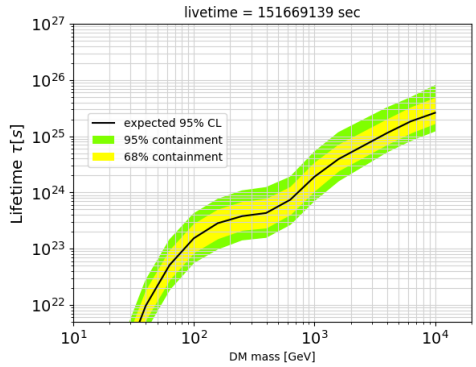

(b) $b\bar{b}$, HE

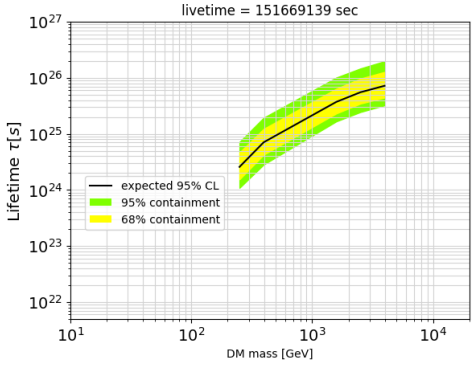

(c) WW, LE

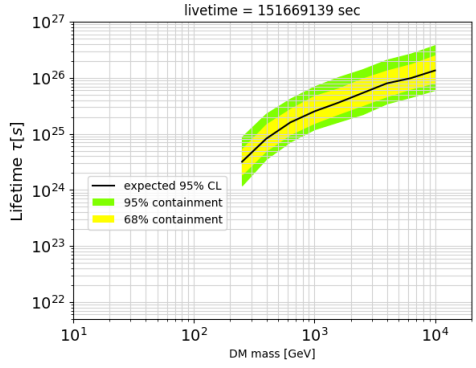

(d) WW, HE

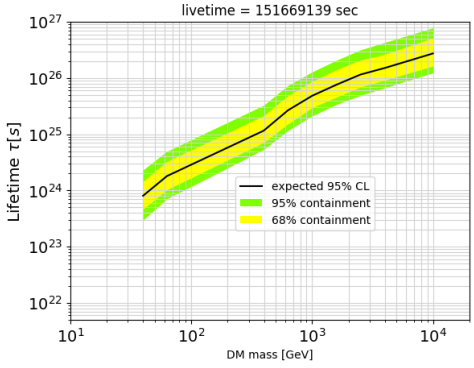

(e) $\tau\bar{\tau}$, LE

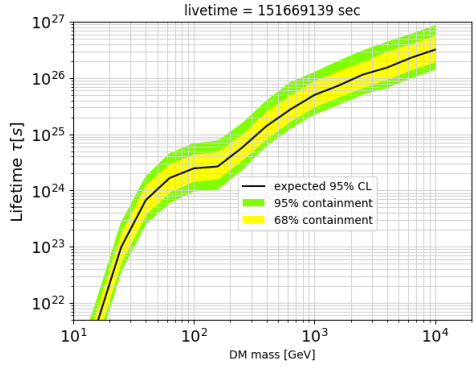

(f) $\tau\bar{\tau}$, HE

Figure 7.19: Sensitivity of the analysis to DM decays into $b\bar{b}, WW, \tau\bar{\tau}$ as a function of the DM mass m_{DM}. *Left*: In the case of the LE selection. *Right*: In the case of the HE selection.

Comparison with a purely angular study

We have mentioned earlier that whether or not we were working on a 2-dimensional grid for the evaluation of the sensitivity of the analysis to the four channels used to decide on the value of the BDT score cut would only change estimates by about a factor of two. However, we want to point out that this statement does not hold anymore at higher masses when a line search is involved. This is because the line feature is dramatically boosted, and therefore improves our sensitivity estimates when it is included in the fits. We show this statement at work through the following figure, where we depict the sensitivity estimates obtained by—only—taking six 30-degrees wide bins between $\psi = 0\,\mathrm{deg}$ and $\psi = 180\,\mathrm{deg}$. As you can see, both in the case of DM annihilation and decay, almost 2 orders of magnitude of sensitivity are lost by not considering the spectral information of the events. We have done here the comparison with the HE samples, but a similar gap is observed at high mass with the LE samples.

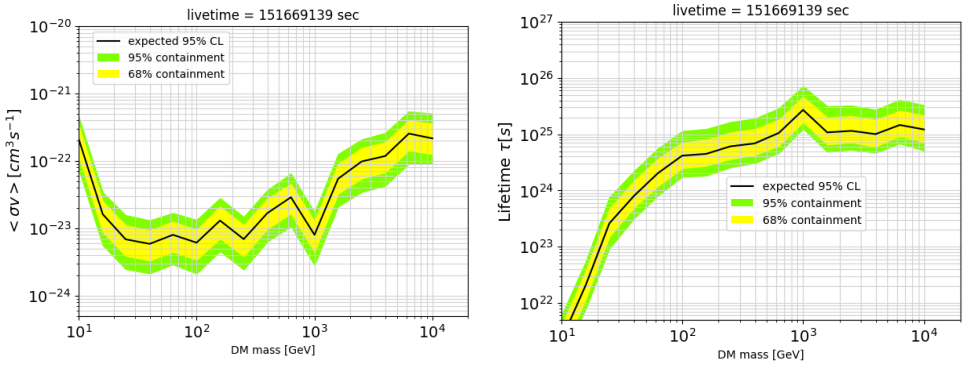

(a) Annihilation ***(b)*** Decay

Figure 7.20: Sensitivity of the analysis to neutrino lines as a function of the DM mass m_{DM} in the case of a purely directional study. The peaks at 1 TeV come from statistical fluctuations in the MC simulations.

Comparison with other studies

For the sake of comparison, we present here the limits that we have obtained in the case of the DM annihilation scenario on the $\tau^+\tau^-$ channel (right) to those already referenced in the literature (left).

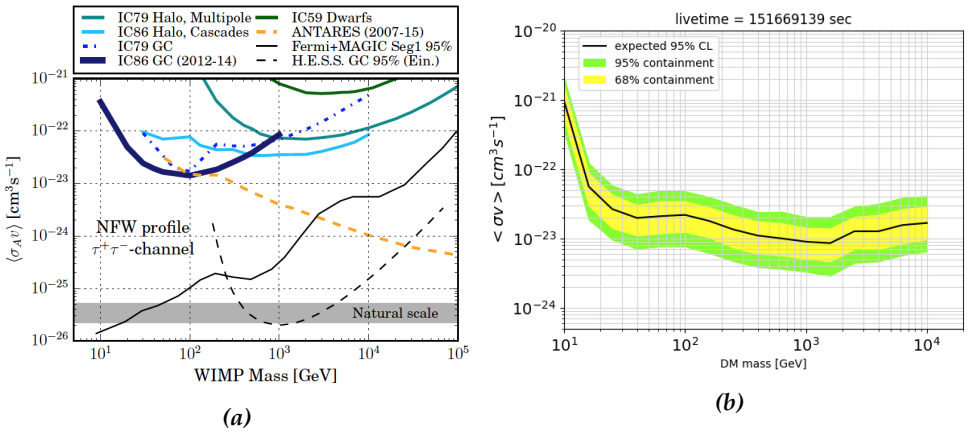

Figure 7.21: Sensitivity of the analysis to neutrino lines as a function of the DM mass m_{DM} in the case of DM annihilation. *Left*: literature. *Right*: our estimates.

7.5 What should you take away from this chapter?

This chapter has been dedicated to the construction of a sample of five years of low-energy cascades seen with the DeepCore sub-detector. The data selection procedure behind this sample had originally been used for another DM analysis but only applied to one year of data. Besides the possibility to develop and work on a 5-year extension, our interests in using this sample included the ability to probe a lower range of DM masses (down to $\sim$ 10 GeV); the possibility—as *associate members*—to run a feature-oriented DM analysis (as in Chapter 6) and to add the angular information of the events; the freedom to work on an event-by-event basis; and, finally, the fact that, by using cascades seen by DeepCore—which is located at the very bottom of the IceCube detector—, a great deal of the atmospheric muon background was removed.

We have seen that the filtering is organised in Levels. Four Levels were involved in our case, and we have systematically described the cuts that were performed on the samples by passing from one to the other (Sec. 7.3). At the final stage of the data selection, *i.e.* to pass from Level 3 to Level 4, we have introduced *Boosted Decision Trees* as a tool to discriminate background(-like) from signal(-like) events on the basis of a score. Two BDTs were used—one optimized for the search of LE signals, the other for the search of HE signals—, and we therefore ended up with two different samples at Level 4. Each of these samples was then used to search for DM-induced signals, in particular lines.

Since the unblinding request to analyse the 5 years of (real) data is under progress, we have restricted ourselves in this dissertation to the estimation of the *sensitivity* of the analysis. We have taken advantage of the possibility to use 2-dimensional fits (grid of reconstructed energy and angle with respect to the GC). Given the results presented in Figs. 7.11, 7.12, 7.13 and 7.14, we have been able to strategically position the cuts at the last level of the data selection, in the sense that they optimize the sensitivity reach of the analysis. The sensitivity to neutrinos lines are presented as a function of the DM mass in Figs. 7.15 (annihilation) and 7.16 (decay). For the sake of comparison, we show in Fig. 7.22 those limits obtained in the HE scenario together with the compilation of limits presented in Chapters 1 and 6. In the annihilation scenario, you can see that our estimates are the best ones in the 100 GeV – 10 TeV mass window (beware also that our estimates are given at the 95 % CL, whereas all of the black curves are given at the 90 % CL). That the green and blue curves give together the best sensitivity estimates beyond 100 GeV is in great part the result of a feature-oriented analysis, as a line feature gets more and more prominent with increasing mass (see comparison with a purely angular study in Fig.7.21).

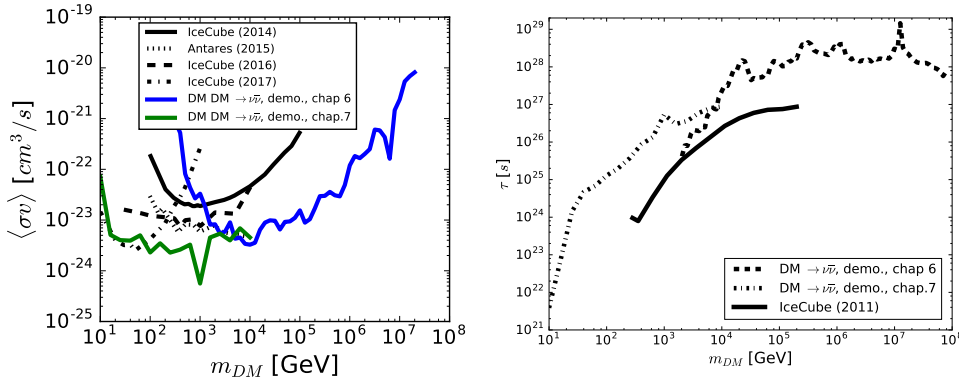

(a) Annihilation

(b) Decay

Figure 7.22: Compilation of limits. *Left:* same as in Fig. 6.3 with the addition of the 95 % CL expected limit derived in this Chapter (green curve). *Right:* Limits on the inverse decay width of DM into $\nu\overline{\nu}$ as a function of the DM mass. The limits derived in Chapter 6 and this chapter are respectively shown in dashed and dashed-dotted (95 %CL). Those derived in Ref. [118] by the IceCube Collaboration (2011) are denoted by the continuous curve (90 % CL). Beware that the peaks around 1 TeV are coming from poor statistics in the simulations, as opposed to the peaks around 6.3 PeV (left) and 12.6 PeV (right) which are physical (Glashow resonance).

CHAPTER 8

General Conclusions

The time has now come to draw the general conclusions of this thesis and position the results that we have obtained within broader and future contexts. Recall that the modern understanding of our Universe as a whole is currently based on the ΛCDM paradigm, of which a great deal of the energy budget—about a fourth—is ascribed to something called "Dark Matter" (DM). What makes up the DM is still a mystery to which almost a century of gravitational evidence has failed to find a clear-cut explanation. However, under the assumption that DM is made of particles, this lack of tangibility is being addressed by indirect, direct and collider searches, and the synergy that exists between the three. We have focused on the former type.

More specifically, the common thread of this dissertation has been the possibility to observe gamma-ray lines, neutrino lines, and spectral features alike *beyond* the GeV scale. These signals can *e.g.* be produced in the 2-body decays of DM particles, and because astrophysical backgrounds cannot produce such features at these energies, they constitute the *only compelling* indirect signatures of the existence of DM particles in our Universe. This explains why a great deal of passion and excitement generally surrounds any potential hint in this direction. Besides the introductory material, this message was relayed in Part I and was used to motivate the rest of the thesis.

In the second part, the emphasis has been put on the connection between the production of gamma-ray lines and their "multi-messenger" counterparts. This has been done in two specific cases: the decay of millicharged DM particles with mono-energetic γ rays in the final state (Chapter 2), and the decay of DM particles (regardless of their charge) with a simultaneous production of mono-energetic γ rays *and* neutrinos (Chapter 3). Because of the scales already probed by the dedicated γ-ray line searches (at least $\sim 10^{12}$ GeV in the former case and $\sim 10^{15}$ GeV in the latter), we have each time studied the connection with the production of other CRs—simply put, the amount of CRs emitted per γ-ray line emission—in the context of an effective field theory. Even allowing for BSM fields in the effective theory, we have each time found very restrictive lists of effective operators. On that basis, we have derived complementary sets of limit estimates on the intensity of a γ-ray line. We have shown that, depending on the experimental conjecture at hand—*i.e.* evidence for an excess of CRs

or evidence for a line, or both—, a discrimination between different effective operators was *possible*, potentially enabling the distinction of UV completions in the case of a discovery. In particular, regarding the question of whether, in a "multi-messenger context", the observation of a γ-ray line in a near future could be attributable to the decay of DM particles, we have highlighted interesting scenarios in which this would be possible. In particular we have shown that if a gamma-ray line was observed, it could be due to the fact that the DM particle is millicharged. Shedding light on this possible property of the DM particle would obviously be key to understand the underlying theory of DM. We have also shown that in specific theoretical scenarios, and given the experimental situation, DM could be discovered in a "spectacular" way, that is to say from the observation of *both* a gamma-ray and neutrino lines. Recall that operators with a scalar field involved non-negligible 3-body decays beyond the TeV scale, and that these decays were responsible, besides extra-contributions to the CR fluxes in general, for the appearance of new line-like features in the γ-ray and neutrino spectra.

The third and last part of this thesis has been dedicated to the search for DM-induced signals in the neutrino spectrum with the IceCube detector. To get into the swing of things, we have given in Chapter 4 an overview of the detection principles of the neutrino and its properties, with a strong emphasis on its detection in ice through the Cherenkov effect. We have then introduced the IceCube detector (arrays, DAQ, ...) and added a few words about what the field of hybrid detection at the South Pole was about. After these two introductory chapters, two analyses were performed by our care, respectively in Chapters 6 and 7. We have reminded the reader of the importance of neutrino line searches in a *spectral* analysis—much less considered in the literature—, especially because they are the ones that may capture some of the Particle Physics aspects of the DM. The first analysis involved the Mese sample and has turned out inconclusive in terms of a discovery. However, we have clearly shown the ability for the limit estimates on the DM decay width—into neutrino lines—to be competitive with their γ-ray equivalent above ~ 10 TeV. The second work involved the development *and* the analysis of 5 years of cascades seen with the DeepCore detector. We have explained that filtering and cleaning were needed not only to downsize the amount of data to be analysed but also to remove as much background events as possible. We have then explained how the different levels were built in the case of interest, and have finally exposed the sensitivity estimates of the DM search at the final level of the data selection. The results were encouraging, even if the sensitivity estimates do not reach the typical value expected from the thermal freeze out. The estimation of *observed* limits and of the systematics is left for the near future, as the analysis must still be reviewed by the whole IceCube Collaboration, in part on the basis of the sensitivity estimates that we have shown here. The redaction of a draft has already started, and the incorporation of the search for DM-induced signals combined with observed limit estimates will follow accordingly.

Through this thesis, we hope to have aroused the interest of the reader and convinced him of the non-trivial nature of the DM problem. That it is at the crossroads between several fields makes it a fascinating topic from which a lot can be—and has been—learned. Moreover, it makes communication between the theoretical and experimental communities key for the elaboration and optimisation of current and

future detection techniques. In this perspective, we hope that the recent discovery of gravitational waves is *just* the beginning of a long series of discoveries that will open new windows on the dark side of our Universe and revolutionize the comprehension that we have of it.

Appendices

APPENDIX A

Millicharged DM decay

A.1 Branching ratios for $(D_\mu\overline{\Psi})\sigma^{\mu\nu}(D_\nu\Psi_{\mathbf{DM}})\Phi$ (non-singlet DM)

We have presented in Chapter 2 the relative branching ratios of the different decay channels induced by the $D_\mu D_\nu\overline{\Psi}\sigma^{\mu\nu}\Psi_{\rm DM}$, $D_\mu D_\nu\overline{\Psi}\sigma^{\mu\nu}\Psi_{\rm DM}\Phi$, and $\overline{\Psi}\sigma^{\mu\nu}D_\mu D_\nu\Psi_{\rm DM}\Phi$ operators at the 2-body decay level. We have also presented these ratios for the $D_\mu\overline{\Psi}\sigma^{\mu\nu}D_\nu\Psi_{\rm DM}\Phi$ operator, but only under the assumption that Ψ and $\Psi_{\rm DM}$ were SM singlets. In any other case, we get much longer expression and this is why you were referred to this Appendix in case you had any interest in them.

Assuming that neither of $\Psi_{\rm DM}$ or Ψ is a SM singlet but that $T_3^{\rm DM} = T_3^{\psi} = 0$, the branching ratios take—modulo a global common factor—the following form:

$$BR_{\gamma\psi} = Q_{\rm DM}^2 \tag{A.1}$$

$$BR_{Z\psi} = 0 \tag{A.2}$$

$$\begin{aligned} BR_{W^+\psi^-} = BR_{W^-\psi^+} = \frac{g^2}{16}(1-(\frac{m_W}{m_{\rm DM}})^2)\left(\frac{m_{\rm DM}^2-m_W^2}{m_W^2}(1+10(\frac{m_W}{m_{\rm DM}})^2+(\frac{m_W}{m_{\rm DM}})^4)\right. \\ \left. + \frac{(m_{\rm DM}^2-m_W^2)^3}{m_W^2 m_{\rm DM}^4} - 2(1+(\frac{m_W}{m_{\rm DM}})^2-(\frac{m_W}{m_{\rm DM}})^4-(\frac{m_{\rm DM}}{m_W})^2)\right). \end{aligned} \tag{A.3}$$

In the case where $T_3^{\rm DM} = T_3^{\psi} \neq 0$, we have:

$$BR_{\gamma\psi} = Q_{\rm DM}^2 \tag{A.4}$$

$$BR_{Z\psi} = (1-(\frac{m_Z}{m_{\rm DM}})^2)^2(1+\frac{1}{2}(\frac{m_Z}{m_{\rm DM}})^2)\frac{g^2}{4c_\epsilon^2} \tag{A.5}$$

$$\begin{aligned} BR_{W^+\psi^-} = BR_{W^-\psi^+} = \frac{g^2}{32}(1-(\frac{m_W}{m_{\rm DM}})^2)\left(\frac{m_{\rm DM}^2-m_W^2}{m_W^2}(1+10(\frac{m_W}{m_{\rm DM}})^2+(\frac{m_W}{m_{\rm DM}})^4)\right. \\ \left. + \frac{(m_{\rm DM}^2-m_W^2)^3}{m_W^2 m_{\rm DM}^4} - 2(1+(\frac{m_W}{m_{\rm DM}})^2-(\frac{m_W}{m_{\rm DM}})^4-(\frac{m_{\rm DM}}{m_W})^2)\right). \end{aligned} \tag{A.6}$$

A.2 Covariant derivative in the kinetic mixing scenario with a massive gauge boson

We review in this section the kinetic mixing scenario under the assumption that the $U(1)'$ gauge group is broken. What we aim to show is that the covariant derivative does *not* include a coupling to the photon when it applies to a field that is originally neutral under the SM.

Since the mass of the new gauge boson cannot come from the SM scalar H, we rely on the presence of an extra (complex) scalar field Φ. This scalar field behaves like a singlet under the SM gauge group and has a non-zero charge under $U(1)'$ so as to realise a symmetry breaking. In comparison with the SM lagrangian $\mathcal{L}_{\text{SM}}$ and Eq. (2.1), this model has the following new terms

$$|D_\mu \Phi|^2 - m_\Phi^2 |\Phi|^2 + \rho |\Phi|^4 - \kappa |H|^2 |\Phi|^2, \tag{A.7}$$

where m_Φ, ρ and κ parametrize the scalar potential of Φ.

To find the mass eigenstates in the gauge sector, we start by performing the same non-unitary transformation as that presented in Eq. (2.2). Then, after the $U(1)' \times SU(2)_L \times U(1)_Y \to U(1)_{\text{em}}$ symmetry breaking has taken place, we find that

$$|D_\mu H|^2 + |D_\mu \Phi|^2 \ni \frac{v^2}{2}\left(\frac{g}{2} W_\mu^3 + \frac{g_Y}{2}\left(A'_\mu \frac{\epsilon}{\sqrt{1-\epsilon^2}} - B'_\mu\right)\right)^2 + \frac{g'^2 \xi^2}{2(1-\epsilon^2)} A'_\mu A'^\mu. \tag{A.8}$$

In the latter expression, g' is chosen such that $Q'_\phi = 1$.[1] As for $v/\sqrt{2}$ and $\xi/\sqrt{2}$, they respectively denote the *vev* of H and ϕ. Using the following relations,

$$\frac{gv}{2} = m_Z \cos\theta_W \;\text{ and }\; \frac{g_Y v}{2} = m_Z \sin\theta_W, \tag{A.9}$$

the mass terms that we have found in Eq. (A.8) can be re-expressed as

$$\frac{m_Z^2}{2}\left(\cos\theta_W W_\mu^3 + \sin\theta_W \left(A'_\mu \frac{\epsilon}{\sqrt{1-\epsilon^2}} - B'_\mu\right)\right)^2 + \frac{g'^2 \xi^2}{2(1-\epsilon^2)} A'_\mu A'^\mu, \tag{A.10}$$

from where we can already see that we will end up with two massive and one massless gauge bosons. After defining the following rotation:

$$\begin{pmatrix} B'_\mu \\ W_\mu^3 \\ A'_\mu \end{pmatrix} = \begin{pmatrix} \cos\theta_W & -\sin\theta_W & 0 \\ \sin\theta_W & \cos\theta_W & 0 \\ 0 & 0 & 1 \end{pmatrix} \begin{pmatrix} A_\mu^\gamma \\ Z'_\mu \\ \widetilde{Z}_\mu \end{pmatrix}, \tag{A.11}$$

the mass terms in Eq. (A.10) become

$$\frac{m_Z^2}{2}\left[\sin\theta \frac{\epsilon}{\sqrt{1-\epsilon^2}} \widetilde{Z}_\mu + Z'_\mu\right]^2 + \frac{g'^2 \xi^2}{2(1-\epsilon^2)} \widetilde{Z}_\mu \widetilde{Z}^\mu, \tag{A.12}$$

[1] This freedom comes from the abelian nature of $U(1)'$.

identifying the photon with A^{γ}_{μ}. A last rotation is needed to diagonalise the mass terms in Eq. (A.12). To find this rotation, we start by searching for the eigenvalues $\lambda_{\pm}$ of the bilinear form in Eq. (A.12):

$$0 = \mathrm{Det}(M^2 - \lambda I) = \begin{vmatrix} m_Z^2 \sin^2\theta_W \frac{\epsilon^2}{(1-\epsilon^2)} + \frac{g'^2\xi^2}{(1-\epsilon^2)} - \lambda & m_Z^2 \sin\theta_W \frac{\epsilon}{\sqrt{1-\epsilon^2}} \\ m_Z^2 \sin\theta_W \frac{\epsilon}{\sqrt{1-\epsilon^2}} & m_Z^2 - \lambda \end{vmatrix}. \quad \text{(A.13)}$$

Solving this equation gives:

$$\lambda_{\pm} = \frac{m_Z^2}{2}\left[1 + \frac{\sin^2\theta_W\epsilon^2}{(1-\epsilon^2)} + \frac{g'^2\xi^2}{m_Z^2(1-\epsilon^2)} \pm \sqrt{\left(1 - \frac{\sin^2\theta_W\epsilon^2}{(1-\epsilon^2)} - \frac{g'^2\xi^2}{m_Z^2(1-\epsilon^2)}\right)^2 + 4\frac{\sin^2\theta_W\epsilon^2}{(1-\epsilon^2)}}\right]. \quad \text{(A.14)}$$

Our last rotation is then defined through

$$\begin{pmatrix} Z'_{\mu} \\ \widetilde{Z}_{\mu} \end{pmatrix} = \begin{pmatrix} \cos\alpha & -\sin\alpha \\ \sin\alpha & \cos\alpha \end{pmatrix} \begin{pmatrix} Z \\ Z_s \end{pmatrix}, \quad \text{(A.15)}$$

where

$$\tan(2\alpha) = \frac{\frac{2\epsilon\sin\theta_W}{\sqrt{1-\epsilon^2}}}{1 - \frac{\sin^2\theta_W\epsilon^2}{(1-\epsilon^2)} - \frac{g'^2\xi^2}{m_Z^2(1-\epsilon^2)}}, \quad \text{(A.16)}$$

The consecutive transformations of Eqs. (2.2), (A.11) and (A.12) imply in particular that D_{μ} can be re-written as:

$$\begin{aligned} D_{\mu} = {} & \partial_{\mu} + igT^1W^1_{\mu} + igT^2W^2_{\mu} \\ & + iA^{\gamma}_{\mu}\frac{gg_Y}{\sqrt{g^2+g_Y^2}}Q_{SM} \\ & + iZ_{\mu}\left(\cos\alpha\left(gT^3\cos\theta_W - g_Y\frac{Y}{2}\sin\theta_W\right) + \sin\alpha\left(-g_Y\frac{Y}{2}\frac{\epsilon}{\sqrt{1-\epsilon^2}} + \frac{g'Q'}{\sqrt{1-\epsilon^2}}\right)\right) \\ & + iZ_{\mu,s}\left(-\sin\alpha\left(gT^3\cos\theta_W - g_Y\frac{Y}{2}\sin\theta_W\right) + \cos\alpha\left(-g_Y\frac{Y}{2}\frac{\epsilon}{\sqrt{1-\epsilon^2}} + \frac{g'Q'}{\sqrt{1-\epsilon^2}}\right)\right). \end{aligned} \quad \text{(A.17)}$$

It is crystal clear from this expression that, in the context of the massive kinetic mixing scenario, a field with $Q_{SM} = 0$ cannot acquire a millicharge.

A.3 Covariant derivative in the Stueckelberg scenario

We derive now the expression of the covariant derivative in the Stueckelberg scenario—no pun intended. As already stated in Sec. 2.2, the Stueckelberg mechanism allows to give a millicharge to an originally neutral particle without having to break the extra $U(1)'$ symmetry.

We add the following gauge invariant to the SM lagrangian:

$$-\frac{1}{2}\left(\partial^{\mu}\sigma + M_1 C^{\mu} + M_2 B^{\mu}\right)^2, \tag{A.18}$$

where B^{μ}/C^{μ} is the gauge boson associated to $U(1)_Y/U(1)'$, and where σ is a real scalar that carries a charge under the hidden and visible sectors (it couples to C^{μ} *and* B^{μ}). This scalar basically plays the *rôle* of the longitudinal component of the field that becomes massive.

The variation of the different fields under a $U(1)_Y$ gauge transformation are defined through the following expressions:

$$\delta_Y \sigma = -M_2 \epsilon_Y, \quad \text{(A.19)} \qquad \delta_Y B_{\mu} = \partial_{\mu}\epsilon_Y, \quad \text{(A.20)} \qquad \delta_Y C_{\mu} = 0 \qquad \text{(A.21)}$$

and the variations induced by a $U(1)'$ transformation are given by:

$$\delta' \sigma = -M_1 \epsilon', \quad \text{(A.22)} \qquad \delta' B_{\mu} = 0, \qquad \text{(A.23)} \qquad \delta' C_{\mu} = \partial_{\mu}\epsilon', \quad \text{(A.24)}$$

where ϵ_Y and ϵ' are real arbitrary functions.With these expressions in hand, you can easily check that the variation of Eq. (A.18) is zero.

After the electroweak symmetry breaking, the mass matrix of C^{μ}, B^{μ} and $W^{3\mu}$ takes the following form:

$$\mathbf{M}^2 = \begin{pmatrix} M_1^2 & M_1 M_2 & 0 \\ M_1 M_2 & M_2^2 + \frac{1}{4} g_Y^2 v^2 & -\frac{1}{4} g_Y g v^2 \\ 0 & -\frac{1}{4} g_Y g v^2 & \frac{1}{4} g v^2 \end{pmatrix}. \tag{A.25}$$

This matrix has a zero determinant, highlighting the presence of at least one vector eigenstate with zero mass, which we identify with the photon. This matrix is also symmetric, meaning that it is diagonalisable with the help of an orthogonal transformation $\mathbf{O}$. The corresponding eigenvalues are:

$$\begin{cases} M^2 & = 0 \\ M_{\pm}^2 & = M_1^2 + M_2^2 + \frac{v^2}{4}\left(g_Y^2 \frac{M_1^2 + M_2^2}{M_1^2} + g^2\right) \pm \sqrt{M_1^2 + M_2^2 + \frac{v^2}{4}\left(g_Y^2 \frac{M_1^2 + M_2^2}{M_1^2} + g^2\right)}. \end{cases} \tag{A.26}$$

We define the eigenstates $(Z'_{\mu}, Z_{\mu}, A_{\mu}^{\gamma})^T = O^T (C_{\mu}, B_{\mu}, W_{\mu}^3)^T$, and parametrize the matrix O in terms of three rotation angles (θ, ϕ, ψ):

$$= \begin{pmatrix} c_{\psi}c_{\phi} - s_{\theta}s_{\phi}s_{\psi} & -s_{\psi}c_{\phi} - s_{\theta}s_{\phi}c_{\psi} & -c_{\theta}s_{\phi} \\ c_{\psi}s_{\phi} + s_{\theta}c_{\phi}s_{\psi} & -s_{\psi}s_{\phi} + s_{\theta}c_{\phi}c_{\psi} & c_{\theta}c_{\phi} \\ -c_{\theta}s_{\psi} & -c_{\theta}c_{\psi} & s_{\theta} \end{pmatrix}. \tag{A.27}$$

Those angles are related to the parameters of the model via the following expressions:

$$\tan\theta = \frac{g_Y}{g}\cos\phi, \tag{A.28}$$

$$\tan\phi = \frac{M_2}{M_1} \text{ and} \tag{A.29}$$

$$\tan\psi = \frac{\tan\theta\tan\phi M_W^2}{\cos\theta(M_+^2 - (1+\tan^2\theta)M_W^2)}. \tag{A.30}$$

After the orthogonal transformation of Eq. (A.27),

$$\begin{aligned} D_\mu =& \partial_\mu + iZ'_\mu\left(g'Q'(c_\psi c_\phi - s_\phi s_\theta s_\psi) - gT^3 c_\theta s_\psi + g_Y\frac{Y}{2}(c_\psi s_\phi + s_\theta c_\phi s_\psi)\right) \\ &+ iZ_\mu\left(g'Q'(-s_\psi c_\phi - s_\theta s_\phi c_\psi) - gT^3 c_\theta c_\psi + g_Y\frac{Y}{2}(-s_\psi s_\phi + s_\theta c_\phi c_\psi)\right) \\ &+ iA^\gamma_\mu\left(-g'Q'c_\theta s_\phi + gT^3 s_\theta + g_Y\frac{Y}{2}c_\theta c_\phi\right) \\ &+ igT^1W^1_\mu + igT^2W^2_\mu. \end{aligned} \tag{A.31}$$

Assuming that $Q_{\text{SM}} \equiv T_3 + \frac{Y}{2} = 0$ and using $\tan\theta = \frac{g_Y}{g}\cos\phi$, we find that $D_\mu \ni iA^\gamma_\mu(-)g'Q'c_\theta s_\phi$, that is to say the existence of a coupling to the photon as soon as Q' is non-zero.

APPENDIX B

Multi-messenger lines from DM decay

B.1 Constraints on the suppression scale Λ

Let us recall that all the curves plotted in Figs. 3.2, 3.7 and 3.8 correspond to upper limits on the DM decay width into line and line-like signals. The colored curves are deduced from constraints on other signals induced by the effective operators (γ and $\tilde{p}$ continua), and when they are weaker than "direct" constraints from monochromatic line searches, they fall into the grey region. As explained in Sec. 3.5, we could also translate these limits on decay widths Γ into limits on Λ, the suppression—or cut-off—scale of the operator. If we assume that the pre-factor to the dimension-five and -six operators is $1/\Lambda$ and $1/\Lambda^2$, respectively, the lower limits on Λ are those of Figs. B.1, B.2 and B.3. These three figures are respectively given for dimension 5 operators, dimension 6 operators with dominant 2-body decays and dimension 6 operators with relevant 3-body decays. The labelling in each plot (A, C, D, E, $\widetilde{A}$, $\widetilde{C}$, $\widetilde{D}$ and $\widetilde{E}$) is that listed in Table 3.3 and Eqs. (3.16)–(3.19), where it can be read off to which particular operator these limits apply. The limits shown on Λ are from the CR continuum (dashed curve), the neutrino-line (dotted curve) and the gamma-line (solid curve) signals. For a given operator and $m_{\rm DM}$, the figures show which is the strongest constraint.

It can be noted that all operators of the same dimensionality give limits on Λ that are less than an order of magnitude different from each other. For the dimension-six operators, the limits are around the GUT scale at the lower DM masses and rise to just below the Planck scale at the highest masses considered. For the dimension-five operators, limits on Λ are pushed towards scales higher than 10^{18} GeV.

From Figs. B.1, B.2 and B.3, it is clear that the current limits on gamma and neutrino lines can be of similar strength and they can both be stronger than the limits from the continuum of CRs in the DM mass range between about 10 and 50 TeV for some operators. That means that you could have a detection of both lines (*if* they happen to be just below current limits) without violating any current constraints from other induced CR signals.

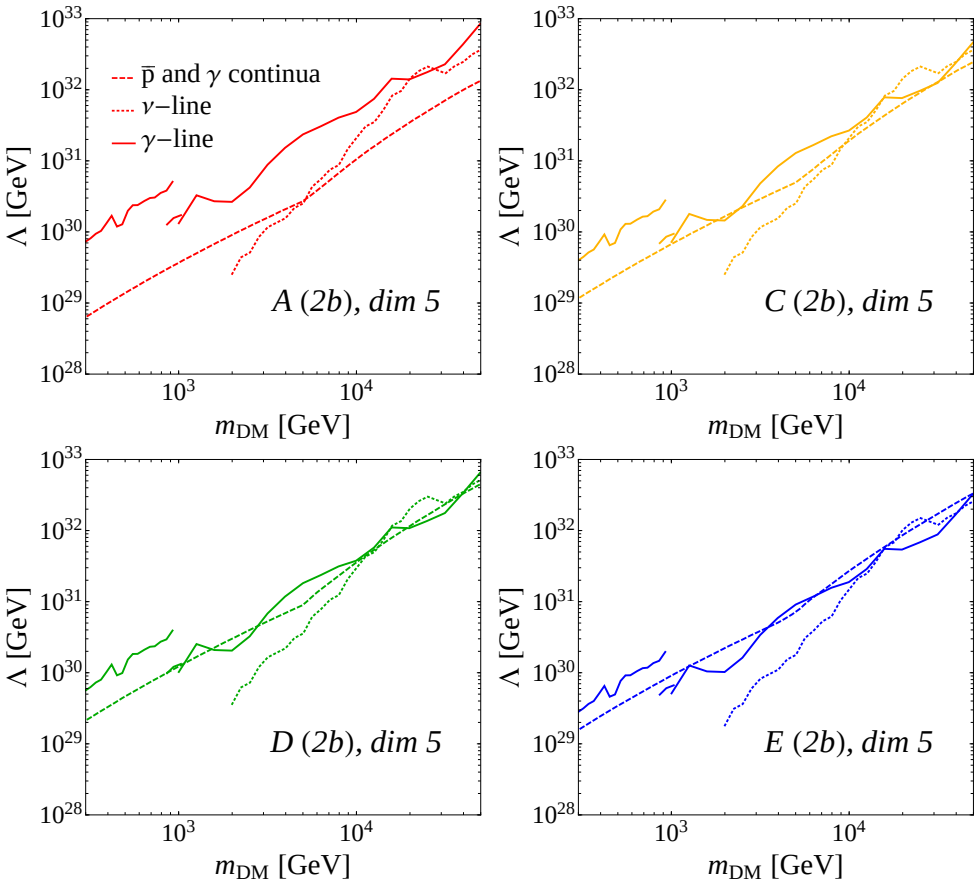

Figure B.1: Lower bounds on the BSM dimentional parameter Λ for the dimension 5 operators discussed in Chapter 3. *Dashed curve:* limits from $\overline{p}$ and γ continuum signal searches. *Solid curve:* limits from gamma-line searches. *Dotted curve:* limits from neutrino-line searches.

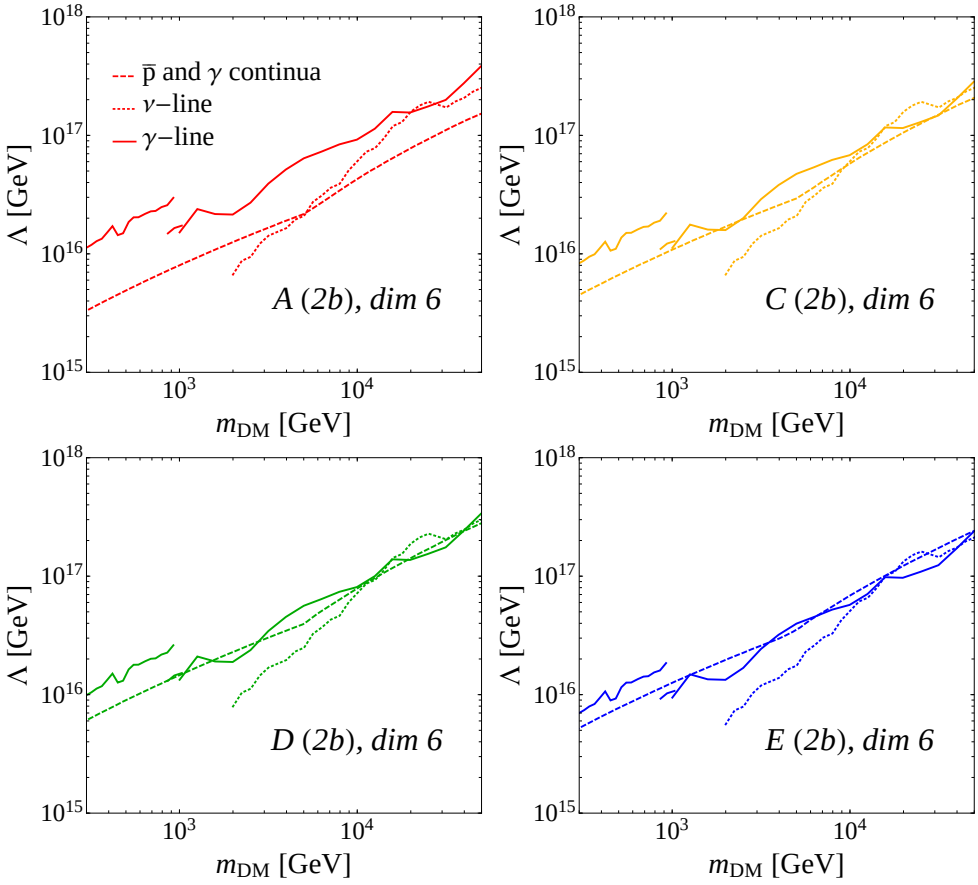

Figure B.2: Same as in figure B.1, but for dimension 6 operators with non-relevant 3-body decays.

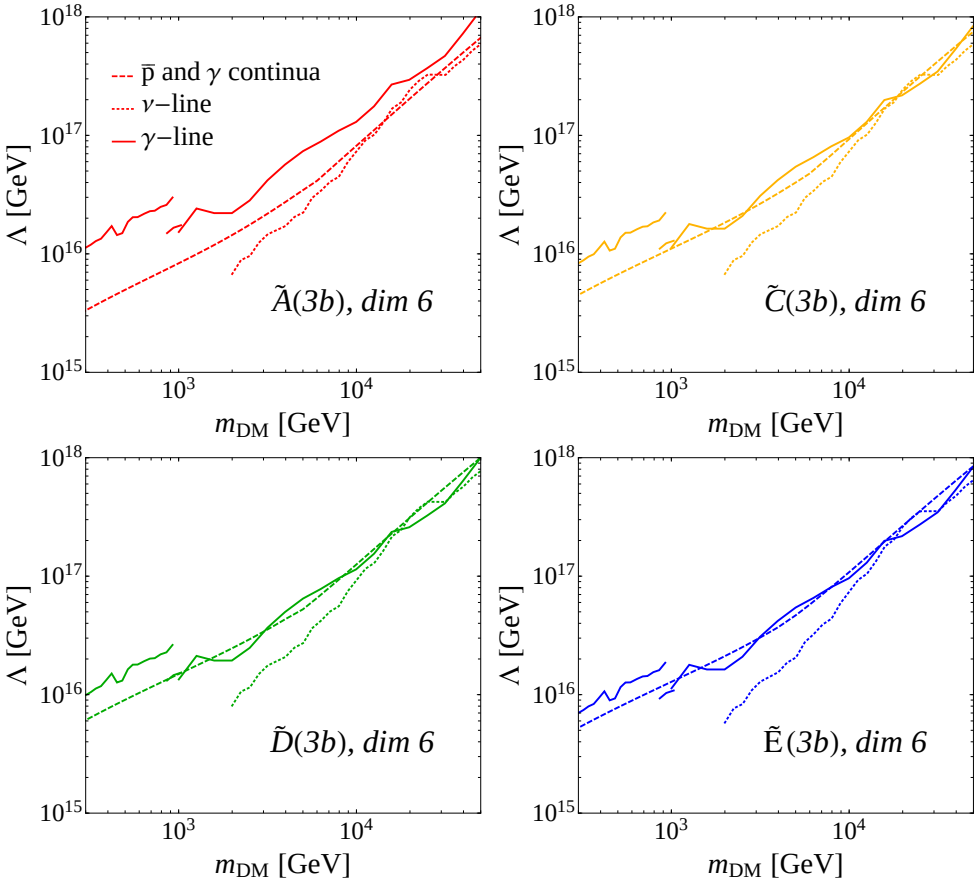

Figure B.3: Same as in figure B.1, but for dimension 6 operators *with* relevant 3-body decays.

APPENDIX C

The IceCube Neutrino Observatory

C.1 Local coordinate system

The local coordinate system is depicted in the following figure:

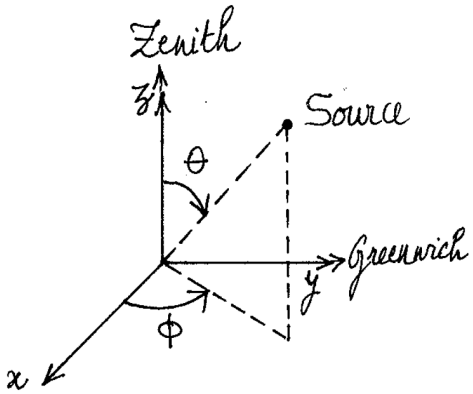

Figure C.1: The local coordinate system. The origin of the system corresponds to the center of the In Ice array. The angles θ and ϕ respectively correspond to the zenith and azimuth angles, and the z and y axes respectively point towards the surface and the Greenwich meridian.

For the purpose of our DM analyses, we also give the expression of the angle ψ made between the Galactic Center and an event of zenith θ and azimuth ϕ:

$$\cos\psi = \cos\theta\cos\theta_{\rm GC} + \sin\theta\sin\theta_{\rm GC}\cos(\phi - \phi_{\rm GC}), \tag{C.1}$$

where $\theta_{\rm GC}$ and $\phi_{\rm GC}$ respectively denote the zenith and azimuth of the GC.

APPENDIX D

Search for neutrino spectral features induced by DM at IceCube

D.1 Effect of the ν and $\overline{\nu}$ flavour composition on the results

We collect in this appendix some complementary limits that might be of interest, all derived by the method described in Section 6.4.

Figure D.1 shows the 95 % CL lower limits on DM particle lifetime into a monochromatic neutrino in the cases of pure electron, muon or tau neutrinos injected at the DM source and with equal parts of ν and $\overline{\nu}$. The neutrino flavor oscillations from Section 4.4.1 are used for the propagation from source to Earth's surface.

In Fig. D.2, we use the same setup, but assume that only neutrinos or anti-neutrinos are injected by the DM decay.

For Fig. D.3, we assume that the incoming fluxes *at Earth* are 100 % pure ν_e, ν_μ or ν_τ. As in the previous figure, we show limits separately for neutrinos and anti-neutrino injected at DM decays. These (hypothetical) pure flavor fluxes incoming to Earth could potentially be partly mimicked by non standard flavor oscillation effects from: neutrino decay [237, 238], sterile neutrinos [239], a pseudo-Dirac nature of neutrinos [240], Lorentz or CPT violations [241] or gravity-induced decoherence [242]. In any case, these limits clearly illustrate the main differences in sensitivity reach with this data set for extreme cases (*i.e.* for pure flavor and particle/anti-particle fluxes).

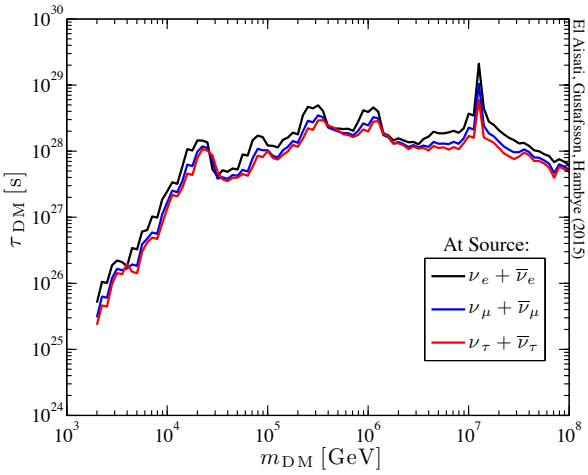

Figure D.1: 95 % CL limits on the lifetime of DM particle decay into monochromatic neutrinos for pure e (black), μ (blue) or τ (red) neutrinos injected at *Source* and with equal parts of ν and $\overline{\nu}$.

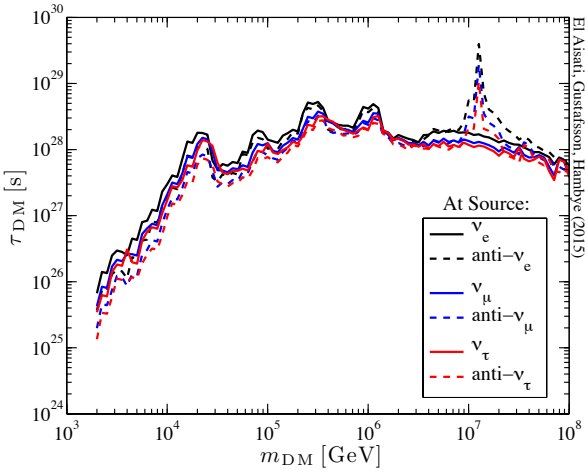

Figure D.2: Same as Fig. D.1 with the pure ν_e, ν_μ and ν_τ at *Source*, but also separated into neutrinos (solid) or anti-neutrinos (dashed)

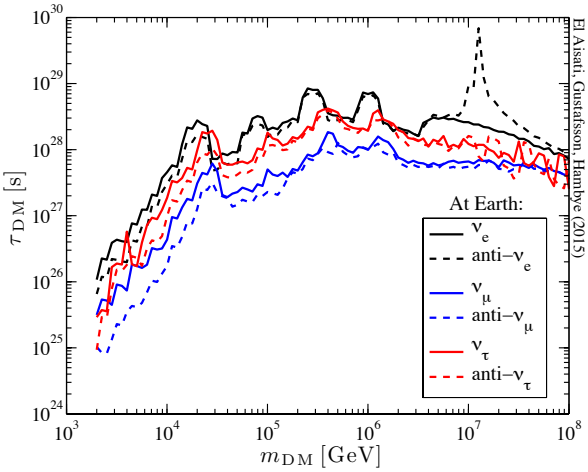

Figure D.3: Same as Fig. D.2 but in the case of pure ν_e, ν_μ and ν_τ fluxes at *Earth's surface*. A pure flavor flux is typically not realistic due to neutrino oscillations, but the plot clearly illustrates the differences in effective area depending on the incoming neutrino flavor.

Bibliography

[1] P. A. R. Ade *et al.* [Planck Collaboration], *"Planck 2015 results. XIII. Cosmological parameters,"* Astron. Astrophys. **594** (2016) A13 Doi:10.1051/0004-6361/201525830 [arXiv:1502.01589 [astro-ph.CO]].

[2] M. G. Aartsen *et al.* [IceCube Collaboration], *"Observation of High-Energy Astrophysical Neutrinos in Three Years of IceCube Data,"* Phys. Rev. Lett. **113**, 101101 (2014) [arXiv:1405.5303 [astro-ph.HE]].

[3] M. G. Aartsen *et al.* [IceCube Collaboration], *"Atmospheric and Astrophysical Neutrinos above 1 TeV Interacting in IceCube,"* Phys.Rev.D **91**, 022001 (2015) [arXiv:1410.1749 [astro-ph.HE]].

[4] E. Öpik, (1915), *"Selective absorption of light in space, and the dynamics of the Universe"* Bull. de la Soc. Astr. de Russie **21**, 150.

[5] J. Jeans, *"The motions of stars in a Kapteyn universe"*, Monthly Notices of the Royal Astronomical Society, Vol. **82**, p.122-132.

[6] J. H. Oort, *"The force exerted by the stellar system in the direction perpendicular to the galactic plane and some related problems"*, Bulletin of the Astronomical Institutes of the Netherlands, Vol. **6**, p.249.

[7] F. Zwicky, *"Die Rotverschiebung von extragalaktischen Nebeln,"* Helv. Phys. Acta **6** (1933) 110 [Gen. Rel. Grav. **41** (2009) 207]. doi:10.1007/s10714-008-0707-4.

[8] J. Einasto, *"Dark Matter,"* Astronomy and Astrophysics 2010, [Eds. Oddbjorn Engvold, Rolf Stabell, Bozena Czerny, John Lattanzio], in Encyclopedia of Life Support Systems (EOLSS), Developed under the Auspices of the UNESCO, Eolss Publishers, Oxford ,UK [arXiv:0901.0632 [astro-ph.CO]].

[9] `http://www.damtp.cam.ac.uk/research/gr/public/bb_history.html`

[10] R. Durrer, *"The Cosmic Microwave Background"*. Cambridge University Press (2012). Doi: 10.1017/CBO9780511817205.

[11] E. W. Kolb and M. S. Turner, *"The Early Universe,"* Front. Phys. **69** (1990) 1.

[12] S. Dodelson, *"Modern Cosmology,"* Amsterdam (Netherlands): Academic Pr. (2003) 440 p.

[13] A. A. Penzias and R. W. Wilson, *"A Measurement of excess antenna temperature at 4080-Mc/s,"* Astrophys. J. **142** (1965) 419. Doi:10.1086/148307.

[14] R. H. Dicke, P. J. .E. Peebles, P. G. Roll, D. T. Wilkinson *"Cosmic Black-Body Radiation"*. Astrophys. J. **142** (1965) 414-419.

[15] `http://background.uchicago.edu/~whu/intermediate/baryons.html`

[16] V. Springel *et al.*, *"First results from the IllustrisTNG simulations: matter and galaxy clustering,"* arXiv:1707.03397 [astro-ph.GA].

[17] J. A. Peacock and S. J. Dodds, *"Reconstructing the linear power spectrum of cosmological mass fluctuations,"* Mon. Not. Roy. Astron. Soc. **267** (1994) 1020 Doi:10.1093/mnras/267.4.1020 [astro-ph/9311057].

[18] Y. Wang, R. J. Brunner and J. C. Dolence, *"The SDSS Galaxy Angular Two-Point Correlation Function,"* Mon. Not. Roy. Astron. Soc. **432** (2013) 1961 Doi:10.1093/mnras/stt450 [arXiv:1303.2432 [astro-ph.CO]].

[19] M. Ata *et al.*, *"The clustering of the SDSS-IV extended Baryon Oscillation Spectroscopic Survey DR14 quasar sample: first measurement of baryon acoustic oscillations between redshift 0.8 and 2.2,"* Mon. Not. Roy. Astron. Soc. **473** (2018) no.4, 4773 Doi:10.1093/mnras/stx2630 [arXiv:1705.06373 [astro-ph.CO]].

[20] B. A. Bassett and R. Hlozek, *"Baryon Acoustic Oscillations,"* Dark Energy, Ed. P. Ruiz-Lapuente (2010, ISBN-13: 9780521518888) [arXiv:0910.5224 [astro-ph.CO]].

[21] H. C. van de Hulst, E. Raimond, and H. van Woerden, *"Rotation and density distribution of the Andromeda nebula derived from observations of the 21-cm line"* Bulletin of the Astronomical Institutes of the Netherlands, Vol. **14**, p.1.

[22] V. C. Rubin, N. Thonnard, W. K. , Jr. Ford, *"Extended rotation curves of high-luminosity spiral galaxies. IV - Systematic dynamical properties, SA through SC"*, Astrophysical Journal, Part 2 - Letters to the Editor, vol. **225**, Nov. 1, 1978, p. L107-L111.

[23] F. D.Kahn and L. Woltjer, *"Intergalactic Matter and the Galaxy"*, Astrophysical Journal, vol. **130**, p.705. Doi:10.1086/146762.

[24] W. Tucker *et al.*, *"1E0657-56: a contender for the hottest known cluster of galaxies,"* Astrophys. J. **496** (1998) L5. Doi:10.1086/311234 [astro-ph/9801120].

[25] D. Clowe, M. Bradac, A. H. Gonzalez, M. Markevitch, S. W. Randall, C. Jones and D. Zaritsky, *"A direct empirical proof of the existence of dark matter,"* Astrophys. J. **648** (2006) L109. Doi:10.1086/508162 [astro-ph/0608407].

[26] E. J. Tollerud, J. S. Bullock, L. E. Strigari and B. Willman, *"Hundreds of Milky Way Satellites? Luminosity Bias in the Satellite Luminosity Function,"* Astrophys. J. **688** (2008) 277. Doi:10.1086/592102 [arXiv:0806.4381 [astro-ph]].

[27] `http://space.mit.edu/home/tegmark/sdss.html`

[28] S. Tulin and H. B. Yu, *"Dark Matter Self-interactions and Small Scale Structure,"* arXiv:1705.02358 [hep-ph].

[29] A. Pontzen and F. Governato, *"Cold dark matter heats up,"* Nature **506** (2014) 171. Doi:10.1038/nature12953 [arXiv:1402.1764 [astro-ph.CO]].

[30] M. Kawasaki, A. Kusenko, Y. Tada and T. T. Yanagida, *"Primordial black holes as dark matter in supergravity inflation models,"* Phys. Rev. D **94** (2016) no.8, 083523. Doi:10.1103/PhysRevD.94.083523 [arXiv:1606.07631 [astro-ph.CO]].

[31] S. Tremaine and J. E. Gunn, *"Dynamical Role of Light Neutral Leptons in Cosmology,"* Phys. Rev. Lett. **42** (1979) 407. Doi:10.1103/PhysRevLett.42.407.

[32] T. D. Brandt, *"Constraints on MACHO Dark Matter from Compact Stellar Systems in Ultra-Faint Dwarf Galaxies,"* Astrophys. J. **824** (2016) no.2, L31 Doi:10.3847/2041-8205/824/2/L31 [arXiv:1605.03665 [astro-ph.GA]].

[33] K. Griest and M. Kamionkowski, *"Unitarity Limits on the Mass and Radius of Dark Matter Particles,"* Phys. Rev. Lett. **64** (1990) 615. Doi:10.1103/PhysRevLett.64.615.

[34] H. Baer, K. Y. Choi, J. E. Kim and L. Roszkowski, *"Dark matter production in the early Universe: beyond the thermal WIMP paradigm,"* Phys. Rept. **555** (2015) 1. Doi:10.1016/j.physrep.2014.10.002 [arXiv:1407.0017 [hep-ph]].

[35] M. Klasen, M. Pohl and G. Sigl, *"Indirect and direct search for dark matter,"* Prog. Part. Nucl. Phys. **85** (2015) 1. Doi:10.1016/j.ppnp.2015.07.001 [arXiv:1507.03800 [hep-ph]].

[36] M. Taoso, G. Bertone and A. Masiero, *"Dark Matter Candidates: A Ten-Point Test,"* JCAP **0803** (2008) 022. Doi:10.1088/1475-7516/2008/03/022 [arXiv:0711.4996 [astro-ph]].

[37] C. Dvorkin, K. Blum and M. Kamionkowski, *"Constraining Dark Matter-Baryon Scattering with Linear Cosmology,"* Phys. Rev. D **89** (2014) no.2, 023519. Doi:10.1103/PhysRevD.89.023519 [arXiv:1311.2937 [astro-ph.CO]].

[38] K. Kadota, T. Sekiguchi and H. Tashiro, *"A new constraint on millicharged dark matter from galaxy clusters,"* arXiv:1602.04009 [astro-ph.CO].

[39] N. Vinyoles and H. Vogel, *"Minicharged Particles from the Sun: A Cutting-Edge Bound,"* JCAP **1603** (2016) no.03, 002. Doi:10.1088/1475-7516/2016/03/002 [arXiv:1511.01122 [hep-ph]].

[40] C. S. Frenk and S. D. M. White, *"Dark matter and cosmic structure,"* Annalen Phys. **524** (2012) 507. Doi:10.1002/andp.201200212 [arXiv:1210.0544 [astro-ph.CO]].

[41] G. R. Blumenthal, S. M. Faber, J. R. Primack and M. J. Rees, *"Formation of Galaxies and Large Scale Structure with Cold Dark Matter,"* Nature **311** (1984) 517. Doi:10.1038/311517a0.

[42] M. Goetz and J. Sommer-Larsen, *"Galaxy formation: warm dark matter, missing satellites, and the angular momentum problem,"* Astrophys. Space Sci. **284** (2003) 341. Doi:10.1023/A:1024073909753 [astro-ph/0210599].

[43] F. Couchot, S. Henrot-Versillé, O. Perdereau, S. Plaszczynski, B. Rouillé D'Orfeuil, M. Spinelli and M. Tristram, *"Cosmological constraints on the neutrino mass including systematic uncertainties,"* Astron. Astrophys. [Astron. Astrophys. **606** (2017) A104]. Doi:10.1051/0004-6361/201730927 [arXiv:1703.10829 [astro-ph.CO]].

[44] S. W. Randall, M. Markevitch, D. Clowe, A. H. Gonzalez and M. Bradac, *"Constraints on the Self-Interaction Cross-Section of Dark Matter from Numerical Simulations of the Merging Galaxy Cluster 1E 0657-56,"* Astrophys. J. **R679** (2008) 1173. Doi:10.1086/587859 [arXiv:0704.0261 [astro-ph]].

[45] M. Kaplinghat, S. Tulin and H. B. Yu, *"Dark Matter Halos as Particle Colliders: Unified Solution to Small-Scale Structure Puzzles from Dwarfs to Clusters,"* Phys. Rev. Lett. **116** (2016) no.4, 041302. Doi:10.1103/PhysRevLett.116.041302 [arXiv:1508.03339 [astro-ph.CO]].

[46] G. Gelmini and P. Gondolo, *"DM Production Mechanisms,"* In Bertone, G. : *"Particle dark matter"* 121-141 [arXiv:1009.3690 [astro-ph.CO]].

[47] L. J. Hall, K. Jedamzik, J. March-Russell and S. M. West, *"Freeze-In Production of FIMP Dark Matter,"* JHEP **1003** (2010) 080 Doi:10.1007/JHEP03(2010)080 [arXiv:0911.1120 [hep-ph]].

[48] A. M. Boesgaard and G. Steigman, *"Big Bang Nucleosynthesis: Theories and Observations,"* Ann. Rev. Astron. Astrophys. **23** (1985) 319. Doi:10.1146/annurev.aa.23.090185.001535

[49] E. Fermi, *"Trends to a Theory of beta Radiation. (In Italian),"* Nuovo Cim. **11** (1934) 1. Doi:10.1007/BF02959820

[50] W. Buchmuller and D. Wyler, *"Effective Lagrangian Analysis of New Interactions and Flavor Conservation,"* Nucl. Phys. B **268** (1986) 621. Doi:10.1016/0550-3213(86)90262-2

[51] H. Georgi, *"Effective field theory,"* Ann. Rev. Nucl. Part. Sci. **43** (1993) 209. Doi:10.1146/annurev.ns.43.120193.001233

[52] T. Marrodán Undagoitia and L. Rauch, *"Dark matter direct-detection experiments,"* J. Phys. G **43** (2016) no.1, 013001. Doi:10.1088/0954-3899/43/1/013001 [arXiv:1509.08767 [physics.ins-det]].

[53] T. Piffl *et al.*, *"The RAVE survey: the Galactic escape speed and the mass of the Milky Way,"* Astron. Astrophys. **562** (2014) A91. Doi:10.1051/0004-6361/201322531 [arXiv:1309.4293 [astro-ph.GA]].

[54] J. D. Vergados, S. H. Hansen and O. Host, *"The impact of going beyond the Maxwell distribution in direct dark matter detection rates,"* Phys. Rev. D **77** (2008) 023509. Doi:10.1103/PhysRevD.77.023509 [arXiv:0711.4895 [astro-ph]].

[55] N. Bozorgnia, R. Catena and T. Schwetz, *"Anisotropic dark matter distribution functions and impact on WIMP direct detection,"* JCAP **1312** (2013) 050. Doi:10.1088/1475-7516/2013/12/050 [arXiv:1310.0468 [astro-ph.CO]].

[56] M. Vogelsberger *et al.*, *"Phase-space structure in the local dark matter distribution and its signature in direct detection experiments,"* Mon. Not. Roy. Astron. Soc. **395** (2009) 797. Doi:10.1111/j.1365-2966.2009.14630.x [arXiv:0812.0362 [astro-ph]].

[57] A. Tan *et al.* [PandaX-II Collaboration], *"Dark Matter Results from First 98.7 Days of Data from the PandaX-II Experiment,"* Phys. Rev. Lett. **117** (2016) no.12, 121303. Doi:10.1103/PhysRevLett.117.121303 [arXiv:1607.07400 [hep-ex]].

[58] E. Aprile *et al.* [XENON100 Collaboration], *"XENON100 Dark Matter Results from a Combination of 477 Live Days,"* Phys. Rev. D **94** (2016) no.12, 122001. Doi:10.1103/PhysRevD.94.122001 [arXiv:1609.06154 [astro-ph.CO]].

[59] D. S. Akerib *et al.* [LUX Collaboration], *"Results from a search for dark matter in the complete LUX exposure,"* Phys. Rev. Lett. **118** (2017) no.2, 021303. Doi:10.1103/PhysRevLett.118.021303 [arXiv:1608.07648 [astro-ph.CO]].

[60] E. Aprile *et al.* [XENON Collaboration], *"First Dark Matter Search Results from the XENON1T Experiment,"* Phys. Rev. Lett. **119** (2017) no.18, 181301. Doi:10.1103/PhysRevLett.119.181301 [arXiv:1705.06655 [astro-ph.CO]].

[61] R. Bernabei *et al.* [DAMA Collaboration], *"First results from DAMA/LIBRA and the combined results with DAMA/NaI,"* Eur. Phys. J. C **56** (2008) 333. Doi:10.1140/epjc/s10052-008-0662-y [arXiv:0804.2741 [astro-ph]].

[62] R. Agnese *et al.* [SuperCDMS Collaboration], *"Search for Low-Mass Weakly Interacting Massive Particles with SuperCDMS,"* Phys. Rev. Lett. **112** (2014) no.24, 241302. Doi:10.1103/PhysRevLett.112.241302 [arXiv:1402.7137 [hep-ex]].

[63] C. E. Aalseth *et al.* [CoGeNT Collaboration], *"Search for An Annual Modulation in Three Years of CoGeNT Dark Matter Detector Data,"* arXiv:1401.3295 [astro-ph.CO].

[64] E. Barbosa de Souza *et al.* [DM-Ice Collaboration], *"First search for a dark matter annual modulation signal with NaI(Tl) in the Southern Hemisphere by DM-Ice17,"* Phys. Rev. D **95** (2017) no.3, 032006. Doi:10.1103/PhysRevD.95.032006 [arXiv:1602.05939 [physics.ins-det]].

[65] R. Essig, J. Mardon and T. Volansky, *"Direct Detection of Sub-GeV Dark Matter,"* Phys. Rev. D **85** (2012) 076007. Doi:10.1103/PhysRevD.85.076007 [arXiv:1108.5383 [hep-ph]].

[66] T. M. Hong, *"Dark matter searches at the LHC,"* arXiv:1709.02304 [hep-ex].

[67] M. Aaboud *et al.* [ATLAS Collaboration], *"Search for resonances in diphoton events at $\sqrt{s}$=13 TeV with the ATLAS detector,"* JHEP **1609** (2016) 001. Doi:10.1007/JHEP09(2016)001 [arXiv:1606.03833 [hep-ex]].

[68] V. Khachatryan *et al.* [CMS Collaboration], *"Search for Resonant Production of High-Mass Photon Pairs in Proton-Proton Collisions at $\sqrt{s}$ =8 and 13 TeV,"* Phys. Rev. Lett. **117** (2016) no.5, 051802. Doi:10.1103/PhysRevLett.117.051802 [arXiv:1606.04093 [hep-ex]].

[69] G. Aad *et al.* [ATLAS Collaboration], *"Search for invisible decays of a Higgs boson using vector-boson fusion in pp collisions at $\sqrt{s} = 8$ TeV with the ATLAS detector,"* JHEP **1601** (2016) 172. Doi:10.1007/JHEP01(2016)172 [arXiv:1508.07869 [hep-ex]].

[70] A. W. Strong, I. V. Moskalenko and V. S. Ptuskin, *"Cosmic-ray propagation and interactions in the Galaxy,"* Ann. Rev. Nucl. Part. Sci. **57** (2007) 285. Doi:10.1146/annurev.nucl.57.090506.123011 [astro-ph/0701517].

[71] T. Delahaye, R. Lineros, F. Donato, N. Fornengo and P. Salati, *"Positrons from dark matter annihilation in the galactic halo: Theoretical uncertainties,"* Phys. Rev. D **77** (2008) 063527. Doi:10.1103/PhysRevD.77.063527 [arXiv:0712.2312 [astro-ph]].

[72] R. Kissmann, *"PICARD: A novel code for the Galactic Cosmic Ray propagation problem,"* Astropart. Phys. **55** (2014) 37. Doi:10.1016/j.astropartphys.2014.02.002 [arXiv:1401.4035 [astro-ph.HE]].

[73] C. Evoli, D. Gaggero, A. Vittino, G. Di Bernardo, M. Di Mauro, A. Ligorini, P. Ullio and D. Grasso, *"Cosmic-ray propagation with DRAGON2: I. numerical solver and astrophysical ingredients,"* JCAP **1702** (2017) no.02, 015. Doi:10.1088/1475-7516/2017/02/015 [arXiv:1607.07886 [astro-ph.HE]].

[74] S. Della Torre *et al.*, *"HelMod: A Comprehensive Treatment of the Cosmic Ray Transport Through the Heliosphere,"* arXiv:1612.08445 [astro-ph.HE].

[75] M. Cirelli *et al.*, *"PPPC 4 DM ID: A Poor Particle Physicist Cookbook for Dark Matter Indirect Detection,"* JCAP **1103**, 051 (2011) [Erratum-ibid. **1210**, E01 (2012)] [arXiv:1012.4515 [hep-ph], arXiv:1012.4515 [hep-ph]].

[76] V. Formato [AMS-02 Collaboration], *"Precision Measurement of Boron-to-Carbon ratio in Cosmic Rays from 2 GV to 2 TV with the Alpha Magnetic Spectrometer on the International Space Station,"* arXiv:1612.09160 [astro-ph.HE].

[77] F. Donato, N. Fornengo, D. Maurin and P. Salati, *"Antiprotons in cosmic rays from neutralino annihilation,"* Phys. Rev. D **69** (2004) 063501 [arXiv:0306207 [astro-ph]].

[78] P. Gondolo, G. Gelmini and S. Sarkar, *"Cosmic neutrinos from unstable relic particles,"* Nucl. Phys. B **392** (1993) 111 Doi:10.1016/0550-3213(93)90199-Y [hep-ph/9209236].

[79] E. Sefusatti, G. Zaharijas, P. D. Serpico, D. Theurel and M. Gustafsson, *"Extragalactic gamma-ray signal from dark matter annihilation: an appraisal,"* Mon. Not. Roy. Astron. Soc. **441** (2014) no.3, 1861. Doi:10.1093/mnras/stu686 [arXiv:1401.2117 [astro-ph.CO]].

[80] M. Di Mauro, F. Donato, N. Fornengo, R. Lineros and A. Vittino, *"Interpretation of AMS-02 electrons and positrons data,"* JCAP **1404** (2014) 006. Doi:10.1088/1475-7516/2014/04/006 [arXiv:1402.0321 [astro-ph.HE]].

[81] O. Adriani *et al.* [Pamela Collaboration], *"An anomalous positron abundance in cosmic rays with energies 1.5-100 GeV,"* Nature **458** (2009) 607. Doi:10.1038/nature07942 [arXiv:0810.4995 [astro-ph]].

[82] J. Chang *et al.*, *"An excess of cosmic ray electrons at energies of 300-800 GeV,"* Nature **456** (2008) 362. Doi:10.1038/nature07477.

[83] S. Torii *et al.* [PPB-BETS Collaboration], *"High-energy electron observations by PPB-BETS flight in Antarctica,"* arXiv:0809.0760 [astro-ph].

[84] A. A. Abdo *et al.* [Fermi-LAT Collaboration], *"Measurement of the Cosmic Ray e+ plus e- spectrum from 20 GeV to 1 TeV with the Fermi Large Area Telescope,"* Phys. Rev. Lett. **102** (2009) 181101. Doi:10.1103/PhysRevLett.102.181101 [arXiv:0905.0025 [astro-ph.HE]].

[85] M. Aguilar *et al.* [AMS Collaboration], *"First Result from the Alpha Magnetic Spectrometer on the International Space Station: Precision Measurement of the Positron Fraction in Primary Cosmic Rays of 0.5–350 GeV,"* Phys. Rev. Lett. **110** (2013) 141102. Doi:10.1103/PhysRevLett.110.141102.

[86] M. Di Mauro, F. Donato, N. Fornengo and A. Vittino, *"Dark matter vs. astrophysics in the interpretation of AMS-02 electron and positron data,"* JCAP **1605** (2016) no.05, 031. Doi:10.1088/1475-7516/2016/05/031 [arXiv:1507.07001 [astro-ph.HE]].

[87] T. Bringmann, F. Calore, M. Di Mauro and F. Donato, *"Constraining dark matter annihilation with the isotropic γ-ray background: updated limits and future potential,"* Phys. Rev. D **89** (2014) no.2, 023012. Doi:10.1103/PhysRevD.89.023012 [arXiv:1303.3284 [astro-ph.CO]].

[88] M. Di Mauro and F. Donato, *"Composition of the Fermi-LAT isotropic gamma-ray background intensity: Emission from extragalactic point sources and dark matter annihilations,"* Phys. Rev. D **91** (2015) 123001 [arXiv:1501.05316 [astro-ph.HE]].

[89] L. A. Cavasonza, H. Gast, M. Krämer, M. Pellen and S. Schael, *"Constraints on leptophilic dark matter from the AMS-02 experiment,"* Astrophys. J. **839** (2017) no.1, 36. Doi:10.3847/1538-4357/aa624d [arXiv:1612.06634 [hep-ph]].

[90] O. Adriani *et al.*, *"Measurement of the flux of primary cosmic ray antiprotons with energies of 60-MeV to 350-GeV in the Pamela experiment,"* JETP Lett. **96** (2013) 621 [Pisma Zh. Eksp. Teor. Fiz. **96** (2012) 693]. Doi:10.1134/S002136401222002X.

[91] M. Aguilar *et al.* [AMS Collaboration], *"Precision Measurement of the Proton Flux in Primary Cosmic Rays from Rigidity 1 GV to 1.8 TV with the Alpha Magnetic Spectrometer on the International Space Station,"* Phys. Rev. Lett. **114** (2015) 171103. Doi:10.1103/PhysRevLett.114.171103.

[92] G. Giesen, M. Boudaud, Y. Génolini, V. Poulin, M. Cirelli, P. Salati and P. D. Serpico, *"AMS-02 antiprotons, at last! Secondary astrophysical component and immediate implications for Dark Matter,"* JCAP **1509** (2015) no.09, 023. Doi:10.1088/1475-7516/2015/09/023, 10.1088/1475-7516/2015/9/023 [arXiv:1504.04276 [astro-ph.HE]].

[93] E. Bulbul, M. Markevitch, A. Foster, R. K. Smith, M. Loewenstein and S. W. Randall, *"Detection of An Unidentified Emission Line in the Stacked X-ray spectrum of Galaxy Clusters,"* Astrophys. J. **789** (2014) 13. Doi:10.1088/0004-637X/789/1/13 [arXiv:1402.2301 [astro-ph.CO]].

[94] W. N. Johnson, F. R. ,Jr. Harnden, R. C. Haymes, *"The Spectrum of Low-Energy Gamma Radiation from the Galactic-Center Region."* Astrophysical Journal, vol. **172**, p.L1.

[95] T. Bringmann, X. Huang, A. Ibarra, S. Vogl and C. Weniger, *"Fermi LAT Search for Internal Bremsstrahlung Signatures from Dark Matter Annihilation,"* JCAP **1207** (2012) 054. Doi:10.1088/1475-7516/2012/07/054 [arXiv:1203.1312 [hep-ph]].

[96] C. Weniger, *"A Tentative Gamma-Ray Line from Dark Matter Annihilation at the Fermi Large Area Telescope,"* JCAP **1208** (2012) 007. Doi:10.1088/1475-7516/2012/08/007 [arXiv:1204.2797 [hep-ph]].

[97] M. Ackermann *et al.* [Fermi-LAT Collaboration], *"Search for gamma-ray spectral lines with the Fermi large area telescope and dark matter implications,"* Phys. Rev. D **88**, 082002 (2013) [arXiv:1305.5597 [astro-ph.HE]].

[98] L. Goodenough and D. Hooper, *"Possible Evidence For Dark Matter Annihilation In The Inner Milky Way From The Fermi Gamma Ray Space Telescope,"* arXiv:0910.2998 [hep-ph].

[99] V. Vitale *et al.* [Fermi-LAT Collaboration], *"Indirect Search for Dark Matter from the center of the Milky Way with the Fermi-Large Area Telescope,"* arXiv:0912.3828 [astro-ph.HE].

[100] K. N. Abazajian and M. Kaplinghat, *"Detection of a Gamma-Ray Source in the Galactic Center Consistent with Extended Emission from Dark Matter Annihilation and Concentrated Astrophysical Emission,"* Phys. Rev. D **86** (2012) 083511 Erratum: [Phys. Rev. D **87** (2013) 129902] Doi:10.1103/PhysRevD.86.083511, 10.1103/PhysRevD.87.129902 [arXiv:1207.6047 [astro-ph.HE]].

[101] M. Ackermann *et al.* [Fermi-LAT Collaboration], *"The Fermi Galactic Center GeV Excess and Implications for Dark Matter,"* Astrophys. J. **840** (2017) no.1, 43. Doi:10.3847/1538-4357/aa6cab [arXiv:1704.03910 [astro-ph.HE]].

[102] J. Knodlseder *et al.*, *"The All-sky distribution of 511 keV electron-positron annihilation emission,"* Astron. Astrophys. **441** (2005) 513. Doi:10.1051/0004-6361:20042063 [astro-ph/0506026].

[103] N. Prantzos *et al.*, *"The 511 keV emission from positron annihilation in the Galaxy,"* Rev. Mod. Phys. **83** (2011) 1001. Doi:10.1103/RevModPhys.83.1001 [arXiv:1009.4620 [astro-ph.HE]].

[104] F. A. Aharonian *et al.* [Hitomi Collaboration], *"$Hitomi$ constraints on the 3.5 keV line in the Perseus galaxy cluster,"* Astrophys. J. **837** (2017) no.1, L15. Doi:10.3847/2041-8213/aa61fa [arXiv:1607.07420 [astro-ph.HE]].

[105] F. Takayama and M. Yamaguchi, *"Gravitino dark matter without R-parity,"* Phys. Lett. B **485** (2000) 388 [hep-ph/0005214].

[106] W. Buchmuller, L. Covi, K. Hamaguchi, A. Ibarra and T. Yanagida, *"Gravitino Dark Matter in R-Parity Breaking Vacua,"* JHEP **0703**, 037 (2007) [hep-ph/0702184 [HEP-PH]].

[107] A. Ibarra, S. Lopez Gehler and M. Pato, *"Dark matter constraints from box-shaped gamma-ray features,"* JCAP **1207** (2012) 043 [arXiv:1205.0007 [hep-ph]].

[108] L. Bergstrom, T. Bringmann, M. Eriksson and M. Gustafsson, *"Gamma rays from Kaluza-Klein dark matter,"* Phys. Rev. Lett. **94**, 131301 (2005) [astro-ph/0410359].

[109] L. Bergstrom, T. Bringmann, M. Eriksson and M. Gustafsson, *"Gamma rays from heavy neutralino dark matter,"* Phys. Rev. Lett. **95**, 241301 (2005) [hep-ph/0507229].

[110] T. Bringmann, L. Bergstrom and J. Edsjo, *"New Gamma-Ray Contributions to Supersymmetric Dark Matter Annihilation,"* JHEP **0801** (2008) 049 [arXiv:0710.3169 [hep-ph]].

[111] M. Ackermann *et al.* [Fermi-LAT Collaboration], *"Updated search for spectral lines from Galactic dark matter interactions with pass 8 data from the Fermi Large Area Telescope,"* Phys. Rev. D **91** (2015) 12, 122002. Doi:10.1103/PhysRevD.91.122002 [arXiv:1506.00013 [astro-ph.HE]].

[112] A. Abramowski *et al.* [H.E.S.S. Collaboration], *"Search for photon line-like signatures from Dark Matter annihilations with H.E.S.S,"* Phys. Rev. Lett. **110** (2013) 041301 [arXiv:1301.1173 [astro-ph.HE]].

[113] H. Abdalla *et al.* [H.E.S.S. Collaboration], *"H.E.S.S. Limits on Linelike Dark Matter Signatures in the 100 GeV to 2 TeV Energy Range Close to the Galactic Center,"* Phys. Rev. Lett. **117** (2016) no.15, 151302. Doi:10.1103/PhysRevLett.117.151302 [arXiv:1609.08091 [astro-ph.HE]].

[114] M. Gustafsson, T. Hambye and T. Scarna, *"Effective Theory of Dark Matter Decay into Monochromatic Photons and its Implications: Constraints from Associated Cosmic-Ray Emission,"* Phys. Lett. B **724** (2013) 288 [arXiv:1303.4423 [hep-ph]].

[115] M. G. Aartsen *et al.* [IceCube Collaboration], *"Energy Reconstruction Methods in the IceCube Neutrino Telescope,"* JINST **9** (2014) P03009 [arXiv:1311.4767 [physics.ins-det]].

[116] M. G. Aartsen *et al.* [IceCube Collaboration], *"Multipole analysis of IceCube data to search for dark matter accumulated in the Galactic halo,"* Eur. Phys. J. C **75** (2015) no.99, 20 Doi:10.1140/epjc/s10052-014-3224-5 [arXiv:1406.6868 [astro-ph.HE]].

[117] S. Adrian-Martinez *et al.* [ANTARES Collaboration], *"Search of Dark Matter Annihilation in the Galactic Centre using the ANTARES Neutrino Telescope,"* JCAP **1510** (2015) no.10, 068 Doi:10.1088/1475-7516/2015/10/068 [arXiv:1505.04866 [astro-ph.HE]].

[118] R. Abbasi *et al.* [IceCube Collaboration], *"Search for dark matter from the Galactic halo with the IceCube Neutrino Telescope,"* Phys. Rev. D **84** (2011) 022004 Doi:10.1103/PhysRevD.84.022004 [arXiv:1101.3349 [astro-ph.HE]].

[119] F. S. Queiroz, C. E. Yaguna and C. Weniger, *"Gamma-ray Limits on Neutrino Lines,"* JCAP **1605** (2016) no.05, 050 Doi:10.1088/1475-7516/2016/05/050 [arXiv:1602.05966 [hep-ph]].

[120] M. G. Aartsen *et al.* [IceCube Collaboration], *"Search for Neutrinos from Dark Matter Self-Annihilations in the center of the Milky Way with 3 years of IceCube/DeepCore,"* Eur. Phys. J. C **77** (2017) no.9, 627 Doi:10.1140/epjc/s10052-017-5213-y [arXiv:1705.08103 [hep-ex]].

[121] C. El Aisati, T. Hambye and T. Scarnà, *"Can a millicharged dark matter particle emit an observable γ-ray line?,"* JHEP **1408** (2014) 133 [arXiv:1403.1280 [hep-ph]].

[122] B. Holdom, *"Two U(1)'s and Epsilon Charge Shifts"*, Phys. Lett. B **166** (1986) 196.

[123] R. Foot and X. -G. He, *"Comment on Z-Z' mixing in extended gauge theories"*, Phys. Lett. B **267** (1991) 509.

[124] B. Kors, P. Nath, *"A Stueckelberg extension of the Standard Model"*, Phys. Lett. B **586** (2004) 366-372 [arXiv:0402047[hep-ph]].

[125] D. Feldman, Z. Liu, P. Nath, *"Probing a very narrow Z-prime boson with CDF and D0 data"*, Phys.Rev.Lett. **97** (2006) 021801 [arXiv:0603039[hep-ph]].

[126] O. Adriani *et al.* [Pamela Collaboration], *"Pamela results on the cosmic-ray antiproton flux from 60 MeV to 180 GeV in kinetic energy,"* Phys. Rev. Lett. **105**, 121101 (2010) [arXiv:1007.0821 [astro-ph.HE]].

[127] A. A. Abdo *et al.* [Fermi-LAT Collaboration], *"The Spectrum of the Isotropic Diffuse Gamma-Ray Emission Derived From First-Year Fermi Large Area Telescope Data,"* Phys. Rev. Lett. **104** (2010) 101101. Doi:10.1103/PhysRevLett.104.101101 [arXiv:1002.3603 [astro-ph.HE]].

[128] Fourth International Fermi Symposium, October 28-November 2, 2012, Monterey, USA `http://Fermi.gsfc.nasa.gov/science/mtgs/symposia/2012/program/fri/AAlbert.pdf`

[129] A. A. Abdo *et al.* [Fermi-LAT Collaboration], *The Spectrum of the Isotropic Diffuse Gamma-Ray Emission Derived From First-Year Fermi Large Area Telescope Data*, Phys. Rev. Lett. **104** (2010) 101101 [arXiv:1002.3603 [astro-ph.HE]].

[130] A. Abramowski *et al.* [H.E.S.S. Collaboration], *Search for photon line-like signatures from Dark Matter annihilations with H.E.S.S*, Phys. Rev. Lett. **110** (2013) 041301 [arXiv:1301.1173 [astro-ph.HE]].

[131] D. Feldman, Z. Liu and P. Nath, *"The Stueckelberg Z-prime Extension with Kinetic Mixing and Milli-Charged Dark Matter From the Hidden Sector,"* Phys. Rev. D **75** (2007) 115001 [arXiv:0702123 [hep-ph]].

[132] N. F. Bell, A. J. Galea and K. Petraki, *"Lifetime Constraints for Late Dark Matter Decay"*, Phys. Rev. D **82** (2010) 023514 [arXiv:1004.1008 [astro-ph.HE]].

[133] M. Frigerio, T. Hambye and E. Masso, *"Sub-GeV dark matter as pseudo-Goldstone from the seesaw scale"*, Phys. Rev. X **1** (2011) 021026 [arXiv:1107.4564 [hep-ph]].

[134] C. El Aisati, M. Gustafsson, T. Hambye and T. Scarna, *"Dark Matter Decay to a Photon and a Neutrino: the Double Monochromatic Smoking Gun Scenario,"* Phys. Rev. D **93** (2016) no.4, 043535. Doi:10.1103/PhysRevD.93.043535 [arXiv:1510.05008 [hep-ph]].

[135] A. Esmaili, A. Ibarra and O. L. G. Peres, *"Probing the stability of superheavy dark matter particles with high-energy neutrinos,"* JCAP **1211** (2012) 034 [arXiv:1205.5281 [hep-ph]].

[136] C. Rott, K. Kohri and S. C. Park, *"Superheavy dark matter and IceCube neutrino signals: Bounds on decaying dark matter,"* Phys. Rev. D **92** (2015) 2, 023529. Doi:10.1103/PhysRevD.92.023529 [arXiv:1408.4575 [hep-ph]].

[137] A. Esmaili, S. K. Kang and P. D. Serpico, *"IceCube events and decaying dark matter: hints and constraints,"* JCAP **12** (2014) 054 [arXiv:1410.5979 [hep-ph]].

[138] B. Feldstein, A. Kusenko, S. Matsumoto and T. T. Yanagida, *"Neutrinos at IceCube from Heavy Decaying Dark Matter,"* Phys. Rev. D **88** (2013) 1, 015004 [arXiv:1303.7320 [hep-ph]].

[139] C. El Aisati, M. Gustafsson and T. Hambye, *"New Search for Monochromatic Neutrinos from Dark Matter Decay,"* Phys. Rev. D **92** (2015) no.12, 123515. Doi:10.1103/PhysRevD.92.123515 [arXiv:1506.02657 [hep-ph]].

[140] M. Ackermann *et al.* [Fermi-LAT Collaboration], *"The spectrum of isotropic diffuse gamma-ray emission between 100 MeV and 820 GeV,"* Astrophys. J. **799**, 86 (2015) [arXiv:1410.3696 [astro-ph.HE]].

[141] T. Scarnà, *"Gamma-ray lines from the dark side of matter,"* PhD thesis, Sec. 3.4.2, p. 71, `http://difusion.ulb.ac.be/vufind/Record/ULB-DIPOT:oai:dipot.ulb.ac.be:2013/209170/Holdings`

[142] T. Toma, *"Internal Bremsstrahlung Signature of Real Scalar Dark Matter and Consistency with Thermal Relic Density,"* Phys. Rev. Lett. **111** (2013) 091301. Doi:10.1103/PhysRevLett.111.091301 [arXiv:1307.6181 [hep-ph]].

[143] F. Giacchino, L. Lopez-Honorez and M. H. G. Tytgat, *"Scalar Dark Matter Models with Significant Internal Bremsstrahlung,"* JCAP **1310** (2013) 025. Doi:10.1088/1475-7516/2013/10/025 [arXiv:1307.6480 [hep-ph]].

[144] A. Ibarra, T. Toma, M. Totzauer and S. Wild, *"Sharp Gamma-ray Spectral Features from Scalar Dark Matter Annihilations,"* Phys. Rev. D **90** (2014) 4, 043526 [arXiv:1405.6917 [hep-ph]].

[145] F. Giacchino, L. Lopez-Honorez and M. H. G. Tytgat, *"Bremsstrahlung and Gamma Ray Lines in 3 Scenarios of Dark Matter Annihilation,"* JCAP **1408** (2014) 046. Doi:10.1088/1475-7516/2014/08/046. [arXiv:1405.6921 [hep-ph]].

[146] M. Cirelli, N. Fornengo and A. Strumia, *"Minimal dark matter,"* Nucl. Phys. B **753** (2006) 178 [arXiv:0512090 [hep-ph]].

[147] M. Cirelli, A. Strumia and M. Tamburini, *"Cosmology and Astrophysics of Minimal Dark Matter,"* Nucl. Phys. B **787** (2007) 152-175 [arXiv:0706.4071[hep-ph]]

[148] M. Cirelli, T. Hambye, P. Panci, F. Sala and M. Taoso, *"Gamma ray tests of Minimal Dark Matter,"* JCAP **1510** (2015) no.10, 026. Doi:10.1088/1475-7516/2015/10/026 [arXiv:1507.05519 [hep-ph]].

[149] C. Garcia-Cely, A. Ibarra, A. S. Lamperstorfer and M. H. G. Tytgat, *"Gamma-rays from Heavy Minimal Dark Matter,"* JCAP **1510** (2015) no.10, 058. Doi:10.1088/1475-7516/2015/10/058 [arXiv:1507.05536 [hep-ph]].

[150] S. Ando and K. Ishiwata, *"Constraints on decaying dark matter from the extragalactic gamma-ray background,"* JCAP **1505**, no. 05, 024 (2015) [arXiv:1502.02007 [astro-ph.CO]].

[151] AMS-02 Collaboration, Talks at the *"AMS Days at CERN"*, April 15-17, 2015.

[152] A. Ibarra, A. S. Lamperstorfer and J. Silk, *"Dark matter annihilations and decays after the AMS-02 positron measurements,"* Phys. Rev. D **89**, no. 6, 063539 (2014) [arXiv:1309.2570 [hep-ph]].

[153] C. L. Cowan, F. Reines, F. B. Harrison, H. W. Kruse and A. D. McGuire, *"Detection of the free neutrino: A Confirmation,"* Science **124** (1956) 103. DOI:10.1126/science.124.3212.103.

[154] W. Pauli, *"Dear radioactive ladies and gentlemen,"* Phys. Today **31N9** (1978) 27.

[155] P. A. Cherenkov, *"Visible light from clear liquids under the action of gamma radiation,"* C. R. (DokI.) Acad. Sci. URSS 2:451-4, 1934.

[156] G. A. Askaryan, *"Excess negative charge of an electron-photon shower and its coherent radio emission,"* Sov. Phys. JETP **14** (1962) no.2, 441 [Zh. Eksp. Teor. Fiz. **41** (1961) 616].

[157] G. A. Askarian, B. A. Dolgoshein, A. N. Kalinovsky and N. V. Mokhov, *"Acoustic Detection Of High-energy Particle Showers In Water,"* Nucl. Instrum. Meth. **164** (1979) 267. DOI:10.1016/0029-554X(79)90244-1.

[158] The ARIANNA Collaboration, `https://arianna.ps.uci.edu`.

[159] J. A. Vandenbroucke, *"Acoustic detection of astrophysical neutrinos in South Pole ice"*, PhD thesis (2009). University of California, Berkeley.

[160] R. Gandhi, C. Quigg, M. H. Reno and I. Sarcevic, *"Ultrahigh-energy neutrino interactions,"* Astropart. Phys. **5** (1996) 81 DOI:10.1016/0927-6505(96)00008-4 [hep-ph/9512364].

[161] J. A. Formaggio and G. P. Zeller, *"From eV to EeV: Neutrino Cross Sections Across Energy Scales,"* Rev. Mod. Phys. **84** (2012) 1307 DOI:10.1103/RevModPhys.84.1307 [arXiv:1305.7513 [hep-ex]].

[162] S. L. Glashow, *"Resonant Scattering of Antineutrinos,"* Phys. Rev. **118** (1960) 316.

[163] J. D. Jackson, *"Classical Electrodynamics,"* Wiley (1975).

[164] `http://pdg.lbl.gov/2016/AtomicNuclearProperties/HTML/water_ice.html`.

[165] `http://pdg.lbl.gov/2016/reviews/rpp2016-rev-passage-particles-matter.pdf`.

[166] L. D. Landau and I. Pomeranchuk, *"Limits of applicability of the theory of bremsstrahlung electrons and pair production at high-energies,"* Dokl. Akad. Nauk Ser. Fiz. **92** (1953) 535.

[167] D. Chirkin and W. Rhode, *"Muon Monte Carlo: A High-precision tool for muon propagation through matter,"* hep-ph/0407075.

[168] T. DeYoung, S. Razzaque and D. F. Cowen, *"Astrophysical tau neutrino detection in kilometer-scale Cherenkov detectors via muonic tau decay,"* Astropart. Phys. **27** (2007) 238 DOI:10.1016/j.astropartphys.2006.11.003 [astro-ph/0608486].

[169] D. F. Cowen [IceCube Collaboration], *"Tau neutrinos in IceCube,"* J. Phys. Conf. Ser. **60** (2007) 227. DOI:10.1088/1742-6596/60/1/048

[170] M. P. Kowalski, "Search for neutrino induced cascades with the AMANDA-II detector." PhD thesis, Humboldt University (Berlin), 2003.

[171] R. Mohapatra and P. Pal, *"Massive Neutrinos in Physics and Astrophysics"*. World Scientific Lecture Notes in Physics, vol **41**.

[172] B. Pontecorvo, JETP (USSR) **7**, 172 (1958) [Zh. Eksp. Teor. Fiz. 34, 247 (1958)] Z. Maki, M. Nakagawa and S. Sakata, Prog. Theor. Phys. **28**, 870 (1962).

[173] R. Davis, Jr., D. S. Harmer and K. C. Hoffman, *"Search for neutrinos from the sun,"* Phys. Rev. Lett. **20** (1968) 1205. Doi:10.1103/PhysRevLett.20.1205

[174] Y. Fukuda *et al.* [Super-Kamiokande Collaboration], *"Evidence for oscillation of atmospheric neutrinos,"* Phys. Rev. Lett. **81** (1998) 1562 Doi:10.1103/PhysRevLett.81.1562 [hep-ex/9807003].

[175] I. Esteban, M. C. Gonzalez-Garcia, M. Maltoni, I. Martinez-Soler and T. Schwetz, *"Updated fit to three neutrino mixing: exploring the accelerator-reactor complementarity,"* JHEP **1701** (2017) 087 Doi:10.1007/JHEP01(2017)087 [arXiv:1611.01514 [hep-ph]].

[176] L. Wolfenstein, *"Neutrino Oscillations in Matter,"* Phys. Rev. D **17** (1978) 2369. Doi:10.1103/PhysRevD.17.2369

[177] S. P. Mikheev and A. Y. Smirnov, *"Resonant amplification of neutrino oscillations in matter and solar neutrino spectroscopy,"* Nuovo Cim. C **9** (1986) 17. Doi:10.1007/BF02508049

[178] V. A. Naumov, *"High-energy neutrino oscillations in absorbing matter,"* Phys. Lett. B **529** (2002) 199 Doi:10.1016/S0370-2693(02)01258-3 [hep-ph/0112249].

[179] M. Wallraff and C. Wiebusch, *"Calculation of oscillation probabilities of atmospheric neutrinos using nuCraft,"* Comput. Phys. Commun. **197** (2015) 185. Doi:10.1016/j.cpc.2015.07.010 [arXiv:1409.1387 [astro-ph.IM]].

[180] M. A. Markov, *"On high energy neutrino physics"* (1960).

[181] R. Abbasi *et al.* [IceCube Collaboration], *"The IceCube Data Acquisition System: Signal Capture, Digitization, and Timestamping,"* Nucl. Instrum. Meth. A **601** (2009) 294 Doi:10.1016/j.nima.2009.01.001 [arXiv:0810.4930 [physics.ins-det]].

[182] The AMANDA High-Energy Neutrino Detector, `http://amanda.uci.edu`.

[183] C. Wiebusch [IceCube Collaboration], *"Physics Capabilities of the IceCube DeepCore Detector,"* arXiv:0907.2263 [astro-ph.IM].

[184] M. G. Aartsen *et al.* [IceCube Collaboration], *"Measurement of South Pole ice transparency with the IceCube LED calibration system,"* Nucl. Instrum. Meth. A **711** (2013) 73 Doi:10.1016/j.nima.2013.01.054 [arXiv:1301.5361 [astro-ph.IM]].

[185] M. Ackermann *et al.*, *"Optical properties of deep glacial ice at the South Pole,"* J. Geophys. Res. Atmos. **111** (2006) no.D13, D13203. Doi:10.1029/2005JD006687

[186] K. Woschnagg, P. B. Price, *"Temperature dependence of absorption in ice at 532 nm"*, Applied Optics 40 (2001)2496.

[187] D. Chirkin [IceCube Collaboration]. *"Evidence of optical anisotropy of the South Pole ice"*.

[188] A. Einstein, *"Concerning an heuristic point of view toward the emission and transformation of light,"* Annalen Phys. **17** (1905) 132.

[189] A. Achterberg *et al.* [IceCube Collaboration], *"First Year Performance of The IceCube Neutrino Telescope,"* Astropart. Phys. **26** (2006) 155. DOI:10.1016/j.astropartphys.2006.06.007 [astro-ph/0604450].

[190] `https://www.sense-pro.org/lll-sensors/pmt`

[191] M. G. Aartsen *et al.* [IceCube Collaboration], *"The IceCube Neutrino Observatory: Instrumentation and Online Systems,"* JINST **12** (2017) no.03, P03012 DOI:10.1088/1748-0221/12/03/P03012 [arXiv:1612.05093 [astro-ph.IM]].

[192] M. G. Aartsen *et al.* [IceCube Collaboration], *"PINGU: A Vision for Neutrino and Particle Physics at the South Pole,"* J. Phys. G **44** (2017) no.5, 054006. DOI:10.1088/1361-6471/44/5/054006 [arXiv:1607.02671 [hep-ex]].

[193] M. G. Aartsen *et al.* [IceCube Collaboration], *"The IceCube Neutrino Observatory - Contributions to ICRC 2017 Part IV: Searches for Beyond the Standard Model Physics,"* arXiv:1710.01197 [astro-ph.HE].

[194] IceCube Collaboration, `http://icecube.wisc.edu/science/data/HEnu_above1tev`

[195] A. Bhattacharya, M. H. Reno and I. Sarcevic, *"Reconciling neutrino flux from heavy dark matter decay and recent events at IceCube,"* JHEP **1406** (2014) 110 [arXiv:1403.1862 [hep-ph]].

[196] D. Heck, G. Schatz, T. Thouw, J. Knapp and J. N. Capdevielle, *"Corsika: A Monte Carlo code to simulate extensive air showers,"* FZKA-6019.

[197] D. Chirkin, *"Cosmic Ray Energy Spectrum Measurement with the Antarctic Muon and Neutrino Detector Array (AMANDA)"*. PhD thesis. University of California at Berkeley, 2003.

[198] A. Gazizov and M. P. Kowalski, *"Anis: High energy neutrino generator for neutrino telescopes,"* Comput. Phys. Commun. **172** (2005) 203 DOI:10.1016/j.cpc.2005.03.113 [astro-ph/0406439].

[199] C. Andreopoulos *et al.*, *"The Genie Neutrino Monte Carlo Generator,"* Nucl. Instrum. Meth. A **614** (2010) 87 DOI:10.1016/j.nima.2009.12.009 [arXiv:0905.2517 [hep-ph]].

[200] J. K. Becker, *"High-energy neutrinos in the context of multimessenger physics,"* Phys. Rept. **458** (2008) 173 [arXiv:0710.1557 [astro-ph]].

[201] A. Loeb and E. Waxman, *"The Cumulative background of high energy neutrinos from starburst galaxies,"* JCAP **0605** (2006) 003 [astro-ph/0601695].

[202] G. Cowan, *"Statistical Data Analysis"*, Oxford University Press (1998).

[203] J. Van Santen, talk at the ICRC 2017 in Busan, South Korea. `https://indico.snu.ac.kr/indico/event/15/session/3/contribution/689/material/slides/0.pdf`

[204] K. Murase, M. Ahlers and B. C. Lacki, *"Testing the Hadronuclear Origin of PeV Neutrinos Observed with IceCube,"* Phys. Rev. D **88** (2013) no.12, 121301 Doi:10.1103/PhysRevD.88.121301 [arXiv:1306.3417 [astro-ph.HE]].

[205] K. Bechtol, M. Ahlers, M. Di Mauro, M. Ajello and J. Vandenbroucke, *"Evidence against star-forming galaxies as the dominant source of IceCube neutrinos,"* Astrophys. J. **836** (2017) no.1, 47 Doi:10.3847/1538-4357/836/1/47 [arXiv:1511.00688 [astro-ph.HE]].

[206] J. Neyman, Phil. Trans. Royal Soc. London, Series A, 236 333-80 (1937).

[207] M. Gustafsson [Fermi-LAT Collaboration], *"Fermi-LAT and the Gamma-Ray Line Search,"* arXiv:1310.2953 [astro-ph.HE].

[208] R. Abbasi *et al.* [IceCube Collaboration], *"Search for Neutrinos from Annihilating Dark Matter in the Direction of the Galactic Center with the 40-String IceCube Neutrino Observatory,"* arXiv:1210.3557 [hep-ex].

[209] M. G. Aartsen *et al.* [IceCube Collaboration], *"Search for Dark Matter Annihilation in the Galactic Center with IceCube-79,"* Eur. Phys. J. C **75**, no. 10, 492 (2015) [arXiv:1505.07259 [astro-ph.HE]].

[210] G. J. Feldman and R. D. Cousins, *"A Unified approach to the classical statistical analysis of small signals,"* Phys. Rev. D **57**, 3873 (1998) [physics/9711021 [physics.data-an]].

[211] H. Chernoff, Annals Math. Statist. **25**, 573 (1938).

[212] S. Wilks, Annals Math. Statist. **9**, 60 (1938).

[213] A. Esmaili and P. D. Serpico, *"Are IceCube neutrinos unveiling PeV-scale decaying dark matter?,"* JCAP **1311**, 054 (2013) [arXiv:1308.1105 [hep-ph]].

[214] Y. Ema, R. Jinno and T. Moroi, *"Cosmic-Ray Neutrinos from the Decay of Long-Lived Particle and the Recent IceCube Result,"* Phys. Lett. B **733** (2014) 120 [arXiv:1312.3501 [hep-ph]].

[215] Y. Bai, R. Lu and J. Salvado, *"Geometric Compatibility of IceCube TeV-PeV Neutrino Excess and its Galactic Dark Matter Origin,"* arXiv:1311.5864 [hep-ph].

[216] T. Higaki, R. Kitano and R. Sato, *"Neutrinoful Universe,"* JHEP **1407** (2014) 044 [arXiv:1405.0013 [hep-ph]].

[217] A. Bhattacharya, R. Gandhi and A. Gupta, *"The Direct Detection of Boosted Dark Matter at High Energies and PeV events at IceCube,"* JCAP **1503** (2015) 03, 027 [arXiv:1407.3280 [hep-ph]].

[218] Y. Ema, R. Jinno and T. Moroi, *"Cosmological Implications of High-Energy Neutrino Emission from the Decay of Long-Lived Particle,"* JHEP **1410** (2014) 150 [arXiv:1408.1745 [hep-ph]].

[219] C. S. Fong, H. Minakata, B. Panes and R. Z. Funchal, *"Possible Interpretations of IceCube High-Energy Neutrino Events,"* JHEP **1502** (2015) 189 [arXiv:1411.5318 [hep-ph]].

[220] E. Dudas, Y. Mambrini and K. A. Olive, *"Monochromatic neutrinos generated by dark matter and the seesaw mechanism,"* Phys. Rev. D **91** (2015) 7, 075001 [arXiv:1412.3459 [hep-ph]].

[221] K. Murase, R. Laha, S. Ando and M. Ahlers, *"Testing the Dark Matter Scenario for PeV Neutrinos Observed in IceCube,"* Phys. Rev. Lett. **115** (2015) 7, 071301 DOI:10.1103/PhysRevLett.115.071301 [arXiv:1503.04663 [hep-ph]].

[222] E. Gross, `http://people.stat.sfu.ca/~lockhart/richard/banff2010/gross.pdf`

[223] *"Search for signatures of heavy decaying dark matter with IceCube"*, The IceCube Collaboration, `https://pos.sissa.it/301/923/pdf`

[224] M. G. Aartsen *et al.* [IceCube Collaboration], *"IceCube-Gen2: A Vision for the Future of Neutrino Astronomy in Antarctica,"* arXiv:1412.5106 [astro-ph.HE].

[225] M. G. Aartsen *et al.* [IceCube Collaboration], *"IceCube-Gen2 - The Next Generation Neutrino Observatory at the South Pole: Contributions to ICRC 2015,"* arXiv:1510.05228 [astro-ph.IM].

[226] B. Kayser, *"Neutrino physics,"* eConf C **040802**, L004 (2004) [hep-ph/0506165].

[227] H. Taavola, "Dar Matter in the Galactic Halo: A Search Using Neutrino Induced Cascades in the DeepCore Extension of IceCube." (2015). Electronic version available at `https://uu.diva-portal.org/smash/get/diva2:861958/FULLTEXT01.pdf`.

[228] M. G. Aartsen *et al.* [IceCube Collaboration], *"All-flavour Search for Neutrinos from Dark Matter Annihilations in the Milky Way with IceCube/DeepCore,"* Eur. Phys. J. C **76** (2016) no.10, 531. DOI:10.1140/epjc/s10052-016-4375-3 [arXiv:1606.00209 [astro-ph.HE]].

[229] S. Tilav *et al.* [IceCube Collaboration], *"Atmospheric Variations as Observed by IceCube,"* arXiv:1001.0776 [astro-ph.HE].

[230] J. R. Hoerandel, *"On the knee in the energy spectrum of cosmic rays,"* Astropart. Phys. **19** (2003) 193. DOI:10.1016/S0927-6505(02)00198-6 [astro-ph/0210453].

[231] Thomas Gaisser, `https://internal-apps.icecube.wisc.edu/reports/data/icecube/2011/02/004/icecube_201102004_v2.pdf`

[232] M. Honda, T. Kajita, K. Kasahara, S. Midorikawa and T. Sanuki, *"Calculation of atmospheric neutrino flux using the interaction model calibrated with atmospheric muon data,"* Phys. Rev. D **75** (2007) 043006. DOI:10.1103/PhysRevD.75.043006 [astro-ph/0611418].

[233] Christopher Weaver. Code available at `http://code.icecube.wisc.edu/svn/sandbox/cweaver/NewNuFlux`.

[234] D. Chirkin, `http://icecube.wisc.edu/~dima/work/BKP/DCS/MMC/muon.pdf`

[235] D. Chirkin, `http://icecube.wisc.edu/~dima/work/WISC/ppc/`

[236] T. Hastie, R. Tibshirani, J. Friedman, *"The Elements of Statistical Learning"* (Springer, 2009).

[237] J. F. Beacom, N. F. Bell, D. Hooper, S. Pakvasa and T. J. Weiler, *"Decay of high-energy astrophysical neutrinos,"* Phys. Rev. Lett. **90** (2003) 181301 [hep-ph/0211305].

[238] P. Baerwald, M. Bustamante and W. Winter, *"Neutrino Decays over Cosmological Distances and the Implications for Neutrino Telescopes,"* JCAP **1210**, 020 (2012) [arXiv:1208.4600 [astro-ph.CO]].

[239] H. Athar, M. Jezabek and O. Yasuda, *"Effects of neutrino mixing on high-energy cosmic neutrino flux,"* Phys. Rev. D **62**, 103007 (2000) [hep-ph/0005104].

[240] J. F. Beacom, N. F. Bell, D. Hooper, J. G. Learned, S. Pakvasa and T. J. Weiler, *"PseudoDirac neutrinos: A Challenge for neutrino telescopes,"* Phys. Rev. Lett. **92**, 011101 (2004) [hep-ph/0307151].

[241] D. Hooper, D. Morgan and E. Winstanley, *"Lorentz and CPT invariance violation in high-energy neutrinos,"* Phys. Rev. D **72**, 065009 (2005) [hep-ph/0506091].

[242] L. A. Anchordoqui, H. Goldberg, M. C. Gonzalez-Garcia, F. Halzen, D. Hooper, S. Sarkar and T. J. Weiler, *"Probing Planck scale physics with IceCube,"* Phys. Rev. D **72** (2005) 065019 [hep-ph/0506168].